

PLANET FORMATION: PROTOPLANETARY DISK REMOVAL AND ROTATIONAL STABILITY
OF PLANETS

by

Isamu Manuel Matsuyama

A thesis submitted in conformity with the requirements
for the degree of Doctor of Philosophy
Graduate Department of Astronomy and Astrophysics
University of Toronto

Copyright © 2005 by Isamu Manuel Matsuyama

Abstract

Planet formation: protoplanetary disk removal and rotational stability of planets

Isamu Manuel Matsuyama

Doctor of Philosophy

Graduate Department of Astronomy and Astrophysics

University of Toronto

2005

There are many unsolved problems in the physics of planet formation and the evolution of their parent disk is expected to play an important role in resolving them. In part I of this thesis, I discuss the evolution of protoplanetary disks under the influence of viscous evolution, photoevaporation from the central source, and photoevaporation by external stars; and explore the consequences for planet formation.

The discovery of hot jupiters orbiting at a few AU from their stars compliments earlier detections of massive planets on very small orbits. The short period orbits strongly suggest that planet migration has occurred, with the likely mechanism being tidal interactions between the planets and the gas disks out of which they formed. The newly discovered long period planets, together with the gas giant planets in our solar system, show that migration is either absent or rapidly halted in at least some systems. I propose a mechanism for halting type-II migration at several AU in a gas disk: the formation of a photoevaporation gap prevents planets outside the gap from migrating down to the star.

The final planet location relative to the habitable zone is often used to discuss the planet habitability. But a planet in the habitable zone may experience large amplitude motion of its rotation axis, which may cause severe climate variations and have major consequences for the development of life. In part II of this thesis, I investigate the true polar wander (TPW) rotational stability of planets. I revisit the classic problem of the long-term rotational stability of planets in response to loading using a new, generalized theoretical development based on the fluid limit of viscoelastic Love number theory. Finally, I explore the time dependent (rather than the equilibrium fluid limit) rotational stability of planets by considering the example of an ice age Earth. I present a new treatment of the linearized Euler equations that govern rotation perturbations on a viscoelastic planet driven by surface loading.

Acknowledgements

I would like to thank my supervisor, Prof. Norman Murray, for his guidance and for generously providing his time and resources. His easy grasp of physics helped me to complete this thesis.

I am very grateful to my geophysics supervisor, Prof. Jerry Mitrovica, for his enthusiastic support and guidance throughout the Ph.D. program. Jerry, it has been a pleasure to work with you and I look forward to many years of friendship and collaboration.

I couldn't have made it without the enthusiastic support and guidance of my M.Sc. supervisor, Prof. Doug Johnstone. Doug, thank you for pushing me and guiding me through the first steps of the graduate program. I hope that our friendship and collaboration continues for many years to come.

I learned much from the many discussions with Prof. Yanquin Wu. I would like to acknowledge Professors Jayawardhana and O'Connell for serving on my examination committee. Special thanks to Prof. O'Connell for agreeing to be my external reviewer and for providing constructive comments. I have learned and benefited much from the scientific collaborations with Lee Hartmann, John Wahr, Archie Paulson, Taylor Perron, Michael Manga, and Mark Richards.

I would like to thank Marc Goodman, Margaret Fukunaga, and Maria Wong for always being very helpful.

I owe my deepest gratitude to my parents, Myriam and Isamu. Okashan, siempre hemos sido poco expresivos, así que quiero aprovechar para agradecerle por todo el esfuerzo y sacarnos a los cuatro adelante.

Finally, I would like to thank Michelle Grando for her love and companionship. Michi, gracias por compartir conmigo todos los momentos felices y por tu apoyo en tiempos más difíciles durante el doctorado.

Contents

I	Photoevaporation of Protoplanetary Disks and Planet Formation	3
1	Introduction	5
2	Disk Model	7
2.1	The thin accretion disk	7
2.2	The star disk accretion shock	12
2.3	The hot ionized disk atmosphere	15
2.4	The warm neutral disk atmosphere	16
3	Disk evolution and photoevaporation	17
3.1	EUV photoevaporation from the central source	17
3.2	EUV photoevaporation by external stars	24
3.3	FUV photoevaporation by external stars	28
3.4	Discussion and summary	31
4	Halting type-II planet migration by disk photoevaporation from the central source	35
4.1	Introduction	35
4.2	Model	36
4.3	Discussion	36
4.4	Conclusions	40
5	Final comments and future work	43
II	True polar wander rotational stability of planets	45
1	Introduction	47
2	True polar wander adiabatic invariant for a quasi-rigid body	51
2.1	Equations of motion for a quasi-rigid body	51

2.2	Hamiltonian for a quasi-rigid body	53
2.3	Adiabatic invariant for a quasi-rigid body	54
2.4	Summary	55
3	True polar wander of a quasi-rigid body	57
3.1	Inertia tensor for a distribution of mass anomalies on a sphere	58
3.2	TPW driven by a colony of beetles	59
3.2.1	Order of magnitude estimate for the true polar wander speed	59
3.2.2	‘Memory’ of the quasi-rigid body	60
3.2.3	Numerical model for a colony of randomly crawling beetles	62
3.3	True polar wander of a randomly evolving body	66
3.4	Application to planets: oblateness distribution	68
4	Inertia tensor perturbations	69
4.1	Inertia tensor perturbations: direct load contribution	69
4.1.1	Inertia tensor perturbations: direct axisymmetric load contribution	70
4.2	Surface load gravitational potential	72
4.2.1	Surface load gravitational potential: point mass at the north pole	74
4.3	A mapping between gravitational potential and inertia perturbations	77
4.3.1	Mapping for an axisymmetric gravitational potential	78
4.4	Inertia tensor perturbations: load-induced deformation	78
4.4.1	Inertia tensor perturbations: axisymmetric load-induced deformation	79
4.5	Inertia tensor perturbations: rotationally-induced deformation	80
4.5.1	Centrifugal potential	80
4.5.2	Centrifugal potential - a spherical harmonic expansion	81
4.5.3	Inertia tensor perturbations associated with rotational deformation	83
4.6	Fluid limit inertia tensor perturbations	84
4.6.1	Fluid Love numbers	84
4.6.2	Fluid limit inertia tensor perturbations	87
5	True polar wander of dynamic planets with lithospheres	89
5.1	Introduction	89
5.2	Inertia tensor perturbations	92
5.2.1	Inertia Perturbations: The Surface Mass Load	92
5.2.2	Inertia Perturbations: Rotational Effects	93
5.2.3	Total Inertia Perturbations	95
5.2.4	Willemann (1984) Revisited	96
5.3	Results	97

5.3.1	Axisymmetric loads	98
5.3.2	Bills and James (1999)	105
5.3.3	Non-axisymmetric loads	106
5.4	The Impact of Internally-Supported Inertia Perturbations	113
5.5	Final Remarks	116
6	True polar wander of an ice-age Earth	119
6.1	Introduction	119
6.2	The Linearized Euler Equations: The Liouville Equations	121
6.3	Inertia Perturbations	123
6.3.1	Inertia perturbations: the ice load	124
6.3.2	Inertia perturbations: rotational effects	126
6.4	The Liouville Equations Revisited	127
6.5	k_f - The Traditional Approximation	129
6.6	k_f - A New Approach	137
6.7	The Physics of GIA-Induced TPW: A Summary	147
6.8	Final Remarks	151
7	Summary	153
III	Appendices	159
A	Numerical solution for the viscous diffusion equation	161
B	Rotational stability of free rigid bodies	163
B.1	Geometric description using the energy ellipsoid and the angular momentum sphere	163
B.2	Equation of motion for a rigid oblate ellipsoid	165
C	Inertia tensor for a distribution of mass anomalies on a sphere in the centre of mass reference frame	169
D	Spherical harmonic convention adopted in this thesis	171
E	Inverse Laplace transform of the linearized Liouville equation	173
	Bibliography	175

Preface

The first two extrasolar planets were discovered around the pulsar PSR 1257+12 (Wolszczan, 1994). Soon after, the first extrasolar planet orbiting a main sequence star, 51 Pegasi, was announced by Mayor & Queloz (1995). As of this writing, 168 extrasolar planets in 144 planetary systems have been discovered (<http://cfa-www.harvard.edu/planets/catalog.html>). The vast majority of these planets are more massive than Saturn, and most either orbit very close to the stars or travel on much more eccentric orbits than any of the planets in our solar system. Their discovery provides a wealth of information for theories of gas giant planet formation; however, they tell us relatively little about the formation of Earth-mass (terrestrial) planets. The only evidence for extrasolar terrestrial planets were the pulsar planets around PSR 1257+12, until the first detection of an extrasolar terrestrial planet orbiting a main sequence star was announced on June 13, 2005 (http://www.carnegieinstitution.org/news_releases/news_0506_13.html). This planet orbits the star GJ 876 at an orbital distance of ~ 0.02 AU, indicating a very different formation history from our planet. Ironically, the extrasolar planets around the pulsar PSR 1257+12, which may have formed under very different conditions, are more Earth-like than this newly discovered planet orbiting a ‘normal’ main sequence star in terms of their orbits and masses (Konacki & Wolszczan, 2003).

In the standard solar nebula theory, planet formation starts with very diffuse material in molecular clouds. The molecular cloud is somehow induced to collapse, and angular momentum conservation leads to the formation of a central condensation (the star) surrounded by a protoplanetary disk. The presence of disks around low-mass young stellar objects, which was initially inferred from their infrared excess emission (Adams et al., 1987) and now directly imaged (Bally et al., 2000), supports this scenario. There are three main stages in the standard theory for terrestrial planet formation from their parent protoplanetary disk. First, dust particles with sizes of $\sim 1 \mu\text{m}$ settle in the disk mid-plane. Next, planetesimals, or solid objects of sizes in the range $\sim 0.1 - 1$ km, form from the dust disk. Finally, the planetesimals interact gravitationally and collide to form terrestrial planets. Two very different mechanisms have been proposed for the formation of the gas giant planets. The generally accepted explanation, core accretion, follows from the last stage of terrestrial planet formation. In this case, the terrestrial planets become the cores of the gas giants and acquire gaseous envelopes from the gas component of the disk. The other theory, disk

instability, suggests that gas giants form quickly from the gravitational collapse of gas clumps in the disk within which the dust component coagulates and settles to form the cores. There are many unsolved problems in each of the planet formation stages mentioned above and the evolution of the parent disk is expected to play an important role. In part I of this thesis, I will discuss the evolution of protoplanetary disks and explore the consequences for planet formation.

The discovery of extrasolar planets raises the question of whether they can support life. The Circumstellar habitable zone is an imaginary spherical shell of space surrounding stars where the surface temperatures of an Earth-like planet might maintain liquid water where life could potentially survive. The 4.5 Gyr continuously habitable zone in our solar system is estimated to be between 0.95 to 1.15 AU (Kasting et al., 1993). The recently discovered extrasolar terrestrial planet is clearly outside the habitable zone since it is orbiting its parent star at ~ 0.02 AU. However, the number of observed extrasolar terrestrial planets is expected to increase in the coming years, and some of them may be in the habitable zone of their parent stars. Large amplitude planet reorientation may cause severe climate variations and have major consequences for development of life, and thus, complicates the discussion of planetary habitability. In the solar system, the obliquities of the terrestrial planets could have experienced large-scale chaotic variations on time scales of ~ 10 Myr due to resonances between the precessions of the spin axis and orbit axis (Laskar & Robutel, 1993). In its present state, the Earth avoids a chaotic obliquity zone since it is subject to a large lunar torque; hence, the moon may be considered as an Earth climate regulator (Laskar et al., 1993). There are currently no constraints for the rotational state of extrasolar planets. However, the characterization of their oblateness and rotation may be available in the near future (Barnes & Fortney, 2003). In part II of this thesis, I investigate a distinctly different, torque-free, rotational motion of planets: true polar wander.

Part I

Photoevaporation of Protoplanetary Disks and Planet Formation

Chapter 1

Introduction

The *Hubble Space Telescope* (*HST*) has provided clear evidence of gas disks surrounding young stars in the Orion Nebula. Narrow band images reveal circumstellar protoplanetary disks (proplyds) seen in silhouette against either the background nebular light or the proplyd’s own ionization front (Bally et al., 2000). These disks have been identified as “evaporating” by Johnstone et al. (1998). Theoretically, disks should be ubiquitous. Any breaking of the spherical symmetry of the protostellar collapse will result in in-falling material being deflected from the radial direction, and disks forming around the central stars. Spherical symmetry may be broken either when the central star core is magnetized, or when the protostellar cloud has initial angular momentum. Magnetic fields tend to produce large pseudo-disks; since the material is not solely rotationally supported (Galli & Shu, 1993). Alternatively, even small initial rotational velocities in the protostellar cloud produce rotationally supported disks containing most of the angular momentum of the system (Terebey et al., 1984). For most theoretical models of the collapse of rotating clouds, the majority of the cloud material falls first onto the disk. Thus, as the molecular core collapses the disk mass increases. However, it is unlikely that the disk mass, M_d , becomes larger than the superior limit, $M_{max} \sim 0.3M_*$, where M_* is the mass of the central star. At this superior limit the disk becomes gravitationally unstable, angular momentum is transported outward by spiral density waves, and the disk accretes material toward the central star at almost the same rate as it is receiving material from the molecular core (Larson, 1984).

Planet formation is an exciting possible outcome of proto-stellar disk evolution. The coplanarity and circularity of the planetary orbits in our solar system support this notion. Explaining the origin of the solar system and extrasolar systems requires an understanding not only how the disks form, we also need to understand the disk evolution. In particular, the disk removal timescale and the timescale to assemble planets determine the possibility of planet formation. Shu et al. (1993) proposed photoevaporation of the solar nebula as the gas removal mechanism that explains the differences in envelope masses between the gas-rich giants, Jupiter and Saturn; and the gas-poor giants, Uranus and Neptune. Hollenbach et al. (2000) generalized the discussion, describing the

variety of possible disk removal mechanisms. The dominant disk removal mechanism at the inner parts of the disk is viscous accretion onto the central star. However, this process is incapable of removing the entire disk in a finite time because the accretion rate decreases as the viscous disk spreads, and the disk lifetime becomes infinite. Other possible disk removal mechanisms are planet formation, stellar encounters, stellar winds or disk winds, and photoevaporation by ultraviolet photons. [Hollenbach et al. \(2000\)](#) concluded that planet formation is a minor disk removal mechanism, and that the dominant mechanisms for a wide range of disk sizes are viscous accretion and photoevaporation, operating in concert within the disk.

Recently, [Clarke, Gendrin, & Sotomayor \(2001\)](#) have studied the observational consequences of the evolution of disks through a combination of photoevaporation and viscous disk evolution. Their study focused on photoevaporation due to ultraviolet photons produced in the disk-star accretion shock under the assumption that the accretion luminosity was constant during accretion and switched off when the inner disk was cleared. Using this model [Clarke et al. \(2001\)](#) were able to reproduce the observed millimeter fluxes of stars with disks as a function of the observed accretion rate. In this thesis, I focus on the physical properties of the disk under a variety of photoevaporation and viscous scenarios in order to understand the internal disk evolution.

I use a time dependent α -disk model ([Shakura & Sunyaev, 1973](#)) with the parameters of [Hartmann et al. \(1998\)](#) that are consistent with observed mass accretion rates in T Tauri stars (TTSs). The disk model is described in Chapter 2. I then consider the disk evolution under the influence of viscous diffusion, photoevaporation by the central source, and photoevaporation by external stars in Chapter 3. Photoevaporation by external stars is studied using the model and parameterization of [Johnstone et al. \(1998\)](#), in their study of the Orion Nebula. Photoevaporation by the central star is modeled with solutions originally found for high mass stars ([Hollenbach et al., 1994](#)) and normalized to TTSs ([Shu et al., 1993](#)); however, in order to study disk evolution, approximations for the time dependence of evaporation are included in the model by estimating the continual change in the accretion shock emission of ultraviolet photons as the accretion rate subsides. In agreement with [Hollenbach et al. \(2000\)](#) and [Clarke et al. \(2001\)](#), I show that it is possible to remove the entire disk in a finite time. However, I show that the rapid removal of the inner disk, described by [Clarke et al. \(2001\)](#) is not self-consistent in the case of accretion powered photoevaporation. I further show that gaps in the disk are a natural outcome of the combination of viscous accretion and photoevaporation by the central star. I study the possibility of halting planet migration by the formation of these gaps in Chapter 4. Finally, the main results are summarized in Chapter 5, which also includes an outline of some outstanding issues and possible directions for future research.

Chapter 2

Disk Model

2.1 The thin accretion disk

With viscosity present in the disk, the energy of the shear motions between annuli is dissipated as heat, and angular momentum is transported from annuli with smaller specific angular momenta to annuli with larger specific angular momenta. If the total angular momentum in the disk is conserved a minimum energy state is approached as the inner material moves closer to the central star and the outer material spreads outward, with the outward transport of specific angular momentum (Pringle, 1981). Considering angular momentum and mass conservation of an annulus of material at a radius, R , in a geometrically thin disk with viscosity, ν , the surface density evolution is described by

$$\frac{\partial \Sigma}{\partial t} = \frac{3}{R} \frac{\partial}{\partial R} \left[R^{1/2} \frac{\partial}{\partial R} \left(\nu \Sigma R^{1/2} \right) \right], \quad (2.1)$$

where Σ is the surface density, ν is the kinematic viscosity, and t is the time. In this formulation it is assumed that most of the mass is in the central star; therefore, the self gravity of the disk is ignored. The characteristic evolutionary timescale due to viscous spreading can be estimated as $t_\nu \sim R^2/\nu$ from equation (2.1). The explicit evolution of the disk depends on a detailed description of the viscosity, which is weakly constrained by present observations. However, a standard approach is to assume that the viscosity is a function of the sound speed in the disk and the disk thickness. For this case, I can isolate all our uncertainty about the viscous mechanism in a dimensionless parameter, $\alpha \leq 1$, with the standard α -prescription of Shakura & Sunyaev (1973). I write

$$\nu = \alpha c_s H, \quad (2.2)$$

where c_s is the sound speed at the disk mid plane and H is the thickness of the disk. With this prescription the viscosity takes the form

$$\nu(R) = \alpha \frac{k}{m_p} \left(\frac{1}{GM_\star} \right)^{1/2} R^{3/2} T_d(R), \quad (2.3)$$

where $m_p \sim 2.3m_H$ is the mean particle mass, M_\star is the central star mass, and T_d is the disk temperature at the mid plane. [Hartmann et al. \(1998\)](#) estimate $\alpha \sim 10^{-2} - 10^{-3}$ from the observed TTSs disk sizes, and they show that the observed variation in mass accretion rates can be accounted for by initial disk masses between 0.01 and 0.2 M_\odot .

I solve equation (2.1) numerically using a backward time finite differencing scheme (see Appendix A). It is necessary to solve a set of simultaneous linear equations at each time step given an initial density distribution and two boundary conditions. The inner boundary is $R_{min} = 10^{-2}$ AU and the outer boundary, R_{max} , is chosen such that the outer disk edge never reaches R_{max} . The boundary conditions are chosen such that the total mass and the total angular momentum in the disk are conserved. In other words, there is no input of mass or external torques at the inner or external boundaries. I define the disk edge, R_d , such that the mass between R_d and R_{max} is less than a fraction 10^{-6} of the disk mass. This assures that the contribution to the disk mass from all the annuli with $R > R_d$ is negligible.

If the disk mid-plane temperature distribution follows a power law I can write

$$T_d(R) = T_0 r^{-\delta}, \quad (2.4)$$

where $r \equiv R/R_0$ and R_0 is a radial distance scale. Using equation (2.4) in equation (2.3) yields

$$\nu(R) = \nu_0 r^\gamma, \quad (2.5)$$

where

$$\nu_0 = \alpha \frac{k}{m_p} \left(\frac{1}{GM_\star} \right)^{1/2} T_0 R_0^{3/2} \quad (2.6)$$

and the power law coefficients are related by $\gamma = 3/2 - \delta$.

Assuming a power law for the disk mid-plane temperature allows one to obtain similarity solutions for equation (2.1) of the form ([Lynden-Bell & Pringle, 1974](#); [Hartmann et al., 1998](#))

$$\Sigma = \frac{C}{3\pi\nu_0 r^\gamma} \tau^{-(5/2-\gamma)/(2-\gamma)} \exp\left(-\frac{r^{(2-\gamma)}}{\tau}\right), \quad (2.7)$$

with a scaling constant C that is a function of the initial disk mass and dimensionless variables given by r and

$$\tau \equiv t/t_s + 1, \quad (2.8)$$

where the viscous scaling time is given by

$$t_s = \frac{1}{3(2-\gamma)^2} \frac{R_0^2}{\nu_0}. \quad (2.9)$$

The viscous scaling time corresponds to the viscous diffusion timescale $t_\nu \sim R^2/\nu$ at the radius R_0 . The scaling constant C can be found by integrating equation (2.7) over the complete disk surface at $t = 0$ and comparing the resulting expression to the initial disk mass $M(0)$. This gives

$$M(0) = \int_{R_{min}}^{\infty} \Sigma(R, t=0) 2\pi R dR = \frac{2CR_0^2}{3\nu_0(2-\gamma)} \int_{x_{min}}^{\infty} dx e^{-x} = \frac{2CR_0^2}{3\nu_0(2-\gamma)} \exp\left(-r_{min}^{(2-\gamma)}\right), \quad (2.10)$$

where $r_{min} = R_{min}/R_0$ and $x_{min} = r_{min}^{(2-\gamma)}$. Similarly, I can integrate equation (2.7) over the complete disk surface to obtain the time dependent total disk mass

$$M(t) = \int_{R_{min}}^{\infty} \Sigma(R, t) 2\pi R dR = \frac{2CR_0^2}{3\nu_0(2-\gamma)} \tau^{-\left[\frac{1}{2(2-\gamma)}\right]} \int_{x_{min}}^{\infty} dx e^{-x} = M(0) \tau^{-\left[\frac{1}{2(2-\gamma)}\right]} \quad (2.11)$$

Given a solution for Σ (2.7), the disk flow velocity can be found by solving

$$v_R = -\frac{3}{\Sigma R^{1/2}} \frac{\partial}{\partial R} (\nu \Sigma R^{1/2}), \quad (2.12)$$

where I adopt a positive sign for outward flow. Replacing equation (2.7) in the last equation yields

$$v_R(R, t) = \frac{3\nu_0}{R_0} \left[\frac{(2-\gamma)r}{\tau} - \frac{r^{(\gamma-1)}}{2} \right]. \quad (2.13)$$

Note that the disk flow velocity is independent of the disk mass. Since the disk must expand to conserve the total angular momentum as material is accreted onto the central star, the disk flow velocity changes direction at the transition radius, which I denote as R_t . This location can be found by setting $v_R = 0$ in equation (2.13), which gives

$$R_t = R_0 \left[\frac{\tau}{2(2-\gamma)} \right]^{1/(2-\gamma)}. \quad (2.14)$$

The disk flow at $R > R_t$ is outward, while for $R < R_t$ is inward. The mass flow can be written as

$$\dot{M}(R, t) = \Sigma(R, t) 2\pi R v_R = C \left[\frac{2(2-\gamma)r^{(2-\gamma)}}{\tau} - 1 \right] \tau^{-(5/2-\gamma)/(2-\gamma)} \exp\left(-\frac{r^{(2-\gamma)}}{\tau}\right), \quad (2.15)$$

where I use equations (2.7) and (2.13). The mass flow at the disk inner boundary $R = R_{min}$ (i.e., $r = r_{min}$) provides the disk mass accretion rate onto the central star, which I denote as \dot{M}_{acc} .

Setting $R = R_{min}$ in equation (2.15) gives

$$\dot{M}_{acc}(t) = \dot{M}(R_{min}, t) = C \left[\frac{2(2-\gamma)r_{min}^{(2-\gamma)}}{\tau} - 1 \right] \tau^{-(5/2-\gamma)/(2-\gamma)} \exp\left(-\frac{r_{min}^{(2-\gamma)}}{\tau}\right), \quad (2.16)$$

where I use equation (2.10).

For the purposes of the following discussion, I consider the limit $\tau \gg 1$ (i.e., times much longer than the viscous time) and $r \sim 1$ (i.e., radial scales comparable to the disk size). In this case, equations (2.7), (2.13), (2.15), and (2.16) can be approximated as

$$\Sigma(R, t) \sim \frac{C}{3\pi\nu_0} \left(\frac{R}{R_0}\right)^{-\gamma} \left(\frac{t}{t_s}\right)^{-(5/2-\gamma)/(2-\gamma)}, \quad (2.17)$$

$$v_R(R, t) = -\frac{3\nu_0}{2R_0} \left(\frac{R}{R_0}\right)^{(\gamma-1)}. \quad (2.18)$$

$$\dot{M}(t) = \dot{M}_{acc}(t) \sim -C \left(\frac{t}{t_s}\right)^{-(5/2-\gamma)/(2-\gamma)}. \quad (2.19)$$

In this limit the mass flow is always inward, which is consistent with $R_t \gg R_0$ from equation (2.14) with $\tau \gg 1$. Furthermore, the mass flow becomes independent of the disk location. The disk dispersal time, which I define as $t_D \equiv M/\dot{M}$ can be found from direct substitution of equations (2.19) and (2.11). This gives

$$t_D(t) \sim \frac{M(0)}{C} \left(\frac{t}{t_s}\right), \quad (2.20)$$

and thus, the disk dispersal time is independent of the power law coefficient γ , and is always linear with time.

The potential energy of accreting gas is converted to thermal energy and released as radiation by viscous processes. Assuming thermodynamic equilibrium, the local energy balance at each radius is described by

$$\frac{3}{8\pi} \frac{GM_\star \dot{M}}{R^3} \left[1 - \left(\frac{R_\star}{R}\right)^{1/2} \right] = \sigma T_s^4, \quad (2.21)$$

where σ is Stefan-Boltzmann constant and T_s is the disk surface temperature (Frank et al., 2002). For simplicity, I ignore the vertical temperature gradient and assume $T_d = T_s$. Equation (2.21) implies a temperature distribution $T_s \propto R^{-3/4}$ for a constant accretion rate at each radius. However, the temperature distribution in the outer disk required to explain observations is much shallower, approximately $T_s \propto R^{-1/2}$ (Kenyon & Hartmann, 1987). The reason for this behavior is that the optically-thick disk photosphere is curved away from the disk mid-plane, or flared, allowing radiation from the central star to dominate the outer disk heating (Kenyon & Hartmann, 1987). Flared disk models have been shown to account for the observed disk emission satisfactorily (Chiang

& Goldreich, 1997; D’Alessio et al., 1998, 1999), and the dominance of stellar irradiation heating over viscous dissipation is demonstrated by the detection of silicate emission features, which arise from the temperature inversion due to external heating (Calvet et al., 1992; Chiang & Goldreich, 1997). I adopt the observed disk temperature distribution (Kenyon & Hartmann, 1987; D’Alessio et al., 1998), $T_d = (10\text{K}) (R/100\text{AU})^{-1/2}$.

In this case, the initial surface density distribution is given by equation (2.7) with $\gamma = 1$, which gives

$$\Sigma(R, t) = \frac{M(0)e^{r_{min}}}{2\pi R_0^2} r^{-1} \tau^{-3/2} e^{-r/\tau}. \quad (2.22)$$

I choose $R_0 = 10$ AU as the radial scaling scale. The physical meaning of R_0 is that a fraction $1 - e^{-q}$ of the initial disk mass resides inside qR_0 . For example, $\sim 60\%$ of the mass resides inside R_0 and $\sim 90\%$ of the mass resides inside $2R_0$. Our choice for R_0 may seem small considering the typical observed disk sizes of ~ 100 AU. However, as I will show below, the disk expands to conserve angular momentum and the disk size at $\sim 1 - 10$ Myr, which is the typical disk life time, is consistent with the observed values.

Equation (2.22) provides an excellent starting initial condition for studying the interaction of disk evaporation and viscous evolution for various reasons. First, in the absence of photoevaporation any initial surface density distribution will diffuse to the solution given by equation (2.22) in the viscous diffusion timescale, $t_s = R_0^2/3\nu_0$, which is much shorter than the disk removal timescale. Second, I am interested in the disk evolution well after the initial disk formation during which time viscous diffusion should have produced a disk profile reasonably close to the asymptotic solution. Third, the formation of structure in the disk surface density due to photoevaporation occurs at late stages of the disk evolution, at timescales much longer than the viscous diffusion timescale.

To illustrate the validity of these arguments I computed the evolution of models with different initial surface density distributions. Figure 2.1 shows snapshots of the solutions for $\gamma = 1$ and (a) a Gaussian ring, (b) a similarity solution with a gap, and (c) a similarity solution. Any gaps or ring-like structures are quickly removed compared to the disk lifetime; therefore, such structures are unlikely to be seen when only viscous accretion is considered. For a ring as initial distribution (Fig. 2.1a), the surface density of the inner regions increases initially as the disk spreads in both directions, but it eventually starts decreasing with time as material flows out the inner edge. This is not the case for the other two initial distributions (Figures 2.1b and 2.1c) because material is flowing off the inner edge from the beginning of the disk evolution. For all the initial distributions, the surface density in the outer regions increases as the disk expands to conserve the total angular momentum. The surface density approaches the power law asymptotic solution $\Sigma \propto R^{-1}$ in all cases at intermediate disk locations that are not influenced by the boundary conditions.

Figure 2.2 illustrates a) the disk mass M_d , b) the accretion rate \dot{M}_d , c) the disk size R_d and the

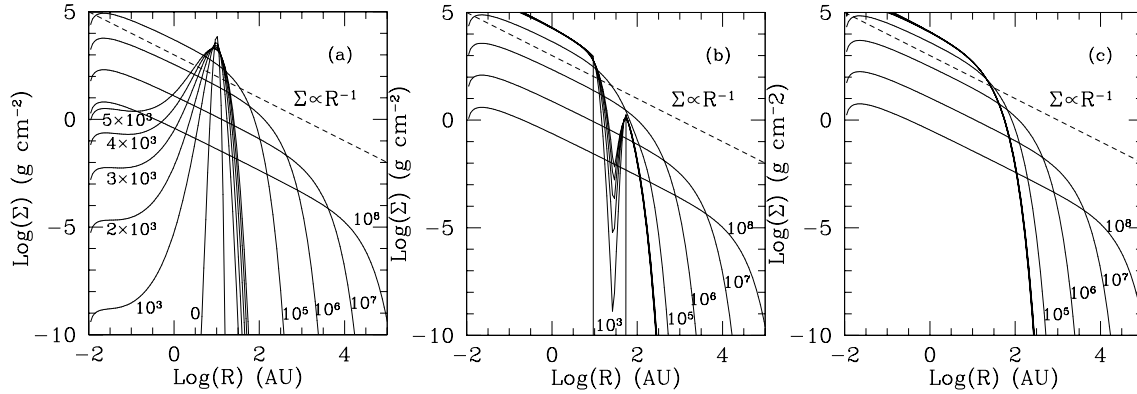


Figure 2.1 Snapshots of the viscous evolution of the surface density distribution for $\gamma = 1$ and initial surface density of (a) a Gaussian annulus centered at 10 AU, (b) a similarity solution with $R_0 = 10$ AU with a gap between 10 AU and 50 AU, and (c) a similarity solution with $R_0 = 10$ AU. The curves represent $t = 0, 10^3, 2 \times 10^3, 3 \times 10^3, 4 \times 10^3, 5 \times 10^3, 10^5, 10^6, 10^7,$ and 10^8 yr. The dotted line corresponds to a an arbitrary line $\propto R^{-1}$.

transition radius R_T , and d) the dispersal time as a function of time for the initial surface density distribution in Figure 2.1c. All the different initial distributions considered in Figure 2.1 result in very similar time evolutions for all the quantities shown in Figure 2.2. The initial disk mass is $M(0) = 0.1M_\odot$, and it takes ~ 10 Myr to reduce the disk mass to $\sim 0.01M_\odot$; by this time the disk has grown to $r_d \sim 10^4$ AU, and the disk keeps expanding to conserve the total angular momentum. The disk mass, accretion rate, size, transition radius, and dispersal follow the asymptotic solutions

$$M \propto t^{-1/2} \quad \dot{M} \propto t^{-3/2}, \quad R_t \propto t \text{ and } t_D \propto t$$

as expected from equations (2.11), (2.19), (2.14), and (2.20) with $\gamma = 1$.

Figure 2.2 illustrates that it is formally not possible to remove the entire disk in a finite time by viscous diffusion alone in different ways. First, the accretion rate decreases faster than the disk mass and this causes the dispersal time to increase with time. Furthermore, the dispersal time is always longer than the age of the disk. Finally, as the transition radius increases a larger fraction of disk material will be accreted onto the central star; however, the transition radius is always smaller than the edge of the disk and both quantities approach the same power-law. Therefore, the transition radius will never reach the disk edge.

2.2 The star disk accretion shock

The hot continuum excess emission or “blue veiling” present in TTSs, originally explained as being due to boundary layer emission (Lynden-Bell & Pringle, 1974; Bertout et al., 1988), is now thought to arise from accretion shocks at the base of stellar magnetospheric columns, along which material

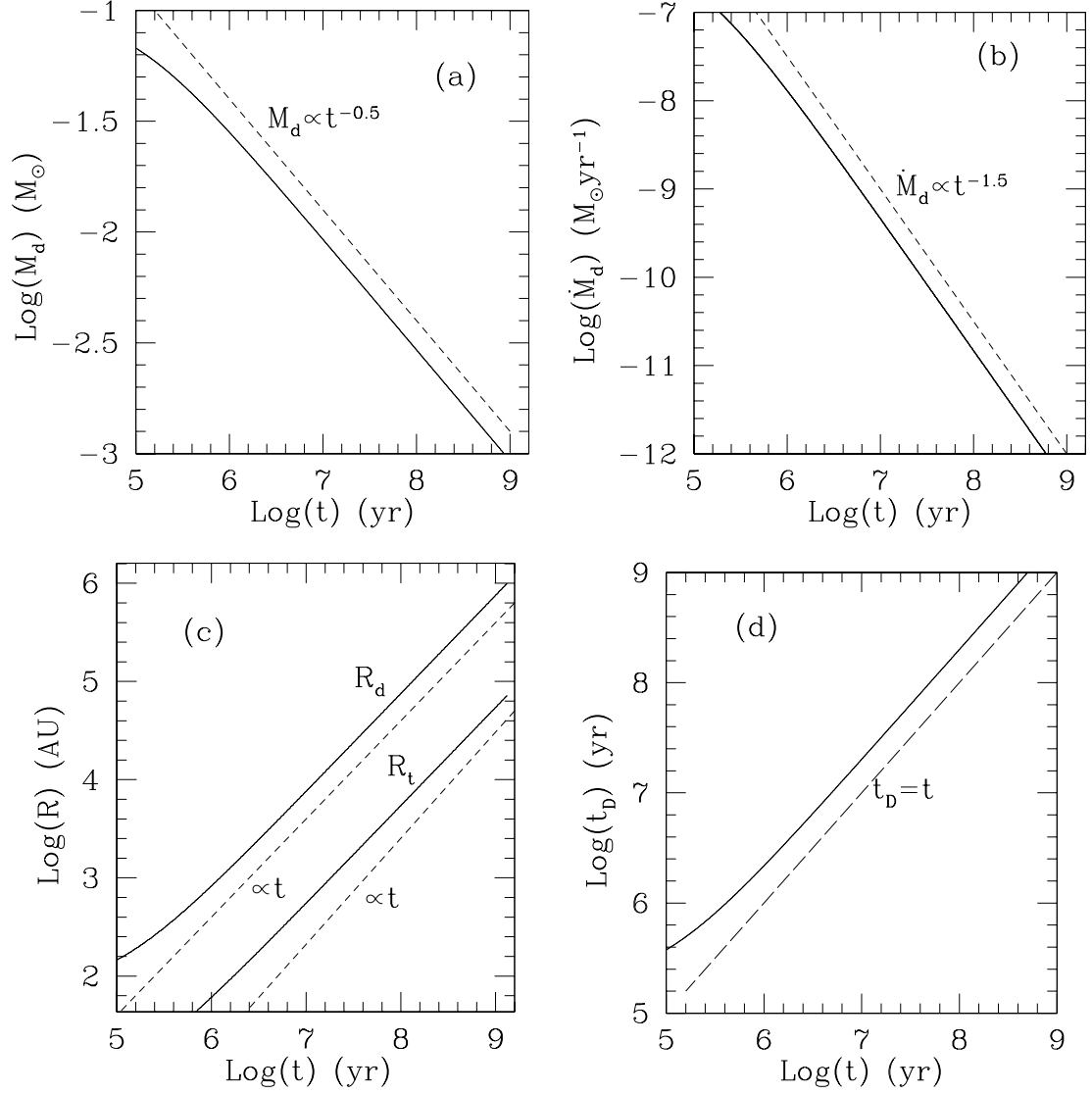


Figure 2.2 a) Disk mass M_d , b) accretion rate \dot{M}_d , c) disk size R_d and transition radius R_T , and d) dispersal time $t_D \equiv M_d/\dot{M}_d$ for a initial surface density distribution given by equation (2.22) with $R_0 = 10$ AU. All the quantities shown approach a power law solution illustrated with the dotted lines. The dashed line in Figure d) indicates the location where the dispersal time would equal the elapsed disk lifetime.

from the disk accretes (Königl, 1991; Hartmann et al., 1994; see Hartmann 1998 and references therein). The observed emission at both UV (1000–3000Å) and visible (3500–7000Å) wavelengths for TTSs is consistent with predictions based on this model (Calvet & Gullbring, 1998; Gullbring et al., 2000). In the boundary layer model, disk material is rotating at nearly Keplerian velocity at the stellar radius; as material is accreted it has to slow down and emit its kinetic energy, which amounts to nearly half of the accretion luminosity

$$L_{acc} = \frac{GM_{\star}\dot{M}}{R_{\star}}.$$

Therefore, the maximum luminosity of the excess continuum is

$$L_{bl} \sim \frac{GM_{\star}\dot{M}}{2R_{\star}},$$

while the disk emission accounts for the other half.

In contrast, in magnetospheric accretion, material falls from several stellar radii, reaching the stellar surface at velocities close to free fall from infinity, so that a larger fraction of the accretion luminosity is released at the accretion shock. The kinetic energy flux at the accretion shock can be written as

$$F_{as} = \frac{1}{2}\rho v_{ff}^2, \quad (2.23)$$

where ρ is the density of the accreting material and v_{ff} is the free fall velocity. Using mass conservation allows one to obtain

$$\rho = \frac{\dot{M}}{Av_{ff}}, \quad (2.24)$$

where A is the area of the accretion shock column. The free fall velocity at the stellar surface is given by

$$v_{ff} = \left(\frac{2GM_{\star}}{R_{\star}}\right)^{1/2} \left(1 - \frac{R_{\star}}{R_{min}}\right)^{1/2}, \quad (2.25)$$

where R_{min} is the radius where the magnetosphere truncates the disk. Finally, replacing equations (2.24) and (2.25) in equation (2.23) allows one to obtain the accretion shock luminosity

$$L_{as} = F_{as}A = \frac{GM_{\star}\dot{M}}{R_{\star}} \left(1 - \frac{R_{\star}}{R_{min}}\right). \quad (2.26)$$

The observational data (Meyer et al., 1997) suggests that $R_{min} \sim 5R_{\star}$, in which case $\sim 80\%$ of the accretion energy comes out from the accretion shock.

The veiling continua of accreting TTSs is not that of a simple blackbody. Nevertheless, it appears that the FUV continuum can be roughly approximated as having a characteristic temperature $\sim 10^4\text{K}$ (Johns-Krull et al., 2000; Gullbring et al., 2000).

2.3 The hot ionized disk atmosphere

The EUV ($h\nu > 13.6\text{eV}$) photons from the central star, the accretion shock, or the external stars are capable of ionizing hydrogen and evaporating material from the disk surface. This mechanism affects the disk surface layer and forms an ionized atmosphere above the thin viscous disk. [Hollenbach et al. \(1994\)](#) describe analytical solutions for this atmosphere assuming a typical H_{II} region temperature, $T_{II} \sim 10^4$ K. The equilibrium temperature arises from balance between heating, due primarily to incident ionizing photons; and cooling, due primarily to forbidden line radiation. Using Euler's equation and assuming hydrostatic equilibrium in the z -direction, I can write the number density of electrons for an isothermal atmosphere as

$$n(R, z) = n_0(R, z = 0)e^{-z^2/2H^2}, \quad (2.27)$$

where $n_0(R)$ is the number density at the disk base $z = 0$ and

$$H = c_{II} \left(\frac{R}{GM_\star} \right)^{1/2} R, \quad (2.28)$$

is the scale height. In the last equation

$$c_{II} = \left(\frac{kT_{II}}{m_{II}} \right)^{1/2} \quad (2.29)$$

is the isothermal sound speed of the gas at the ionized hydrogen gas equilibrium temperature and $T_{II} \sim 10^4\text{K}$, and mean particle mass, $m_{II} = 1.13 \times 10^{-24}$ g. The scale height grows with increasing radius until it becomes equal the gravitational radius,

$$R_{II} = \frac{GM_\star}{c_{II}^2}. \quad (2.30)$$

The relevance of this radius is not only geometrical, but also dynamical. The sum of the kinetic energy and the thermal energy per unit mass at the gravitational radius is

$$\frac{1}{2}\Omega^2 R_{II}^2 + \frac{3kT_{II}}{2m_{II}} = \frac{2GM_\star}{R_{II}}, \quad (2.31)$$

where $\Omega = (GM_\star/R_{II}^3)^{1/2}$ is the Keplerian angular velocity. Gas material has twice the negative energy of the gravitational potential energy, that is, it has more than enough energy to escape to infinity as a disk wind at R_{II} . [Shu et al. \(1993\)](#) show that the gravitational radius for the solar nebula is at the orbital distance of Saturn, giving a possible explanation for the sharp differences in envelope masses between the gas-rich giants, Jupiter and Saturn, and the gas-poor giants, Uranus and Neptune. Since the gas material at R_{II} already has more than the minimum energy to escape, some mass loss occurs even inside R_{II} , and gas particles become gravitationally bound to the central

star at a location between the central star radius, R_\star , and the gravitational radius.

Alternatively, I can define the gravitational radius such that the total energy at the gravitational radius is zero. That is, it is assumed that the particles at the gravitational radius have enough energy to escape from the gravitational potential of the central star with vanishing final speeds. This condition can be written as

$$\frac{1}{2}\Omega^2 R_{II}^2 + \frac{3}{2}c_{II}^2 - \frac{GM_\star}{R_{II}} \sim 0,$$

which gives

$$R_{II} \sim \frac{GM_\star}{3c_{II}^2},$$

This simple order of magnitude estimate is consistent with recent estimates from hydrodynamical simulations (Font et al., 2004). Liffman (2003) argues for $R_{II} \sim GM/(5c_{II}^2)$ by assuming a steady state, adiabatic, axisymmetric flow.

I introduce the dimensionless parameter β_{II} and write

$$R_{II} = \beta_{II} \frac{GM}{c_{II}^2} = \beta_{II} \frac{GM_\star m_{II}}{k_B T_{II}} \sim 9 \text{ AU} \beta_{II} \left(\frac{M_\star}{M_\odot} \right) \left(\frac{T_{II}}{10^4 \text{K}} \right)^{-1}, \quad (2.32)$$

where $1/5 < \beta_{II} < 1$, to absorb the uncertainty in the location of the gravitational radius in this parameter. An additional factor that makes β_{II} smaller is the fact that material can also be removed inside R_{II} due to the pressure gradients in the flow.

2.4 The warm neutral disk atmosphere

The FUV ($6 < h\nu < 13.6\text{eV}$) photons from the central star, the accretion shock, or external stars are capable of dissociating H_2 and CO ; and will affect the disk structure. The FUV photons penetrate the ionized region and create a neutral hydrogen layer with temperature, $T_I \sim 10^3\text{K}$. Following the same arguments for the ionized atmosphere, I can define a gravitational radius for the neutral layer as

$$R_I = \beta_I \frac{GM_\star}{c_I^2} = \beta_I \frac{GM_\star m_I}{k_B T_I} \sim 100 \beta_I \left(\frac{M_\star}{M_\odot} \right) \left(\frac{T_I}{10^3 \text{K}} \right)^{-1} \text{ AU}, \quad (2.33)$$

where $T_I \sim 10^3\text{K}$ is neutral hydrogen equilibrium temperature and $m_I \sim 1.35m_H$ is the mean particle mass in the neutral layer. A recent study by Adams et al. (2004) shows that significant mass loss still takes places as long as $\beta_I \gtrsim 0.1 - 0.2$.

Chapter 3

Disk evolution and photoevaporation

3.1 EUV photoevaporation from the central source

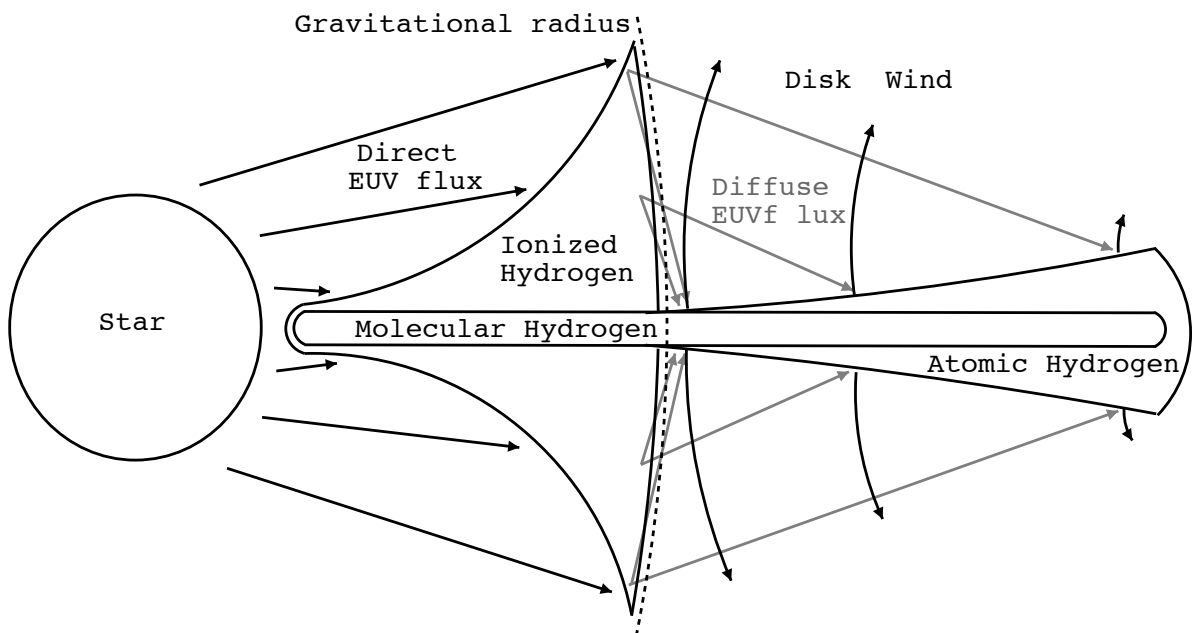


Figure 3.1 Schematic diagram illustrating disk erosion by photoevaporation from the central source. The direct EUV flux is absorbed and scattered in the ionized hydrogen atmosphere. Photoevaporation removes material predominantly at the gravitational radius (dotted line), where the diffuse EUV flux suffers less attenuation and shines onto the disk with the largest incident angle.

Hollenbach et al. (1994) found analytic solutions for the photoevaporation mass loss rate by EUV photons from the central star. These photons are attenuated by recombined hydrogen atoms and scattering from dust in the ionized atmosphere; providing a source of diffuse EUV photons. The ionized atmosphere absorbs a significant fraction of the direct incident flux, and the diffuse field dominates the flux onto the disk. Disk material is gravitationally bound inside the gravitational

radius, R_{II} , and it flows out the disk base at the sound speed, c_{II} , outside the gravitational radius. Figure 3.1 provides a schematic illustration of the basic physical elements discussed above. Given the number density of ionized hydrogen at the disk base, $n_{II}(R)$, I can calculate the evaporation rate:

$$\dot{\Sigma}_{ph}(R) = \begin{cases} 2m_{II}n_{II}(R)c_{II}, & \text{if } R > R_{II}; \\ 0, & \text{otherwise,} \end{cases} \quad (3.1)$$

where the factor of two accounts for photoevaporation from both sides of the disk. A self-regulating mechanism is established at the disk base and it is possible to find the number density in this region. If the number density at the disk base were lower than the equilibrium value, the diffuse EUV photons would penetrate deeper into the disk, producing more ionizations, and the number of ionized hydrogen would increase. On the other hand, if the number density were higher than the equilibrium value, the recombinations and the scattering from dust in the ionized atmosphere would prevent the diffuse EUV photons from reaching the disk base, and the number of ionizations would decrease.

Assuming ionization equilibrium, [Hollenbach et al. \(1994\)](#) found the number density at the disk base for the “weak” and “strong” stellar wind cases. In the weak stellar wind case, the stellar wind ram pressure is smaller than the thermal pressure for $R < R_{II}$ and the atmosphere is static. Gas material is evaporated at the rate given by equation (3.1) outside the gravitational radius. The dominant flux of EUV photons producing the flow is from the diffuse field that shines vertically downward onto the disk at the gravitational radius; therefore, most of the gas is evaporated from this region. In the strong stellar wind case, the stellar wind ram pressure is higher than the thermal pressure even outside R_{II} . Although disk material evaporates in the vicinity of R_{II} , the dominant flow occurs where the stellar wind ram pressure equals the thermal pressure, at a characteristic radius, $R_w > R_{II}$. Due to large uncertainties in both the wind mass loss rate, the effects of collimation in the wind, and the ionization flux from the central star, it is not clear whether or not the strong wind condition is met for low mass stars ([Hollenbach et al., 2000](#)). In this thesis, I only consider the weak stellar wind case. The number density at the disk base for the weak stellar wind case is

$$n_{II}(R) = \begin{cases} 3.1 \times 10^5 \left(\frac{\phi}{10^{40} \text{s}^{-1}} \right)^{1/2} \left(\frac{R}{1 \text{AU}} \right)^{-5/2} \text{cm}^{-3}, & \text{if } R > R_{II}; \\ n_{II}(R_{II}) \left(\frac{R}{R_{II}} \right)^{-5/2}, & \text{otherwise,} \end{cases}, \quad (3.2)$$

where ϕ is the ionizing photon luminosity from the central source.

There are no direct observational constraints on the fluxes at EUV ($< 912\text{\AA}$) wavelengths due to interstellar absorption. I estimate the EUV flux from the spectra of TTSs ([Johns-Krull et al., 2000](#), figure 3) and the corresponding distances to the star ([Valenti et al., 2000](#), table 1) by assuming

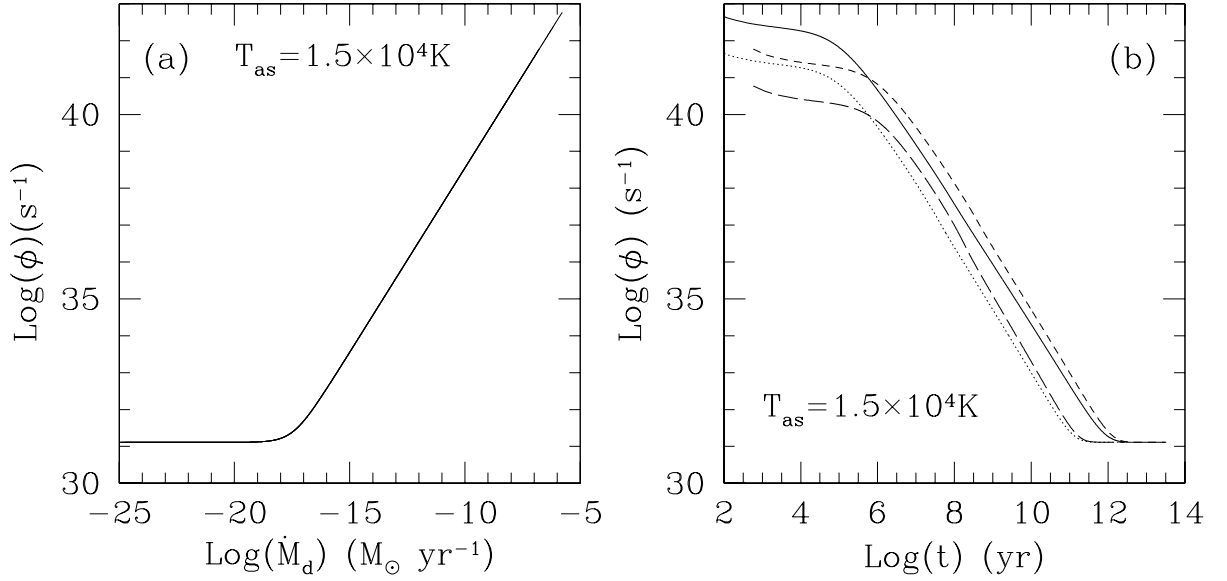


Figure 3.2 Number of ionizing photons, ϕ , as a function of accretion rate and disk lifetime for different disk parameters that cover the parameter space from observations. Solid line with parameters, $\alpha = 10^{-2}$ and $M_d(0) = 10^{-1} M_{\odot}$. Dotted line, $\alpha = 10^{-3}$ and $M_d(0) = 10^{-1} M_{\odot}$. Short-dashed line, $\alpha = 10^{-2}$ and $M_d(0) = 10^{-2} M_{\odot}$. Long-dashed line, $\alpha = 10^{-3}$ and $M_d(0) = 10^{-2} M_{\odot}$. The disk is removed by viscous accretion and photoevaporation from the central source. The ionizing flux approaches the constant value ($\phi = 1.29 \times 10^{31} \text{s}^{-1}$) corresponding to the quiescent stellar photosphere at late stages of the disk evolution when the accretion rates are very small.

black-body emission. First, I calculate the ratio for the fluxes at two different wavelengths,

$$\frac{F_\lambda}{F_{\lambda'}} = \frac{B_\lambda}{B_{\lambda'}} = \left(\frac{\lambda'}{\lambda}\right)^5 \left(\frac{e^{x'} - 1}{e^x - 1}\right), \quad (3.3)$$

where $x = (hc/\lambda k_B T)$ and $x' = (hc/\lambda' k_B T)$. Next, I can solve equation (3.3) for the temperature numerically or by assuming $e^x \gg 1$ and $e^{x'} \gg 1$ which I verify a posteriori. Using energy conservation

$$F_\lambda 4\pi d^2 = \pi B_\lambda A, \quad (3.4)$$

where d is the distance to the star and πB_λ is the flux at the stellar surface, allows one to obtain the stellar surface effective area A . The total luminosity is given by

$$L = A\sigma T^4,$$

where σ is Stefan-Boltzmann's constant. The fraction of EUV photons is

$$\eta = \frac{\int_{\nu_{EUV}}^{\infty} B_\nu(T) d\nu}{\int_0^{\infty} B_\nu(T) d\nu} = \frac{15}{\pi^4} \int_{\nu_{EUV}}^{\infty} B_\nu d\nu,$$

and thus, the number of ionizing photons can be estimated as

$$\frac{L_{EUV}}{h\nu_{EUV}} = \eta \frac{A\sigma T^4}{(13.6\text{eV})}.$$

Table 3.1 summarize our estimates for seven TTSs. I obtain ionizing fluxes in the range \sim

Index	Star	F_{1769}	F_{1250}	$T(K)$	$d(pc)$	$A(10^{15}m^2)$	$L_{EUV}(erg\ s^{-1})$	$\phi_{EUV}(s^{-1})$
3	LkH α 264	7.42	4.0	1430	140	2.34	2.55×10^{15}	1.17×10^{40}
9	BP Tau	6.02	3.25	1440	140	1.89	2.08×10^{15}	9.54×10^{39}
13	T Tau	4.94	6.9	2480	140	0.137	3.25×10^{16}	1.49×10^{41}
27	DR Tau	11.4	1.9	953	140	64.5	1.62×10^{14}	7.44×10^{38}
35	RW Aur A	13.5	7.0	1410	140	47.3	4.14×10^{15}	1.90×10^{40}
93	TW Hya	30.8	28	1860	140	0.335	6.32×10^{15}	2.9×10^{40}
113	RU Lup	23.1	4.5	997	140	89.1	4.95×10^{14}	2.27×10^{39}

Table 3.1 Estimated temperature, effective area, and EUV flux for TTSs.

$10^{39-41} s^{-1}$. Extrapolating the FUV flux may underestimate the EUV flux. In fact, Alexander et al. (2005) argue for higher EUV fluxes in the range $\sim 10^{41-44} s^{-1}$ by analyzing emission measures taken from the literature. However, these values are subject to large uncertainties.

One possible source of ionizing photons is the accretion shock luminosity. The observed emission at both UV (1000 – 3000Å) and visible (3500 – 7000Å) wavelengths is consistent with predictions based on the accretion shock model (Calvet & Gullbring, 1998; Gullbring et al., 2000). Clarke

et al. (2001) used essentially the same model for the photoevaporation component of disk dispersal used here; however, they assumed that the ionizing flux was constant during the disk evolution. In contrast, I explicitly model the ultraviolet photons produced in the accretion layer as a function of time. The total ionizing flux is $\phi = \phi_\star + \phi_{as}$, where ϕ_\star is the ionizing flux from the stellar photosphere and ϕ_{as} is the ionizing flux from the accretion shock. I assume the parameters of typical TTSs under the assumption that only the quiescent star produces ultraviolet photons. In fact, these stars are chromospherically active (Feigelson & Montmerle, 1999), providing an additional source of ionizing photons. However, both the time dependence of the chromospheric activity and the rate of ionizing photon production are poorly constrained at present and thus I take the limiting case of an insignificant chromosphere. The luminosity is $L_\star = 1L_\odot$, the surface temperature is $T_\star = 4000\text{K}$, the stellar radius is $R_\star = 2R_\odot$, and the accretion shock temperature is $T_{as} = 1.5 \times 10^4\text{K}$ (Johns-Krull et al., 2000; Kenyon et al., 1989). I calculate the accretion luminosity using equation (2.26), and the fraction of ionizing photons from this luminosity with the accretion shock temperature. For illustration, Figure 3.2a plots the corresponding ionizing flux for typical accretion rates during the disk evolution. The constant ionizing flux ($\phi = 10^{41}\text{s}^{-1}$) assumed by Clarke et al. (2001) is only produced for high accretion rates ($\sim 10^{-8}\dot{M}_\odot\text{yr}^{-1}$) at early stages of the disk evolution. I plot in Figure 3.2b the time dependence of the ionizing flux for several possible disk scenarios that cover the parameter space of observations. It is clear that the ionizing flux is not constant, it decreases with the accretion rate as the disk loses its mass. Even for high viscosities, $\alpha \sim 10^{-2}$, and initially massive disks, $M(0) \sim 10^{-1}M_\odot$, corresponding to high initial accretion rates, the ionizing flux decreases to values well below $\sim 10^{41}\text{s}^{-1}$. Thus, it is essential to compute the ionizing flux self-consistently from the accretion luminosity when considering photoevaporation from the inner disk.

The surface density evolution under the influence of viscous diffusion and photoevaporation by the central source is given by

$$\frac{\partial \Sigma}{\partial t} = \frac{3}{R} \frac{\partial}{\partial R} \left[R^{1/2} \frac{\partial}{\partial R} \left(\nu \Sigma R^{1/2} \right) \right] - \dot{\Sigma}_{ph}. \quad (3.5)$$

Combining photoevaporation with viscous accretion is done numerically. At each time step, photoevaporation induced mass loss and viscous accretion induced disk evolution are solved, with the time step chosen such that the mass removed due to each mechanism is negligible compared to the instantaneous disk mass. The mass removal rate by photoevaporation is determined by equation (3.1) and the surface density, since it is only possible to photoevaporate material at locations where $\Sigma > 0$.

Figure 3.3 shows snapshots of the surface density distribution for two representative cases: a model with high viscosity ($\alpha = 10^{-2}$) and a massive initial disk [$M(0) = 10^{-1}M_\odot$], and a model with low viscosity ($\alpha = 10^{-3}$) and a small initial disk [$M(0) = 10^{-2}M_\odot$]. In both cases

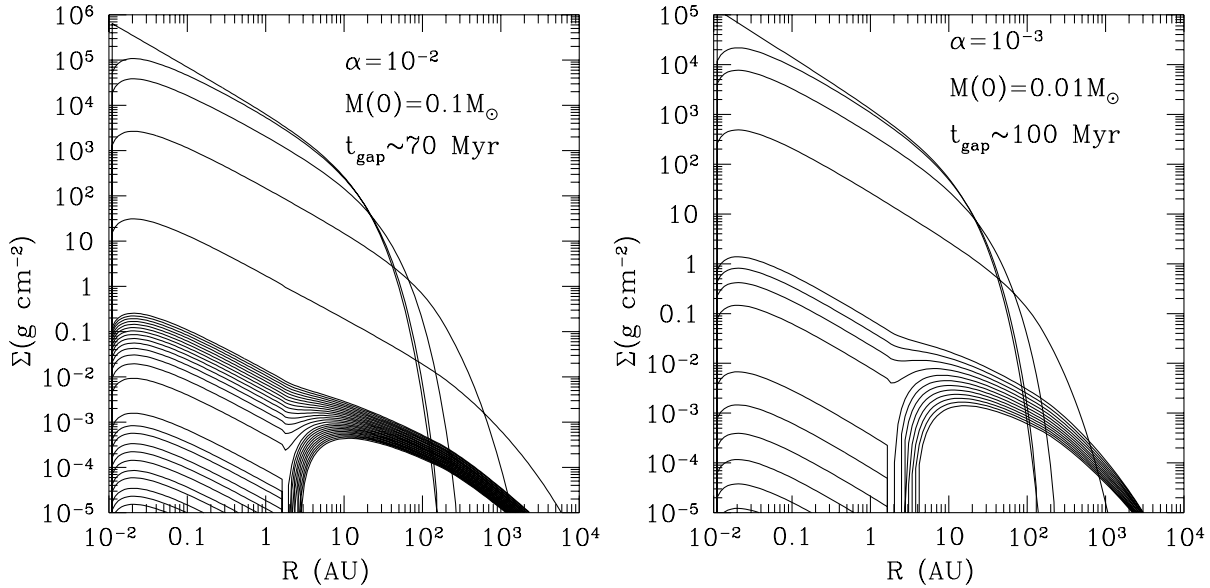


Figure 3.3 Snapshots of the surface density for two representative models under the influence of viscous diffusion and photoevaporation from the central source. I assume a central star with $M_{\star} = 0.5M_{\odot}$ and $\beta_{II} = 0.5$, which corresponds to $R_{II} \sim 2\text{AU}$. Left, model with high viscosity ($\alpha = 10^{-2}$) and massive initial disk ($M(0) = 10^{-1}M_{\odot}$). The first four five snapshots represent $t = 0, 10^{-2}, 0.1, 1,$ and 10 Myr. After the gap forms at $t_{\text{gap}} \sim 70\text{Myr}$, the time step between each snapshot is $\sim 1.7\text{Myr}$. The disk mass corresponding to the last surface density distribution shown (at $t \sim 100$ Myr) is $\sim 0.2M_J$. Right, model with low viscosity ($\alpha = 10^{-3}$) and small initial disk ($M(0) = 10^{-2}M_{\odot}$). The first four snapshots represent $t = 0, 0.1, 1,$ and 10 Myr. After the gap forms at $t_{\text{gap}} \sim 100\text{Myr}$, the time step between each snapshot is $\sim 9\text{Myr}$. The disk mass corresponding to the last surface density distribution shown (at $t = 1.2 \times 10^9\text{yr}$) is $\sim 0.1M_J$.

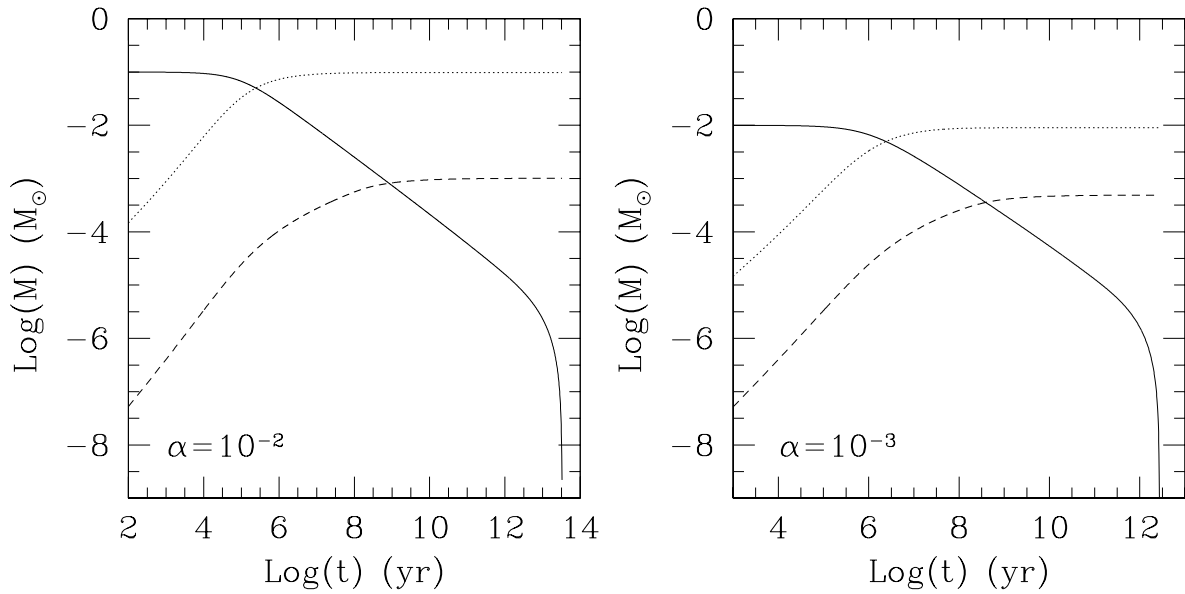


Figure 3.4 Disk mass (solid line), disk mass accreted toward the central star (dotted line), and disk mass removed by photoevaporation from the central source (short-dashed line) as a function of disk lifetime for the two representative models. The disk is removed due to viscous diffusion and photoevaporation from the central source.

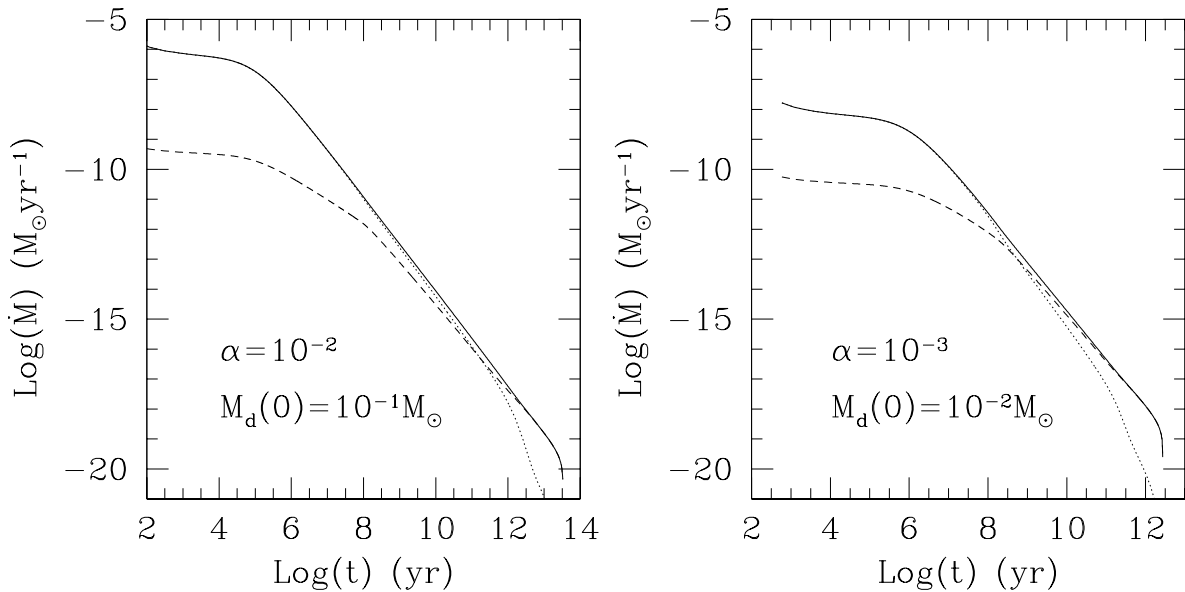


Figure 3.5 Total mass removal rate (solid line), mass removal rate due to accretion (dotted line), and mass removal rate due to photoevaporation by the central source (short-dashed line) vs. disk lifetime for the two representative models.

a gap structure forms during the later stages of the disk evolution. Disk material is accreted toward the central star and photoevaporation from the central source removes material outside the gravitational radius. Figure 3.4 shows the remaining disk mass, the disk mass accreted toward the central star, and the disk mass removed by photoevaporation. Most of the initial disk mass is accreted toward the central star in both cases. Photoevaporation removes all the material in the vicinity of the gravitational radius when the surface density at this radius is low ($\sim 10^{-1} \text{g cm}^{-2}$), and divides the disk into an inner and an outer annulus. The subsequent evolution is dominated by two counteracting effects; viscous diffusion attempts to spread both annuli and remove the gap structure while photoevaporation removes material predominantly at the gravitational radius and reopens the gap. The outcome of the combination of the two mechanisms is an efficient mass removal from the disk. Disk material at the outer edge of the inner annulus is viscously spread beyond the gravitational radius, where it is removed by photoevaporation. Clarke et al. (2001) showed that it is possible to quickly remove the inner disk. The inner disk for the model discussed here is also quickly removed; however, on a longer time scale compared to Clarke et al. (2001)'s predictions. This difference arises because Clarke et al. (2001) assume a constant ionizing flux while I calculate the ionizing flux from the accretion luminosity. For the latter model, the ionizing flux from the accretion shock decreases (see Figure 3.2b) as the accretion rate decreases (see Figure 3.5) until it reaches the constant value ($1.29 \times 10^{31} \text{s}^{-1}$) corresponding to the quiescent stellar photosphere. Therefore, removing the inner disk and maintaining a high ionizing flux ($\sim 10^{41} \text{s}^{-1}$) is not self-consistent. When the gap starts to open, at $t_{gap} \sim 100 \text{ Myr}$, the ionizing flux has been reduced to $\sim 10^{38} \text{ s}^{-1}$. The strong dominance of viscous diffusion over photoevaporation (see Figures 3.4 and 3.5) produce unrealistically long disk lifetimes ($\sim 10^{12} - 10^{13} \text{ yr}$; see Figure 3.4) unless the stellar ionizing flux is extremely enhanced through an active chromosphere (Figure 3.2b can be used to estimate the time at which this model would break down if the chromospheric activity produced a significant ionizing flux ϕ_{ch} . For example, if $\phi_{ch} = 10^{35} \text{ s}^{-1}$ for more than $\sim 10^9 \text{ yr}$ then the calculated models would begin to diverge from reality.) As the outer disk spreads to distances far from the gravitational radius where photoevaporation becomes inefficient, other removal mechanisms such as stellar encounters become important and will limit the disk lifetime.

3.2 EUV photoevaporation by external stars

Stellar disks are also dispersed by external stars and this is a likely situation for the disks surrounded by ionization fronts in the Trapezium Cluster (Bally et al., 2000). Johnstone et al. (1998) found models for EUV dominated external photoevaporation based on observations of the proplyds in the Orion Nebula. In this scenario the disk is heated by UV photons from the nearby O stars. Since the inner annuli have a small surface area compared to the outer annuli, their contribution to the process is very small. Most of the material is removed at the disk edge, R_d , and photoevaporation

from the disk can be approximated by photoevaporation from a sphere with radius R_d . The EUV photons control the flux close to the central star; heating the gas to $T_{II} \sim 10^4\text{K}$ and creating an ionization front. Following [Johnstone et al. \(1998\)](#), the mass loss rate for EUV photoevaporation can be approximated by

$$\dot{M}^{EUV} = \begin{cases} 7 \times 10^{-12} \left(\frac{\Phi_i}{10^{49}\text{s}^{-1}} \right)^{1/2} \left(\frac{d}{1\text{pc}} \right)^{-1} \left(\frac{R_d}{1\text{AU}} \right)^{3/2} \text{M}_\odot \text{yr}^{-1}, & \text{if } R > R_g; \\ 0, & \text{otherwise} \end{cases} \quad (3.6)$$

where ϕ_i is the ionization rate of the external star and d is the distance to the external star. Most of the mass is evaporated from the outer disk annuli because they have the largest surface area. I assume the Trapezium Cluster conditions, where most of the flux, $\phi_i \sim 10^{49}\text{s}^{-1}$ is from θ^1 Ori C. The EUV photons dominate the flux for the proplyds orbiting at distances $\lesssim 0.03$ pc from the external star ([Johnstone et al., 1998](#); [Störzer & Hollenbach, 1999](#)), and I assume $d = 0.02$ pc in the following models. The surface density evaporation rate is the mass loss rate divided by the effective area of the disk:

$$\dot{\Sigma}_{ext}^{EUV} = \begin{cases} \frac{\dot{M}^{EUV}}{\pi(R_d^2 - R_{II}^2)}, & \text{if } R > R_{II}; \\ 0. & \text{otherwise} \end{cases} \quad (3.7)$$

The disk is removed due to accretion toward the central star, photoevaporation from the central source, and EUV photoevaporation by the external stars. In this case, the surface density evolution is given by

$$\frac{\partial \Sigma}{\partial t} = \frac{3}{R} \frac{\partial}{\partial R} \left[R^{1/2} \frac{\partial}{\partial R} \left(\nu \Sigma R^{1/2} \right) \right] - \dot{\Sigma}_{ph} - \dot{\Sigma}_{ext}^{EUV}. \quad (3.8)$$

The disk evolution is strongly affected by the external radiation field. Photoevaporation by the external star dominates the ionizing flux at large radii where material is efficiently evaporated. Hence, photoevaporation by the central star is a minor disk removal mechanism. I show the results for two models with the same parameters as before (see §3.1). Figure 3.6 shows snapshots of the surface density distribution. Viscous diffusion spreads the disk in both directions and photoevaporation from the external star removes the outer parts; and thus, the disk size remains constant at the gravitational radius until the disk is completely removed. The disk truncation is in good agreement with the two dimensional simulations of [Richling & Yorke \(2000\)](#). However, their simulation stops at $t \sim 10^4\text{yr}$, before the disk is completely removed. There is no formation of gap structures due to the strong dominance of EUV photoevaporation from the external stars over photoevaporation from the central source. The disk is quickly removed as viscous accretion, photoevaporation by the central star, and EUV photoevaporation by the external star work in tandem. The strong dominance of photoevaporation by the external star is also illustrated in the total mass removed by photoevaporation (see Figure 3.7) and the mass removal rate (see Figure 3.8). Photoevaporation

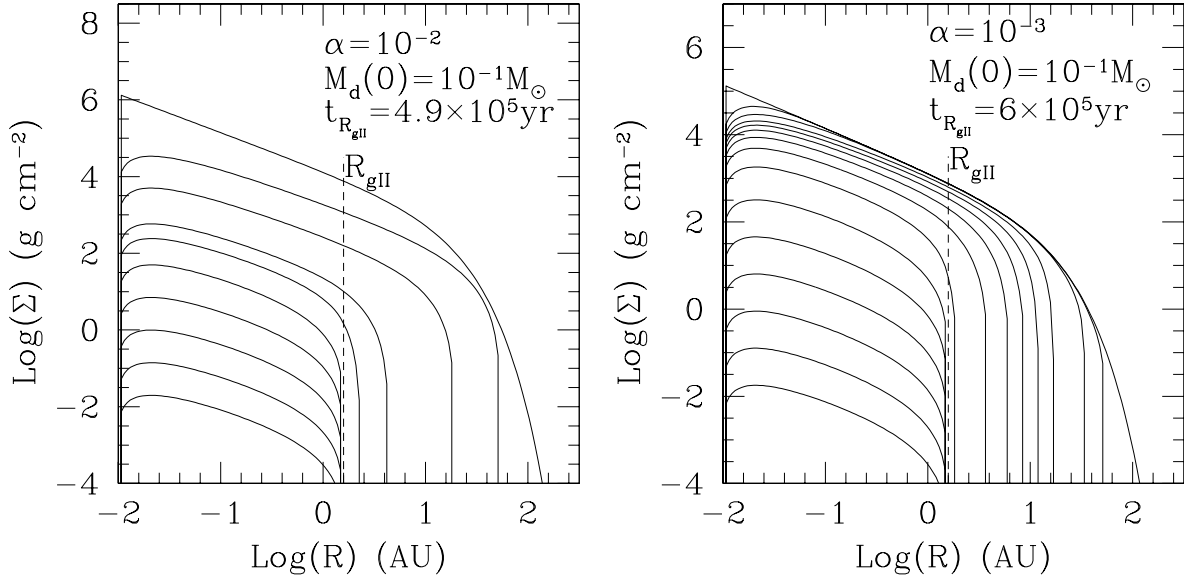


Figure 3.6 Snapshots of the surface density for two representative models considering viscous diffusion, photoevaporation from the central source, and EUV photoevaporation by external stars. The dashed lines indicate the location of the EUV gravitational radius, r_{gII} ; and t_{gap} is the time when gap structures start forming. Left, model with high viscosity ($\alpha = 10^{-2}$) and massive initial disk ($M_d(0) = 10^{-1} M_{\odot}$). The curves represent $t = 0, 2 \times 10^5, 4 \times 10^5, 4.7 \times 10^5, 4.8 \times 10^5, 4.9 \times 10^5, 5 \times 10^5, 5.1 \times 10^5, 5.2 \times 10^5$, and $5.3 \times 10^5 \text{ yr}$. The disk edge reaches the EUV gravitational radius at $t_{R_{gII}} \sim 4.9 \times 10^5 \text{ yr}$, when the disk mass is $\sim 10^{-6} M_{\odot}$. The disk mass corresponding to the last surface density distribution shown (at $t = 5.3 \times 10^5 \text{ yr}$) is $\sim 10^{-9} M_{\odot}$. Right, model with low viscosity ($\alpha = 10^{-3}$) and small initial disk ($M_d(0) = 10^{-2} M_{\odot}$). The curves represent $t = 0, 10^3, 10^4, 10^5, 2 \times 10^5, 3 \times 10^5, 4 \times 10^5, 5 \times 10^5, 6 \times 10^5, 7 \times 10^5, 8 \times 10^5, 9 \times 10^5, 10^6, 1.1 \times 10^6$, and $1.2 \times 10^6 \text{ yr}$. The disk edge reaches the EUV gravitational radius at $t_{R_{gII}} \sim 6 \times 10^5 \text{ yr}$, when the disk mass is $\sim 10^{-5} M_{\odot}$. The disk mass corresponding to the last surface density distribution shown (at $t = 1.2 \times 10^6 \text{ yr}$) is $\sim 10^{-9} M_{\odot}$.

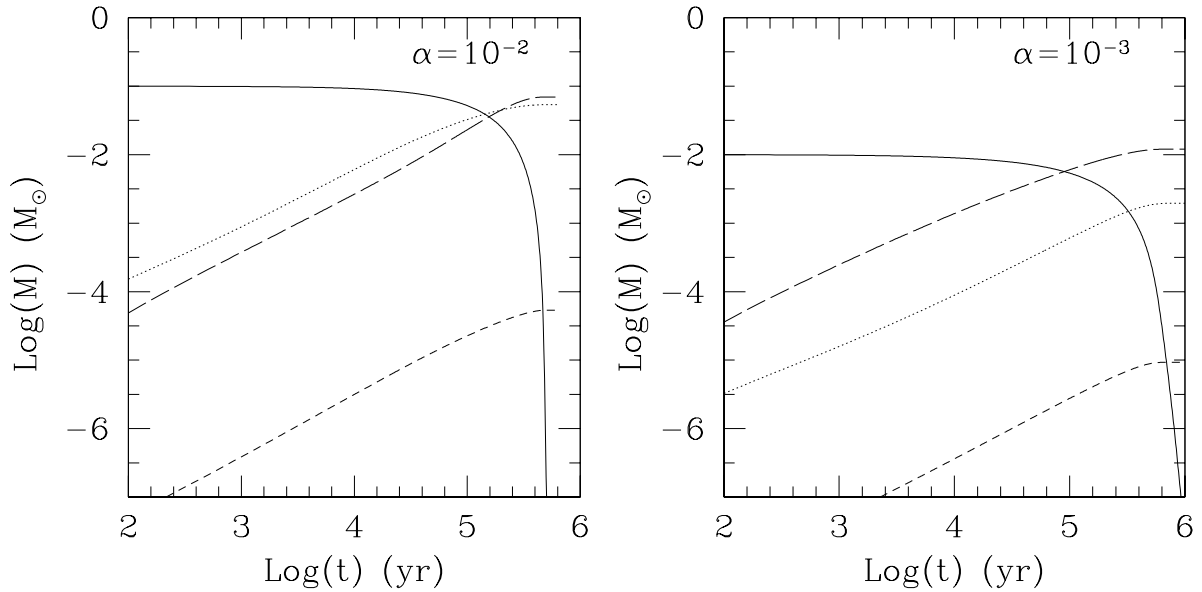


Figure 3.7 Disk mass (solid line), disk mass accreted toward the central star (dotted line), disk mass removed by photoevaporation from the central source (short-dashed line), and disk mass removed by EUV photoevaporation by external stars (long-dashed line) vs. disk lifetime for the two representative models.

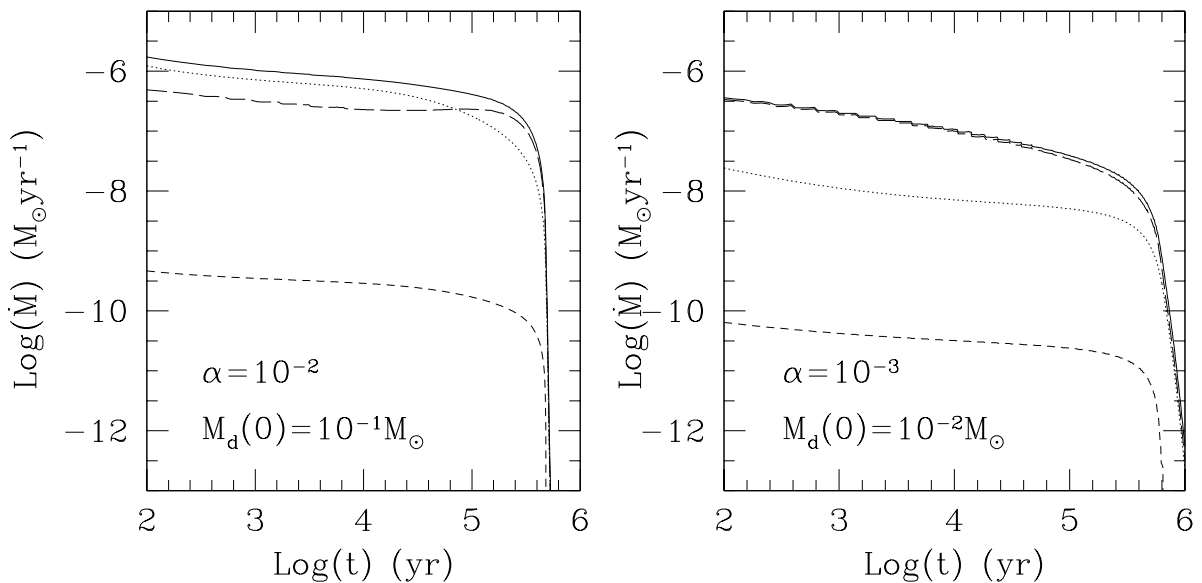


Figure 3.8 Total mass removal rate (solid line), mass removal rate due to accretion (dotted line), mass removal rate due to photoevaporation by the central source (short-dashed line), and disk mass removed by EUV photoevaporation by external stars (long-dashed line) as a function of disk lifetime for the two representative models. The disk is removed by viscous diffusion, photoevaporation from the central source, and EUV photoevaporation by external stars.

by the external stars removes most of the disk mass and changes dramatically the disk evolution, in particular, it is possible to completely remove the disk in $\sim 10^6$ yr.

3.3 FUV photoevaporation by external stars

While the EUV photons create an ionization front and heat the gas to the temperature, $T_{II} \sim 10^4$ K, the FUV photons penetrate this ionized region and heat a neutral hydrogen layer to the temperature, $T_I \sim 10^3$ K. At large distances from the external star the FUV photons dominate and the neutral layer launches a supersonic flow. [Johnstone et al. \(1998\)](#) also found models for FUV dominated external photoevaporation based on observations of the proplyds in the Orion Nebula. The mass loss rate by photoevaporation can be approximated by

$$\dot{M}^{FUV} = \begin{cases} 2 \times 10^{-9} \left(\frac{N_D}{5 \times 10^{21} \text{cm}^{-2}} \right) \left(\frac{R_d}{1 \text{AU}} \right) M_\odot \text{yr}^{-1}, & \text{if } R > R_I; \\ 0, & \text{otherwise,} \end{cases} \quad (3.9)$$

where N_D is the column density from the ionization front to the disk surface, and R_I is the gravitational radius for the neutral layer. In the following models it is assumed that $N_D \sim 5 \times 10^{21} \text{cm}^{-2}$ based on the numerical results of [Störzer & Hollenbach \(1998\)](#). For the Trapezium Cluster, the FUV photons dominate the flux for the proplyds orbiting at a distances $\gg 0.03$ pc from the external stars ([Johnstone et al., 1998](#); [Störzer & Hollenbach, 1999](#)). The surface density photoevaporation rate for the FUV dominated flow is the mass loss rate divided by the effective area of the disk:

$$\dot{\Sigma}_{ext}^{FUV}(R) = \begin{cases} \frac{\dot{M}^{FUV}}{\pi(R_d^2 - R_I^2)}, & \text{if } R > R_I; \\ 0, & \text{otherwise.} \end{cases} \quad (3.10)$$

The disk mass is removed due to viscous accretion toward the central star, photoevaporation from the central source, and FUV photoevaporation by the external stars. In this case, the surface density evolution is given by

$$\frac{\partial \Sigma}{\partial t} = \frac{3}{R} \frac{\partial}{\partial R} \left[R^{1/2} \frac{\partial}{\partial R} \left(\nu \Sigma R^{1/2} \right) \right] + \dot{\Sigma}_{ph} + \dot{\Sigma}_{ext}^{FUV}. \quad (3.11)$$

I show the results for the two representative models with the same parameters as before. Figure 3.9 shows snapshots of the surface density evolution. The outer disk ($R > R_I$) is removed by FUV photoevaporation from the external star, and the disk edge is reduced to the FUV gravitational radius. The disk size remains roughly constant at this radius until the disk is completely removed. At the final stages of the disk evolution ($t \sim t_{gap}$), when the surface density is very low ($\Sigma \sim 10^{-5} \text{g cm}^{-2}$), a gap structure is created by photoevaporation from the central source. The gap formation is possible because photoevaporation from the central source and photoevaporation by

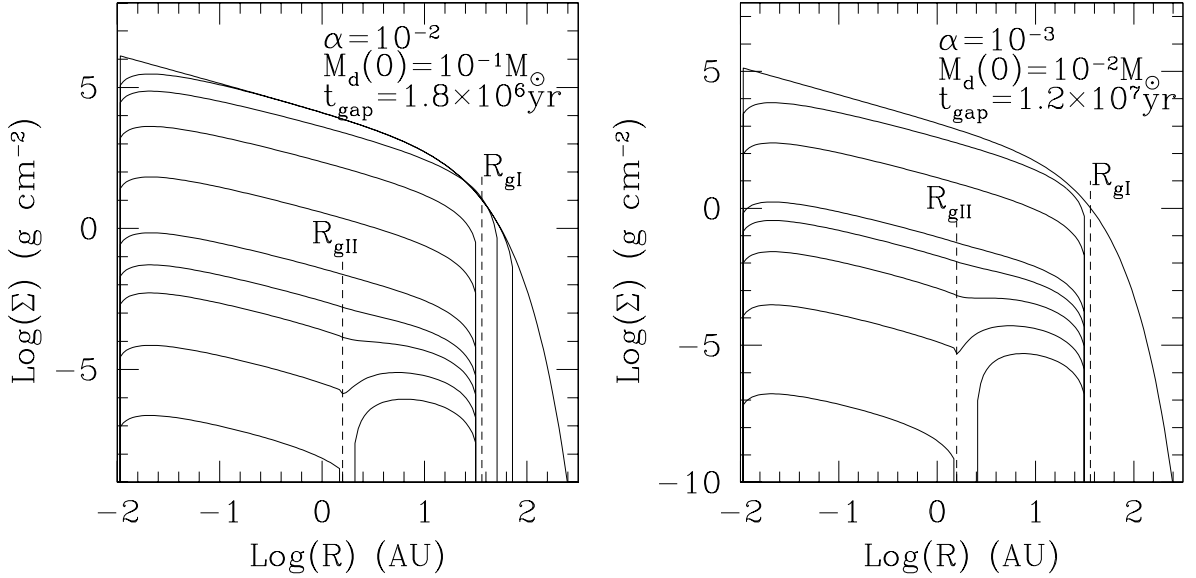


Figure 3.9 Snapshots of the surface density for two representative models with viscous diffusion, photoevaporation from the central source, and EUV photoevaporation by external stars. The dashed lines indicate the location of the EUV gravitational radius, r_{gII} , the FUV gravitational radius, r_{gI} . A gap structure forms at $t \sim t_{\text{gap}}$. Left, model with high viscosity ($\alpha = 10^{-2}$) and massive initial disk ($M_d(0) = 10^{-1} M_\odot$). The curves represent $t = 0, 10^3, 10^5, 5 \times 10^5, 10^6, 1.5 \times 10^6, 1.7 \times 10^6, 1.8 \times 10^6, 1.9 \times 10^6, 2 \times 10^6 \text{ yr}$. The disk edge reaches the FUV gravitational radius, R_{gI} , at $t \sim 10^5 \text{ yr}$, when the disk mass is $\sim 3 \times 10^{-2} M_\odot$. A gap structure forms at $t_{\text{gap}} \sim 1.8 \times 10^6 \text{ yr}$, when the disk is almost completely removed ($M_d \sim 10^{-8} M_\odot$). The disk mass corresponding to the last surface density distribution shown (at $t = 2 \times 10^6 \text{ yr}$) is $\sim 10^{-10} M_\odot$. Right, model with low viscosity ($\alpha = 10^{-3}$) and small initial disk ($M_d(0) = 10^{-2} M_\odot$). The curves represent $t = 0, 10^6, 5 \times 10^6, 10^7, 1.1 \times 10^7, 1.2 \times 10^7, 1.3 \times 10^7, 1.4 \times 10^7 \text{ yr}$. The disk edge is reduced to the FUV gravitational radius, R_{gI} , at $t \sim 10^6 \text{ yr}$, when the disk mass is $\sim 4 \times 10^{-3} M_\odot$. A gap structure starts forming at $t_{\text{gap}} \sim 1.2 \times 10^7 \text{ yr}$, when the disk mass is reduced to $\sim 10^{-7} M_\odot$. The disk mass corresponding to the last surface density distribution shown (at $t = 1.4 \times 10^7 \text{ yr}$) is $\sim 10^{-9} M_\odot$.

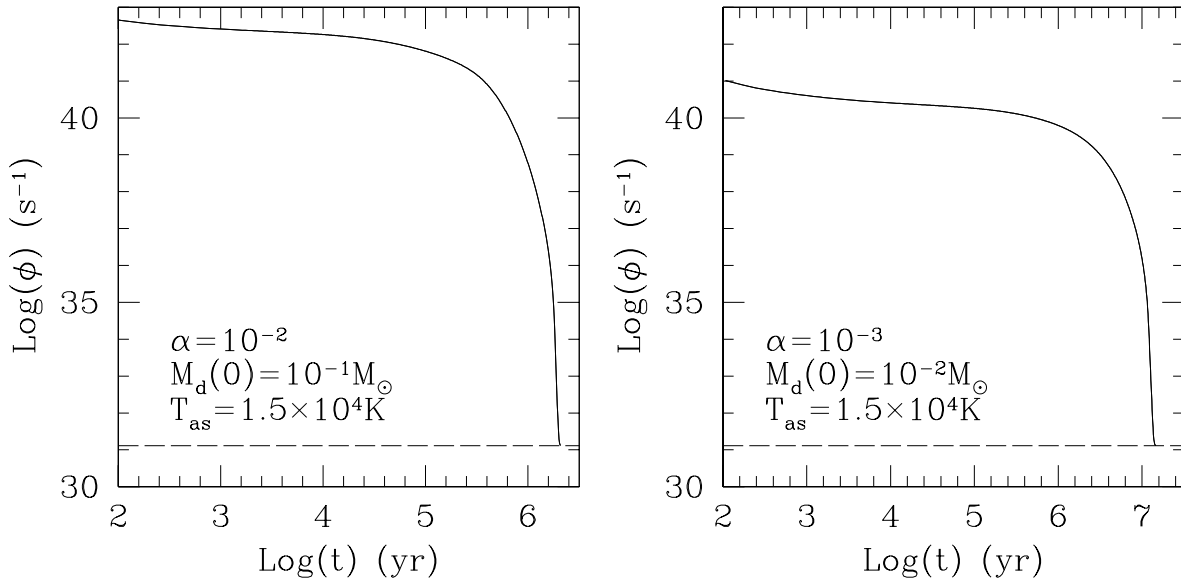


Figure 3.10 Ionizing flux from the central source for disk removal by viscous accretion, photoevaporation from the central source, and FUV photoevaporation by external stars as a function of disk lifetime. The ionizing flux decreases at late stages of the disk evolution with the accretion rate. The long-dashed line indicates the constant ionizing flux from the quiescent stellar photosphere ($\phi_{\star} = 1.29 \times 10^{31} \text{s}^{-1}$).

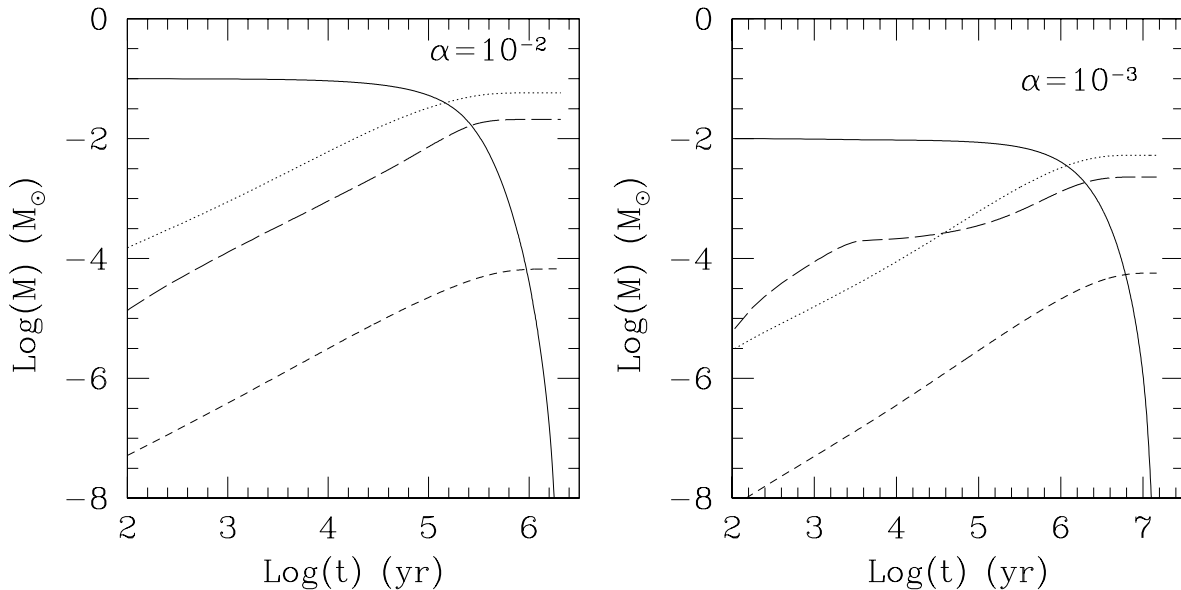


Figure 3.11 Disk mass (solid line), disk mass accreted toward the central star (dotted line), disk mass removed by photoevaporation from the central source (short-dashed line), and disk mass removed by FUV photoevaporation by external stars (long-dashed line) vs. disk lifetime for the two representative models.

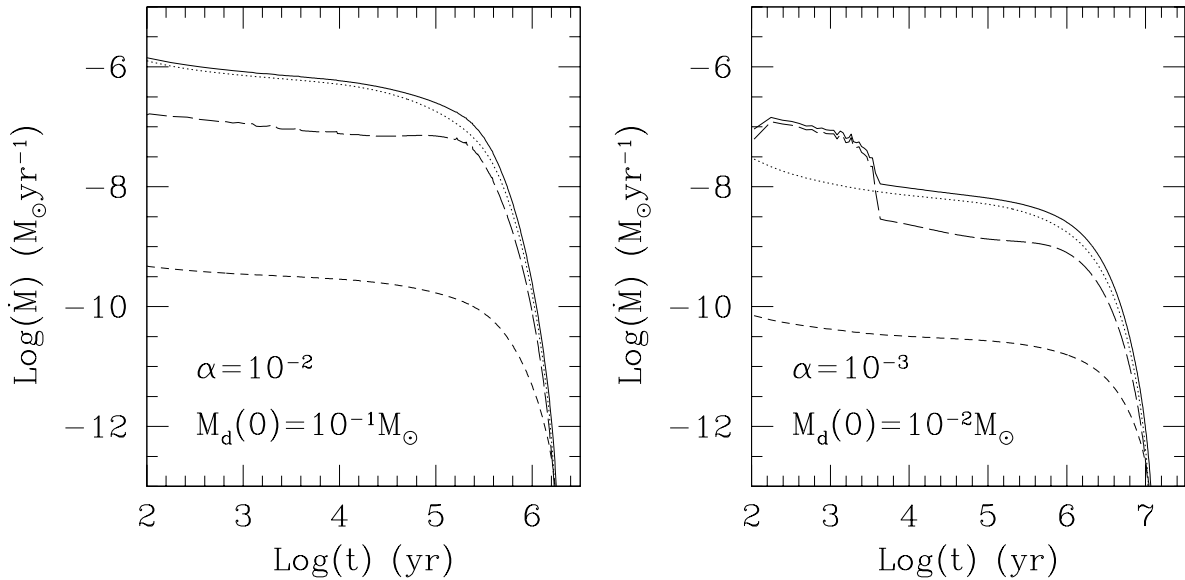


Figure 3.12 Total mass removal rate (solid line), mass removal rate due to accretion (dotted line), mass removal rate due to photoevaporation by the central source (short-dashed line), and mass removal rate by the external stars (long-dashed line) as a function of disk lifetime for

Figure 3.13 the two representative models. The disk is removed by viscous diffusion, photoevaporation from the central source, and FUV photoevaporation by external stars.

the external stars are dominant at different locations (R_{II} and $R_I > R_{II}$ respectively). Both annuli are removed as viscous accretion, viscous spreading, and photoevaporation work in resonance (see Figures 3.11 and 3.12). The outer annulus is removed by the combination of viscous spreading, photoevaporation from the central source, and photoevaporation by the external stars. On the other hand, the inner annulus is removed by the combination of viscous accretion toward the central star, viscous spreading, and photoevaporation from the central source. The efficient inner disk removal is self-consistent since I have calculated the ionizing flux from the accretion luminosity and the quiescent stellar photosphere. As the inner disk is removed, the contribution from the accretion luminosity becomes negligible; as a result, the ionizing flux reaches the value corresponding to the quiescent stellar photosphere, $\phi_\star = 1.29 \times 10^{31} \text{s}^{-1}$ (Figure 3.10). Again, the active chromosphere of these low-mass stars has not been included; however, in this situation the lack of chromospheric ionizing flux is much less important as the timescale for disk evaporation has been set by the disk truncation due to the external source.

3.4 Discussion and summary

I have studied the possibility of disk removal by the combination of viscous diffusion and photoevaporation, assuming that the ultraviolet photons responsible for evaporation arises either from

the quiescent stellar photosphere, the accretion shock, or external O stars. It is not possible to remove the entire disk when the only disk removal mechanism is viscous accretion: the disk spreads indefinitely in order to conserve total angular momentum while material is accreted onto the central star. Mass loss due to photoevaporation removes material along with its specific angular momentum; thus, it is possible to accrete material toward the central star and reduce the amount of disk spreading. The combination of the two mechanisms can result in finite disk lifetimes.

The distinctive features of photoevaporation by the ionizing flux from the central source are the formation of a gap around the EUV gravitational radius at late stages of the disk evolution and the lack of a finite time for the complete dispersal of the disk. The gap forms for the observed range of accretion shock temperatures ($\sim 1 - 3 \times 10^4$ K) and the disk becomes divided into an inner and an outer annulus. The inner annulus is quickly removed by the combination of viscous accretion, viscous spreading of material beyond the EUV gravitational radius, and photoevaporation at this radius. The outer annulus is removed as viscous spreading of material toward the gravitational radius and photoevaporation work in resonance. [Clarke et al. \(2001\)](#) considered models with photoevaporation by a constant central ionizing flux combined with viscous evolution, and showed that the timescales to remove the inner annulus is much shorter than that of the outer annuli. I calculate the ionizing flux from the accretion luminosity self-consistently and find a similar result. However, the inner annulus is removed on a longer time scale. It is not possible to quickly remove the inner annuli and maintain a high ionizing flux at the same time because the accretion rate decreases. The formal disk lifetime is found to be in the range $10^{12} - 10^{13}$ yr for $10^{-3} < \alpha < 10^{-2}$ and initial disk masses $10^{-2} < M(0) < 10^{-1}M_{\odot}$, much longer than the star lifetime. Introducing a stellar chromosphere will produce models intermediate between those presented here and those of [Clarke et al. \(2001\)](#).

Stellar disk material can also be evaporated by external stars. This is a likely situation for the disks surrounded by ionization fronts in the Trapezium Cluster ([Johnstone et al., 1998](#); [Störzer & Hollenbach, 1999](#); [Bally et al., 2000](#)). The EUV photons dominate the flux for the proplyds orbiting at a distance $d \lesssim 0.03$ pc, and the FUV photons dominate for the proplyds at more typical distances ($d \gg 0.03$ pc) from the massive external stars.

I consider photoevaporation due to both the central source and external stars. There is no gap formation for disks nearby external hot stars since their ionizing flux removes all the disk material outside the EUV gravitational radius. The disk is quickly removed by viscous accretion, viscous spreading, and photoevaporation outside the gravitational radius. The disk lifetime is in the range $0.1 - 1$ Myr for the same parameters as before, where the shorter lifetimes correspond to shorter viscous evolution timescales of high viscosities. The disk lifetimes are shorter by roughly two orders of magnitude when compared to the models with only photoevaporation from the central source. The short disk lifetimes are due to the strong influence of the external radiation field at the outer disk, where most of the disk mass initially resides.

The disk evolution is very different at larger, more typical distances ($d \gg 0.03$ pc) from the external stars due to the different locations where photoevaporation is efficient. The disk material in the vicinity of the EUV gravitational radius is removed by photoevaporation from the central source. Similarly, the disk material in the neighborhood of the FUV gravitational radius is removed by external FUV photoevaporation. The effect of external photoevaporation is initially very dominant; quickly reducing the disk size to the FUV gravitational radius. After this disk truncation, the disk mass is removed at two locations. At the inner edge, disk material is viscously accreted onto the central. On the other hand, viscous diffusion spreads the disk material beyond the FUV gravitational radius, and FUV photoevaporation removes the disk material at this location. The combination of this mechanisms decreases the disk surface density. At the last stages of the disk evolution, when the surface density is very low ($\Sigma \sim 10^{-4}$ g cm $^{-2}$), the ionizing flux from the central source opens a gap in the disk. After the gap forms the inner annulus is quickly removed since it cannot be resupplied with material from the outer annulus. The disk lifetime is in the range 1 – 10 Myr for the same parameters as before, where the shorter disk lifetimes correspond to the shorter viscous evolution timescales of high viscosities.

Observations suggest that the timescale for all the stars in young clusters to lose their disks is ~ 6 Myr (Haisch et al., 2001; Hillenbrand, 2002), in agreement with the disk lifetimes for the proplyds nearby external hot stars (0.1 – 1 Myr). The disk removal timescale is an important constraint on the timescale allowed for planet formation. It is very attractive to study the possibility of planet formation in star forming regions since this process follows star and disk formation. If the influence of massive external stars in star forming regions is not demolishing for planet formation, star forming regions are natural birthplaces of extrasolar planets. Numerical simulations suggest a timescale for terrestrial planet formation in the range $\sim 10 - 100$ Myr (Beauge & Aarseth, 1990; Chambers, 2001), and a typical timescale for giant planet formation by core accretion that range from a few million years to more than 10 Myr (Bodenheimer et al., 2000; Ikoma et al., 2000). It is thus not possible to form planets by core accretion around stars in the neighborhood of massive O stars (i.e. EUV external photoevaporation) because the disk lifetime is too short (0.1 – 1 Myr). On the other hand, at typical distances from the external stars ($d \gg 0.03$ pc), the disk lifetimes are long enough (1 – 10 Myr) to allow for the formation of terrestrial and giant planets. There are no constraints on planet formation in the absence of EUV or FUV fluxes from external stars.

Chapter 4

Halting type-II planet migration by disk photoevaporation from the central source

4.1 Introduction

It is believed that gas giants do not generally form at small orbital distances from the central star (Boss, 1995). Thus, a natural explanation for extra solar planets orbiting close to the central star is that these planets formed further away in the protoplanetary disk and migrated inward to where they are now observed. A variety of mechanisms have been proposed to explain planet migration: the interaction between a planet and a planetesimal disk (Murray et al., 1998), the gravitational interaction between two or more Jupiter mass planets (Rasio & Ford, 1996), and the tidal gravitational interaction between the planet and the surrounding disk gas (Goldreich & Tremaine, 1979, 1980). The last mechanism, focused on in this thesis, is expected to be dominant at early times since the surrounding gaseous disk is required for the formation of planets.

If the perturbation exerted on the disk by the planet is small, the disk structure is not greatly altered, and the planet moves inward relative to the surrounding gas (Ward, 1997). This type of migration is referred to as ‘type-I’. However, if the planet is large it may open a gap in the disk (Goldreich & Tremaine, 1980). The planet is locked to the disk and moves either inward or outward in lock-step with the gaseous disk. This slower migration is referred to as ‘type-II’.

In this chapter, I propose a mechanism for halting type-II migration: photoevaporation driven by radiation from the central star. The planet’s final location is consistent with the solar system and the growing class of extra solar planets with nearly circular orbits outside of a few AU (see Tinney et al. 2002, see, Figure 4). Photoevaporation by the central star was proposed by Shu et al. (1993) and Hollenbach et al. (1994) as a way to remove a gas disk. Hollenbach et al. (2000) generalized the

discussion, describing the variety of possible disk removal mechanisms: accretion, planet formation, stellar encounters, stellar winds or disk winds, and photoevaporation by ultraviolet photons from the central source or massive external stars. [Hollenbach et al. \(2000\)](#) concluded that the dominant mechanisms for a wide range of disk sizes are viscous accretion and photoevaporation, operating in concert within the disk. In this chapter, I consider photoevaporation by the central source and viscous accretion.

4.2 Model

The model for disk removal used here is described in Chapter 2 (see also [Matsuyama, Johnstone, & Hartmann, 2003](#)). Additionally, I assume a planet with a large mass, which opens a narrow gap in the disk, and assume that planet migration proceeds in lock-step with the disk evolution (type-II migration). Given a solution for equation (3.5), I find the drift velocity from equation (2.12) to describe the evolution of the disk stream lines.

As discussed in Chapter 3, there are currently no strong observational constraints on the intrinsic ionizing flux from the central star, ϕ_\star . The EUV flux for the sun is $\sim 2.6 \times 10^{37} \text{s}^{-1}$ (see [Wilhelm et al. 1998](#), Fig. 10b). Since TTSs are chromospherically active ([D'Alessio et al., 1998](#)), their EUV fluxes must be higher by few orders of magnitude. I estimated the ionizing flux from the FUV spectra of TTSs and the corresponding distances to these stars in §3.1. The typical estimated values are in the range $\sim 10^{39-41} \text{s}^{-1}$, and [Alexander et al. \(2005\)](#) argue for $\sim 10^{41-44} \text{s}^{-1}$ by analyzing emission measures taken from the literature. However, these values are subject to large uncertainties.

I studied the disk evolution under the assumption that the dominant ionizing flux source is the accretion shock in Chapter 3. For completeness, I explore the impact of strong intrinsic stellar fluxes in this chapter. I assume that the active stellar chromosphere produce an EUV flux of constant magnitude $\phi_\star = 10^{40} \text{s}^{-1}$, and that half of the accretion luminosity is radiated as hot continuum from accretion shocks. I characterize the accretion shock luminosity as blackbody emission at $T_{as} = 10^4 \text{K}$ ([Kenyon et al., 1989](#); [Johns-Krull et al., 2000](#)). For these parameters, the dominant ionizing flux source is the stellar chromosphere.

Combining photoevaporation with viscous accretion is done numerically (see Appendix A). At each time step, photoevaporation induced mass loss and viscous diffusion induced disk evolution are solved. The simulation is stopped when the disk mass is $1M_J$.

4.3 Discussion

At a given disk radius, a gap forms when the mass transported by viscous accretion is equal to the mass removed by photoevaporation. This occurs when the photoevaporation time scale, $\Sigma/\dot{\Sigma}_{ph}$, is

equal to the viscous diffusion time scale, $R^2/3\nu$, at the gravitational radius R_{II} . Therefore, I can estimate the surface density for gap formation at the gravitational radius,

$$\Sigma_{gap} \sim 2 \left(\frac{\alpha}{10^{-3}} \right)^{-1} \left(\frac{\phi_\star}{10^{40} \text{s}^{-1}} \right)^{1/2} \left(\frac{R_g}{2.4 \text{AU}} \right)^{-1} \text{g cm}^{-2}. \quad (4.1)$$

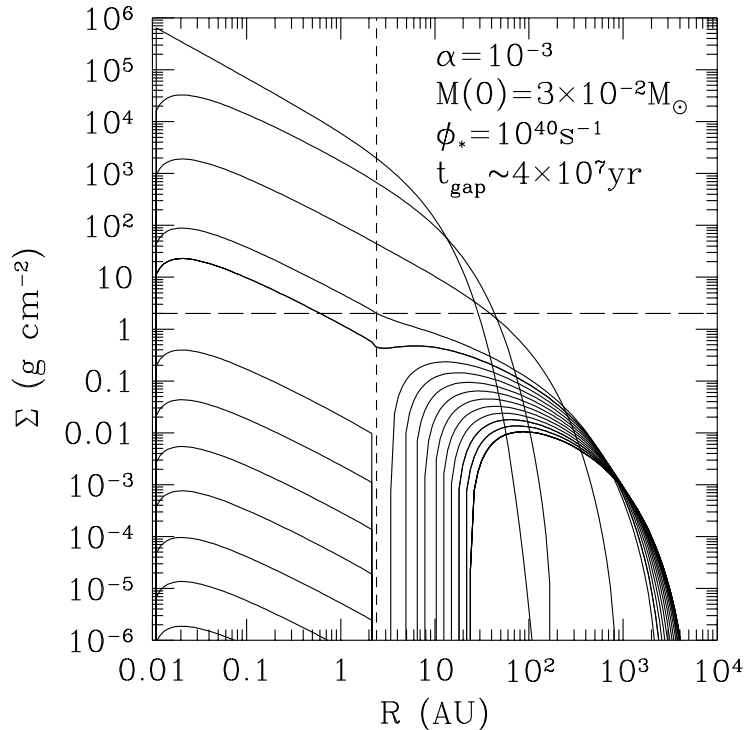


Figure 4.1 Snapshots of the surface density for a fiducial model under the influence of viscous diffusion and photoevaporation from the central source. The model corresponds to $\alpha = 10^{-3}$, and an initial disk mass, $M(0) = 0.03M_\odot$. The short-dashed line indicates the location of the gravitational radius and the long-dashed line corresponds to the minimum surface density for gap formation by photoevaporation. The solid curves represent $t = 0, 1, 10, 36, 42, 47, 52, 57, 62, 67, 72, 77, 82, 87,$ and 92 Myr. The gap structure starts forming at $t_{gap} \sim 40$ Myr, when the disk mass is $\sim 3M_J$ and the surface density at the gravitational radius is $\Sigma_{gap}(R_{II}) \sim 2 \text{g cm}^{-2}$ (long-dashed line).

Figure 4.1 shows snapshots of the disk surface density distribution for a disk with initial mass, $M(0) = 0.03M_\odot$ and $\alpha = 10^{-3}$. A gap starts forming at the gravitational radius when the surface density reaches $\Sigma_{gap} \sim 2 \text{g cm}^{-2}$ during the last stages ($t_{gap} \sim 40$ Myr) of the disk evolution and the disk is divided into two annuli. The subsequent evolution is dominated by two competing effects; viscous diffusion attempts to spread both annuli and remove the gap structure while photoevaporation removes material predominantly at the gravitational radius, reopening the gap. The material in the inner annulus is quickly removed both at the inner edge, by accretion onto the central star, and at the outer edge, by the combination of viscous spreading and photoevaporation.

In contrast, the outer annulus loses material primarily from its inner edge. The inner edge of the outer annulus recedes from the star as photoevaporation removes disk material, thereby reducing the mass removal rate in accordance with equations (3.1) and (3.2).

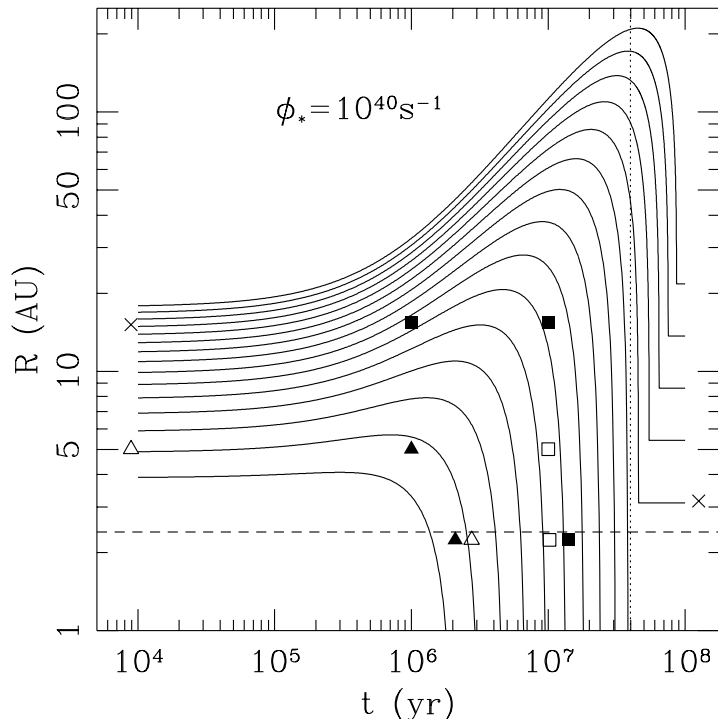


Figure 4.2 Disk stream lines for the fiducial model with $M(0) = 0.03M_{\odot}$ and $\alpha = 10^{-3}$. The initial spacing (at $t = 10^4$ yr) between the streamlines is 1AU, covering the disk from 4AU to 18AU. The short-dashed line indicates the location of the gravitational radius, $R_g = 2.4$ AU, and the dotted line represents the time when the photoevaporation gap starts forming, $t_{gap} \sim 4 \times 10^7$ yr. Planets forming at $R \sim 5$ AU and tidally locking to the disk early ($t = 10^4$ yr) (open triangles) or late (solid triangles) fall onto the central star at $t \sim 2.5 \times 10^6$ yr. In contrast, a planet starting with initial semi-major axis $R \sim 15$ AU at $t = 10^4$ yr (crosses) stops migrating when it reaches the photoevaporation gap.

I model a planet which has opened a narrow gap in the disk. In order for the gap to be maintained, the tidal torque exerted by the planet must exceed the viscous torque. This requires that the planet mass is greater than the critical mass,

$$M_c \sim M_{\star} (81\pi\alpha c_s^2/8v_k^2) \quad (4.2)$$

(see, e.g., [Lin & Papaloizou 1993](#)). The planet is initially tidally locked to the disk and moves with the gas, migrating outward or inward depending on its initial location. This migration may stop for two reasons. First, the combination of photoevaporation from the central source and viscous spreading removes disk mass, reducing the gravitational interaction between the planet and the

disk and allowing the planet to decouple its orbit from that of the gas. Second, the planet will stop if it reaches the gap created by photoevaporation, as the tidal torques are unable to influence the planet across such a large opening.

I describe the evolution of the disk stream lines by using equation (2.12). Figure 4.2 shows the disk stream lines which start between 4 and 18AU, at $t = 10^4$ yr, where there is enough mass to form a Jupiter mass planet in an annulus of width 4AU. After the planet opens a gap it migrates along the disk stream lines; therefore, I can follow planet migration in Figure 4.2 for different planet gap opening locations and times. The disk mass outside the gravitational radius is reduced to Jupiter’s mass in $\sim 10^8$ yr (see Figure 4.3); therefore, a migrating planet with Jupiter’s mass stops migrating at any disk location soon after this time. However, a migrating planet may reach the inner disk boundary ($R_{min} = 10^{-2}$ AU) or the photoevaporation gap before the disk mass is reduced to Jupiter’s mass.

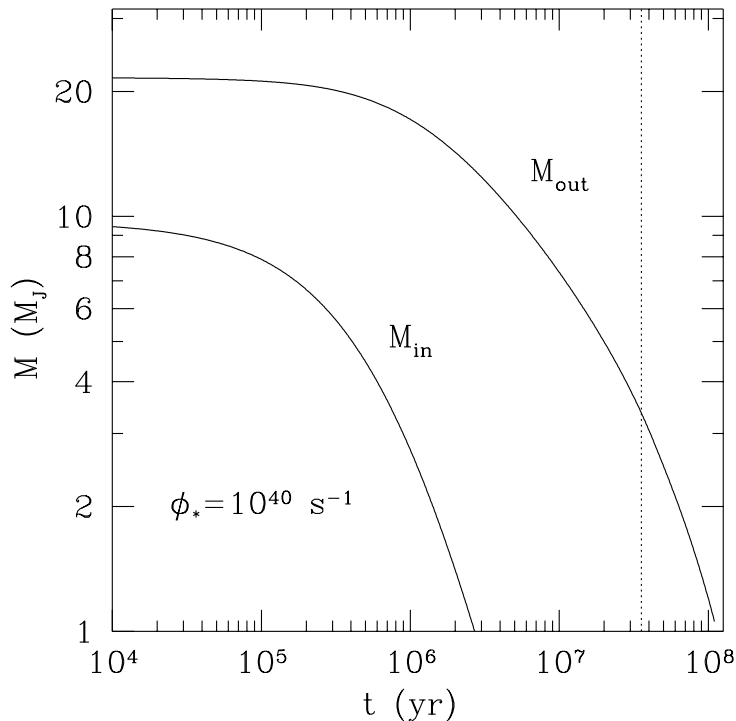


Figure 4.3 Disk mass outside the gravitational radius, M_{out} , and disk mass inside the gravitational radius, M_{in} , as a function of disk lifetime for the fiducial model. The dotted line indicates the time, $t_{gap} \sim 40$ Myr, when the gap structure starts forming.

Figure 4.2 provides information on which initial locations, and times, allow a planet tidally locked to the disk to survive. It is difficult to time the gaseous disk removal in such a manner as to maintain planets at large distances from the central star. A planet which opens a narrow gap at $t = 10^4$ yr only survives if its initial disk location is greater than the critical radius ~ 14 AU,

because the planet reaches the outer edge of the photoevaporation gap after the gap has formed. Since the disk expands rapidly at early times, this critical radius increases with later planet gap opening timescales; i.e. the later the planet forms, the further away from the central star it has to be in order to survive. However, this behavior changes after the photoevaporation induced gap forms. If the planet forms at a time similar to when the photoevaporation gap forms, $t_{gap} \sim 40$ Myr, it survives as long as it originates outside the gravitational radius.

ϕ_\star (s^{-1})	t_{gap} (Myr)	t_{final} (Myr)	R_i (AU)							
			12	14	16	18	20	22	24	26
			R_f (AU)							
10^{39}	80	149							8.2	22.9
10^{40}	40	74					4.4	9.3	19.5	44.9
10^{41}	20	35				5.8	9.8	16.6	28.2	47.7
10^{42}	10	15	2.7	4.6	7.5	11.5	17.5	26.8	39.4	

Table 4.1 Final planet locations R_f for different stellar EUV fluxes ϕ_\star and initial planet gap opening locations R_i . The times when the photoevaporation gap forms and the disk mass is reduced to $0.1M_J$ are denoted as t_{gap} and t_{final} respectively.

I summarize the results for different stellar EUV fluxes in the range $10^{39-42} \text{ s}^{-1}$ in table 4.1. The disk mass is reduced to $0.1M_J$ in $\sim 15-150$ Myr for this range of EUV fluxes. These time scales are longer than typically observed dust disk lifetimes ($\sim 1-10$ Myr). However, the disk presence is usually inferred from observations in the near-infrared, which is sensitive to the hot inner disk (< 0.1 AU; Hillenbrand, 2002). The inner disk is quickly removed after the photoevaporation gap forms while the outer disk continues to spread to conserve angular momentum. The photoevaporation gap formation occurs at $\sim 5-40$ Myr, which is in agreement with the observed inner disk life times. The possibility of halting type-II migration increases for high stellar ionizing fluxes since the photoevaporation gap formation occurs earlier. The number of disk streamlines that stop outside the gravitational radius increases (slowly) with the stellar EUV flux.

4.4 Conclusions

In this chapter, I have studied different scenarios in which a planet undergoing type-II migration survives due to the formation of a gap by photoevaporation from the central source. If the planet gap opening occurs close to when the photoevaporation gap forms (at $t \sim 40$ Myr for our fiducial model), the final semi-major axis of the planet is near the gravitational radius ($\sim 2.4\text{AU}$) for a wide range of initial semi-major axes. This scenario requires long time scales for planet formation ($1-100$ Myr), similar to those predicted by the core accretion model (Pollack et al., 1996; Bodenheimer et al., 2000).

I can also predict the final semi-major axis when considering rapid planet formation by disk

instability (Boss, 2000). Our disk initially spreads outward under the influence of viscosity, allowing planets that form early at small radii to move out beyond R_{II} before the photoevaporation gap opens, and enhancing their survival rate. The rate and amount of viscous spreading in real disks depends on the initial surface density profile and any continuing accretion onto the disk. If the planet induced gap opening occurs at early stages of the disk evolution (for example, at $t \sim 10^4 \text{yr}$), all the planets initially located inside $\sim 14 \text{AU}$ will reach the disk inner boundary at the central star. The only planets which survive are those which form at a narrow range of semi-major axes ($14 \lesssim R \lesssim 18 \text{AU}$). However, viscous diffusion spreads this narrow range during planet migration, and the final semi-major axis distribution is $3 \lesssim R \lesssim 22 \text{AU}$. This final distribution of planets has similarities to our own solar system and it suggests that the gas giants could have formed at $\sim 14 - 18 \text{AU}$ and migrated to their current locations. Furthermore, the initial planet locations are in agreement with recent simulations of planet formation by disk fragmentation (Mayer et al., 2002).

The minimum surface density for gap opening by photoevaporation, Σ_{gap} , and the disk size, R_{II} , determine the disk mass outside the gravitational radius. In our fiducial model, the mass outside the gravitational radius at the time of gap opening is $2\pi\Sigma_{gap}R_{II}(R_d - R_{II}) \sim 3M_J$; therefore it is possible to consider migration of a Jupiter mass planet. However, for lower ionizing fluxes (i.e. $\phi_\star \lesssim 10^{40} \text{s}^{-1}$), the minimum surface density for gap opening by photoevaporation becomes smaller (see equation 4.1) and the halting of planet migration becomes marginal. For example, for $\phi_\star = 10^{38} \text{s}^{-1}$, the minimum surface density for gap opening and the disk mass outside the gravitational radius are smaller by one order of magnitude (i.e., $\Sigma_{gap} \sim 0.2 \text{gcm}^{-2}$ and $M_{out} \sim 0.3M_J$).

The gravitational radius R_{II} roughly coincides with the location of the asteroid belt in the solar system. It is well known that the surface density of heavy elements reaches a severe local minimum in the asteroid belt; this is usually attributed to long term gravitational effects from Jupiter, although it is not clear that the amount of depletion that results is sufficient (Holman & Murray, 1996; Liou & Malhotra, 1997). Simple estimates show that the planetesimal formation time scale is much shorter than the gap formation time, so it is not clear that the formation of a photoevaporation gap would significantly reduce the surface density of planetesimals, but the coincidence is intriguing.

The photoevaporation gap opening timescale ($\sim 40 \text{Myr}$) is long compared to the typically observed gaseous disk lifetimes ($1 - 10 \text{Myr}$). However, the disk lifetime for stars outside stellar clusters is considerably longer than the disk lifetime for stars in the hostile stellar clusters (Matsuyama et al., 2003). In addition, there is evidence that some stars retain disks between $10 - 100 \text{Myr}$ (see Hillenbrand 2002, Figure 2).

It is also possible to halt both type-I and type-II migration in stellar clusters by removing the entire disk. This is a likely situation for the disks surrounded by ionization fronts in the Trapezium Cluster (Johnstone et al., 1998; Störzer & Hollenbach, 1999; Bally et al., 2000). As discussed in

§3.2 and §3.3, the disk lifetime due to photoevaporation by external stars is in the range 0.1 – 1 Myr in the neighborhood of massive O stars, and between 1 – 10 Myr at reasonable distances ($\sim 0.03 - 0.3$ pc) from external O stars. These timescales are in agreement with observational estimates for the lifetime of protoplanetary disks in stellar clusters (Haisch et al., 2001). Since the outer disk is removed first, there is no photoevaporation gap formation. This scenario is possible when considering the rapid planet formation by disk instability; on the other hand, it is uncertain whether gas giant planets form by core accretion in these short-lived disks.

Chapter 5

Final comments and future work

The major aim of part I of this thesis has been to study the evolution of protoplanetary disks under the influence of viscous evolution, photoevaporation from the central source, and photoevaporation by external stars. In Chapter 3, I adopt the typical parameters of T Tauri Stars (TTSs) and the Trapezium Cluster conditions to discuss the disk evolution. The photoionizing flux from the central source is assumed to arise both from the quiescent star and accretion shocks. The accretion flux is calculated self-consistently from the accretion mass loss rate. I find that the disk cannot be entirely removed using only viscous evolution and photoionization from the disk-star accretion shock. However, when FUV photoevaporation by external massive stars is included the disk is removed in $\sim 1 - 10$ Myr; and when EUV photoevaporation by external massive stars is included the disk is removed in $\sim 0.1 - 1$ Myr.

An intriguing feature of photoevaporation by the central star is the formation of a gap in the disk at late stages of the disk evolution. As the gap starts forming, viscous spreading and photoevaporation work in resonance. When viscous accretion and photoevaporation by the central star and external massive stars are considered, the disk shrinks and is truncated at the gravitational radius, where it is quickly removed by the combination of viscous accretion, viscous spreading, photoevaporation from the central source, and photoevaporation by the external stars. There is no gap formation for disks nearby external massive stars because the outer annuli are quickly removed by the dominant EUV flux. On the other hand, at larger, more typical distances ($d \gg 0.03\text{pc}$) from the external stars the flux is FUV dominated. As a consequence, the disk is efficiently evaporated at two different locations; forming a gap during the last stages of the disk evolution.

The recent discovery of Jupiter-mass planets orbiting at a few AU from their stars compliments earlier detections of massive planets on very small orbits. The short period orbits strongly suggest that planet migration has occurred, with the likely mechanism being tidal interactions between the planets and the gas disks out of which they formed. The newly discovered long period planets, together with the gas giant planets in our solar system, show that migration is either absent or rapidly halted in at least some systems. In Chapter 4, I propose a mechanism for halting type-II

migration at several AU in a gas disk. Photoevaporation of the disk by irradiation from the central star can produce a gap in the disk at a few AU, preventing planets outside the gap from migrating down to the star. This would result in an excess of systems with planets at or just outside the photoevaporation radius.

In this thesis I only considered the possibility of halting type-II migration. Halting the migration of Earth-mass planets has strong implications for their habitability and detectability. In particular, the presence of liquid water is determined by the planet final location and the protoplanetary disk location where water condensates (Sasselov & Lecar, 2000). The time scale for type-I migration is estimated to be ~ 1 Myr for an Earth-size planet at 5 AU Tanaka et al. (2002). This time scale is shorter than the photoevaporation gap formation time, and thus, it is not possible to halt type-I migration by this mechanism unless the stellar EUV flux is very high ($\sim 10^{44} \text{ s}^{-1}$), as argued by Alexander et al. (2005). However, this possibility must be studied by explicitly including planet-disk interactions (Lin & Papaloizou, 1986) since the planet moves across the disk stream lines during type-I migration.

Finally, photoevaporation may also play a significant role during the very first stages of planet formation. In the standard theory of planet formation by core accretion, the first step is the assembly of kilometer-sized objects, or planetesimals, from dust particles in a protoplanetary disk. It remains controversial whether planetesimals form by collision-induced dust sticking (Poppe et al., 2000) or by gravitational instability (Goldreich & Ward, 1973). The surrounding gas affects both mechanisms. Because gas orbits the central star more slowly than a solid body due to gas pressure, solid bodies feel a head wind. On the one hand, small bodies—dust grains—are entrained in the gas disk and orbit the central star with the gas speed. On the other hand, the head wind removes angular momentum from larger bodies, causing them to drift towards the central star. The angular momentum loss is small for planetesimals; however, the drifting is very rapid for meter-sized objects (Weidenschilling, 1977). Hence, planetesimal formation by dust sticking becomes challenging when bodies reach this critical size. Gravitational instability avoids the gas drag problem by direct assembly of planetesimals from bodies that are smaller than the threshold $\sim \text{m}$ size. However, the slowly orbiting gas causes vertical shear of the dust layer; generating Kelvin-Helmholtz turbulence. The resulting turbulent motion prevents dust grains from settling towards the mid-plane to form a gravitationally unstable thin disk (Cuzzi et al., 1993). Since the gas can only stir a finite amount of solids, increasing the dust to gas ratio may result in gravitational instability (Sekiya, 1998).

Increasing the dust to gas ratio can be done by either collecting dust in one place or removing some of the gas. Dust particles have a tendency to pile up due to variations in orbital speeds induced by gas drag (Youdin & Shu, 2002), or local solid density enhancements (Goodman & Pindor, 2000). Photoevaporation of the gas has been proposed as a possible mechanism for augmenting the dust to gas ratio (Sekiya, 1983). However, a detailed study for this scenario is yet to be done.

Part II

True polar wander rotational stability of planets

Chapter 1

Introduction

Large scale reorientation of the rotation pole may cause severe climate and sea level variations and have major consequences for the habitability of planets. The rotational stability of planets can be conveniently separated into two parts: (i) precession and nutation and (ii) true polar wander (TPW).

Precession and nutation refer to motions of the rotation vector as viewed from space and are a consequence of external torques acting on the equatorial bulge of the planet. On Earth, the precession due to the gravitational torques exerted by the Sun and the Moon causes its rotation axis to sweep out a cone of 23° once in ~ 26000 years. Since the relative positions of Moon, Earth and Sun are varying with time, there are additional motions called nutations with periods that are directly related to the periods of the orbital motions of the planets.

The TPW rotational stability of planets is the primary focus of part II. This thesis will not be concerned with precession or nutation. TPW refers to the torque-free response of the rotation axis to adjustments in the inertia tensor. In this case, the angular momentum vector remains constant as viewed from space. [Goldreich & Toomre \(1969\)](#) showed that an object in principal axis rotation will continue in this state, even if its principal axis slowly migrates large distances though the body. This critical result is derived in Chapter 2. In general, both the magnitudes and directions of the principal axes may change with respect to a reference frame fixed to the planet, and thus the rotation axis is said to ‘wander’ with respect to this frame.

In Chapter 3, following the example of [Gold \(1955\)](#) and [Goldreich & Toomre \(1969\)](#), I consider the rotational stability of simple quasi-rigid bodies consisting of a colony of randomly crawling beetles (i.e., randomly distributed mass anomalies). The beetles (mass anomalies) may be regarded as external or internal processes responsible for changes in the inertia tensor of a planet. Of course, planets differ from these simplified models, primarily in that they can deform in response to these processes. Nevertheless, the rotational stability of these simplified quasi-rigid bodies serves to illustrate the basic physics involved in TPW.

Turning to deformable planets, in Chapter 4 I adopt spherically symmetric, linear (Maxwell)

viscoelastic rheology and derive general expressions for the time dependent and fluid limit inertia tensor variations associated with: (1) the direct effect of surface mass loads, (2) the deformation of the planet driven by these loads, and (3) the deformation of the planet driven by rotation. The next two chapters adopt these expressions to revisit several long-standing problems in planetary rotation.

In Chapter 5, I consider the long term rotational stability of planets in response to mass loading. Gold (1955) and Goldreich & Toomre (1969) considered uncompensated surface mass loads and concluded that a mass of any size (e.g., a ‘beetle’) would drive a TPW that ultimately reorients the load to the equator. Their work was extended by Willemann (1984) who treated the more self-consistent problem where the presence of a lithosphere leads to both imperfect load compensation and a remnant rotational bulge. His analysis predicts a TPW that is independent of the lithospheric strength. Willemann (1984) assumed that the planet’s response to a surface mass and potential tidal-effective forcing is identical (at spherical harmonic degree two). I extend his analysis by relaxing this assumption and also by treating the case of non-axisymmetric loading.

Paleomagnetic studies provide observational constraints on long term TPW on Earth by assuming that the magnetic and rotation axis remain aligned over long time scales. An apparent polar wander path (APWP) shows past locations of Earth’s rotation pole, defined as the time averaged paleomagnetic pole, relative to a given lithospheric plate. Although plate motion is the main cause of APW, TPW is also a contributor. It is possible to remove the effects of plate motions from APWP’s to determine the TPW history. These studies suggest $10 - 30^\circ$ of TPW over the last 100 – 200 Myr (Prévot et al., 2000; Sager & Koppers, 2000; Besse & Courtillot, 2002). During more ancient periods, it is possible to infer TPW when polar motion dominates plate motion. This may occur during inertia interchange TPW (IITPW) events, when the two largest principal axes exchange their moments and the rotation pole migrates by $\sim 90^\circ$. This special type of TPW has been inferred from APWP’s during the Cambrian period (~ 500 Ma), and it is speculated as a possible cause for the profound biotic diversification during this period (Kirschvink et al., 1997).

The long term TPW is associated with the gradual redistribution of density inhomogeneities within the Earth by the convective processes responsible for plate motions (e.g., Steinberger & O’Connell, 1997; Richards et al., 1997; Forte & Mitrovica, 1997; Richards et al., 1999; Greff-Lefftz, 2004). These studies assume, following the arguments by Gold (1955) and Goldreich & Toomre (1969), that the rotational bulge of the Earth will ultimately respond hydrostatically to a change in the orientation of the rotation vector. However, as discussed in §5.2.2, the development of the Earth’s lithosphere implies that a non-hydrostatic remnant rotational bulge may contribute to the rotational stability. Our theoretical analysis in Chapter 5 can be used to assess whether the assumption made in previous simulations of long term TPW on Earth might be sensitive to the presence of a lithosphere.

There are several reasons to believe that Mars may also have undergone TPW. On Mars,

partially compensated relief is an important source of the non-hydrostatic inertia tensor, the most striking topographic feature being Tharsis, the largest gravity anomaly in the solar system. Tharsis could have formed on the equator, but more likely formed elsewhere and then migrated to the equator via TPW. [Melosh \(1980\)](#) argues for $\lesssim 25^\circ$ of TPW by removing the Tharsis anomaly from the gravity field and recomputing the ancient pole position from the residual gravity anomalies. [Schultz & Lutz \(1988\)](#) propose a larger TPW ($\sim 90^\circ$), since deposits in the equatorial provinces of Mesogaea and Arabia bear strong resemblance to present day polar deposits. The location of giant impact basins on a single great circle may record heliocentric asteroid orbital planes that coincide with the equator of Mars before TPW occurred ([Arkani-Hamed, 2005](#)). Similar evidence exists for craters formed by oblique impacts, which may record former equatorial satellites ([Schultz & Lutz-Garihan, 1982](#)). Paleomagnetic data provides evidence that an early magnetic field was not aligned with the present rotation axis ([Arkani-Hamed & Boutin, 2004](#)). However, [Grimm & Solomon \(1986\)](#) calculated the predicted lithospheric stress field due to TPW, and conclude that either no substantial TPW occurred, or that the last episode of significant TPW occurred prior to development of most of the preserved surface features. [Willemann \(1984\)](#) considered the rotational stability associated with Tharsis emplaced and bounded the predicted reorientation to $\lesssim 18^\circ$. In Chapter 5 I explore whether our revised theory permits higher load-induced excursions of the martian pole.

Next; in Chapter 6, I investigate the time dependent rotational stability by applying the inertia tensor perturbations derived in Chapter 4 to an ice age Earth. I present a new treatment of the linearized Euler equations that govern rotation perturbations on a viscoelastic planet driven by surface loading.

The Earth's rotation axis is currently undergoing TPW driven by past and present changes in surface ice mass distributions. The response of the Earth to these events is generally referred to as glacial isostatic adjustment (GIA). Optical astrometric observations of star positions taken over the last century indicate a drift of the rotation pole towards $\sim 80^\circ\text{W}$ longitude (Hudson Bay) at a rate of $\sim 1^\circ/\text{Myr}$ ([McCarthy & Luzum, 1996](#); [Gross & Vondrak, 1999](#)). Numerical and theoretical predictions of present-day rates of polar motion due to GIA exhibit a strong sensitivity to the adopted lower mantle viscosity, and thus, have been used to constrain this parameter ([Yuen et al., 1982](#); [Peltier & Wu, 1983](#); [Spada et al., 1992a](#); [Peltier & Jiang, 1996](#); [Milne & Mitrovica, 1996](#); [Vermeersen & Sabadini, 1996](#); [Vermeersen et al., 1997](#)). In a series of recent papers, [Nakada \(2000, 2002\)](#) argued that predictions of TPW are also sensitive to the choice of rheology for the lithosphere; finite-viscosity viscoelastic or purely elastic. In this regard, [Nakada \(2002\)](#) pointed out an apparent paradox in his results; namely, predictions of present-day TPW speed for the case of a viscoelastic lithosphere did not converge to the predictions based on an elastic lithosphere, even when he adopted viscosities in the former as high as 10^{40} Pa s. Our goal in Chapter 6 is to resolve this paradox while revisiting the rotational stability of an ice age Earth.

Finally, the main results are summarized in Chapter 7, which also includes an outline of some outstanding issues and possible directions for future research.

Chapter 2

True polar wander adiabatic invariant for a quasi-rigid body

Following the seminal analysis of [Goldreich & Toomre \(1969\)](#), studies of long-term true polar wander generally assume that the solid angle between the angular momentum vector and the principal axis of inertia with the largest moment is an adiabatic invariant (a quantity whose total change tends to zero as the rate of the external parameters tends to zero). I follow their analysis in this Chapter to illustrate the validity of this critical assumption. The work of [Goldreich & Toomre \(1969\)](#) was extended by [Fisher \(1974\)](#) who considered TPW of a viscoelastic Earth model.

For a rigid body, the free nutations are stable about either the principal axis with the largest of the three moments of inertia, or the axis with the smallest moment. The angular momentum vector sweeps out the surface of a cone whose solid angle is constant (see [Appendix B](#)), and the adiabatic invariance is satisfied.

Since the state of lowest kinetic energy for a rigid body corresponds to rotation about the principal axis associated with the largest moment of inertia (see [Appendix B](#)), any internal energy dissipation will tend to drive the body to that state. I assume that the planet is a ‘quasi-rigid body’, in the sense that the characteristic time scales of the processes responsible for changes in the planet inertia tensor are longer than the slowest of the nutations experienced at any stage of the evolution of the body.

2.1 Equations of motion for a quasi-rigid body

The rotational state of a quasi-rigid body can be described by the rotation vector $\Omega_i(t)$, the inertia tensor I_{ij} , and the three components of the excess angular momentum $h_i(t)$. The excess angular momentum arises because the body is not truly rigid, and it is defined as the excess (or deficit) with respect to the angular momentum in the case of rigid body rotation. For simplicity, and with no loss of generality, I choose the principal axes reference frame with origin at the centre of mass

to diagonalize the inertia tensor. The total angular momentum is

$$L_i(t) = I_{ij}(t)\Omega_j(t) + h_i(t), \quad (2.1)$$

and angular momentum conservation in the rotating body frame in the absence of external torques yields

$$0 = \left(\frac{d\mathbf{L}}{dt} \right) + \boldsymbol{\Omega} \times \mathbf{L}. \quad (2.2)$$

The last equation is generally referred to as Euler's equation. For simplicity, I use the normalized quantities $\bar{L}_i(t) \equiv L_i(t)/L$ and $\bar{h}_i(t) \equiv h_i(t)/L$, where L is the magnitude of L_i , to rewrite equations (2.1) and (2.2) as

$$\mathbf{D} \cdot (\bar{\mathbf{L}} - \bar{\mathbf{h}}) = \boldsymbol{\Omega} \quad (2.3)$$

and

$$\frac{d\bar{\mathbf{L}}}{dt} = \bar{\mathbf{L}} \times \boldsymbol{\Omega}, \quad (2.4)$$

where I define $D_{ij} \equiv L/I_{ij}$ and I_{ij} is the diagonalized inertia tensor. Combining these two equations gives

$$\frac{d\bar{L}_i}{dt} = \epsilon_{ijk} \bar{L}_j D_{kl} (\bar{L}_l - \bar{h}_l), \quad (2.5)$$

which is known as Liouville's equation, and corresponds to the generalization of Euler's equation to bodies that are non-rigid. The three components of this equation are

$$\begin{aligned} \frac{d\bar{L}_1}{dt} &= \bar{L}_2 D_3 (\bar{L}_3 - \bar{h}_3) - \bar{L}_3 D_2 (\bar{L}_2 - \bar{h}_2) \\ \frac{d\bar{L}_2}{dt} &= \bar{L}_3 D_1 (\bar{L}_1 - \bar{h}_1) - \bar{L}_1 D_3 (\bar{L}_3 - \bar{h}_3) \\ \frac{d\bar{L}_3}{dt} &= \bar{L}_1 D_2 (\bar{L}_2 - \bar{h}_2) - \bar{L}_2 D_1 (\bar{L}_1 - \bar{h}_1). \end{aligned} \quad (2.6)$$

In the absence of external torques, the magnitude of the angular momentum vector must be conserved and I can use the constraint $\sum_i \bar{L}_i^2 = 1$. I use spherical coordinates

$$\bar{L}_1 = \sin \theta \cos \phi \quad \bar{L}_2 = \sin \theta \sin \phi \quad \bar{L}_3 = \cos \theta \quad (2.7)$$

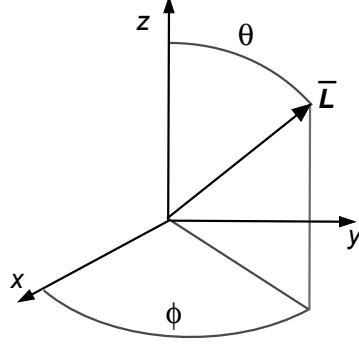


Figure 2.1 Normalized angular momentum vector $\bar{\mathbf{L}}$ in spherical coordinates.

for the normalized angular momentum (see Figure 2.1) to write equation 2.6 as

$$\begin{aligned} \dot{\theta} \cos \theta \cos \phi - \dot{\phi} \sin \theta \sin \phi &= D_3 \sin \theta \sin \phi (\cos \theta - \bar{h}_3) - D_2 \cos \theta (\sin \theta \sin \phi - \bar{h}_2) \\ \dot{\theta} \cos \theta \sin \phi + \dot{\phi} \sin \theta \cos \phi &= D_1 \cos \theta (\sin \theta \cos \phi - \bar{h}_1) - D_3 \sin \theta \cos \phi (\cos \theta - \bar{h}_3) \\ -\dot{\theta} \sin \theta &= D_2 \sin \theta \cos \phi (\sin \theta \sin \phi - \bar{h}_2) - D_1 \sin \theta \sin \phi (\sin \theta \cos \phi - \bar{h}_1) \end{aligned} \quad (2.8)$$

The equation of motion for θ (from the third line of the last set of equations) is

$$\dot{\theta} = D_2 \cos \phi (\bar{h}_2 - \sin \theta \sin \phi) + D_1 \sin \phi (\sin \theta \cos \phi - \bar{h}_1). \quad (2.9)$$

Multiplying the first and second lines of equation 2.8 by $-\sin \phi$ and $\cos \phi$ respectively and adding the resulting equations eliminates $\dot{\theta}$, and provides the equation of motion for ϕ :

$$\begin{aligned} \dot{\phi} \sin \theta &= D_3 \sin \theta (\bar{h}_3 - \cos \theta) + D_2 \cos \theta \sin \phi (\sin \theta \sin \phi - \bar{h}_2) \\ &+ D_1 \cos \theta \cos \phi (\sin \theta \cos \phi - \bar{h}_1). \end{aligned} \quad (2.10)$$

2.2 Hamiltonian for a quasi-rigid body

As I discuss in the following section, I must find the appropriate Hamiltonian with its generalized coordinate and conjugate momentum in order to find the adiabatic invariant. Following [Goldreich & Toomre \(1969\)](#), I assume the Hamiltonian

$$\mathcal{H}(q, p; t) \equiv \left(\frac{L}{2} \right) \bar{\mathbf{L}} \cdot \mathbf{D} \cdot (\bar{\mathbf{L}} - 2\bar{\mathbf{h}}), \quad (2.11)$$

with generalized coordinate $q \equiv \phi$ and conjugate momentum $p \equiv L(1 - \cos \theta)$.

For this choice I must verify that the canonical equations

$$\frac{dq}{dt} = \frac{\partial \mathcal{H}}{\partial p} \quad \text{and} \quad \frac{dp}{dt} = -\frac{\partial \mathcal{H}}{\partial q} \quad (2.12)$$

are equivalent to the previously derived equations of motion (equations 2.9 and 2.10). The Hamiltonian as a function of θ and ϕ is

$$\begin{aligned}\mathcal{H} &\equiv \frac{L}{2} [D_1(\bar{L}_1^2 - 2\bar{L}_1\bar{h}_1) + D_2(\bar{L}_2^2 - 2\bar{L}_2\bar{h}_2) + D_3(\bar{L}_3^2 - 2\bar{L}_3\bar{h}_3)] \\ &= \frac{L}{2} [D_1(\sin^2\theta\cos^2\phi - 2\bar{h}_1\sin\theta\cos\phi) + D_2(\sin^2\theta\sin^2\phi - 2\bar{h}_2\sin\theta\sin\phi) \\ &\quad + D_3(\cos^2\theta - 2\bar{h}_3\cos\theta)],\end{aligned}\tag{2.13}$$

and the canonical equations (2.12)

$$\dot{\phi} = \frac{d\theta}{dp} \frac{\partial\mathcal{H}}{\partial\theta} = \frac{1}{L\sin\theta} \frac{\partial\mathcal{H}}{\partial\theta} \quad \text{and} \quad \dot{\theta} \frac{dp}{d\theta} = \dot{\theta}L\sin\theta = -\frac{\partial\mathcal{H}}{\partial\phi}\tag{2.14}$$

become

$$\begin{aligned}\dot{\phi}\sin\theta &= D_1\cos\theta\cos\phi(\sin\theta\cos\phi - \bar{h}_1) + D_2\cos\theta\sin\phi(\sin\theta\sin\phi - \bar{h}_2) \\ &\quad + D_3\sin\theta(\bar{h}_3 - \cos\theta)\end{aligned}\tag{2.15}$$

and

$$\dot{\theta} = D_1\sin\phi(\sin\theta\cos\phi - \bar{h}_1) + D_2\cos\phi(-\sin\theta\sin\phi + \bar{h}_2).\tag{2.16}$$

These equations are equivalent to equations 2.9 and 2.10. Therefore, I can conclude that I have chosen the appropriate Hamiltonian.

2.3 Adiabatic invariant for a quasi-rigid body

An adiabatic invariant is a quantity whose total change tends to zero, as the rate of the external parameters tends to zero. The adiabatic invariant is given by the action integral $J = \oint pdq$ where \oint indicates integration over one complete period corresponding to the coordinate q (Lenard, 1959; Navarro & Garrido, 1968). In a precise formulation, J is an adiabatic invariant to the m th order, if it is possible to find a positive constant M such that for the change δJ of the quantity J in the interval T the inequality

$$|\delta J| < \left(\frac{1}{T}\right)^m M\tag{2.17}$$

holds as $T \rightarrow \infty$ (Lenard, 1959; Navarro & Garrido, 1968). That is, although J may not be an exact invariant, it is conserved to very high accuracy when a prescribed total change of the body parameters occurs sufficiently slowly. Since I am interested in the long term stability of free nutations, slow here means that the characteristic time scales of the processes responsible for changes in the body inertia tensor are longer than the slowest of the nutations experienced at any

stage.

Using the the generalized coordinate $q = \phi$ and conjugate momentum $p = L(1 - \cos \theta)$ allows one to obtain

$$\oint pdq = L \int_0^{2\pi} (1 - \cos \theta) d\phi = L \int_0^{2\pi} d\phi [-\cos \theta]_0^\theta = L \int_0^{2\pi} \int_0^\theta d\phi \sin \theta' d\theta'.$$

The adiabatic invariant is L (a constant) times the solid angle enclosed by the motion of the normalized angular momentum $\bar{\mathbf{L}}(t) \equiv \mathbf{L}(t)/L$ (see Figure 2.1).

2.4 Summary

Any slow changes (slower than the slowest of the nutations) in the shape of a free quasi-rigid body preserve as an adiabatic invariant the solid angle traced out by the body's angular momentum vector as viewed from its principal axes. This rotational adiabatic invariant applies to polar wandering. If the body were once in the low energy state of free precession around the principal axis associated with the largest moment of inertia (see Appendix B), it will continue to be in that state wherever that axis may have shifted.

I will use the adiabatic invariant in the following Chapters to assume that the rotation axis is aligned with the principal axis associated with the largest moment of inertia. TPW occurs if the orientation of this principal axis changes due to changes in the inertia tensor. I consider possible causes for changes in the inertia tensor in Chapter 4.

Chapter 3

True polar wander of a quasi-rigid body

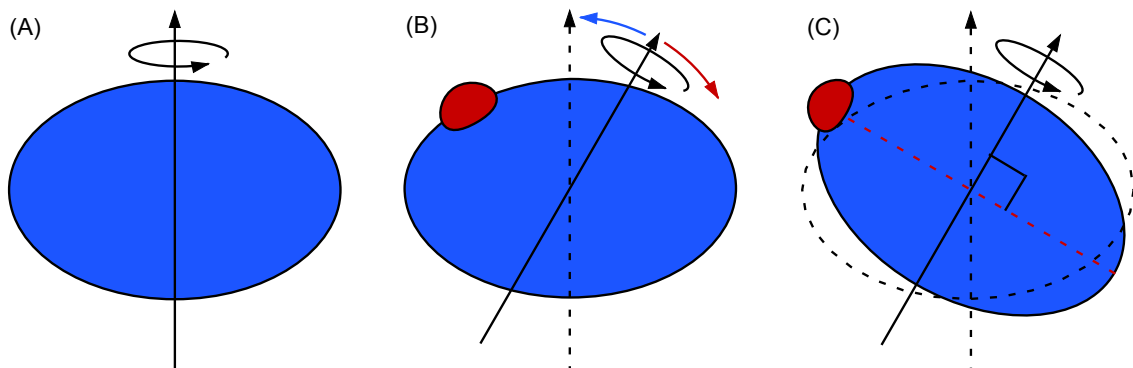


Figure 3.1 Schematic illustrating the stability of a hydrostatic planet subject to a surface mass load (the red ‘beetle’). The initial hydrostatic rotational bulge (blue ellipse) is aligned with the initial rotation axis (A). The load pushes the rotation axis away (red arrow) and the hydrostatic rotational bulge stabilizes the pole (blue arrow) (B). After a time period that is long relative to the relaxation of the hydrostatic flattening, the initial bulge (dotted line ellipse) is assumed to perfectly relax to the new pole location (C). The process continues until the load reaches the new planetary equator and TPW ceases (C).

Gold (1955) discussed the stability of a hydrostatic planet subject to an anomalous (i.e., non-hydrostatic or imperfectly compensated) load (Figure 3.1A-C) with a model of a crawling beetle on a rotating spherical body. I assume that the the solid angle traced out by the principal axis associated with the largest moment of inertia and the angular momentum vector is an adiabatic invariant (see Chapter 2). The rotation pole wanders relative to the body as the beetle crawls on the body surface since the beetle’s position defines the orientation of the principal axes of inertia. The beetle would act to push the rotation pole away in a reference frame fixed to the body (Figure 3.1B). In the short term, the hydrostatic rotational bulge would act to stabilize the pole (Figure

3.1B). However, since the hydrostatic rotational bulge of the planet would, in time, relax to any new orientation of the rotation pole, all memory of this previous orientation would ultimately vanish (Figure 3.1C). That is, a hydrostatic bulge provides no long-term rotational stability and TPW would be governed solely by the location of the beetle.

Gold (1955)'s arguments were extended by Goldreich & Toomre (1969) who demonstrated that a quasi-rigid body consisting of a gradual redistribution of masses (e.g., a set of crawling beetles) on a sphere could drive rapid (relative to the speed of the beetles) reorientation of the rotation pole. Indeed, the rate of TPW would only be limited by the characteristic decay time governing the relaxation of the rotational (hydrostatic) bulge, which in turn would be a function of the viscosity structure of the body. I will illustrate the efficiency of this type of TPW in the following sections with an order of magnitude analysis and by considering numerical models.

Since TPW is governed by the inertia tensor principal axes direction, I calculate the inertia tensor for a general mass distribution (e.g., a colony of beetles) on a sphere in §3.1. Two numerical models are considered to illustrate the TPW of a quasi-rigid body. The first model, described in §3.2, consists of a sphere with a colony of randomly crawling beetles. The second model, described in §3.3, is a randomly evolving, almost spherical body.

3.1 Inertia tensor for a distribution of mass anomalies on a sphere

Given the mass M and radius a of the sphere, and the masses m_n and position vectors \mathbf{a}_n for a distribution of mass anomalies (e.g., the beetles), one can calculate the total inertia tensor. The inertia tensor can be diagonalized in a reference frame with origin at the centre of mass of the system. Since I assume small mass perturbations ($m_n \ll M$) that are randomly distributed on the surface of the sphere, I can assume that the centre of mass coincides with the centre of the sphere (I verify the validity of this assumption a posteriori). The inertia tensor for the sphere and the N mass anomalies is

$$I_{ij}(t) = \frac{2}{5}Ma^2\delta_{ij} + \sum_{n=1}^N m_n(t) [\delta_{ij}a_n^2(t) - a_{n,i}(t)a_{n,j}(t)], \quad (3.1)$$

where $a_{n,i}$ denotes the i th component of the position vector for the n th mass. I calculate the inertia tensor in a reference frame with origin at the centre of mass in Appendix C. The principal axes are solely determined by the mass anomalies since these are the only non-spherical contributions to the inertia tensor. Furthermore, the principal axes orientation is independent of the size of the mass anomalies relative to the mass of the sphere. Therefore, arbitrarily small mass anomalies can steer the planet. I use the rotational adiabatic invariant to assume that the rotation axis (and angular momentum vector) is aligned with the principal axis associated with the largest moment of inertia. This is a reasonable assumption since any internal energy dissipation will drive the body to that low

energy state (see Appendix B). The adiabatically invariant solid angle traced out by the rotation axis around this principal axis is zero in this case. That is, the principal axis associated with the largest moment of inertia and the rotation axis must be aligned at all times. The pole wanders due to changes in the inertia tensor as the principal axes direction change.

3.2 True polar wander of a sphere with a colony of randomly crawling beetles

I consider the classic example of a quasi-rigid body consisting of a sphere with a colony of randomly crawling N beetles. Order of magnitude estimates for the TPW speed and the ‘memory’ of this quasi-rigid body are presented in §3.2.1 and §3.2.2. A numerical model is considered in §3.2.3.

3.2.1 Order of magnitude estimate for the true polar wander speed

If I assume that the typical time scale for each crawling to occur, τ_{crawl} , is much longer than the relaxation time scale of the rotational bulge τ_{bulge} , an order of magnitude estimate for the TPW speed stems from the fact that the gross properties of an earlier beetle distribution must be lost by the time a typical beetle has covered the distance to its neighbor. A crawling beetle with angular speed w_b meets its neighbor after a time interval τ_{tpw} , when it has covered the solid angle

$$\Omega \sim 2\pi[1 - \cos(w_b\tau_{tpw})] \sim \frac{4\pi}{N}. \quad (3.2)$$

For $N \gg 1$, this solid angle is small and I can assume $w_b\tau_{tpw} \ll 1$ to write

$$\cos(w_b\tau_{tpw}) \sim 1 - \frac{w_b^2\tau_{tpw}^2}{2} \sim 1 - \frac{2}{N} \rightarrow \tau_{tpw} \sim \frac{2}{N^{1/2}w_b}. \quad (3.3)$$

The ‘memory’ for an earlier beetle distribution is lost after a time interval $\sim N^{-1/2}w_b^{-1}$, and a new set of principal axes is defined. The TPW speed can be estimated as

$$w_{tpw} \sim \frac{\delta}{\tau_{tpw}} \sim w_b N^{1/2} \delta, \quad (3.4)$$

where δ is the amount of TPW. The exact value for the amount of TPW depends on the beetles’ distribution. A 90° shift in the rotation pole occurs when the maximum and intermediate moments of inertia are exchanged and is generally referred to as an inertia interchange true polar wander (IITPW) event. Here, for an order of magnitude estimate, I can assume an IITPW event when the ‘memory’ for an earlier beetle distribution is lost. The rate of movement of the principal axes w_{tpw} exceeds the net speeds of the beetles by a factor of the order of $N^{1/2}$. Note that this estimate is consistent with Gold (1955)’s example of a single beetle since $w_b \sim w_{tpw}$ for $N = 1$. I remind the

reader that I have ignored the relaxation of the rotational bulge. This estimates is valid as long as the the rotational bulge can relax on a time scale shorter than w_{tpw}^{-1} .

3.2.2 ‘Memory’ of the quasi-rigid body

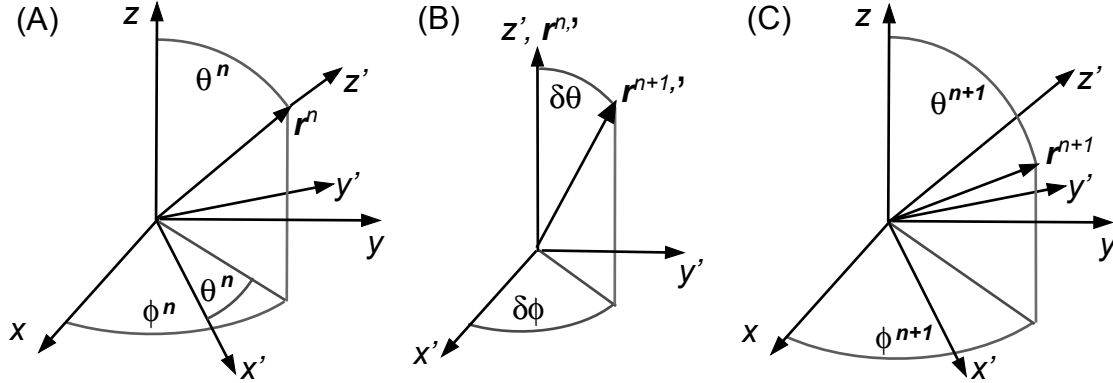


Figure 3.2 Position vector of a randomly crawling beetle in two reference frames. The initial and final (after a random crawl step) position vectors, \mathbf{r}^n and \mathbf{r}^{n+1} , are shown on panels (A) and (C) respectively. Panel (B) shows the final position vector in a reference frame with the z' -axis aligned with the initial position vector.

The gross properties of an earlier beetle distribution must be lost by the time a typical beetle has covered the distance to its neighbor. Hence, the ‘memory’ of the quasi-rigid body can be defined as the number of random crawl steps for an arbitrary beetle to meet its neighbor.

I begin by calculating the average solid angle covered by a beetle after an arbitrary number of random crawling steps. I assume that each beetle covers the solid angle $\delta\Omega = \int_0^{2\pi} \int_0^{\delta\theta} \sin\theta d\theta d\phi = 2\pi(1 - \cos\delta\theta)$, where $\delta\theta$ is the opening angle of each random crawl (see Figure 3.2B).

The average solid angle covered by a beetle after N random crawls can be estimated by using reference frame rotations. Let us assume that the the beetle position vector after n random crawling steps is given by $\mathbf{r}^n = (\sin\theta^n \cos\phi^n, \sin\theta^n \sin\phi^n, \cos\theta^n)$ as shown in Figure 3.2A. I denote the new beetle position vector after a random crawl as \mathbf{r}^{n+1} . I can write this vector in a reference frame with the z' axis along the original beetle’s position (see Figures 3.2A,B). In this frame, I denote the original beetle position vector as $\mathbf{r}^{n,\prime}$ and the new position as $\mathbf{r}^{n+1,\prime}$ (see Figure 3.2B). The new beetle position vector can be written as $\mathbf{r}^{n+1,\prime} = (\sin\delta\theta \cos\delta\phi, \sin\delta\theta \sin\delta\phi, \cos\delta\theta)$ (see Figure 3.2B). Next, I write this new position vector in the original reference frame by using: (i) a rotation around y' of $-\theta^n$ and (ii) a rotation around z' of $-\phi^n$ (see Figures 3.2A,C). This gives

$$\mathbf{r}^{n+1} = \begin{pmatrix} \cos\phi^n & -\sin\phi^n & 0 \\ \sin\phi^n & \cos\phi^n & 0 \\ 0 & 0 & 1 \end{pmatrix} \begin{pmatrix} \cos\theta^n & 0 & -\sin\theta^n \\ 0 & 1 & 0 \\ \sin\theta^n & 0 & \cos\theta^n \end{pmatrix} \begin{pmatrix} \sin\delta\theta \cos\delta\phi \\ \sin\delta\theta \sin\delta\phi \\ \cos\delta\theta \end{pmatrix}, \quad (3.5)$$

where $\mathbf{r}^{n+1} = (\sin \theta^{n+1} \cos \phi^{n+1}, \sin \theta^{n+1} \sin \phi^{n+1}, \cos \theta^{n+1})$. I use the z component of equation (3.5) to write

$$\cos \theta^{n+1} = \sin \theta^n \sin \delta\theta \cos \phi^n + \cos \theta^n \cos \delta\theta. \quad (3.6)$$

Using equation (3.5) allows one to obtain the opening angle of the solid angle after an arbitrary number of random crawling steps. I start with $\theta^{n=0} = 0$ to obtain

$$\begin{aligned} \cos \theta^1 &= \cos \delta\theta \\ \cos \theta^2 &= \sin \theta^1 \sin \delta\theta \cos \phi^1 + (\cos \delta\theta)^2 \\ \cos \theta^3 &= \sin \theta^2 \sin \delta\theta \cos \phi^2 + (\cos \delta\theta)^3 \\ &\vdots \\ \cos \theta^n &= \sin \theta^{n-1} \sin \delta\theta \cos \phi^{n-1} + (\cos \delta\theta)^n. \end{aligned} \quad (3.7)$$

Taking the time average of the last equation yields

$$\langle \cos \theta^n \rangle = \sin \delta\theta \langle \sin \theta^{n-1} \cos \phi^{n-1} \rangle + \cos^n \delta\theta, \quad (3.8)$$

where $\langle \rangle$ designates a time average. The time average $\langle \sin \theta^{n-1} \cos \phi^{n-1} \rangle$ must vanish since ϕ^{n-1} is uniformly distributed between 0 and 2π for a random crawl, and θ^n and ϕ^n are uncorrelated. If I neglect this term, equation (3.8) becomes $\langle \cos \theta^n \rangle = (\cos \delta\theta)^n$ and the average solid angle covered by a beetle after n random crawls can be written as

$$\langle \Omega^n \rangle = 2\pi(1 - \cos^n \delta\theta). \quad (3.9)$$

I note that the last equation satisfies $\langle \Omega^{n=1} \rangle = 2\pi(1 - \cos \delta\theta)$, and $\langle \Omega^n \rangle = 0$ for $\delta\theta = 0$, as expected.

I can estimate the number of random crawls corresponding to the memory of this quasi-rigid body, which I denote as n_{mem} . For N beetles, an arbitrary beetle meets its neighbor when

$$\frac{4\pi}{N} = \langle \Omega^{n_{mem}} \rangle = 2\pi(1 - \cos^{n_{mem}} \delta\theta). \quad (3.10)$$

Finally, I solve the last equation for n_{mem} to obtain

$$n_{mem} = \frac{\ln(1 - 2/N)}{\ln(\cos \delta\theta)}. \quad (3.11)$$

If each random crawl covers a small solid angle (i.e., $\delta\theta \ll 1$), I can assume $n_{mem} \gg 1$ to approximate

the last equation as

$$n_{mem} \sim \frac{\ln(1 - 2/N)}{\ln(1 - \delta\theta^2/2)} \sim \frac{4}{N\delta\theta^2}. \quad (3.12)$$

This estimate illustrates that the memory for an earlier beetle distribution can be lost very quickly for a large colony of beetles.

3.2.3 Numerical model for a colony of randomly crawling beetles

In this section, I consider a numerical model for the quasi-rigid body adopted in the previous sections. I generate a random distribution of beetles (mass anomalies) on the surface of a sphere with radius a and mass M by choosing the appropriate spherical coordinates θ and ϕ . Since the surface area element of a sphere as a function of these coordinates is $dS = a^2 \sin\theta d\theta d\phi$, ϕ must be distributed with uniform probability between 0 and 2π , while θ must be distributed with probability $\sin\theta$ between 0 and π . That is, I must choose θ such that $\int \sin\theta d\theta = \cos\theta$ is uniformly distributed between -1 and 1 (see, e.g., [Press et al., 1992](#), ch. 7.2).

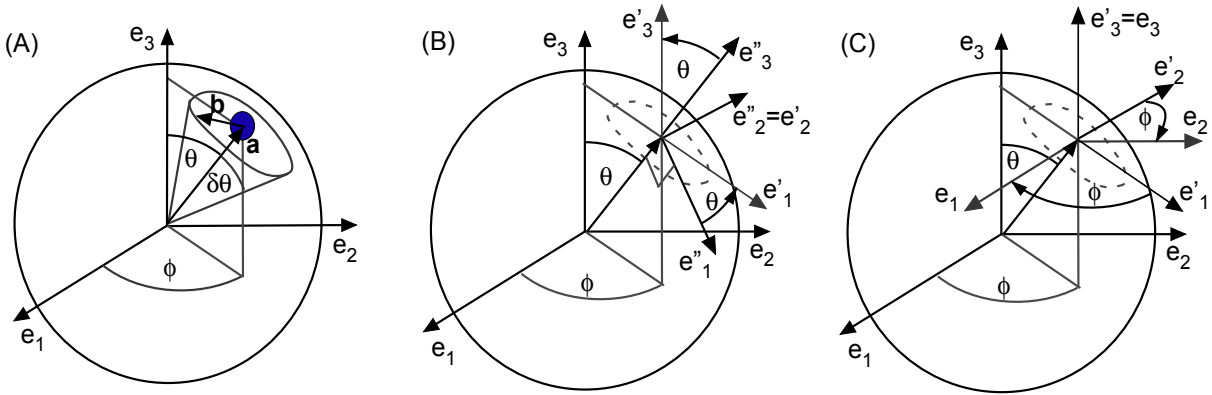


Figure 3.3 Reference frame transformations to describe the change in position of a random crawling beetle (the blue circle). The beetle position is transformed from a reference frame that contains a tangent circle (with e_i'' axes), used to generate the random crawl, to the reference frame used to generate the original beetle's position (with e_i axes).

I assume that each random crawl occurs at the intersection of the sphere with a cone with opening angle $\delta\theta = 2^\circ$ and symmetry axis at the current beetle position, as shown in Figure 3.3A. The direction of each crawl is given by the random selection of a location on a circle that is tangent to the sphere at each beetle position. (see Figure 3.3A). First, I adopt a reference frame that contains this tangent circle in the $e_1'' - e_2''$ plane, as is shown in Figure 3.3B. In this frame, the

random crawl is given by the vector \mathbf{b}'' , with coordinates

$$\begin{aligned} b_1'' &= b \cos \lambda \\ b_2'' &= b \sin \lambda \\ b_3'' &= 0, \end{aligned} \tag{3.13}$$

where $b = a \tan \delta\theta$ and λ is a random variable uniformly distributed between 0 and 2π . Next, I transform the vector representing the random crawl to the reference frame used to generate the original beetle position (indicated by the e_i axes in Figures 3.3A-C) by using two reference frame transformations. The first transformation is a rotation of θ around the e_2'' axis (see Figure 3.3B):

$$\begin{aligned} b_1' &= b_1'' \cos \theta = b \cos \lambda \cos \theta \\ b_2' &= b_2'' = b \sin \lambda \\ b_3' &= -b_1'' \sin \theta = -b \cos \lambda \sin \theta. \end{aligned}$$

The second transformation is a rotation of ϕ around the e_3' axis (see Figure 3.3C):

$$\begin{aligned} b_1 &= b_1' \cos \phi - b_2' \sin \phi = b \cos \lambda \cos \theta \cos \phi - b \sin \lambda \sin \phi \\ b_2 &= b_1' \sin \phi + b_2' \cos \phi = b \cos \lambda \cos \theta \sin \phi + b \sin \lambda \cos \phi \\ b_3 &= b_3' = -b \cos \lambda \sin \theta. \end{aligned} \tag{3.14}$$

Finally, the new position of the i th beetle after a random crawl is given by $\mathbf{r} = \mathbf{a}_i + \mathbf{b}_i$ (see Figure 3.3A). I normalize the resulting vector such that $\mathbf{r} \cdot \mathbf{r} = a^2$ since the beetle must stay on the surface of the sphere.

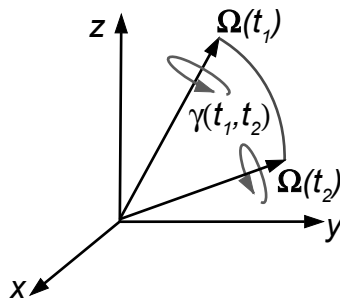


Figure 3.4 TPW angle $\gamma(t_1, t_2)$ associated with the rotation vector $\Omega(t)$ at two different times t_1 and t_2 .

I generate a random distribution of beetles and simulate their random crawling by using equation 3.14. I assume that each beetle has a mass of randomly chosen sign. Since the beetles represent

the only non-spherical contributions to the inertia tensor, the principal axes are solely determined by their location. For a reference frame with origin at the centre of the sphere, the direction of the principal axes is independent of the mass of the beetles $\pm m_b$ relative to the mass of the sphere M . I assume $m_b = 10^{-5}M$ for the model with a reference frame with origin at the centre of mass of the system. I then calculate the total inertia tensor (equation 3.1) and diagonalize it to find the principal axes of inertia (see, e.g., Press et al., 1992, Ch. 11). Since the solid angle between the rotation axis and the principal axis associated with the largest moment of inertia is an adiabatic invariant (§2), I can follow this principal axis as the beetles crawl to describe time evolution of the rotation pole. I denote the TPW angle associated with the rotation vector $\mathbf{\Omega}$ at two different times t_1 and t_2 as $\gamma(t_1, t_2)$ (see Figure 3.4).

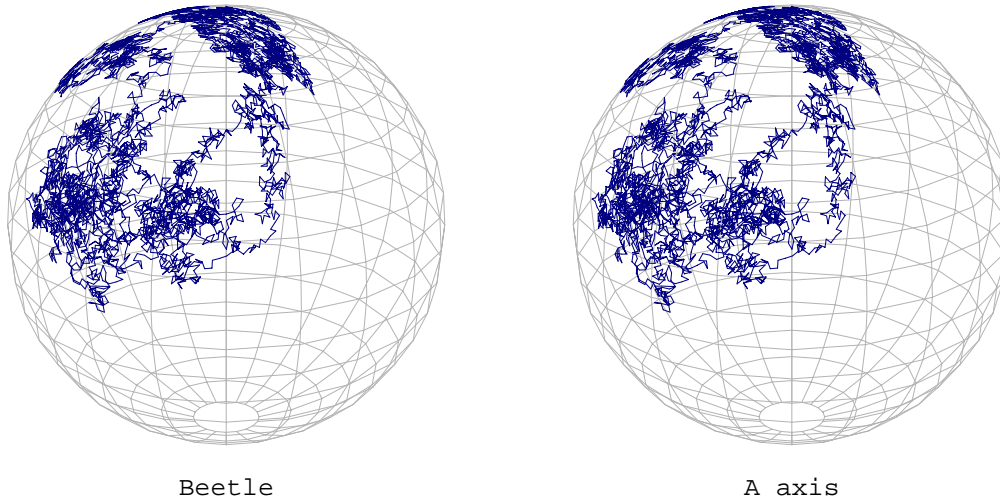


Figure 3.5 Location of a randomly crawling beetle on the surface of a sphere and the corresponding pole of the principal axis associated with the smallest moment of inertia (A axis) for 5000 random crawls. Each random crawl has random direction and amplitude given by a solid angle with an opening angle of $\delta\theta = 2^\circ$ (see figure 3.3A).

As mentioned above, Gold (1955)’s model of a single beetle crawling on the sphere is singular since the two largest moments of inertia are equal, and therefore the principal axis associated with the largest moment of inertia is not well defined. The principal axis with the smallest moment of inertia is well defined since one of its poles must coincide with the beetle’s position. Figure 3.5 shows the beetle location and one of the poles of the principal axis associated with the smallest moment of inertia (I choose the one that must coincide with the beetle position) for 5000 random crawls. The accuracy of the numerical method used to calculate the principal axes of inertia (Press et al., 1992, chapter 11) can be appreciated by comparing the two panels in Figure 3.5. The two panels must be equivalent for an exact numerical solution.

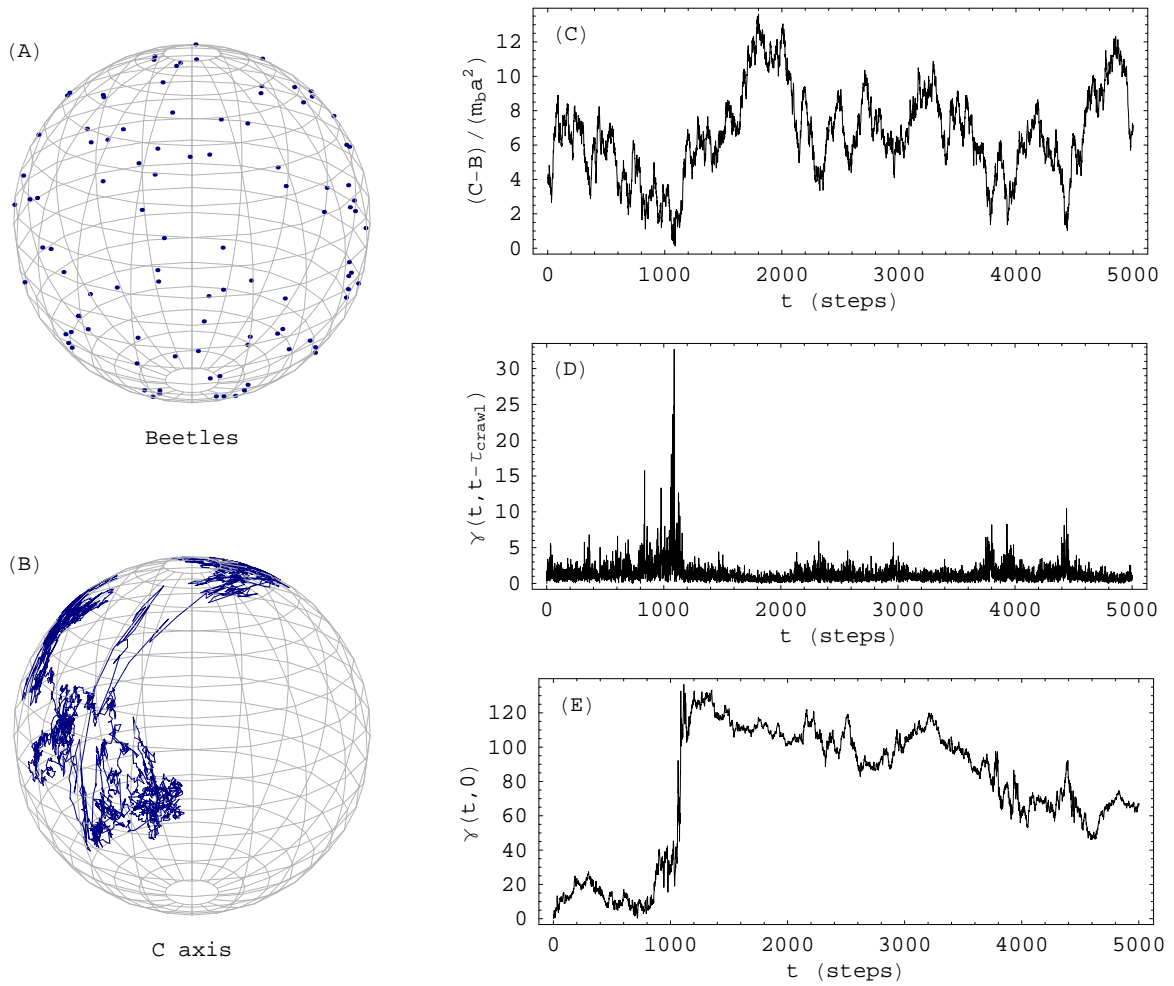


Figure 3.6 True polar wander driven by a colony of 100 randomly crawling beetles in a reference frame with origin at the centre of mass of the system. (A) Initial beetles distribution. (B) Pole of the principal axis associated with the largest moment of inertia for 5000 random crawl time steps. (C) Difference between the two largest principal moments of inertia as a function of time. (D) TPW angle during each random crawl time step as a function of time. (E) TPW angle relative to the initial pole position as a function of time.

I now consider the time evolution of the rotation pole for a model with a colony of 100 randomly crawling beetles. I follow the pole of the principal axis associated with the largest moment of inertia in Figure 3.6. I assume that each random crawl occurs during a time interval τ_{crawl} . Figures 3.6C-E illustrate that large TPW events occur when the difference between the maximum and intermediate moments is small. The minima in Figure 3.6C, which shows the difference between the larger principal moments, coincide with the maxima in Figure 3.6D, which shows the amount of TPW during each random crawl interval. In general, the smaller the difference between the two largest principal moments, the larger the TPW event.

When the two largest principal moments of inertia are equal, the quasi-rigid body can be regarded as a prolate spheroid, without a preferred direction for the principal axis associated with the largest moment of inertia. In this case, the quasi-rigid body becomes rotationally unstable and a 90° TPW event would occur if the maximum and intermediate moments of inertia are exchanged. This rapid motion of the rotation pole is generally referred to as an IITPW event.

3.3 True polar wander of a randomly evolving body

In this section, I use the numerical model of a randomly evolving, almost spherical body considered by Goldreich & Toomre (1969). First, I generate a sequence of N random points on the surface of the sphere as described in the previous section. I then assign to the n th point a mass $m_n(t=0)$ chosen from a Gaussian distribution with zero mean and magnitude m_b . I remind the reader that the size of the mass anomalies relative to the mass of the sphere does not determine direction of the principal axes in a reference frame with origin at the centre of the sphere. I assume $m_b = 10^{-5}M$ for the model with the reference frame origin at the centre of mass of the system. Finally, each mass is turned on and off according to the rule

$$m_n(t) = m_n(t=0) \exp \left[-\pi \left(\frac{t}{\tau_0} - \frac{n}{100} \right)^2 \right]. \quad (3.15)$$

The constants in the last equation were chosen such that $\int_{-\infty}^{\infty} m_n(t) dt = m_n(t=0)$ for every n and that roughly 100 masses are ‘on’ with at least half-intensity at any given instant. The ‘memory’ of this model is $\sim 2\tau_0$ since a different set of masses will be ‘on’ after this time interval has elapsed.

Figure 3.7 illustrates the TPW of this quasi-rigid body for the time interval $0 \leq t \leq 25\tau_0$. Since this time interval contains several ‘memory’ time scales, large TPW events are expected to occur, which is illustrated in Figures 3.7C-E. Consider panels C and E. The minima in Figure 3.6C, which shows the difference between the larger principal moments, coincide with the maxima in Figure 3.7D, which shows the amount of TPW during the last time interval τ_0 at a given time. In general, the smaller the difference between the two largest principal moments, the larger the TPW event.

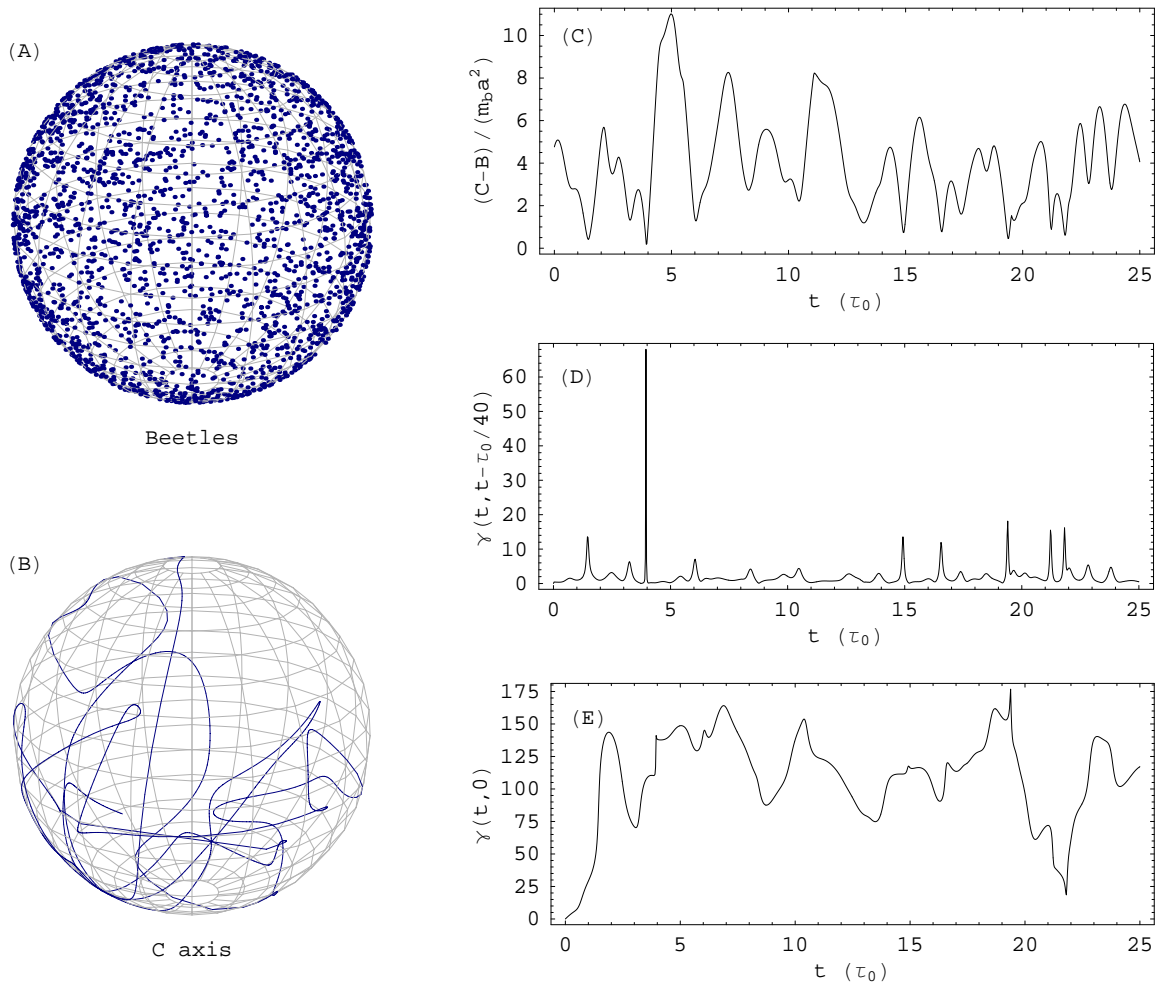


Figure 3.7 TPW for a randomly evolving quasi-rigid body according to equation (3.15) in a reference frame with origin at the centre of mass of the system. (A) Initial ($t = 0$) mass anomalies distribution. (B) Pole of the principal axis associated with the largest moment of inertia for $t < 25\tau_0$. (C) Difference between the two largest principal moments of inertia as a function of time. (D) TPW angle during the ‘memory’ time interval τ_0 as a function of time. (E) TPW angle relative to the initial pole position as a function of time.

3.4 Application to planets: oblateness distribution

If the Earth's rotation were halted and the present rotational bulge were allowed to subside, the principal moments of inertia $A < B < C$ would differ by almost equal increments (Goldreich & Toomre, 1969)

$$\begin{aligned} C - B &\sim 6.9 \times 10^{-6} M a^2 \\ B - A &\sim 7.2 \times 10^{-6} M a^2, \end{aligned} \quad (3.16)$$

where M is the Earth's mass and a is its mean equatorial radius. The hypothetical non-rotating Earth is a good example of a triaxial object. I follow the numerical experiment of Goldreich & Toomre (1969) to calculate the probability distribution of the oblateness, which I denote as $f \equiv (C - B)/(C - A)$, of a quasi-rigid body. I consider the two models used in §3.2 and §3.3. Figure 3.8 shows the distribution of the oblateness for 10^5 quasi-rigid bodies. The probability of producing a triaxial body with $f \sim 0.49$, similar to the hypothetical non-rotating Earth, is very high. In contrast, it is very unlikely that the resulting bodies are nearly oblate ($f \approx 1$) or nearly prolate ($f \approx 0$).

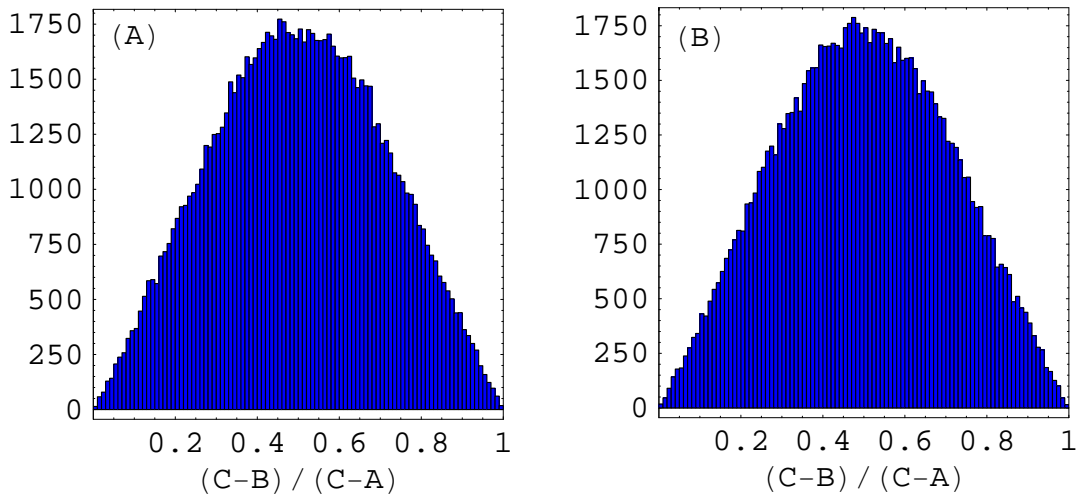


Figure 3.8 Oblateness $f \equiv (C - B)/(C - A)$ histogram for 5000 quasi-rigid bodies with randomly generated mass anomalies. The frames are distinguished on the basis of the assumed mass distribution. (A) Each mass anomaly has a mass with randomly chosen sign and magnitude $m_b = 10^{-5} M$. (B) Each mass is randomly chosen from a Gaussian distribution with zero mean and same magnitude $m_b = 10^{-5} M$.

Chapter 4

Inertia tensor perturbations

The orientation of the principal axis changes due to changes in the inertia tensor. In this Chapter, I derive expressions for inertia tensor variations driven by the loading of a deformable planetary body. I specify three classes of perturbations associated with: (1) the direct effect of any external surface mass load; (2) the deformation of the planet driven by this surface loading; and (3) the deformation of the planet driven by changes in the rotation vector. I denote these inertia tensor perturbations as I_{ij}^L , I_{ij}^{LD} , and I_{ij}^{RD} respectively.

As in treatments of post-glacial load-induced variations in the Earth's rotational state (e.g., [Wu & Peltier 1984](#); [Mitrovica et al. 2001](#)), I make the assumption that the planet may be modeled as a spherically symmetric, linear (Maxwell) viscoelastic body and use well known results in viscoelastic Love number theory.

4.1 Inertia tensor perturbations: direct load contribution

I begin by denoting an arbitrary surface mass load as $L(\theta, \phi, t)$, where θ and ϕ are spherical coordinates and t is time. Next, the surface load is expanded in terms of spherical harmonics, with each harmonic written as $L_{\ell m}(t)$. I will show below that the inertia tensor perturbations only depend on the degrees zero ($\ell = 0$) and two ($\ell = 2$) components of the surface load, which is a well known result. In this section I focus on perturbations in the inertia tensor associated with the direct effect of the surface mass load. These perturbations can be written as

$$I_{ij}^L(t) = \int_S dm (a^2 \delta_{ij} - a_i a_j), \quad (4.1)$$

where $dm = L(\theta, \phi, t) dS$ is an infinitesimal surface mass element, a is the planetary radius, and \int_S denotes an integral over the planetary surface. The last equation can be written as

$$I_{ij}^L(t) = a^2 \int_{\Omega} d\Omega L(\theta, \phi, t) (a^2 \delta_{ij} - a_i a_j), \quad (4.2)$$

where $d\Omega = \sin\theta d\theta d\phi$ is an infinitesimal solid angle element and \int_{Ω} denotes an integral over the complete solid angle.

Let us calculate, as an illustration, one of the components of the inertia tensor perturbation:

$$\begin{aligned}
I_{33}^L(t) &= a^4 \int \int_{\Omega} d\Omega L(\theta, \phi, t) \sin^2 \theta \\
&= a^4 \sum_{\ell=0}^{\infty} \sum_{m=-\ell}^{\ell} L_{\ell m}(t) \int \int_{\Omega} d\Omega Y_{\ell m} \left[\frac{2}{3} \left(Y_{00}^{\dagger} - \frac{1}{\sqrt{5}} Y_{20}^{\dagger} \right) \right] \\
&= a^4 \sum_{\ell=0}^{\infty} \sum_{m=-\ell}^{\ell} L_{\ell m}(t) \left(\frac{8\pi}{3} \delta_{\ell 0} \delta_{m 0} - \frac{8\pi}{3\sqrt{5}} \delta_{\ell 2} \delta_{m 0} \right) \\
&= 4\pi a^4 \left[\frac{2}{3} L_{00}(t) - \frac{2}{3\sqrt{5}} L_{20}(t) \right], \tag{4.3}
\end{aligned}$$

where the orthogonality condition (D.1) is used. One can follow the same procedure for the remaining inertia tensor perturbations to obtain

$$\begin{aligned}
I_{11}^L(t) &= 4\pi a^4 \left[\frac{2}{3} L_{00}(t) + \frac{1}{3\sqrt{5}} L_{20}(t) - \sqrt{\frac{2}{15}} \operatorname{Re}(L_{22}(t)) \right] \\
I_{22}^L(t) &= 4\pi a^4 \left[\frac{2}{3} L_{00}(t) + \frac{1}{3\sqrt{5}} L_{20}(t) + \sqrt{\frac{2}{15}} \operatorname{Re}(L_{22}(t)) \right] \\
I_{33}^L(t) &= 4\pi a^4 \left[\frac{2}{3} L_{00}(t) - \frac{2}{3\sqrt{5}} L_{20}(t) \right] \\
I_{12}^L(t) &= \frac{8\pi a^2}{\sqrt{30}} \operatorname{Im}(L_{22}(t)) \\
I_{13}^L(t) &= \frac{8\pi a^2}{\sqrt{30}} \operatorname{Re}(L_{21}(t)) \\
I_{23}^L(t) &= -\frac{8\pi a^2}{\sqrt{30}} \operatorname{Im}(L_{21}(t)), \tag{4.4}
\end{aligned}$$

where the symbols Re and Im refer to the real and imaginary parts of the complex number. Note that the inertia tensor is symmetric (see equation 4.1).

4.1.1 Inertia tensor perturbations: direct axisymmetric load contribution

Let us consider the special case of inertia tensor perturbations associated with axisymmetric surface loads. I denote the unit vector that represents the symmetry axis of the load as $\mathbf{e}_L = (\sin\theta_L \cos\phi_L, \sin\theta_L \sin\phi_L, \cos\theta_L)$ (Figure 4.1A). It will be convenient to find spherical harmonic expansion coefficients for the same load when the symmetry axis is placed at the pole of the coordinate system (Figure 4.1B). I denote these coefficients as $L'_{\ell m}(t)$, and in this case $L'_{2m} = 0$ for

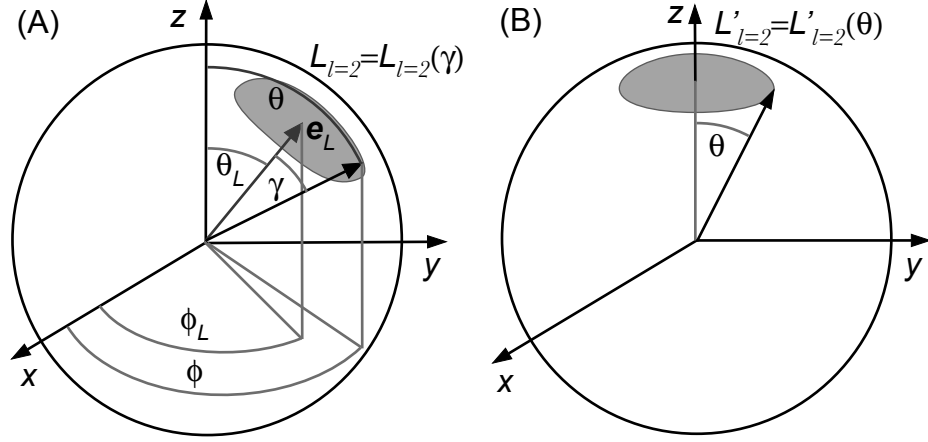


Figure 4.1 (A) Grey disk representing the degree two component of an axisymmetric surface load ($L_{\ell=2} = L_{\ell=2}(\gamma)$) with an arbitrary symmetry axis orientation given by the unit vector $\mathbf{e}_L = (\sin \theta_L \cos \phi_L, \sin \theta_L \sin \phi_L, \cos \theta_L)$. The angle γ denotes the angular distance between this symmetry axis and an arbitrary point on the planet surface with spherical coordinates (θ, ϕ) . (B) The same axisymmetric surface load ($L'_{\ell=2} = L'_{\ell=2}(\theta)$) with the symmetry axis placed along the z -axis.

$m \neq 0$ by cylindrical symmetry. The degree two component of this surface load (denoted by the subscript $\ell = 2$) can be written as

$$L'_{\ell=2}(\theta, t) = L'_{20}(t)Y_{20}(\cos \theta), \quad (4.5)$$

where the spherical harmonics described in Appendix D are used.

The degree two surface load with an arbitrary symmetry axis (Figure 4.1A) can be written as

$$L_{\ell=2}(\theta, \phi, t) = L'_{20}(t)Y_{20}(\cos \gamma), \quad (4.6)$$

where $\cos \gamma = \cos \theta \cos \theta_L + \sin \theta \sin \theta_L \cos(\phi - \phi_L)$. The spherical harmonic in the last equation is a function of the angular distance γ between the degree two load centre, with coordinates (θ_L, ϕ_L) , and an arbitrary point (θ, ϕ) . Using the addition theorem (D.8) one can rewrite equation (4.6) as

$$L(\theta, \phi, t) = \frac{L'_{20}(t)}{\sqrt{5}} \sum_{m=-2}^2 Y_{2m}^\dagger(\theta_L, \phi_L) Y_{2m}(\theta, \phi). \quad (4.7)$$

Therefore, the degree two spherical harmonic expansion coefficients can be written as

$$L_{2m}(t) = \frac{L'_{20}(t)}{\sqrt{5}} Y_{2m}^\dagger(\theta_L, \phi_L). \quad (4.8)$$

Equation 4.8 can be used to find the degree two spherical harmonic expansion for a load with an arbitrary symmetry axis, given the degree two spherical harmonic expansion for the same load

with its symmetry axis placed at the north pole. The following relationships will be used below:

$$\begin{aligned}
L_{20} &= \frac{1}{\sqrt{5}}L'_{20}Y_{20}^\dagger = \frac{1}{2}L'_{20}(3\cos^2\theta_L - 1) \\
L_{21} &= \frac{1}{\sqrt{5}}L'_{20}Y_{21}^\dagger = -\sqrt{\frac{3}{2}}L'_{20}\sin\theta_L\cos\theta_L e^{-i\phi_L} \\
L_{22} &= \frac{1}{\sqrt{5}}L'_{20}Y_{22}^\dagger = \frac{1}{2}\sqrt{\frac{3}{2}}L'_{20}\sin^2\theta_L e^{-i2\phi_L}.
\end{aligned} \tag{4.9}$$

Finally, using equations (4.9) in equation (4.4) yields

$$\begin{aligned}
I_{11}^L(t) &= 4\pi a^4 \left[\frac{2}{3}L_{00}(t) + \frac{1}{6\sqrt{5}}L'_{20}(t)(3\cos^2\theta_L - 1) - \frac{1}{2\sqrt{5}}L'_{20}(t)\sin^2\theta_L\cos(2\phi_L) \right] \\
I_{11}^L(t) &= 4\pi a^4 \left[\frac{2}{3}L_{00}(t) + \frac{1}{6\sqrt{5}}L'_{20}(t)(3\cos^2\theta_L - 1) + \frac{1}{2\sqrt{5}}L'_{20}(t)\sin^2\theta_L\cos(2\phi_L) \right] \\
I_{33}^L(t) &= \frac{8\pi a^4}{3} \left[L_{00}(t) - \frac{1}{2\sqrt{5}}L'_{20}(t)(3\cos^2\theta_L - 1) \right] \\
I_{12}^L(t) &= -\frac{2\pi a^4}{\sqrt{5}}L'_{20}(t)\sin^2\theta_L\sin(2\phi_L) \\
I_{13}^L(t) &= -\frac{4\pi a^4}{\sqrt{5}}L'_{20}(t)\sin\theta_L\cos\theta_L\cos\phi_L \\
I_{23}^L(t) &= -\frac{4\pi a^4}{\sqrt{5}}L'_{20}(t)\sin\theta_L\cos\theta_L\sin\phi_L.
\end{aligned} \tag{4.10}$$

The last set of equations can be written in a compact form as

$$I_{ij}^L(t) = \frac{8\pi a^4}{3}L_{00}(t)\delta_{ij} + \frac{4\pi a^4}{\sqrt{5}}L'_{20}(t) \left(\frac{1}{3}\delta_{ij} - e_{L,i}e_{L,j} \right), \tag{4.11}$$

where δ_{ij} is the Kronecker delta.

4.2 Surface load gravitational potential

For the purposes of the following discussion, I calculate the gravitational potential perturbation of an arbitrary surface load, which I denote as $\mathcal{G}^L(r, \theta, \phi, t)$.

I begin by integrating the contributions from infinitesimal mass elements $dm = L(\theta', \phi', t)a^2 d\Omega'$ over the complete solid angle Ω' to obtain

$$\mathcal{G}^L(r, \theta, \phi, t) = G \int \frac{dm}{|\mathbf{r} - \mathbf{a}|} = Ga^2 \int_{\Omega'} \frac{d\Omega' L(\theta', \phi', t)}{|\mathbf{r} - \mathbf{a}|}, \tag{4.12}$$

(see Figure 4.2). Note that this gravitational potential is defined such that the corresponding force

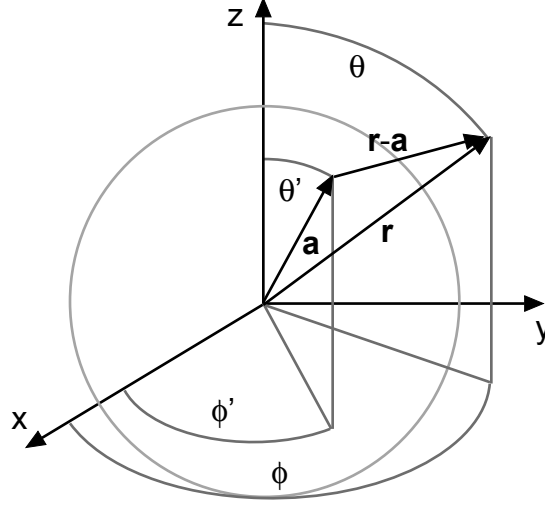


Figure 4.2 Position vectors and spherical coordinates used to calculate the surface load gravitational potential.

is given by $\nabla\mathcal{G}^L$ (and not $-\nabla\mathcal{G}^L$). Replacing the multipole expansion (D.9)

$$\frac{1}{|\mathbf{r} - \mathbf{a}|} = \frac{1}{r} \sum_{\ell'=0}^{\infty} \frac{1}{2^{\ell'+1}} \left(\frac{a}{r}\right)^{\ell'} \sum_{m=-\ell'}^{\ell'} Y_{\ell'm'}^{\dagger}(\theta', \phi') Y_{\ell'm'}(\theta, \phi), \quad (4.13)$$

and the surface load expansion

$$L(\theta', \phi'; t) = \sum_{\ell=0}^{\infty} \sum_{m=-\ell}^{\ell} L_{\ell m}(t) Y_{\ell m}(\theta', \phi') \quad (4.14)$$

in equation (4.12) allows one to obtain

$$\mathcal{G}^L(r, \theta, \phi, t) = \frac{4\pi G a^2}{r} \sum_{\ell=0}^{\infty} \frac{1}{2^{\ell+1}} \left(\frac{a}{r}\right)^{\ell} \sum_{m=-\ell}^{\ell} L_{\ell m}(t) Y_{\ell m}(\theta, \phi), \quad (4.15)$$

where the orthogonality condition (D.1) is used. Hence, the spherical harmonic expansion coefficients for the gravitational potential are

$$\mathcal{G}_{\ell m}^L(r, t) = \frac{4\pi G a^2}{(2\ell + 1)r} \left(\frac{a}{r}\right)^{\ell} L_{\ell m}(t). \quad (4.16)$$

We will be concerned with the gravitational potential at the planet surface ($r = a$) in the following discussion. In this case equation (4.16) becomes

$$\mathcal{G}_{\ell m}^L(t) = \frac{4\pi G a}{(2\ell + 1)} L_{\ell m}(t). \quad (4.17)$$

Finally, one can use equation (4.17) in the expressions (4.4) to obtain

$$\begin{aligned}
I_{11}^L(t) &= \frac{a^3}{G} \left[\frac{2}{3} \mathcal{G}_{00}^L(t) + \frac{\sqrt{5}}{3} \mathcal{G}_{20}^L(t) - \sqrt{\frac{10}{3}} \operatorname{Re}(\mathcal{G}_{22}^L(t)) \right] \\
I_{22}^L(t) &= \frac{a^3}{G} \left[\frac{2}{3} \mathcal{G}_{00}^L(t) + \frac{\sqrt{5}}{3} \mathcal{G}_{20}^L(t) + \sqrt{\frac{10}{3}} \operatorname{Re}(\mathcal{G}_{22}^L(t)) \right] \\
I_{33}^L(t) &= \frac{a^3}{G} \left[\frac{2}{3} \mathcal{G}_{00}^L(t) - \frac{2\sqrt{5}}{3} \mathcal{G}_{20}^L(t) \right] \\
I_{12}^L(t) &= \frac{a^3}{G} \sqrt{\frac{10}{3}} \operatorname{Im}(\mathcal{G}_{22}^L(t)) \\
I_{13}^L(t) &= \frac{a^3}{G} \sqrt{\frac{10}{3}} \operatorname{Re}(\mathcal{G}_{21}^L(t)) \\
I_{23}^L(t) &= -\frac{a^3}{G} \sqrt{\frac{10}{3}} \operatorname{Im}(\mathcal{G}_{21}^L(t)).
\end{aligned} \tag{4.18}$$

For an axisymmetric surface load, using the mapping

$$\begin{aligned}
\mathcal{G}'_{00}(t) &= 4\pi G a L'_{00} \\
\mathcal{G}'_{20}(t) &= \frac{4\pi G a}{5} L'_{20}(t)
\end{aligned} \tag{4.19}$$

in equation (4.11) yields

$$I_{ij}^L = \frac{2a^3}{3G} \mathcal{G}'_{00}(t) \delta_{ij} + \frac{\sqrt{5}a^3}{G} \mathcal{G}'_{20}(t) \left(\frac{1}{3} \delta_{ij} - e_{L,i} e_{L,j} \right), \tag{4.20}$$

where δ_{ij} is the Kronecker delta and $\mathbf{e}_L = (\sin \theta_L \cos \phi_L, \sin \theta_L \sin \phi_L, \cos \theta_L)$ is a unit vector indicating the location of the surface load symmetry axis.

4.2.1 Surface load gravitational potential: point mass at the north pole

In this section, I check the results derived in sections 4.1 and 4.2 by considering the simple case of a point mass at the north pole.

Let us begin by checking the mapping between the inertia tensor and the surface density (4.4). For a point mass at the north pole (i.e. $\theta_L = 0$) the moment of inertia is given by $I_{11}^L = I_{22}^L = ma^2$, $I_{33}^L = 0$, and $I_{ij}^L = 0$ for $i \neq j$. One can write the surface density for a point mass as

$$L(\theta, \phi) = \frac{m}{a^2} \delta(\phi - \phi_L) \delta(\theta - \theta_L) = \frac{m}{4\pi a^2} \sum_{\ell, m} Y_{\ell m}^\dagger(\theta_L, \phi_L) Y_{\ell m}(\theta, \phi), \tag{4.21}$$

where the completeness relation (D.3) is used and $\sum_{\ell, m}$ denotes $\sum_{\ell=0}^{\infty} \sum_{m=-\ell}^{\ell}$ for short. One can verify the mass normalization by integrating the surface density over the complete solid angle Ω .

This gives

$$\int_{\Omega} L(\theta, \phi) a^2 d\Omega = \frac{m}{4\pi} \sum_{\ell, m} Y_{\ell m}^{\dagger}(\theta_L, \phi_L) \int_{\Omega} Y_{00} Y_{\ell m}(\theta, \phi) d\Omega = m,$$

where $Y_{00} = 1$ and the orthogonality condition (D.1) are used. The harmonics for the point mass can be read from equation (4.21). They are given by

$$L_{\ell m} = \frac{m}{4\pi a^2} Y_{\ell m}^{\dagger}(\theta_L, \phi_L), \quad (4.22)$$

and the relevant harmonics for the inertia tensor mapping in equation (4.4) are

$$\begin{aligned} L_{00} &= \frac{m}{4\pi a^2} Y_{00}^{\dagger}(\theta_L = 0) = \frac{m}{4\pi a^2} \\ L_{20} &= \frac{m}{4\pi a^2} Y_{20}^{\dagger}(\theta_L = 0) = \frac{m}{4\pi a^2} \sqrt{5} \left(\frac{3}{2} \cos^2 0 - \frac{1}{2} \right) = \frac{\sqrt{5}m}{4\pi a^2} \\ L_{21} &= L_{2,-1} = L_{22} = L_{2,-2} = 0. \end{aligned} \quad (4.23)$$

Finally, replacing these coefficients in the mapping (4.4) yields

$$\begin{aligned} I_{11}^L &= 4\pi a^4 \left[\frac{2}{3} L_{00} + \frac{1}{3\sqrt{5}} L_{20} - \sqrt{\frac{2}{15}} \operatorname{Re}(L_{22}) \right] = ma^2 \left(\frac{2}{3} + \frac{1}{3\sqrt{5}} \sqrt{5} \right) = ma^2 \\ I_{22}^L &= 4\pi a^4 \left[\frac{2}{3} L_{00} + \frac{1}{3\sqrt{5}} L_{20} + \sqrt{\frac{2}{15}} \operatorname{Re}(L_{22}) \right] = ma^2 \left(\frac{2}{3} + \frac{1}{3\sqrt{5}} \sqrt{5} \right) = ma^2 \\ I_{33}^L &= 4\pi a^4 \left[\frac{2}{3} L_{00} - \frac{2}{3\sqrt{5}} L_{20} \right] = ma^2 \left(\frac{2}{3} - \frac{2}{3\sqrt{5}} \sqrt{5} \right) = 0 \\ I_{12}^L &= I_{13}^L = I_{23}^L = 0, \end{aligned} \quad (4.24)$$

which are the required expressions.

Let us now check the mapping between the surface load and the gravitational potential (4.16). I start by writing the gravitational potential of the point mass at the north pole as

$$\mathcal{G}^L(r) = \frac{Gm}{|\mathbf{r} - \mathbf{a}_0|}, \quad (4.25)$$

where \mathbf{r} is an arbitrary vector and \mathbf{a}_0 denotes the point mass position vector. Next, I use the multipole expansion (D.9) to expand the gravitational in spherical harmonics as

$$\mathcal{G}^L(r, \theta, \phi) = \frac{Gm}{a} \sum_{\ell, m} \frac{1}{2\ell + 1} \left(\frac{a}{r} \right)^{\ell} Y_{\ell m}^{\dagger}(\theta_L, \phi_L) Y_{\ell m}(\theta, \phi). \quad (4.26)$$

We can read the harmonics coefficients

$$\mathcal{G}_{\ell m}^L(r) = \frac{Gm}{r(2\ell + 1)} \left(\frac{a}{r}\right)^\ell Y_{\ell m}^\dagger(\theta_L, \phi_L) \quad (4.27)$$

from the last equation. Finally, replacing equation (4.22) in the last equation yields

$$\mathcal{G}_{\ell m}^L(r) = \frac{4\pi G a^2}{(2\ell + 1)r} \left(\frac{a}{r}\right)^\ell L_{\ell m}(t). \quad (4.28)$$

which is equivalent to equation (4.16).

For illustration, let us evaluate the gravitational potential at $\mathbf{r} = (r, \pi, \phi)$, given in spherical coordinates. In this case, we must have $\mathcal{G}^L(r, \theta = \pi, \phi) = Gm/(r + a)$. One can use the addition theorem (D.8) and equation (4.26) to obtain

$$\mathcal{G}^L(\theta = \pi) = \frac{Gm}{r} \sum_{\ell=0}^{\infty} \left(\frac{a}{r}\right)^\ell P_\ell(-1). \quad (4.29)$$

The series in the last equation can be found by considering the generating function of the Legendre polynomials (e.g, [Arfken & Weber, 1995](#))

$$\sum_{\ell=0}^{\infty} P_\ell(x)t^\ell = \frac{1}{(1 - 2xt + t^2)^{1/2}}. \quad (4.30)$$

Setting $t = a/r$ and $x = -1$ in the last equation gives

$$\sum_{\ell=0}^{\infty} \left(\frac{a}{r}\right)^\ell P_\ell(-1) = \frac{1}{1 + a/r},$$

and replacing the last equation in equation (4.29) yields

$$\mathcal{G}^L(\theta = \pi) = \frac{Gm}{r} \left(\frac{r}{r + a}\right) = \frac{Gm}{r + a} \quad (4.31)$$

as expected.

Finally, let us check the mapping between the inertia tensor and the gravitational potential of the load at the planet surface (i.e., $r = a$) (4.18). The relevant gravitational potential harmonics for this mapping are

$$\begin{aligned} \mathcal{G}_{00}^L &= \frac{4\pi G a}{2\ell + 1} L_{00} = \frac{Gm}{a} \\ \mathcal{G}_{20}^L &= \frac{4\pi G a}{2\ell + 1} L_{20} = \frac{Gm}{\sqrt{5}a} \\ \mathcal{G}_{21}^L &= \mathcal{G}_{2-1} = \mathcal{G}_{22} = \mathcal{G}_{2-2} = 0, \end{aligned} \quad (4.32)$$

where equation (4.28) with $r = a$ is used. Replacing these coefficients in the mapping (4.18) yields

$$\begin{aligned}
I_{11}^L &= \frac{a^3}{G} \left[\frac{2}{3} \mathcal{G}_{00}^L + \frac{\sqrt{5}}{3} \mathcal{G}_{20}^L - \sqrt{\frac{10}{3}} \operatorname{Re}(\mathcal{G}_{22}^L) \right] = ma^2 \left(\frac{2}{3} + \frac{1}{3} \right) = ma^2 \\
I_{22}^L &= \frac{a^3}{G} \left[\frac{2}{3} \mathcal{G}_{00}^L + \frac{\sqrt{5}}{3} \mathcal{G}_{20}^L + \sqrt{\frac{10}{3}} \operatorname{Re}(\mathcal{G}_{22}^L) \right] = ma^2 \left(\frac{2}{3} + \frac{1}{3} \right) = ma^2 \\
I_{33}^L &= \frac{a^3}{G} \left[\frac{2}{3} \mathcal{G}_{00}^L - \frac{2\sqrt{5}}{3} \mathcal{G}_{20}^L \right] = ma^2 \left(\frac{2}{3} - \frac{2}{3} \right) = 0 \\
I_{12}^L &= I_{13}^L = I_{23}^L = 0,
\end{aligned} \tag{4.33}$$

which is the expected inertia tensor for a point mass at the north pole.

4.3 A mapping between gravitational potential and inertia perturbations

In this section, I use the results from the previous section to derive a mapping between an arbitrary gravitational potential, denoted as $\mathcal{G}(\theta, \phi, t)$, and the inertia perturbations, denoted as $I_{ij}^{\mathcal{G}}(t)$, associated with the planet deformation in response to this gravitational potential. The gravitational potential is associated with surface mass redistribution due to an arbitrary cause (e.g., surface loads or deformation).

First, expanding the gravitational potential perturbation in spherical harmonics gives

$$\mathcal{G}(\theta, \phi, t) = \sum_{\ell=0}^{\infty} \sum_{m=-\ell}^{\ell} \mathcal{G}_{\ell m}(t) Y_{\ell m}(\theta, \phi). \tag{4.34}$$

Next, one can use the expressions (4.17) to find the surface load distribution that would produce this gravitational potential perturbation. The spherical harmonic expansion coefficients for this surface load are

$$L_{\ell m}^{\mathcal{G}}(t) = \frac{(2\ell + 1)}{4\pi G a} \mathcal{G}_{\ell m}(t), \tag{4.35}$$

where equation (4.17) is used. Finally, replacing the last equation in equation (4.4) yields

$$\begin{aligned}
I_{11}^{\mathcal{G}}(t) &= \frac{a^3}{G} \left[\frac{2}{3} \mathcal{G}_{00}(t) + \frac{\sqrt{5}}{3} \mathcal{G}_{20}(t) - \sqrt{\frac{10}{3}} \operatorname{Re}(\mathcal{G}_{22}(t)) \right] \\
I_{22}^{\mathcal{G}}(t) &= \frac{a^3}{G} \left[\frac{2}{3} \mathcal{G}_{00}(t) + \frac{\sqrt{5}}{3} \mathcal{G}_{20}(t) + \sqrt{\frac{10}{3}} \operatorname{Re}(\mathcal{G}_{22}(t)) \right] \\
I_{33}^{\mathcal{G}}(t) &= \frac{a^3}{G} \left[\frac{2}{3} \mathcal{G}_{00}(t) - \frac{2\sqrt{5}}{3} \mathcal{G}_{20}(t) \right] \\
I_{12}^{\mathcal{G}}(t) &= \frac{a^3}{G} \sqrt{\frac{10}{3}} \operatorname{Im}(\mathcal{G}_{22}(t)) \\
I_{13}^{\mathcal{G}}(t) &= \frac{a^3}{G} \sqrt{\frac{10}{3}} \operatorname{Re}(\mathcal{G}_{21}(t)) \\
I_{23}^{\mathcal{G}}(t) &= -\frac{a^3}{G} \sqrt{\frac{10}{3}} \operatorname{Im}(\mathcal{G}_{21}(t)).
\end{aligned} \tag{4.36}$$

4.3.1 Mapping for an axisymmetric gravitational potential

Let us consider the mapping between the gravitational potential and the inertia tensor for axisymmetric surface loads. As in the treatment of the surface mass load, I denote the gravitational potential symmetry axis location in spherical coordinates as $(\theta_{\mathcal{G}}, \phi_{\mathcal{G}})$, and the spherical harmonics coefficients for the case when the symmetry axis is at the pole (i.e., $\theta_{\mathcal{G}} = 0$) as $\mathcal{G}'_{\ell 0}(t)$. Then, in analogy with equation (4.8), one can write

$$\mathcal{G}_{2m}(t) = \mathcal{G}'_{20}(t) \frac{Y_{2m}^{\dagger}(\theta_L, \phi_L)}{\sqrt{5}}. \tag{4.37}$$

Using equation (4.20) allows one to obtain

$$I_{ij}^{\mathcal{G}} = \frac{2a^3}{3G} \mathcal{G}_{00}(t) \delta_{ij} + \frac{\sqrt{5}a^3}{G} \mathcal{G}'_{20}(t) \left(\frac{1}{3} \delta_{ij} - e_{\mathcal{G},i} e_{\mathcal{G},j} \right), \tag{4.38}$$

where δ_{ij} is the Kronecker delta and $\mathbf{e}_{\mathcal{G}} = (\sin \theta_{\mathcal{G}} \cos \phi_{\mathcal{G}}, \sin \theta_{\mathcal{G}} \sin \phi_{\mathcal{G}}, \cos \theta_{\mathcal{G}})$ is a unit vector that represents the orientation of the symmetry axis of the gravitational potential.

4.4 Inertia tensor perturbations: load-induced deformation

In addition to the direct contribution to the inertia tensor perturbations the surface load deforms the planet, producing additional perturbations. In this section I focus on predictions of inertia tensor perturbations associated with this deformation, which I denote as I_{ij}^{LD} .

We begin by introducing the non-dimensional k^L surface load Love number. In the time domain,

this Love number has the form (Peltier, 1974, 1976)

$$k_\ell^L(t) = k_\ell^{L,E} \delta(t) + \sum_{k=1}^K r_k^{\ell,L} \exp(-s_k^\ell t), \quad (4.39)$$

where $\delta(t)$ is the Dirac-delta function. The right hand side of this expression represents a superposition of an immediate elastic response (hence the superscript E) and a non-elastic relaxation governed by a sum of K normal modes of pure exponential decay. These modes are defined by an inverse decay time, $s_k^{\ell,L}$, and amplitude, $r_k^{\ell,L}$.

The harmonics for the load-induced gravitational potential $\mathcal{G}^{LD}(\theta, \phi, t)$ can be written as

$$\mathcal{G}_{\ell m}^{LD}(t) = \mathcal{G}_{\ell m}^L(t) * k_\ell^L(t), \quad (4.40)$$

where the asterisk denotes a time convolution and $\mathcal{G}_{\ell m}^L(t)$ are the harmonics for the direct load contribution. Replacing equations (4.17) in equation (4.40) gives

$$\mathcal{G}_{\ell m}^{LD}(t) = \frac{4\pi G a}{(2\ell + 1)} L_{\ell m}(t) * k_\ell^L(t). \quad (4.41)$$

This equation may now be applied to the mapping (4.18) to obtain the inertia perturbations due to the load-induced deformation:

$$\begin{aligned} I_{11}^{LD}(t) &= 4\pi a^4 \left[\frac{2}{3} L_{00}(t) * k_0^L(t) + \frac{1}{3\sqrt{5}} L_{20}(t) * k_2^L(t) - \sqrt{\frac{2}{15}} \text{Re}(L_{22}(t)) * k_2^L(t) \right] \\ I_{22}^{LD}(t) &= 4\pi a^4 \left[\frac{2}{3} L_{00}(t) * k_0^L(t) + \frac{1}{3\sqrt{5}} L_{20}(t) * k_2^L(t) + \sqrt{\frac{2}{15}} \text{Re}(L_{22}(t)) * k_2^L(t) \right] \\ I_{33}^{LD}(t) &= 4\pi a^4 \left[\frac{2}{3} L_{00}(t) * k_0^L(t) - \frac{2}{3\sqrt{5}} L_{20}(t) * k_2^L(t) \right] \\ I_{12}^{LD}(t) &= \frac{8\pi a^4}{\sqrt{30}} \text{Im}(L_{22}(t)) * k_2^L(t) \\ I_{13}^{LD}(t) &= \frac{8\pi a^4}{\sqrt{30}} \text{Re}(L_{21}(t)) * k_2^L(t) \\ I_{23}^{LD}(t) &= -\frac{8\pi a^4}{\sqrt{30}} \text{Im}(L_{21}(t)) * k_2^L(t). \end{aligned} \quad (4.42)$$

4.4.1 Inertia tensor perturbations: axisymmetric load-induced deformation

I now consider the inertia perturbations associated with the planet deformation in response to an axisymmetric surface load. As in the treatment of the direct contribution of the surface mass load to the inertia tensor, let us denote the symmetry axis of this surface load in spherical coordinates as (θ_L, ϕ_L) . The degree two spherical harmonic coefficients of the surface load and the gravitational potential with the symmetry axis at the north pole (i.e., $\theta_L = 0$) are denoted as L'_{20} and $\mathcal{G}_{20}^{LD'}$

respectively. In this case, one can use equation (4.41) to write

$$\mathcal{G}_{\ell 0}^{LD,\prime}(t) = \frac{4\pi G a}{(2\ell + 1)} L'_{\ell 0}(t) * k_{\ell}^L(t). \quad (4.43)$$

Finally, replacing the last equation in the mapping (4.38) yields

$$I_{ij}^{LD} = \frac{8\pi a^4}{3} \delta_{ij} L'_{00}(t) * k_0^L(t) + \frac{4\pi a^4}{\sqrt{5}} \left(\frac{1}{3} \delta_{ij} - e_{L,i} e_{L,j} \right) L'_{20}(t) * k_2^L(t), \quad (4.44)$$

where δ_{ij} is the Kronecker delta and $\mathbf{e}_L = (\sin \theta_L \cos \phi_L, \sin \theta_L \sin \phi_L, \cos \theta_L)$ is a unit vector indicating the orientation of the surface load symmetry axis (which is equivalent to the orientation of the load-induced gravitational potential symmetry axis).

4.5 Inertia tensor perturbations: rotationally-induced deformation

In this section I focus on predictions of perturbations in the inertia tensor associated with the planet deformation associated with rotation, which I denote as I_{ij}^{RD} .

4.5.1 Centrifugal potential

We begin by finding the spherical harmonic expansion for the centrifugal potential. Let us consider a mass element m_i with position vector \mathbf{a} at the surface of a rotating planet. The equation of motion for this mass element can be written as

$$\frac{D^2 \mathbf{a}}{Dt^2} = \frac{d^2 \mathbf{a}}{dr^2} + \boldsymbol{\Omega} \times \boldsymbol{\Omega} \times \mathbf{a}, \quad (4.45)$$

where the left-hand-side represents a time derivative taken in a non-rotating inertial frame, and the first term on the right-hand-side represents a time derivative in the planet frame which rotates with angular velocity $\boldsymbol{\Omega}$. Newton's law in the inertial frame

$$m_i D^2 \mathbf{a} / Dt^2 = \sum \text{Forces} \quad (4.46)$$

becomes

$$m_i \frac{d^2 \mathbf{a}}{dt^2} = \sum \text{Forces} - m_i \boldsymbol{\Omega} \times \boldsymbol{\Omega} \times \mathbf{a}. \quad (4.47)$$

in the rotating planet frame.

Let us describe the motion of a rigid body for illustration. I choose a reference frame with the rotation vector $\boldsymbol{\Omega}$ along the z axis as shown in Figure 4.3A. In this case, $d\mathbf{a}^2/dt^2 = 0$ since the

mass elements are fixed to the body reference frame and equation (4.47) takes the form

$$0 = \sum \text{Forces} - m_i \boldsymbol{\Omega} \times \boldsymbol{\Omega} \times \mathbf{a} = \sum \text{Forces} + m_i \Omega^2 a \sin \theta \mathbf{e}_R. \quad (4.48)$$

The last equation describes the circular motion of each point of the rigid body and the first term corresponds to the centrifugal force.

For a planet, $d^2 \mathbf{a}/dt^2 \neq 0$ since the planet can deform and equation (4.47) can be written as

$$m_i \frac{d^2 \mathbf{a}}{dt^2} = \sum \text{Forces} + F_C, \quad (4.49)$$

where the centrifugal force is defined as

$$F_C \equiv -m_i \boldsymbol{\Omega} \times \boldsymbol{\Omega} \times \mathbf{a}. \quad (4.50)$$

The centrifugal force can be written as

$$F_C \equiv m_i \Omega^2 a \sin \theta \mathbf{e}_R \quad (4.51)$$

in a reference frame with the rotation vector $\boldsymbol{\Omega}$ at the north pole (see Figure 4.3A). The centrifugal potential in this frame can be written as

$$\mathcal{G}^{R,\prime}(\theta, t) \equiv \frac{1}{2} \Omega^2(t) R^2 = \frac{1}{2} \Omega^2(t) a^2 \sin^2 \theta, \quad (4.52)$$

where $R = a \sin \theta$ is used. One can recover the centrifugal acceleration F_C/m_i by taking the gradient of equation (4.52) in cylindrical coordinates:

$$\frac{F_C}{m_i} = \nabla \mathcal{G}^{R,\prime} = \mathbf{e}_R \frac{\partial}{\partial R} \left(\frac{1}{2} \Omega^2 R^2 \right) = \Omega^2 R \mathbf{e}_R = \Omega^2 a \sin \theta \mathbf{e}_R. \quad (4.53)$$

4.5.2 Centrifugal potential - a spherical harmonic expansion

It proves convenient to obtain the spherical harmonic expansion coefficients for a rotation vector with arbitrary orientation from the expansion coefficients for the rotation vector at the north pole (compare Figures 4.3A and B). I denote the centrifugal potential for the rotation vector at the north pole as $\mathcal{G}^{R,\prime}(\theta, t)$. Rewriting equation (4.52) as

$$\mathcal{G}^{R,\prime}(\theta, t) = \frac{1}{3} \Omega^2(t) a^2 - \frac{1}{3\sqrt{5}} \Omega^2(t) a^2 Y_{20}(\theta) \quad (4.54)$$

gives

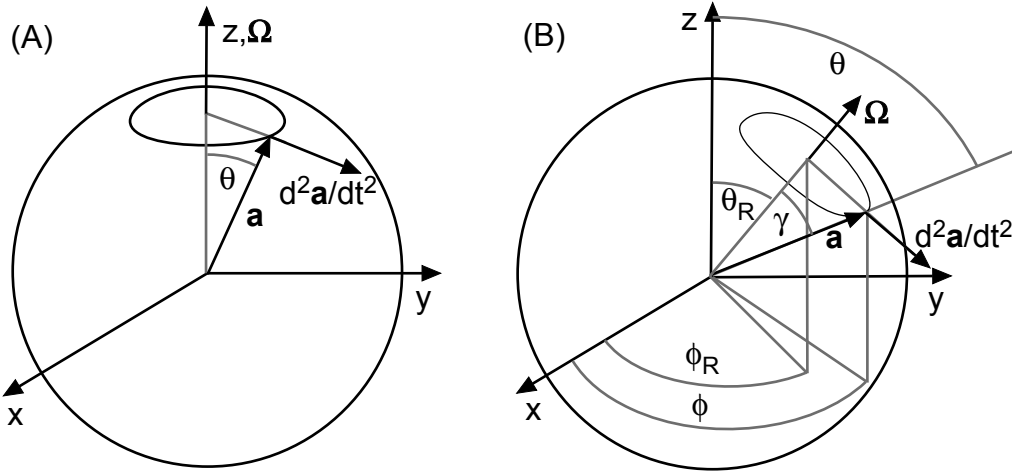


Figure 4.3 Position vectors and spherical coordinates used to calculate the centrifugal potential for the rotation vector Ω . The frames are distinguished on the basis of the rotation vector orientation. (A) rotation vector passing through the north pole. (B) rotation vector with an arbitrary orientation given by the spherical coordinates (θ_R, ϕ_R) . The angle γ denotes the angular distance between the rotation vector and an arbitrary point with coordinates (θ, ϕ) .

$$\begin{aligned}\mathcal{G}_{00}^{R,\prime}(t) &= \frac{a^2\Omega^2(t)}{3} \\ \mathcal{G}_{20}^{R,\prime}(t) &= -\frac{a^2\Omega^2(t)}{3\sqrt{5}}.\end{aligned}\quad (4.55)$$

We now consider the centrifugal potential expansion for a rotation vector with arbitrary orientation, which I denote as $\mathcal{G}^R(\theta, \phi, t)$. I choose a reference frame in which the rotation vector has spherical coordinates (θ_R, ϕ_R) as shown in Figure 4.3B. The centrifugal potential in this frame can be written as

$$\mathcal{G}^R(\gamma, t) = \frac{1}{2}\Omega^2(t)a^2\sin^2\gamma, \quad (4.56)$$

where γ denotes the angular distance between an arbitrary point (with coordinates (θ, ϕ)) and the rotation vector (with coordinates (θ_R, ϕ_R)) (see Figure 4.3B). Since I am interested in the spherical harmonic expansion of the centrifugal potential, I start by rewriting equation (4.56) as

$$\mathcal{G}^R(\gamma, t) = \frac{1}{3}\Omega^2(t)a^2Y_{00} - \frac{1}{3\sqrt{5}}\Omega^2(t)a^2Y_{20}(\gamma). \quad (4.57)$$

Next, replacing the addition theorem (D.8) in the last equation yields

$$\mathcal{G}^R(\theta, \phi, t) = \frac{1}{3}\Omega^2(t)a^2Y_{00} - \frac{1}{15}\Omega^2(t)a^2 \sum_{m=-2}^2 Y_{2m}^\dagger(\theta_R, \phi_R)Y_{2m}(\theta, \phi). \quad (4.58)$$

From the last equation, the spherical harmonic expansion coefficients for the centrifugal potential are

$$\begin{aligned}\mathcal{G}_{00}^R(t) &= \frac{a^2\Omega^2(t)}{3} \\ \mathcal{G}_{2m}^R(\theta_R, \phi_R, t) &= -\frac{a^2\Omega^2(t)}{15} Y_{2m}^\dagger(\theta_R, \phi_R).\end{aligned}\quad (4.59)$$

We note that equations (4.55) and (4.59) are equivalent for $\theta_R = 0$ as expected. The following coefficients will be used below:

$$\begin{aligned}\mathcal{G}_{00}^R(t) &= \frac{a^2\Omega^2(t)}{3} \\ \mathcal{G}_{20}^R(\theta_R, \phi_R, t) &= -\frac{\Omega^2(t)a^2}{6\sqrt{5}} (3\cos^2\theta_R - 1) \\ \mathcal{G}_{21}^R(\theta_R, \phi_R, t) &= \frac{\Omega^2(t)a^2}{\sqrt{30}} \sin\theta_R \cos\theta_R e^{-i\phi_R} \\ \mathcal{G}_{22}^R(\theta_R, \phi_R, t) &= -\frac{\Omega^2(t)a^2}{2\sqrt{30}} \sin^2\theta_R e^{-2i\phi_R}\end{aligned}\quad (4.60)$$

4.5.3 Inertia tensor perturbations associated with rotational deformation

The response of the planet to a potential forcing is governed by tidal (or tidal effective) Love numbers. In analogy with equation (4.39), the time domain form of the viscoelastic tidal k Love number can be written as (Peltier, 1974, 1976)

$$k_\ell^T(t) = k_\ell^{T,E} \delta(t) + \sum_{k=1}^K r_k^{\ell,T} \exp(-s_k^\ell t), \quad (4.61)$$

where $\delta(t)$ is the Dirac-delta function.

The spherical harmonic coefficients of the perturbation to the gravitational equipotential associated with the planet deformation are given by:

$$\mathcal{G}_{2m}^{RD}(\theta_R, \phi_R, t) = \mathcal{G}_{2m}^R(\theta_R, \phi_R, t) * k_2^T(t), \quad (4.62)$$

at degree two and

$$\mathcal{G}_{00}^{RD}(t) = \mathcal{G}_{00}^R(t) * k_0^T(t) \quad (4.63)$$

at degree zero. Equations (4.36), (4.62), and (4.63) can then be combined to yield

$$\begin{aligned}
I_{11}^{RD} &= \frac{a^3}{G} \left[\frac{2}{3} k_0^T(t) * \mathcal{G}_{00}^{RD}(t) + \frac{\sqrt{5}}{3} k_2^T(t) * \mathcal{G}_{20}^R(t) - \sqrt{\frac{10}{3}} k_2^T * \text{Re}(\mathcal{G}_{22}^R(t)) \right] \\
I_{22}^{RD} &= \frac{a^3}{G} \left[\frac{2}{3} k_0^T(t) * \mathcal{G}_{00}^{RD}(t) + \frac{\sqrt{5}}{3} k_2^T(t) * \mathcal{G}_{20}^R(t) + \sqrt{\frac{10}{3}} k_2^T * \text{Re}(\mathcal{G}_{22}^R(t)) \right] \\
I_{33}^{RD} &= \frac{a^3}{G} \left[\frac{2}{3} k_0^T(t) * \mathcal{G}_{00}^{RD}(t) - \frac{2\sqrt{5}}{3} k_2^T(t) * \mathcal{G}_{20}^R(t) \right] \\
I_{12}^{RD} &= \frac{a^3}{G} \sqrt{\frac{10}{3}} k_2^T(t) * \text{Im}(\mathcal{G}_{22}^R(t)) \\
I_{13}^{RD} &= \frac{a^3}{G} \sqrt{\frac{10}{3}} k_2^T(t) * \text{Re}(\mathcal{G}_{21}^R(t)) \\
I_{23}^{RD} &= -\frac{a^3}{G} \sqrt{\frac{10}{3}} k_2^T(t) * \text{Im}(\mathcal{G}_{21}^R(t)), \tag{4.64}
\end{aligned}$$

where I_{ij}^{RD} denotes the inertia tensor perturbations associated with the planet rotational deformation.

Alternatively, one can use the mapping (4.38) to obtain a simple expression for the inertia tensor perturbations associated with the rotationally induced planet deformation. The spherical harmonics coefficients for the gravitational potential associated with the planet deformation in response to the rotation vector at the north pole can be written as

$$\begin{aligned}
\mathcal{G}_{00}^{RD,\prime}(t) &= \mathcal{G}_{00}^{R,\prime}(t) * k_0^T(t) = \frac{a^2}{3} \Omega^2(t) * k_0^T(t) \\
\mathcal{G}_{20}^{RD,\prime}(t) &= \mathcal{G}_{20}^{R,\prime}(t) * k_2^T(t) = -\frac{a^2}{3\sqrt{5}} \Omega^2(t) * k_2^T(t), \tag{4.65}
\end{aligned}$$

where equation (4.60) is used. Replacing equation (4.65) in the mapping (4.38) yields

$$I_{ij}^{RD} = \frac{2a^5}{9G} k_0^T(t) * \Omega^2(t) \delta_{ij} + \frac{a^5}{3G} \left(e_{\Omega,i} e_{\Omega,j} - \frac{1}{3} \delta_{ij} \right) k_2^T(t) * \Omega^2(t), \tag{4.66}$$

where $\mathbf{e}_\Omega = (\sin \theta_R \cos \phi_R, \sin \theta_R \sin \phi_R, \cos \theta_R)$ is a unit vector indicating the orientation of the rotation axis.

4.6 Fluid limit inertia tensor perturbations

4.6.1 Fluid Love numbers

In Chapter 5 I will be concerned with the planet response to surface loads or rotation over time scales much longer than the decay times $1/s_k^\ell$ (see equations 4.39 and 4.61). This limit is referred to as the fluid limit and the corresponding inertia tensor variations can be found by using the so-called

fluid Love numbers.

Let us consider the inertia tensor perturbations associated with surface load. One can formally assume that the load is imposed at $t = 0$. That is, it is assumed that the surface density can be written as

$$L(\theta, \phi, t) = L(\theta, \phi)H(t), \quad (4.67)$$

where

$$H(t) = \begin{cases} 0, & \text{if } t < 0; \\ 1, & \text{otherwise} \end{cases} \quad (4.68)$$

is a Heaviside step function. The spherical harmonic expansion coefficients for this load can be written as

$$L_{lm}(t) = L_{lm}H(t). \quad (4.69)$$

The fluid limit inertia perturbations associated with the load induced planetary deformation are given by

$$\lim_{t \rightarrow \infty} I_{ij}^{LD}(t) \quad (4.70)$$

and are functions of terms of the form

$$\lim_{t \rightarrow \infty} L_{lm}(t) * k_l^L(t) = L_{lm} \lim_{t \rightarrow \infty} k_l^L(t) * H(t) \quad (4.71)$$

(see equations 4.42 and 4.44).

Similarly, the long term rotationally induced inertia variations can be found by formally assuming that the planet starts spinning at $t = 0$. That is,

$$\Omega(t) = \Omega H(t). \quad (4.72)$$

The fluid limit inertia tensor perturbations driven by rotation are

$$\lim_{t \rightarrow \infty} I_{ij}^{RD}(t) \quad (4.73)$$

and are functions of terms of the form

$$\lim_{t \rightarrow \infty} \Omega^2(t) * k_2^T(t) = \Omega^2 \lim_{t \rightarrow \infty} k_2^T(t) * H(t) \quad (4.74)$$

(see equations 4.64 and 4.66).

Let us calculate the fluid limit time convolution for the load Love number by combining equations

(4.39) and (4.71):

$$\begin{aligned}
\lim_{t \rightarrow \infty} k_\ell^L(t) * H(t) &= \lim_{t \rightarrow \infty} \int_0^t k_\ell^{L,E} \delta(t) H(t - \tau) d\tau + \lim_{t \rightarrow \infty} \int_0^t \sum_{k=1}^K r_k^{\ell,L} \exp[-s_k^\ell(t - \tau)] H(\tau) d\tau \\
&= k_\ell^{L,E} + \sum_{k=1}^K r_k^{\ell,L} \lim_{t \rightarrow \infty} \int_0^t \exp[-s_k^\ell(t - \tau)] d\tau \\
&= k_\ell^{L,E} + \sum_{k=1}^K r_k^{\ell,L} \lim_{t \rightarrow \infty} \left\{ \frac{\exp[-s_k^\ell(t - \tau)]}{s_k^\ell} \right\}_0^t \\
&= k_\ell^{L,E} + \sum_{k=1}^K \frac{r_k^{\ell,L}}{s_k^\ell} \lim_{t \rightarrow \infty} [1 - \exp(-s_k^\ell t)] \\
&= k_\ell^{L,E} + \sum_{k=1}^K \frac{r_k^{\ell,L}}{s_k^\ell}. \tag{4.75}
\end{aligned}$$

Similarly, replacing equation (4.61) in equation (4.71) allows one to find the fluid limit time convolution for the tidal Love number:

$$\lim_{t \rightarrow \infty} k_\ell^T(t) * H(t) = k_\ell^{T,E} + \sum_{k=1}^K \frac{r_k^{\ell,T}}{s_k^\ell} \tag{4.76}$$

Equations (4.75) and (4.76) are commonly written as $k_\ell^L(s = 0)$ and $k_2^T(s = 0)$ respectively since equations (4.71) and (4.61) become

$$k_\ell^L(s) = k_\ell^{L,E} + \sum_{k=1}^K \frac{r_k^{\ell,L}}{s + s_k^\ell} \tag{4.77}$$

and

$$k_\ell^T(s) = k_\ell^{T,E} + \sum_{k=1}^K \frac{r_k^{\ell,T}}{s + s_k^\ell}, \tag{4.78}$$

in the Laplace-transform s domain.

In principle, the fluid Love numbers may be computed by considering the fluid, $s = 0$ limit of equations (4.77) and (4.78). In practice, a more accurate prediction of the fluid Love number is obtained via an independent calculation in which all regions of the planet, with the exception of a purely elastic lithospheric plate, are treated as inviscid. (This calculation avoids the difficulty in ensuring that all viscoelastic normal modes have been found.) This is a valid assumption since all of the viscous modes must have decayed in the fluid limit.

For simplicity, I adopt the following common notation for the degree zero and two fluid Love

numbers:

$$\begin{aligned} k_{\ell=0}^L(s=0) &= k_{f,0}^L & k_{\ell=2}^L(s=0) &= k_f^L \\ k_{\ell=0}^L(s=0) &= k_{f,0}^L & k_{\ell=2}^L(s=0) &= k_f^T \end{aligned} \quad (4.79)$$

4.6.2 Fluid limit inertia tensor perturbations

The fluid limit inertia perturbations associated with the the direct contribution of the load and the load induced deformation $I_{ij}^{L,LD} \equiv I_{ij}^L + I_{ij}^{LD}$ can be written as

$$\begin{aligned} I_{11}^{L,LD} &= 4\pi a^4 \left[\frac{2}{3}(1 + k_{f,0}^L)L'_{00} + \frac{1}{6\sqrt{5}}(3\cos^2\theta_L - 1)(1 + k_f^L)L'_{20} \right. \\ &\quad \left. - \frac{1}{2\sqrt{5}}\sin^2\theta_L \cos(2\phi_L)(1 + k_f^L)L'_{20} \right] \\ I_{22}^{L,LD} &= 4\pi a^4 \left[\frac{2}{3}(1 + k_{f,0}^L)L'_{00} + \frac{1}{6\sqrt{5}}(3\cos^2\theta_L - 1)(1 + k_f^L)L'_{20} \right. \\ &\quad \left. + \frac{1}{2\sqrt{5}}\sin^2\theta_L \cos(2\phi_L)(1 + k_f^L)L'_{20} \right] \\ I_{33}^{L,LD} &= \frac{8\pi a^4}{3} \left[(1 + k_{f,0}^L)L'_{00} - \frac{1}{2\sqrt{5}}(3\cos^2\theta_L - 1)(1 + k_f^L)L'_{20} \right] \\ I_{12}^{L,LD} &= -\frac{2\pi a^4}{\sqrt{5}}\sin^2\theta_L \sin(2\phi_L)(1 + k_f^L)L'_{20} \\ I_{13}^{L,LD} &= -\frac{4\pi a^4}{\sqrt{5}}\sin\theta_L \cos\theta_L \cos\phi_L(1 + k_f^L)L'_{20} \\ I_{23}^{L,LD} &= -\frac{4\pi a^4}{\sqrt{5}}\sin\theta_L \cos\theta_L \sin\phi_L(1 + k_f^L)L'_{20}, \end{aligned} \quad (4.80)$$

or

$$I_{ij}^{L,LD} = \frac{8\pi a^4}{3}L'_{00}(1 + k_{f,0}^L)\delta_{ij} + \frac{4\pi a^4}{3\sqrt{5}}L'_{20}(1 + k_f^L) \left(\frac{1}{3}\delta_{ij} - e_{L,i}e_{L,j} \right) \quad (4.81)$$

for an axisymmetric surface load, by replacing the time convolutions in the inertia perturbations (4.10,4.11) and (4.42,4.44) by a simple multiplication with the appropriate fluid load Love number.

Similarly, the fluid limit rotationally induced inertia perturbations can be written as

$$I_{ij}^{RD} = \frac{2a^5}{9G}k_{f,0}^T\Omega^2\delta_{ij} + \frac{a^5\Omega^2}{3G}k_f^T \left(e_{\Omega,i}e_{\Omega,j} - \frac{1}{3}\delta_{ij} \right) \quad (4.82)$$

by replacing the time convolutions in the inertia perturbations (4.66) by a simple multiplication

with the appropriate tidal Love number. One may write each component of equation (4.82):

$$\begin{aligned}
I_{11}^{RD} &= \frac{2a^5}{9G} k_{f,0}^T \Omega^2 - \frac{Ma^3}{18g} k_f^T \Omega^2 [3 \cos^2 \theta_R - 1 - 3 \sin^2 \theta_R \cos 2\phi_R] \\
I_{22}^{RD} &= \frac{2a^5}{9G} k_{f,0}^T \Omega^2 - \frac{Ma^3}{18g} k_f^T \Omega^2 [3 \cos^2 \theta_R - 1 + 3 \sin^2 \theta_R \cos 2\phi_R] \\
I_{33}^{RD} &= \frac{2a^5}{9G} k_{f,0}^T \Omega^2 + \frac{Ma^3}{9g} k_f^T \Omega^2 (3 \cos^2 \theta_R - 1) \\
I_{12}^{RD} &= \frac{a^5}{6G} k_f^T \Omega^2 \sin^2 \theta_R \sin 2\phi_R \\
I_{13}^{RD} &= \frac{a^5}{3G} k_f^T \Omega^2 \sin \theta_R \cos \theta_R \cos \phi_R \\
I_{23}^{RD} &= \frac{a^5}{3G} k_f^T \Omega^2 \sin \theta_R \cos \theta_R \sin \phi_R.
\end{aligned} \tag{4.83}$$

Chapter 5

True polar wander of dynamic planets with lithospheres

5.1 Introduction

The long-term (secular) rotational stability of terrestrial planets subject to surface mass loading and internal convective dynamics is a long-standing problem in geophysics framed by a series of seminal studies (e.g., [Gold, 1955](#); [Goldreich & Toomre, 1969](#)). Figure 5.1 provides a schematic illustration of the basic physical elements that have defined this classic discussion.

[Gold \(1955\)](#), for example, discussed the stability of a hydrostatic planet subject to an anomalous (i.e., non-hydrostatic or imperfectly compensated) load (Figures 5.1A-C). The uncompensated load would act to push the rotation pole away (green arrow, Figure 5.1B) in a reference frame fixed to the load. In the short term, the hydrostatic bulge would act to stabilize the pole (i.e., retard polar motion). However, since the hydrostatic rotational bulge of the planet would, in time, relax to any new orientation of the rotation pole (e.g., Figure 5.1B), all memory of this previous orientation would ultimately vanish (Figure 5.1B,C). That is, a hydrostatic bulge provides no long-term rotational stability and the reorientation of the pole, or so-called true polar wander (TPW), would be governed solely by the location of the uncompensated surface mass load. In particular, a mass excess of any size (indeed, as small as Gold's beetle) would drive a TPW that would eventually reorient the load to the equator (Figure 5.1C). Mathematically, the new (final) pole position would be governed by the principle axis of the non-hydrostatic components of the inertia tensor introduced by the uncompensated load.

The example of [Gold \(1955\)](#) is singular, since two larger moments of inertia are then equal. [Gold \(1955\)](#)'s arguments were extended by [Goldreich & Toomre \(1969\)](#) who demonstrated that a group of anomalous masses moving randomly on the surface (e.g., a set of scurrying beetles) could drive rapid (relative to the speed of the masses) reorientation of the rotation pole (see Chapter 3). Indeed, the rate of TPW would only be limited by the characteristic decay time governing the

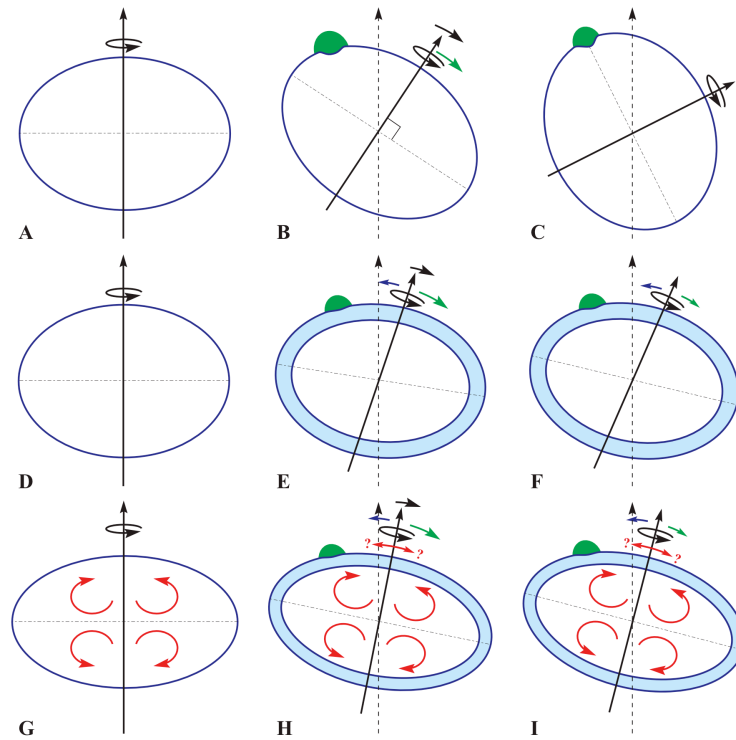


Figure 5.1 Schematic highlighting some basic physical principles governing, and common approximations applied to, the study of the secular stability of planetary rotation. Figure 5.1A-C illustrate arguments described by Gold (1955). An otherwise hydrostatic planet is subject to a surface mass load (the green ‘beetle’) that is at least partially uncompensated. The load pushes the rotation axis away (green arrow) leading to TPW (black arrow) and, after a time period that is long relative to the relaxation of the hydrostatic flattening, the bulge is assumed to perfectly relax to the new pole location (Figure 5.1B,C); there is no memory of the initial pole location. The process continues until the load reaches the planetary equator and TPW ceases. Figure 5.1D-F illustrate the extension to Gold (1955)’s analysis described by Willemann (1984). In this case, the (uncompensated) load-induced push on the rotation pole is retarded (blue arrow) by the incomplete relaxation of the rotational bulge in the presence of an elastic lithosphere (blue shell). The presence of a remnant rotational bulge is evident in the lack of symmetry of the bulge relative to the rotation axis. The final position of the rotation axis (Figure 5.1F) is defined by a balance between the load-induced push and the non-hydrostatic remnant bulge stabilization (green and blue arrows, respectively); the load does not, in general, reach the equator (as it does in Figure 5.1C, where the latter stabilizing effect is absent). Figure 5.1G-I extend Figure 5.1D-F to consider the potential influence of internal convective dynamics on the rotational state. This impact will depend on the amplitude and (principle axis) orientation of convection-induced perturbations to the inertia tensor (hence the question marks attached to the red arrows in Figure 5.1H,I). The cartoon shows the specific case where convection acts to increase the ellipticity of the rotating planet (compare frames D and G); in this case, the ‘excess’ ellipticity will act to stabilize the rotation pole relative to the imposition of the load. The net effect (Figure 5.1I) is a more subdued TPW relative to the case shown in Figure 5.1F.

relaxation of the rotational (hydrostatic) bulge, which in turn would be a function of the viscosity structure of the planet.

Gold (1955)'s arguments, while providing significant insight into the secular rotational stability of planets, involved an underlying inconsistency that was highlighted, and addressed, by Willemann (1984). The hydrostatic figure is the form achieved by a rotating planet with no elastic (i.e., long-term) strength. Such a form would have been presumably established very early in the planet's history (Figure 5.1D). Subsequent cooling of the planet and development of a lithosphere would not alter the flattening of this hydrostatic form (Figure 5.1E); however, the presence of such a lithosphere is the reason why surface mass loads or beetles would not be perfectly compensated. The shortcoming in Gold (1955)'s analysis is that the growth of a lithosphere would also ensure that the initial hydrostatic figure of the planet could not entirely relax to any new orientation associated with TPW (Figure 5.1E,F). Simply put, one cannot have an uncompensated surface mass load and a completely relaxed hydrostatic bulge. This was the central point underlying Willemann (1984)'s analysis. In this case, all memory of the original rotation does not vanish, and the 'remnant of the rotational flattening' (Willemann, 1984) will act to stabilize the rotation vector.

What would the final position of the rotation vector be (i.e., the equilibrium position of the pole when all viscous effects have relaxed)? This position is governed by a balance between the TPW driven by the uncompensated component of the load (which acts to move the load to the equator; green line, Figure 5.1F) and the non-hydrostatic remnant rotational effect (which acts to resist any reorientation of the pole; blue line, Figure 5.1F). Willemann (1984) concluded that the TPW angle will depend on the initial position of the load and its uncompensated size (measured in terms of the degree two geopotential perturbation) relative to the rotational bulge. He furthermore came to the surprising conclusion that the reorientation was independent of the thickness of the lithosphere.

In this Chapter I revisit the general problem addressed by Willemann (1984) using a fluid Love number formulation for the response of the planetary model to surface mass and rotational loading. Following Willemann (1984) I treat the equilibrium position of the rotation pole for time scales sufficiently long to ensure that all viscous relaxation associated with mass loading and bulge adjustment is complete. I adopt the term 'secular rotational stability' to emphasize this focus, and, in this case, the long-term reorientation of the pole is governed by the principle axis of the non-hydrostatic tensor. I use my expressions to generalize (and correct) Willemann (1984)'s results, to explore a series of important special cases (e.g., the Gold (1955) assumption that the hydrostatic bulge relaxes completely in response to a new pole position), and to comment on some more recent analyses of rotational stability which do not appear to have incorporated a remnant rotational bulge (Bills & James, 1999).

I complete my analysis by including a separate section that incorporates non-hydrostatic contributions to the inertia tensor driven by internal convective dynamics (Figure 5.1G-I). Since the amplitude and (principle axis) orientation of such contributions are unknown for all planets with

the possible exception of the Earth, this section is by necessity general (note the question marks in Figure 5.1I); nevertheless, the expressions I derive will be useful for those interested in the sensitivity of traditional predictions of planetary rotational stability (which focus on external loading) to the presence of potential convective regimes. That such regimes are unconstrained for other planets does not diminish their potential relevance; indeed, it would be difficult to argue that the massive Tharsis rise on Mars, the subject of significant interest in the field of Martian rotation stability (e.g., [Willemann, 1984](#); [Bills & James, 1999](#)), does not reflect the action of both external and internal processes. The existence of the latter will alter the TPW that would be inferred by considering a purely external forcing (compare Figure 5.1F,I).

5.2 Inertia tensor perturbations

5.2.1 Inertia Perturbations: The Surface Mass Load

In this section I focus on predictions of perturbations in the inertia tensor associated with the direct and deformational effects of the surface mass load. I will consider the case where the time elapsed since loading is much longer than the decay times associated with the viscoelastic normal modes in equation (4.39). That is, all viscous stresses are presumed to have relaxed. It will be convenient, for the purposes of comparison with previous work (specifically [Willemann, 1984](#)), to consider the special case of a disk load with azimuthal symmetry centered at an arbitrary geographic position (θ_L, ϕ_L) . Let us say that this load, if centered on the north pole, was described by spherical harmonic coefficients $L'_{\ell 0}$. Then, the total inertia tensor perturbation due to the effects of mass loading,

$$I_{ij}^{L,LD} = I_{ij}^L + I_{ij}^{LD}, \quad (5.1)$$

becomes

$$I_{ij}^{L,LD} = \frac{8\pi a^4}{3} L'_{00} (1 + k_{f,0}^L) \delta_{ij} + \frac{4\pi a^4}{\sqrt{5}} L'_{20} (1 + k_f^L) \left(\frac{1}{3} \delta_{ij} - e_{L,i} e_{L,j} \right), \quad (5.2)$$

where equation (4.81) is used, δ_{ij} is the Kronecker delta, and $e_L = (\sin \theta_L \cos \phi_L, \sin \theta_L \sin \phi_L, \cos \theta_L)$ is a unit vector indicating the location of the surface load degree two component centre.

Note that the degree zero component of the inertia tensor perturbation (5.2) is constant for the diagonal elements and zero elsewhere. Thus, these components will not alter the principal axis of the tensor and will therefore have no effect on the reorientation of the pole from its initial state. Accordingly, one can drop these perturbations to generate the degree-two-only expressions:

$$I_{ij}^{L,LD} = \frac{4\pi a^4}{\sqrt{5}} L'_{20} (1 + k_f^L) \left(\frac{1}{3} \delta_{ij} - e_{L,i} e_{L,j} \right), \quad (5.3)$$

When there is no elastic lithosphere, the planet behaves as a purely inviscid material over very

long time scales, and the fluid Love number (at spherical harmonic degree 2), k_f^L , approaches very close to -1. Thus, load induced perturbations in the inertia tensor vanish ($1 + k_f^L \sim 0$) since the load will be (essentially) perfectly compensated. The existence of a non-zero elastic lithosphere introduces a departure from this state since the lithosphere will provide some (elastic) support for the load (i.e, $1 + k_f^L \neq 0$).

5.2.2 Inertia Perturbations: Rotational Effects

The initial, hydrostatic rotational form of a planet will be established during a time when the effective elastic lithospheric thickness is close to zero. As the planet cools, the development over time of an elastic lithosphere of non-zero thickness guarantees that the hydrostatic rotational flattening will never perfectly readjust to a change in the orientation of the rotation pole. In other words, if rotation were to cease, the planet, by virtue of the development of a post-accretion lithosphere, would not assume a spherical form (even in the absence of uncompensated surface loads and internal dynamics). This ‘partially relaxed remnant of the rotational flattening’ (Willemann, 1984; p. 703) contributes a non-hydrostatic component to the inertia tensor that serves as the focus of this section.

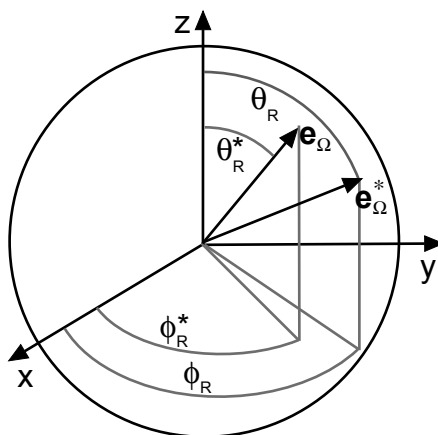


Figure 5.2 Unit vectors \mathbf{e}_Ω^* and \mathbf{e}_Ω indicating the orientation of the initial (at $t = t^*$) and final rotation axes respectively.

We assume, following the Willemann (1984) analysis, a specific sequence of events. In stage I, the hydrostatic form of the planet is established during a period when there is no long-term (elastic) lithospheric strength. This hydrostatic form will perfectly adjust to an arbitrary amount of TPW during stage I. In stage II, an elastic lithospheric shell develops in response to the cooling of the planet. The theory assumes that this development occurs during a period of no TPW; hence the remnant bulge aligns perfectly with the orientation of the rotational pole within this stage. I denote the time at this stage as t^* . Finally, in stage III, (internal and/or external) loading drives TPW in the presence of this remnant bulge.

In this case, the fluid limit inertia perturbations associated with rotation can be written as

$$I_{ij}^{ROT} = I_{ij}^{RD}(k_{f,0}^{T*}, k_f^{T*}, \theta_R^*, \phi_R^*) + I_{ij}^{RD}(k_{f,0}^T, k_f^T, \theta_R, \phi_R) - I_{ij}^{RD}(k_{f,0}^T, k_f^T, \theta_R^*, \phi_R^*), \quad (5.4)$$

where I_{ij}^{RD} is given by equation (4.82), and (θ_R^*, ϕ_R^*) and (θ_R, ϕ_R) are the coordinates of the initial (at $t = t^*$) and final rotation vectors (see figure 5.2). I denote the initial and final rotation vectors as Ω^* and Ω respectively. The first term on the right-hand-side corresponds to the initial flattening before the lithosphere forms, and the last two terms correspond to the planet response to the change in the centrifugal potential (see Figure 5.2). The fluid Love numbers in equation (5.4) are functions of the elastic lithospheric thickness since the lithospheric thickness changes with time. In the case where there is no long term elastic strength in the lithosphere (i.e. for $t < t^*$), I denote the fluid Love numbers as $k_f^{T,*}$ (for degree two) and $k_{f,0}^{T,*}$ (at degree zero). I assume that t^* is very long in the sense that the planet has reached its fluid limit hydrostatic figure before the development of the lithosphere.

Replacing equation (4.82) in equation (5.4) allows one to obtain

$$\begin{aligned} I_{ij}^{ROT} = & \frac{2a^5\Omega^{*2}}{9G} (k_{f,0}^{T*} - k_{f,0}^T) \delta_{ij} + \frac{2a^5\Omega^2}{9G} k_{f,0}^T \delta_{ij} + \frac{a^5\Omega^{*2}}{3G} (k_f^{T*} - k_f^T) \left(e_{\Omega,i}^* e_{\Omega,j}^* - \frac{1}{3} \delta_{ij} \right) \\ & + \frac{a^5\Omega^2}{3G} k_f^T \left(e_{\Omega,i} e_{\Omega,j} - \frac{1}{3} \delta_{ij} \right), \end{aligned} \quad (5.5)$$

where $\mathbf{e}_{\Omega}^* = (\sin \theta_R^* \sin \phi_R^*, \sin \theta_R^* \cos \phi_R^*, \cos \theta_R^*)$ and $\mathbf{e}_{\Omega} = (\sin \theta_R \sin \phi_R, \sin \theta_R \cos \phi_R, \cos \theta_R)$ are unit vectors indicating the orientation of the initial and final rotation axis respectively (see figure 5.2).

Since TPW is driven by non-hydrostatic contributions to the inertia tensor, I am interested in the non-hydrostatic contributions of equation (5.5), which I denote as I_{ij}^{FB} . These inertia tensor perturbations produce a rotational fossil bulge that depends on the initial rotation vector orientation, hence the superscript ‘FB’. Keeping the non-hydrostatic terms (i.e., the terms which depend on Ω^*) in equation (5.5) yields

$$I_{ij}^{FB} = \frac{2a^5\Omega^{*2}}{9G} (k_{f,0}^{T*} - k_{f,0}^T) \delta_{ij} + \frac{a^5\Omega^{*2}}{G} (k_f^{T*} - k_f^T) \left(e_{\Omega,i}^* e_{\Omega,j}^* - \frac{1}{3} \delta_{ij} \right). \quad (5.6)$$

Note that the degree zero component of the inertia tensor perturbation is constant for the diagonal elements and zero elsewhere. Thus, these components will not alter the principal axes of the inertia tensor and will therefore have no effect on the reorientation of the pole from its initial state. Accordingly, one can drop these perturbations to generate the degree-two-only expressions:

$$I_{ij}^{FB} = \frac{a^5\Omega^{*2}}{3G} (k_f^{T*} - k_f^T) \left(e_{\Omega,i}^* e_{\Omega,j}^* - \frac{1}{3} \delta_{ij} \right), \quad (5.7)$$

where $\Omega^{*2} = \Omega^2$ is used since it is assumed that the magnitude of the rotation vector is constant.

It is emphasized that my mathematical treatment of the remnant rotational flattening assumes, following the [Willemann \(1984\)](#) analysis, a specific sequence of events explained above. The theory can easily be extended to account for a continuous phase of both TPW and lithospheric development prior to loading. In this case, the remnant rotational flattening would be determined via an integration that incorporates slow changes in the lithospheric thickness and any reorientation of the pole (where the integration extends from the formation of the hydrostatic planet to the onset of loading).

5.2.3 Total Inertia Perturbations

An expression for the total inertia tensor perturbation (ignoring the spherically symmetric degree zero contributions) due to the effects of an external surface mass loading,

$$I_{ij}^{L,LD,FB} = I_{ij}^L + I_{ij}^{L-D} + I_{ij}^{FB}, \quad (5.8)$$

can be derived by combining equations (5.3) and (5.7):

$$I_{ij}^{L,LD,FB} = \frac{4\pi a^2}{3\sqrt{5}} L'_{20} (1 + k_f^L) \left(\frac{1}{3} \delta_{ij} - e_{L,i} e_{L,j} \right) + \frac{a^5 \Omega^2}{3G} (k_f^{T*} - k_f^T) \left(e_{\Omega,i}^* e_{\Omega,j}^* - \frac{1}{3} \delta_{ij} \right) \quad (5.9)$$

The size of the disk load may be conveniently normalized by considering the ratio of the degree two gravitational potential perturbations due to the direct effect of the load and the hydrostatic rotational bulge before the lithosphere forms. If I denote this ratio as Q' (following the symbolism adopted in [Willemann, 1984](#)), then equations (4.19) and (4.65) yield

$$Q' = -\frac{\frac{4\pi G a}{5} L'_{20}}{-\frac{a^2 \Omega^2}{3\sqrt{5}} k_f^{T*}}. \quad (5.10)$$

Replacing equation (5.10) in my expressions for the total inertia perturbation (5.9) gives

$$I_{ij}^{L,LD,FB} = m' Q' \alpha \left(\frac{1}{3} \delta_{ij} - e_{L,i} e_{L,j} \right) + m' \left(e_{\Omega,i}^* e_{\Omega,j}^* - \frac{1}{3} \delta_{ij} \right), \quad (5.11)$$

where

$$m' = \frac{\Omega^2 a^5}{3G} (k_f^{T*} - k_f^T), \quad (5.12)$$

and

$$\alpha = \frac{1 + k_f^L}{1 - k_f^T / k_f^{T*}}. \quad (5.13)$$

Note that the values m' and α only involve parameters associated with the planetary model (fluid Love numbers, radius, mass, rotation rate). The size of the load is embedded in Q' .

As one further simplification to the equations for the inertia tensor perturbations, one can assume, with no loss of generality, that the load is placed along the great circle of zero longitude ($\phi_L = 0$). In this case the unit vector associate with the load centre orientation becomes $\mathbf{e}_L = (\sin \theta_L, 0, \cos \theta_L)$.

5.2.4 Willemann (1984) Revisited

Equation (5.11) can be directly compared with the derivation by Willemann (1984) for inertia tensor perturbations due to external surface mass loading. His results (see equations 21-24) are:

$$\begin{aligned}
I_{11}^{L,LD,FB} &= \frac{1}{3}m'' \left\{ Q' \left[P_{20}(\theta_L) - \frac{1}{2}P_{22}(\theta_L) \right] - 1 \right\} \\
I_{22}^{L,LD,FB} &= \frac{1}{3}m'' \left\{ Q' \left[P_{20}(\theta_L) + \frac{1}{2}P_{22}(\theta_L) \right] - 1 \right\} \\
I_{33}^{L,LD,FB} &= -\frac{2}{3}m'' [Q' P_{20}(\theta_L) - 1] \\
I_{13}^{L,LD,FB} &= \frac{1}{3}m'' Q' P_{21}(\theta_L) \\
I_{12}^{L,LD,FB} &= I_{23}^{L,L-D,ROT} = 0.
\end{aligned} \tag{5.14}$$

where

$$m'' = \frac{1}{2} \frac{M\Omega^2 a^3}{g} (1 - c), \tag{5.15}$$

and P_{2m} refer to unnormalized Legendre polynomials. Willemann (1984) assumes that the load is placed along the great circle of zero longitude ($\phi_L = 0$) and the initial rotation vector is assumed to be at the north pole (i.e., $\mathbf{e}_\Omega^* = (0, 0, 1)$), as shown in Figure 5.3A. Substituting the appropriate expressions for the Legendre polynomials yields

$$\begin{aligned}
I_{11}^{L,LD,FB} &= \frac{1}{3}m'' [Q'(3 \cos^2 \theta_L - 2) - 1] \\
I_{22}^{L,LD,FB} &= \frac{1}{3}m'' (Q' - 1) \\
I_{33}^{L,LD,FB} &= -\frac{1}{3}m'' [Q'(3 \cos^2 \theta_L - 1) - 2] \\
I_{13}^{L,LD,FB} &= -\frac{1}{2}m'' Q' \sin(2\theta_L) \\
I_{12}^{L,LD,FB} &= I_{23}^{L,LD,FB} = 0.
\end{aligned} \tag{5.16}$$

The last equation can be written as

$$I_{ij}^{L,LD,FB} = m'' Q' \left(\frac{1}{3} \delta_{ij} - e_{L,i} e_{L,j} \right) + m'' \left(e_{\Omega,i}^* e_{\Omega,j}^* - \frac{1}{3} \delta_{ij} \right), \tag{5.17}$$

where $\mathbf{e}_L = (\sin \theta_L, 0, \cos \theta_L)$ and $\mathbf{e}_\Omega^* = (0, 0, 1)$ following Willemann (1984)'s assumptions.

There are two notable differences between my equation (5.11) and equation (5.14). First, the parameters m' and m'' differ by a factor of 3/2. This factor arises because of an error in Willemann (1984)'s expressions for the degree two, order zero potential perturbations associated with both the mass loading and the remnant of the rotational flattening. Since the error is the same for all components of the inertia tensor, it has no effect on the determination of the principle axes and, thus, the orientation of the rotation axis.

A second, more important difference is manifest both in the absence of the term α in equation (5.14) and in a second difference between the parameters m' and m'' . In regard to the latter, m' includes the factor $k_f^{T*} - k_f^T$, while m'' has $(1 - c)$. These differences are a consequence of Willemann (1984)'s assumption that at degree two the planetary response to a surface mass load is identical to the response to a potential forcing. While Willemann (1984) did not adopt a Love number terminology for the load response, his value of c is identical to $-k_f^L$, and thus the term $(1 - c)$ in equation (5.15) can be replaced by $(1 + k_f^L)$. His assumption that the response to a mass load and potential forcing are equivalent is, in Love number terminology, the same as assuming that $k_f^T = -k_f^L$ (and therefore that $k_f^{T*} = -k_f^{L*}$). If one notes that k_f^{L*} is equal to -1 because a load on a planet with no elastic lithosphere will ultimately be perfectly compensated, then Willemann (1984)'s assumption applied to equation (5.11) leads to $\alpha = 1$ and $k_f^{T*} - k_f^T = 1 + k_f^L$. That is, equation (5.14) is obtained.

The error within the term m'' introduced by this assumption is of no consequence since it impacts all the inertia components by the same factor. However, the error introduced by assuming that $\alpha = 1$ will impact the calculated orientation of the rotation pole. This error will, moreover, be dependent on the planetary model, specifically, the density structure and the thickness and rigidity of the elastic lithosphere. Willemann (1984) concluded that the reorientation of the planetary rotation axis in response to a surface mass load is independent of the lithospheric thickness (LT). This is incorrect. The corrected theory (5.11), and in particular the appearance of the term α , introduces a dependence on LT, and, more generally, on the detailed internal structure of the planet (since the fluid Love numbers depend on both).

5.3 Results

The long-term orientation of the rotation vector is governed by the principal axis associated with the largest moment of the non-hydrostatic inertia tensor. In this section, I use the expressions for the tensor derived above to evaluate TPW driven by surface mass loading under a variety of illustrative cases.

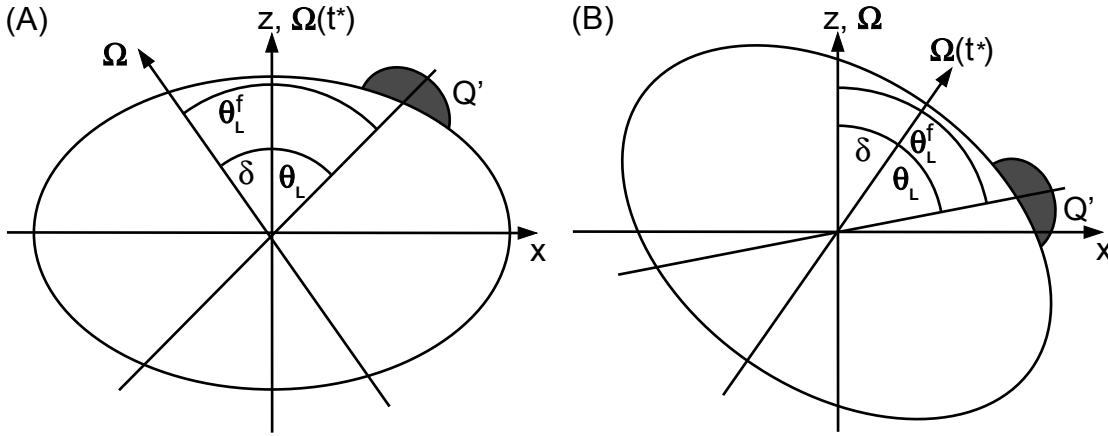


Figure 5.3 Rotation vector and load (gray semi-circle) location for (A) a reference frame with the initial rotation vector $\Omega(t^*)$ at the north pole and (B) the final rotation vector Ω at the north pole. The white ellipse represents the remnant rotational bulge, which is aligned with the initial rotation vector Ω^* . We denote the angles between the final rotation vector and the initial rotation vector, and between the final rotation vector and the centre of the load, as δ and $\theta_L^f = \delta + \theta_L$ respectively.

5.3.1 Axisymmetric loads

We start with the special case treated by [Gold \(1955\)](#) and [Goldreich & Toomre \(1969\)](#): a ‘quasi-rigid’ planetary model in which the surface load (beetle) is not entirely compensated by deformation, while the rotational bulge is able to fully relax to any reorientation of the pole (and thus provides no long term resistance to TPW).

By symmetry, the initial and final rotation vectors and the load centre must be along the same great circle. Without loss of generality, one can choose a reference system in which this great circle corresponds to the great circle of zero longitude ($\phi_R^* = \phi_R = \phi_L = 0$) as shown in [Figure 5.3B](#). Furthermore, for the purposes of the following discussion, it proves convenient to assume that the reference frame is oriented such that the z -axis is fixed to the final rotation vector (see [Figure 5.3B](#)).

Adopting the simplified expressions appropriate for an axisymmetric disk load emplaced on the great circle $\phi_L = 0$, given by [equation 5.11](#) with $\mathbf{e}_L = (\sin \theta_L^f, 0, \cos \theta_L^f)$, and ignoring the terms associated with the rotational fossil bulge, then the non-hydrostatic inertia tensor for this special ‘quasi-rigid’ case is given by:

$$\begin{aligned}
I_{11}^{L,LD} &= \frac{1}{3}m'\alpha Q' \left(3 \cos^2 \theta_L^f - 2\right) \\
I_{22}^{L,LD} &= \frac{1}{3}m'\alpha Q' \\
I_{33}^{L,LD} &= -\frac{1}{3}m'\alpha Q' \left(3 \cos^2 \theta_L^f - 1\right) \\
I_{13}^{L,LD} &= -\frac{1}{2}m'\alpha Q' \sin(2\theta_L^f) \\
I_{12}^{L,LD} &= I_{23}^{L,LD} = 0,
\end{aligned} \tag{5.18}$$

where δ denotes the TPW angle (i.e., the angle between the initial and final rotation axis, where TPW away from the load is taken as positive) and $\theta_L^f = \delta + \theta_L$ (see Figure 5.3B). Since the final rotation axis coincides with the principal axis associated with the largest moment of inertia and I adopt a reference frame where the z-axis coincides with the rotation axis, the inertia tensor must be diagonal, and thus $I_{13}^{L,LD}$ must be zero. This condition yields

$$\delta = \begin{cases} \frac{\pi}{2} - \theta_L, & \text{if } Q' > 0; \\ -\theta_L, & \text{otherwise.} \end{cases} \tag{5.19}$$

Note that this condition ensures that $I_{33}^{L,LD}$ is the principal moment associated with the largest moment of inertia as required. The final colatitude of the load, which will be denoted by θ_L^f , is given by $\delta + \theta_L$ (see Figure 5.3B). Thus, a mass excess ($Q' > 0$) will drive a TPW that brings the load onto the equator (regardless of the size of Q') relative to the final pole location (i.e., $\theta_L^f = \delta + \theta_L = \pi/2$). Physically, the uncompensated surface mass load will move to the equator without any long term resistance (in this special, ‘quasi-rigid’ case) from a remnant rotational bulge. This is, of course, a classic result in rotational dynamics (Gold, 1955; Figure 5.1A-C) and it leads to a second equally seminal result (Goldreich & Toomre, 1969), namely that a set of mass loads moving randomly on the surface can drive large changes in the orientation of the pole with a time scale that may be fast relative to the motion of the surface masses (Chapter 3). Indeed, the time scale is governed by the decay time of the normal modes of viscous relaxation (i.e., the s_k^ℓ in equations 4.39 and 4.61). For completeness, note that TPW driven by a surface mass deficit (i.e., $Q' < 0$) on a ‘quasi-rigid’ planet will act to bring the load onto the pole (case two in equation 5.19; $\theta_L^f = 0$).

Next, I move to the more general case where the presence of an elastic lithospheric shell leads, in addition to an imperfect compensation of the surface mass load, to the incomplete relaxation of the rotational bulge. This was the problem addressed by Willemann (1984). Equation (5.11) provides expressions for the non-hydrostatic inertia elements in this case. I adopt the reference

frame used in the previous discussion (see Figure 5.3B). In this case, equation (5.11) yields

$$\begin{aligned}
I_{11}^{L,LD,FB} &= \frac{1}{3}m' \left[Q'\alpha \left(3 \cos^2 \theta_L^f - 2 \right) - 3 \cos^2 \delta + 2 \right] \\
I_{22}^{L,LD,FB} &= \frac{1}{3}m' (Q'\alpha - 1) \\
I_{33}^{L,LD,FB} &= -\frac{1}{3}m' \left[Q'\alpha \left(3 \cos^2 \theta_L^f - 1 \right) - 3 \cos^2 \delta + 1 \right] \\
I_{13}^{L,LD,FB} &= \frac{1}{2}m' \left[-Q'\alpha \sin(2\theta_L^f) + \sin(2\delta) \right] \\
I_{12}^{L,LD,FB} &= I_{23}^{L,LD,FB} = 0.
\end{aligned} \tag{5.20}$$

This inertia tensor must be diagonal since a reference frame in which the z-axis coincides with the principal axis associated with the largest moment of inertia is adopted, and thus, $I_{13}^{L,LD,FB} = 0$.

This condition gives

$$\delta = \frac{1}{2} \arcsin \left[Q'\alpha \sin(2\theta_L^f) \right] \tag{5.21}$$

or, in terms of the initial load colatitude,

$$\delta = \frac{1}{2} \arctan \left[\frac{Q'\alpha \sin(2\theta_L)}{1 - Q'\alpha \cos(2\theta_L)} \right]. \tag{5.22}$$

As would be expected from the discussion in the last section, equation (5.21) is identical to Willemann (1984)'s result (see his equation 28) with the exception that my $Q'\alpha$ replaces Q' . I will emphasize this mapping by defining $Q_{eff} \equiv Q'\alpha$.

The final location of the pole in this general case is governed by a balance (see Figure 5.1D-F) between the load-induced TPW highlighted above (which acts to move a mass excess to the equator and a mass deficit to the pole) and the stabilizing effect of the remnant rotational flattening (which acts to resist any reorientation of the pole away from its initial location). Under Willemann (1984)'s assumption that the load and rotational forcing are subject to the same level of compensation ($\alpha = 1$), the level of TPW which achieves this balance is independent of the lithospheric thickness. The appearance of α in equation (5.21) (and 5.11) alters the TPW with which this balance is achieved; since α is a function of the thickness and rigidity of the lithospheric as well as the planetary density structure, so too will be the predicted TPW.

Figure 5.4 plots various families of solutions to equation (5.21) as a function of the TPW angle δ , Q_{eff} , the initial load co-latitude (θ_L) and the final load colatitude (θ_L^f). Figure 5.4A (solid lines), for example, shows calculations of δ versus the initial colatitude of the surface mass load for a suite of different values of Q_{eff} (since $Q_{eff} > 0$, a mass excess is assumed in all cases). The dashed lines in this frame join solutions with the same final load colatitude. In contrast, Figure 5.4B shows δ as a function of final load colatitude for the same suite of Q_{eff} values; note, in this case, that results for $Q_{eff} = x$ and $1/x$ are symmetrical around the $Q_{eff} = 1$ solution. Finally, Figure 5.4C plots Q_{eff} versus θ_L^f for a suite of different initial load locations (see caption). This plot makes it simple

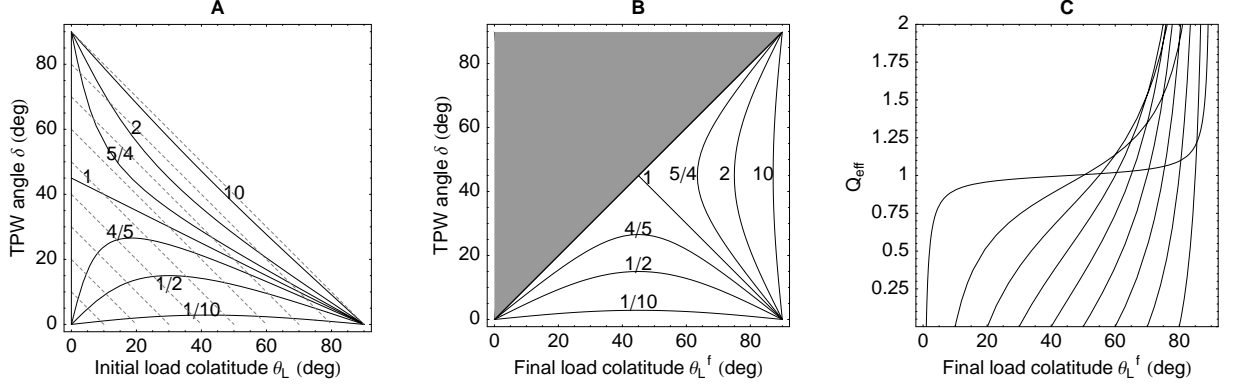


Figure 5.4 TPW solutions based on equations (5.21) and (5.22). (A) Solid lines - TPW angle, δ , versus initial colatitude of the surface mass load, θ_L , for a *suite* of different values of the effective load size, Q_{eff} (as labeled). Dashed lines join $(\delta, \theta_L, Q_{eff})$ solutions with a common final load colatitude, θ_L^f . These lines begin at $\theta_L^f = 10^\circ$ at bottom left and increase in increments of 10° (up to $\theta_L^f = 90^\circ$). (B) TPW angle, δ , versus final load location, θ_L^f , for the same set of Q_{eff} values shown in frame A. The shaded region at top left masks (physically impossible) solutions in which the TPW angle is greater than the final load location. (C) Relationship between Q_{eff} and the final load colatitude, θ_L^f , for different values of the initial load location, θ_L . The value of the latter for each of the lines on the figure can be inferred from the $Q_{eff} = 0$ intercept (i.e., when $Q_{eff} = 0$ the pole does not reorient and therefore the initial and final load locations are the same).

to assess how high Q_{eff} must be to attain a final load location for a specific starting location.

When $Q_{eff} = 1$, the TPW angle δ is identical to the angle from the final equator to the load (i.e., the final latitude of the load); that is, reorientation of the pole is equal to the residual distance between the load and the equator. Mathematically, $\delta = \pi/2 - \theta_L^f$, which is clear from the $Q_{eff} = 1$ solution on Figure 5.4B. As $Q_{eff} \rightarrow \infty$, the uncompensated load dominates any remnant rotational bulge and the final load location approaches the equator. Conversely, when $Q_{eff} \rightarrow 0$, the remnant rotational bulge dominates and the pole is negligibly perturbed by the surface loading. (Both limits are evident on each of the frames on the Figure.)

The results for $Q_{eff} = 1$ and $\theta_L = 0$ are worthy of further comment. In this case alone, the degree two component of the compensated load ‘cancels’ the remnant rotational bulge and all inertia perturbations in equation (5.20) will be zero (note that when $\theta_L = 0$, $\theta_L^f = \delta$). Thus, the polar motion will be undefined since there is no principal axis orientation, and this is reflected in my vertical solid line at $\theta_L = 0$ in Figure 5.4A. Since the orientation of the remnant bulge is governed by the initial rotation axis, this cancellation is only possible when $\theta_L = 0$.

This special case provides one explanation for the clustering of the $Q_{eff} > 1$ and, separately, the $Q_{eff} < 1$ solutions when $\theta_L \sim 0$ in Figure 5.4A. In particular, consider a value of $Q_{eff} = 1 + \epsilon$. The first term on the RHS of this expression may be interpreted as that portion of Q_{eff} which will cancel the inertia perturbation associated with the remnant rotational effect (when $\theta_L = 0$). Thus,

the sign of ϵ will govern the final position of the pole: If $\epsilon > 0$, there will be a mass excess at the pole (relative to the remnant rotational bulge) and, regardless of the magnitude of this excess (that is, the size of ϵ), the load will ultimately move to the equator (i.e., all $Q_{eff} > 1$ solutions cluster at $\delta = 90^\circ$ when $\theta_L \sim 0$); alternatively, if $\epsilon < 0$, there will be a mass deficit at the pole and the load will stay at the pole (i.e., all $Q_{eff} < 1$ solutions cluster at $\delta = 0^\circ$ when $\theta_L \sim 0$).

In the parlance of rotation theory, the 90° shift in the rotation pole when $Q_{eff} > 1$ and $\theta_L = 0$ is a so-called inertial interchange true polar wander (IITPW) event (Goldreich & Toomre, 1969). Such instabilities occur when the (diagonalized) maximum and intermediate non-hydrostatic inertia elements are exchanged by any process. In our case, $\phi_L = 0$ and $I_{22} > I_{11}$, and thus the IITPW condition becomes $I_{22} \geq I_{33}$. Using equation (5.20), this condition may be written as: $Q_{eff} \cos^2 \theta_L^f \geq \cos^2 \delta$. However, for $\theta_L = 0$, $\theta_L^f = \delta$, and therefore the IITPW condition is simply $Q_{eff} \geq 1$, as discussed above.

In the absence of a remnant rotational bulge a beetle of arbitrary size will move to the equator (Gold, 1955; Chapter 3; and equation 5.19). For a planet with a lithosphere, this level of rotational instability will occur in two special cases: (1) when $Q_{eff} \gg 1$, and thus the size of the load is sufficiently large that the remnant bulge becomes inconsequential; and (2) when the (axisymmetric) load is placed near the initial rotation pole ($\theta_L = 0$) and it has a (degree two) amplitude in excess of the bulge signal ($Q_{eff} > 1$).

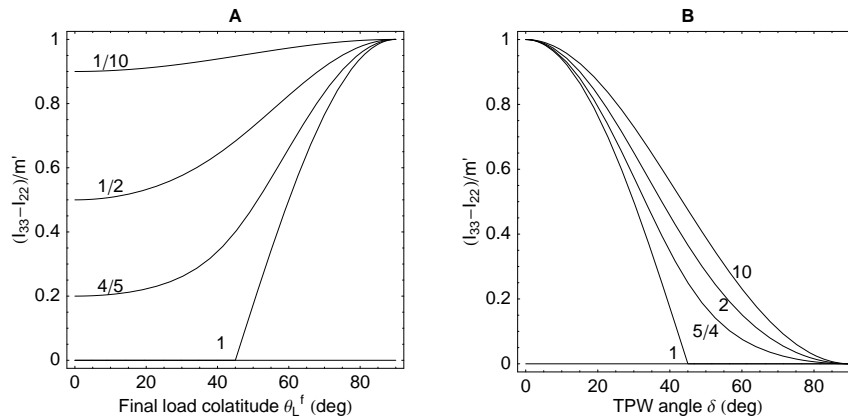


Figure 5.5 Difference between the two largest dimensionless principal moments $(I_{33} - I_{22})/m'$ for a suite of different values of the effective load size, Q_{eff} (as labeled), as a function of the final load colatitude, θ_L^f , for $Q_{eff} \leq 1$ (A), and as a function of the TPW angle, δ , for $Q_{eff} \geq 1$ (B),

The above discussion of rotational stability may also be summarized, quantitatively, by considering the variation in the individual principal moments of inertia as a function of parameters governing load location. Figure 5.5 shows the difference $(I_{33} - I_{22})/m'$ as a function of final load colatitude θ_L^f for $Q_{eff} \leq 1$ and as a function of TPW angle δ for $Q_{eff} \geq 1$. (The change in the abscissa for Q_{eff} less than or greater to one reflects the nature of the results in Figure 5.4B; for each

$Q_{eff} \leq 1$ there are two solutions for a given δ , while for each $Q_{eff} \geq 1$ there are two solutions for a given θ_L^f .) The figure demonstrates that for $Q_{eff} < 1$, the maximum and intermediate moments do not cross, and that the difference $I_{33} - I_{22}$ grows (i.e., the rotational stability increases) as Q_{eff} is reduced. In contrast, for $Q_{eff} \geq 1$, these principal moments do cross as δ approaches 90° , reflecting the conditions for an ITPW event.

Table 5.1 Parameters (radius, density, and rigidity) for the 5-layer Mars model of [Bills & James \(1999\)](#).

Layer	Name	R (km)	ρ (kg m ⁻³)	μ (GPa)
1	Crust	3390.1	2800	45
2	Upper mantle	3293.5	3550	80
3	Middle mantle	2360.0	4050	120
4	Lower mantle	2030.0	4200	155
5	Core	1469.9	7200	0

Table 5.2 Effects of lithospheric thickness (LT) upon the Mars model parameters. We adopt the 5-layer model of Martian structure described by [Bills & James \(1999\)](#). The tidal fluid Love number for LT=0 is $k_f^{T*} = 1.1867$.

LT(km)	k_f^L	k_f^T	$\alpha = \frac{1+k_f^L}{1-k_f^T/k_f^{T*}}$	$\beta = \frac{1}{1-k_f^T/k_f^{T*}}$
50	-0.91643	1.1087	1.2708	15.206
100	-0.85285	1.0373	1.1686	7.9418
200	-0.69063	0.84749	1.0822	3.4982
300	-0.57531	0.71240	1.0625	2.5019
400	-0.48769	0.60973	1.0537	2.0567

The family of solid lines in Figure 5.4A are identical to [Willemann \(1984\)](#)'s curves showing δ versus Q' (rather than Q_{eff}) and the question arises as to how much Q' and Q_{eff} may differ (or, alternatively, to what extent the Love number factor α may diverge from 1). To explore this issue I consider, as an illustrative example, the case of Mars. Fluid load and tidal Love numbers have been computed for the simple 5-layer model of Martian structure described by ([Bills & James, 1999](#); Table 5.1). These values, together with the factor α (equation 5.13) are provided on Table 5.2 for a sequence of elastic LT ranging from 50 km to 400 km. Note that α diverges monotonically from 1 for progressively lower values of lithospheric thickness, reaching a value of 1.27 for the case LT = 50 km.

Ultimately, applying the rotational stability theory described here to a specific loading event requires some estimate of the Q' associated with the loading; that is, following equation (5.10), an estimate of the size of the uncompensated load relative to the rotational bulge of the planet. However, the TPW angle is governed by the parameter Q_{eff} (equation 5.21). In the case of the

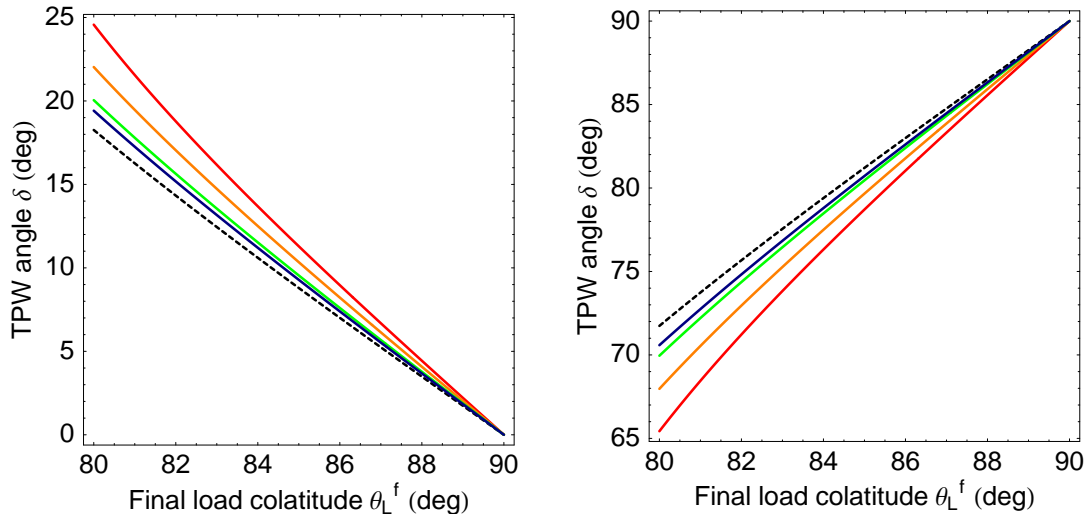


Figure 5.6 TPW angle, δ , versus the final load colatitude, θ_L^f , for the specific load size $Q' = 1.74$. The figure only shows the range $80^\circ < \theta_L^f < 90^\circ$. In this case, two solutions are evident with TPW angles near 20° (left) and 70° (right). On each frame, the lines refer to solutions with lithospheric thickness (LT) of 50 km (red), 100 km (orange), 200 km (green), and 400 km (blue); the value of α for each of these models is given in Table 1. Also shown (dashed line) is the solution based on [Willemann \(1984\)](#)'s theory (which is independent of LT).

model of Mars used to generate Table 5.2, [Willemann \(1984\)](#)'s theory underestimates Q_{eff} by (for example) 27% for the case $LT=50$ km, and 17% for $LT=100$ km. To explore the impact of this discrepancy on the predicted TPW, consider Figure 5.6. The figure shows the computed TPW angle versus the final load location (as in Figure 5.4B) for the case of $Q' = 1.74$ and α values appropriate to the cases of $LT = 50$ km, 100 km, 200 and 400 km in Table 5.2. Also shown in the figure (dashed line) is the (LT-independent) solution associated with [Willemann \(1984\)](#)'s theory ($Q' = 1.74$ and $\alpha = 1$). I adopt the value of $Q' = 1.74$ because it is the upper bound value inferred by [Willemann \(1984\)](#) for the loading of Mars by the Tharsis volcanic province; in this regard, the figure is limited to θ_L^f values ($80 - 90^\circ$) that span estimates for the central colatitude of Tharsis.

Figure 5.6 raises a number of interesting issues. First, [Willemann \(1984\)](#) is often cited to argue that Tharsis could not have driven a significant TPW event on Mars (e.g., [Grimm & Solomon 1986](#); [Banerdt et al. 1992](#); [Ward 1992](#); [Zuber & Smith 1997](#); [Arkani-Hamed 2005](#)). Indeed, [Willemann \(1984\)](#) concluded that the reorientation was ‘certainly less than 18° ’. However, on the basis of [Willemann \(1984\)](#)'s theory, a present location of Tharsis at $80 - 90^\circ$ colatitude is consistent with a TPW event of either $\delta < 18^\circ$ or $\delta > 72^\circ$. (These two solutions are also evident within the $80^\circ < \theta_L^f < 90^\circ$ portion of Figure 5.4B; the physics associated with the latter, large TPW event was described in detail above.) [Willemann \(1984\)](#) dismissed the latter range because it implies an initial load location within 8° of the rotation pole (since the $\delta = 72^\circ$ TPW solution yields a final load location at 80°); he considered this to be unlikely relative to a $\delta < 18^\circ$ solution that implies

an initial load location greater than 62° from the pole. This argument (which appears to discount, a priori, any large TPW event) is completely independent of the physics governing the rotational stability (Figures 5.4B, 5.6).

As expected from Table 5.2, predictions based on my new theory (equation 5.21) converge to Willemann (1984)'s solution for the thick lithosphere cases (LT=300 or 400 km). In contrast, the LT=50 km predictions are significantly different from this solution. In this case, one would conclude that a final Tharsis location between $80 - 90^\circ$ is consistent with a reorientation of the rotation pole of either $\delta < 25^\circ$ or $\delta > 65^\circ$. The latter implies an initial load location within 15° of the pole.

Table 5.2 suggests that the divergence between my results and those derived from Willemann (1984)'s theory will continue as the lithosphere is further thinned and thus that there will be a marked trend toward greater rotational instability for planets with progressively thinner elastic shells. It is difficult to explore this trend because the accuracy of numerical predictions for α becomes problematic when considering very thin shells (since both the numerator and denominator of equation 5.13 approach zero in this case).

Applying the rotational stability theory to the loading of Mars by Tharsis raises an important issue; namely, the LT used in the theory refers to the thickness of the lithosphere at the time of Tharsis development. This thickness may have little relation to the present day thickness of the outer elastic shell of the planet, particularly given the ancient nature of Tharsis (~ 4 Ga). As discussed at the end of §5.2.2, the remnant rotational flattening active at the time of Tharsis loading should actually reflect, in an integral sense, changes in both the pole position and lithospheric thickness across a time interval from the formation of the hydrostatic planet to the onset of Tharsis loading; the TPW calculations above (and those appearing in Willemann, 1984) assume that the lithospheric thickness at the time of Tharsis loading developed during a period of little TPW and thus the remnant bulge is aligned with the unique orientation of the pole during this period.

5.3.2 Bills and James (1999)

In application to Mars, Bills & James (1999) also considered the rotational stability of the planet in response to surface mass loading. Their equation, governing the secular rotational stability, was stated as (see their equation 49):

$$J_2^L \geq 2J_{22}^L \quad (5.23)$$

where J_2^L and J_{22}^L represent the degree two zonal and non-zonal component of the potential perturbation associated with the surface mass load. These harmonics are renormalized versions of the coefficients appearing in equation (4.34). This stability criterion is identical to

$$I_{33}^L + I_{33}^{LD} \geq I_{22}^L + I_{22}^{LD} \quad (5.24)$$

where each side of this equation represents a principal axis. That is, [Bills & James \(1999\)](#) assume that the pole location is governed by the diagonalization of a non-hydrostatic inertia tensor whose sole contribution arises from surface mass loading. The stabilization of the pole due to a remnant rotational bulge is ignored. As discussed above (see also [Willemann, 1984](#)) this oversight will introduce significant errors in the stability analysis.

[Bills & James \(1999\)](#) were, in particular, interested in the impact on the rotational state of departures from load axial symmetry. This issue is the subject of the next section.

5.3.3 Non-axisymmetric loads

Thus far only simple, axisymmetric disk loads have been considered. To end this section I explore the potential impact on the rotational stability of any departures from axisymmetry. Specifically, TPW driven by the spherical harmonic degree two components of a set of disks will be considered. The total load is comprised of two parts. The first, axisymmetric central dome has an uncompensated load size of Q'_1 . The second, smaller disk has an uncompensated load size of Q'_2 . For simplicity, and without loss of generality, I choose a reference frame in which the z-axis coincides with the final rotation axis, as shown in [Figure 5.7](#). Furthermore, I adopt a reference frame in which the initial rotation axis orientation is on the great circle of zero longitude (i.e., $\phi_R^* = 0$, see [Figure 5.7](#)). In this case, if one denotes the TPW angle as δ , the unit vector representing the initial rotation axis orientation becomes

$$\mathbf{e}_\Omega^* = (\sin \delta, 0, \cos \delta). \quad (5.25)$$

The unit vectors representing the load symmetry axis are

$$\mathbf{e}_L^1 = (\sin \theta_1^f \cos \phi_1^f, \sin \theta_1^f \sin \phi_1^f, \cos \theta_1^f) \quad (5.26)$$

and

$$\mathbf{e}_L^2 = (\sin \theta_2^f \cos \phi_2^f, \sin \theta_2^f \sin \phi_2^f, \cos \theta_2^f) \quad (5.27)$$

for the primary and secondary loads respectively, as shown in [Figure 5.7](#).

We use equations [\(5.11\)](#) to write the total non-hydrostatic inertia tensor perturbations as

$$I_{ij}^{L,LD,FB} = m'Q'_1\alpha \left(\frac{1}{3}\delta_{ij} - e_{L,i}^1 e_{L,j}^1 \right) + m'Q'_2\alpha \left(\frac{1}{3}\delta_{ij} - e_{L,i}^2 e_{L,j}^2 \right) + m' \left(e_{\Omega,i}^* e_{\Omega,j}^* - \frac{1}{3}\delta_{ij} \right). \quad (5.28)$$

Replacing equations [\(5.25\)](#) by [\(5.27\)](#) in the last equation yields

$$\begin{aligned}
I_{11}^{L,LD,FB} &= \frac{1}{6}m'\alpha Q'_1 \left[3 \cos^2 \theta_1^f - 1 - 3 \sin^2 \theta_1^f \cos(2\phi_1^f) \right] \\
&\quad + \frac{1}{6}m'\alpha Q'_2 \left[3 \cos^2 \theta_2^f - 1 - 3 \sin^2 \theta_2^f \cos(2\phi_2^f) \right] + \frac{1}{3}m'(-3 \cos^2 \delta + 2) \\
I_{22}^{L,LD,FB} &= \frac{1}{6}m'\alpha Q'_1 \left[3 \cos^2 \theta_1^f - 1 + 3 \sin^2 \theta_1^f \cos(2\phi_1^f) \right] \\
&\quad + \frac{1}{6}m'\alpha Q'_2 \left[3 \cos^2 \theta_2^f - 1 + 3 \sin^2 \theta_2^f \cos(2\phi_2^f) \right] - \frac{1}{3}m' \\
I_{33}^{L,LD,FB} &= -\frac{1}{3}m'\alpha Q'_1(3 \cos^2 \theta_1^f - 1) - \frac{1}{3}m'\alpha Q'_2(3 \cos^2 \theta_2^f - 1) + \frac{1}{3}m'(3 \cos^2 \delta - 1) \\
I_{12}^{L,LD,FB} &= -\frac{m'}{2}\alpha Q'_1 \sin^2 \theta_1^f \sin(2\phi_1^f) - \frac{m'}{2}\alpha Q'_2 \sin^2 \theta_2^f \sin(2\phi_2^f) \\
I_{13}^{L,LD,FB} &= -\frac{m'}{2}\alpha Q'_1 \sin(2\theta_1^f) \cos \phi_1^f - \frac{m'}{2}\alpha Q'_2 \sin(2\theta_2^f) \cos \phi_2^f + \frac{m'}{2} \sin(2\delta) \\
I_{23}^{L,LD,FB} &= -\frac{m'}{2}\alpha Q'_1 \sin(2\theta_1^f) \sin \phi_1^f - \frac{m'}{2}\alpha Q'_2 \sin(2\theta_2^f) \sin \phi_2^f. \tag{5.29}
\end{aligned}$$

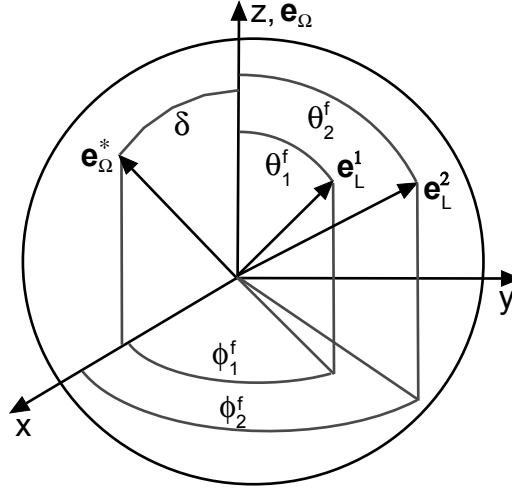


Figure 5.7 Unit vectors and spherical coordinates used to calculate the non-hydrostatic inertia tensor associated with a non-axisymmetric surface mass load and a remnant rotational bulge. The total surface load is composed of an axisymmetric load of degree two size Q'_1 with symmetry centre at $(\theta_L, \phi_L) = (\theta_1^f, \phi_1^f)$; and a secondary load of effective size Q'_2 with symmetry centre at $(\theta_L, \phi_L) = (\theta_2^f, \phi_2^f)$. The orientation of the load symmetry axis is given by the unit vectors $\mathbf{e}_L^1 = (\sin \theta_1^f \cos \phi_1^f, \sin \theta_1^f \sin \phi_1^f, \cos \theta_1^f)$ and $\mathbf{e}_L^2 = (\sin \theta_2^f \cos \phi_2^f, \sin \theta_2^f \sin \phi_2^f, \cos \theta_2^f)$ for the primary and secondary load respectively. The initial rotation axis orientation is given by the unit vector $\mathbf{e}_\Omega^* = (\sin \delta, 0, \cos \delta)$. The final rotation axis is aligned with the z -axis, and thus $\mathbf{e}_\Omega = (0, 0, 1)$.

The reference frame choice allows one to constrain the inertia tensor to be diagonal, and thus

$I_{12}^{L,LD,FB} = I_{13}^{L,LD,FB} = I_{23}^{L,LD,FB} = 0$. This condition gives

$$\begin{aligned} Q'_1 \sin^2 \theta_1^f \sin(2\phi_1^f) + Q'_2 \sin^2 \theta_2^f \sin(2\phi_2^f) &= 0 \\ -\alpha Q'_1 \sin(2\theta_1^f) \cos \phi_1^f - \alpha Q'_2 \sin(2\theta_2^f) \cos \phi_2^f + \sin(2\delta) &= 0 \\ Q'_1 \sin(2\theta_1^f) \sin \phi_1^f + Q'_2 \sin(2\theta_2^f) \sin \phi_2^f &= 0. \end{aligned} \quad (5.30)$$

One can write the condition for IITPW events by setting $I_{22}^{L,LD,FB} = I_{33}^{L,LD,FB}$, which gives

$$\begin{aligned} 2 \cos^2 \delta &= \alpha Q'_1 \left[3 \cos^2 \theta_1^f - 1 + \sin^2 \theta_1^f \cos(2\phi_1^f) \right] \\ &\quad + \alpha Q'_2 \left[3 \cos^2 \theta_2^f - 1 + \sin^2 \theta_2^f \cos(2\phi_2^f) \right] \end{aligned} \quad (5.31)$$

or by setting $I_{11}^{L,LD,FB} = I_{33}^{L,LD,FB}$, which gives

$$\begin{aligned} 4 \cos^2 \delta - 2 &= \alpha Q'_1 \left[3 \cos^2 \theta_1^f - 1 - \sin^2 \theta_1^f \cos(2\phi_1^f) \right] \\ &\quad + \alpha Q'_2 \left[3 \cos^2 \theta_2^f - 1 - \sin^2 \theta_2^f \cos(2\phi_2^f) \right]. \end{aligned} \quad (5.32)$$

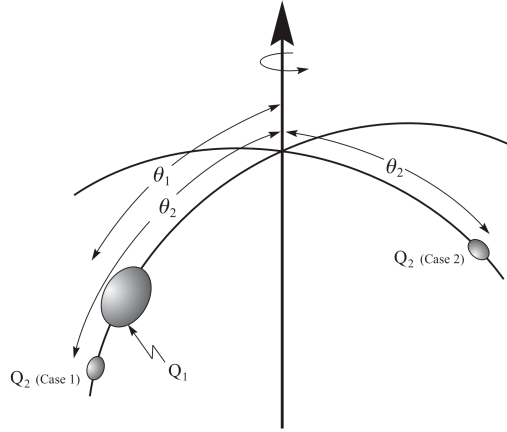


Figure 5.8 Schematic illustration of the initial orientation of the non-axisymmetric surface mass load discussed within the text. In particular, the central, axisymmetric load of size Q_1 and initial colatitude θ_1 (as in Figures 5.4, 5.5) is augmented to include a smaller second disk of size Q_2 . The latter is positioned either on the great circle joining the central disk to the initial pole (Case 1) or 90° from this great circle (Case 2).

We considered two specific scenarios for the non-axisymmetric surface loads as shown in Figure 5.8. The secondary load (with size Q'_2) is positioned either on the great circle joining the central disk to the initial the rotation vector $\Omega(t^*)$ (Case 1) or 90° from this great circle (Case 2). For the purposes of the following discussion, I describe the load sizes in terms of their effective load sizes, which are denoted as $Q_1 = \alpha Q'_1$ and $Q_2 = \alpha Q'_2$.

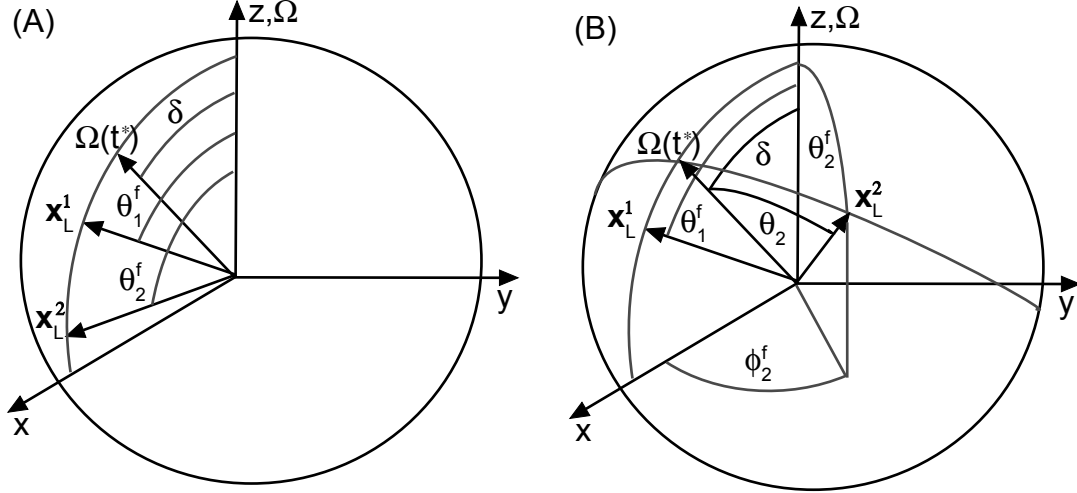


Figure 5.9 Schematic illustration of the two cases considered in Figure 5.8 for a reference frame with the final rotation axis along the z-axis. (A) Case 1 scenario. (B) Case 2 scenario.

It is possible to obtain analytical TPW solutions for the case 1 scenario. In this case, all the initial and final load longitudes are zero ($\phi_1 = \phi_1^f = \phi_2 = \phi_2^f = 0$), and the final and initial load colatitudes are related by $\theta_1^f = \theta_1 + \delta$ and $\theta_2^f = \theta_2 + \delta$ (see Figure 5.9A). The diagonalization constraint (5.30) becomes

$$Q_1 \sin[2(\theta_1 + \delta)] + Q_2 \sin[2(\theta_2 + \delta)] = \sin(2\delta). \quad (5.33)$$

Similarly, the IITPW conditions (5.31,5.32) for the case 1 scenario become

$$Q_1 \cos^2(\theta_1 + \delta) + Q_2 \cos^2(\theta_2 + \delta) = \cos^2 \delta. \quad (5.34)$$

for $I_{22}^{L,LD,FB} = I_{33}^{L,LD,FB}$; and

$$\alpha Q_1' [2 \cos^2(\theta_1 + \delta) - 1] + \alpha Q_2' [2 \cos^2(\theta_2 + \delta) - 1] = 2 \cos^2 \delta - 1, \quad (5.35)$$

for $I_{11}^{L,LD,FB} = I_{33}^{L,LD,FB}$. Note that equations (5.33-5.32) are only valid for the case 1 scenario.

For the case 2 scenario one can write $\phi_1 = \phi_1^f = 0$ and $\theta_1^f = \theta_1 + \delta$. In this case the diagonalization equation (5.30) can be written as

$$\begin{aligned} Q_2' \sin^2 \theta_2^f \sin(2\phi_2^f) &= 0 \\ -\alpha Q_1' \sin[2(\theta_1 + \delta)] - \alpha Q_2' \sin(2\theta_2^f) \cos \phi_2^f + \sin(2\delta) &= 0 \\ Q_2' \sin(2\theta_2^f) \sin \phi_2^f &= 0. \end{aligned} \quad (5.36)$$

Similarly, the IITPW equations (5.31,5.32) for the case 2 scenario become

$$\alpha Q'_1 [2 \cos^2 \theta_1 + \delta] + \alpha Q'_2 [3 \cos^2 \theta_2^f - 1 + \sin^2 \theta_2^f \cos(2\phi_2^f)] = 2 \cos^2 \delta \quad (5.37)$$

for $I_{22}^{L,LD,FB} = I_{33}^{L,LD,FB}$, and

$$\alpha Q'_1 [4 \cos^2 \theta_1 + \delta] - 2 + \alpha Q'_2 [3 \cos^2 \theta_2^f - 1 - \sin^2 \theta_2^f \cos(2\phi_2^f)] = 4 \cos^2 \delta - 2 \quad (5.38)$$

for $I_{11}^{L,LD,FB} = I_{33}^{L,LD,FB}$.

To this point I have been concerned with computing the TPW angle δ along the great circle of zero longitude. The natural question that arises is the following: How effective is the non-axisymmetric component of the surface load in driving TPW off this great circle? Since no real load (or set of loads) is perfectly axisymmetric, Tharsis being a notable example, this question has important relevance to any general consideration of rotational stability.

To consider this issue, I have performed a suite of numerical calculations in which I adopt a specific initial load location θ_1 close to the initial rotation axis and fix Q_2 to some small fraction of Q_1 . I then track the computed TPW while varying the central load amplitude Q_1 . These solutions map out a curve on the surface of the sphere. I have repeated the calculation for various placements of the secondary disk.

In these calculations, a reference frame with the initial rotation axis placed along the z-axis is adopted. In this case, the unit vector representing the initial rotation axis becomes $\mathbf{e}_\Omega^* = (0, 0, 1)$. Similarly, the unit vectors representing the load centre locations become $\mathbf{e}_L^1 = (\sin \theta_1, 0, \cos \theta_1)$ and $\mathbf{e}_L^2 = (\sin \theta_2, 0, \cos \theta_2)$ for the case 1 scenario; and $\mathbf{e}_L^1 = (\sin \theta_1, 0, \cos \theta_1)$ and $\mathbf{e}_L^2 = (0, \sin \theta_2, \cos \theta_2)$ for the case 2 scenario. Replacing these unit vectors in equation (5.28) and diagonalizing the resulting inertia tensor numerically (Press et al., 1992, chapter 11) gives the final rotation axis orientation.

In these tests, summarized in Figures 5.10 and 5.11, the TPW is driven by three contributions to the planetary inertia tensor, where each contribution has its preferred pole location: the fossil rotational bulge acts to move the pole toward the original pole location, while the two surface mass loads drive the pole toward great circles perpendicular to the respective load location vectors (these great circles are given by the solid red and blue lines in Figures 5.8 and 5.10). The equilibrium pole location is given by the balance of these three contributions.

As an example, the top row of Figure 5.10 shows calculations for the Case 1 orientation of the secondary load disk when $\theta_1 = 1^\circ$ and $\theta_2 = 11^\circ$ (or 10° further from the initial pole than the primary disk). As Q_1 is increased from zero to values just above 1, the TPW solutions move along the path followed by the black line. For values of $Q_1 > 1.1$ the pole is within a region bounded by

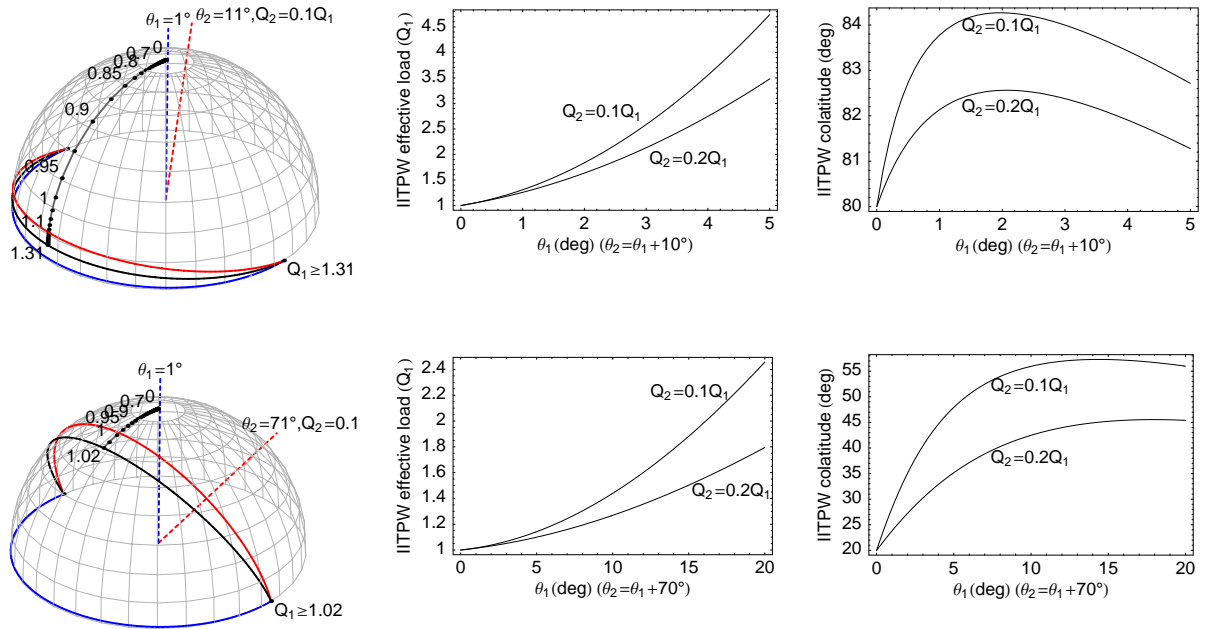


Figure 5.10 Predicted TPW for the non-axisymmetric load scenario shown by Case 1 in Figure 5.8 (i.e., the secondary load falls on the great circle connecting the initial pole location to the primary load). Top left - predicted TPW for a suite of predictions based on varying the effective size of the primary load, Q_1 (as labeled). In this case $\theta_1 = 1^\circ$, $\theta_2 = 11^\circ$ and $Q_2 = 0.1Q_1$. The blue and red great circle arcs are perpendicular to the axes of the primary and secondary loads, respectively. An IITPW event occurs for $Q_1 = 1.31$ and the rotation pole moves to the intersection of the blue and red great circles (i.e., 90° from both the primary and secondary loads; given the symmetry of the problem, the pole can move either clockwise or counterclockwise during this event, hence the two paths shown on the figure). Middle and right frames - the effective primary load, Q_1 , required to produce an IITPW event, as well as the colatitude of the pole when this event is initiated, as a function of the initial load colatitude, θ_1 . Each frame shows results for two scenarios: $Q_2 = 0.1Q_1$ and $Q_2 = 0.2Q_1$. Bottom Row - As in the top row, except for the case where the secondary load is displaced 70° from the primary load. In this case, the middle and right frames explore results for θ_1 values up to 20° .

the principal axes associated with the primary and secondary loads, respectively; in this situation, the primary load continues to push the pole toward the equator, while the secondary load (and remnant rotational bulge) resist this trend. At $Q_1 \sim 1.31$, the pole experiences a major instability defined by a 90° shift away from this great circle. This instability is an IITPW event. In this scenario, since $\theta_1 \neq 0$, the primary load is unable to perfectly cancel the non-hydrostatic remnant rotational bulge; however, the additional inertia tensor contribution from the secondary load makes such a cancellation possible. Note that for values of $Q_1 > 1.31$ the pole position is stable and located at the intersection of the equatorial great circles (red and blue lines) defined by the two loads. As discussed above, the ‘residual’ effective loads (that is, the effective loads after removal of the portion that cancels the remnant rotational bulge), no matter their size, will govern the location of the pole.

The simultaneous solution of equations (5.33) and (5.34) can be used to predict the effective load magnitude (Q_1) and the amount of TPW for which the IITPW event occurs. The remaining frames on the top row of Figure 5.10 show summary results for cases in which θ_1 is varied up to 5° and the secondary load is either 10% (as above) or 20% of the primary load. The 10° shift between load centres is retained. The middle frame shows the Q_1 value necessary for an IITPW event, and the right frame shows the colatitude at which the event will occur. The main point in these results is that as the primary load is moved away from the original pole, the size of the load required to initiate an IITPW event grows rapidly. Indeed, in the case of $\theta_1 = 5^\circ$, a value $Q_1 = 4.7$ is required to initiate an IITPW event.

Figure 5.10 corresponds to a second Case 1 scenario in which the displacement between the primary and secondary loads is increased to 70° . For $\theta_1 = 1^\circ$ and $Q_2 = 0.1Q_1$ (left frame), a Q_1 value above 0.97 will bring the rotation pole into a region within the great circles perpendicular to the two load axes. Furthermore, in the same case, a value of $Q_1 = 1.02$ initiates an IITPW event at a colatitude of $\sim 30^\circ$. As θ_1 is increased up to 20° (middle and right frames), the Q_1 value necessary for the onset of IITPW increases to just 2.4, while the colatitude at which the instability occurs increases to $\sim 55^\circ$. These values drop to 1.8 and 45° , respectively, when $Q_2 = 0.2Q_1$. Clearly, given some upper bound on the size of the primary load, a larger displacement between the primary and secondary loads yields a broader range of load locations that may yield an IITPW event.

Figure 5.11 corresponds to the Case 2 scenario of Figure 5.8, and show a sequence of results (for increasing Q_1) for $\theta_1 = 1^\circ$ and a displacement between loads of either 10° (left frame) or 70° (right frame). In this case, the secondary load acts to deflect the pole location off the great circle joining the initial pole and the primary load. The size of this deflection decreases as the displacement between the primary and secondary loads increases since the great circle perpendicular to the secondary load axis comes into closer alignment with the great circle joining the initial pole and primary load (compare the red great circles in frames A and B). As the size of the primary load (Q_1) is increased, the pole first moves off the latter great circle, but eventually returns toward this great

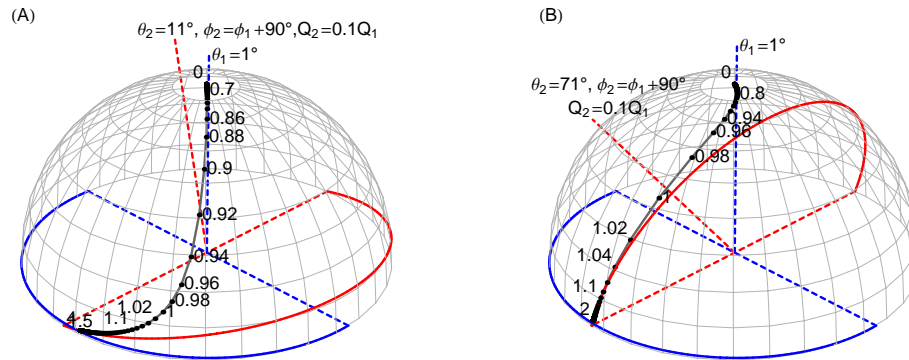


Figure 5.11 Predicted TPW for the non-axisymmetric load scenario shown by Case 2 in Figure 5.8 (i.e., the great circles connecting the initial pole location to the primary and secondary loads are perpendicular). In both frames $Q_2 = 0.1Q_1$ and $\theta_1 = 1^\circ$, and the black line joins results for a sequence of progressively larger values of Q_1 (as labeled). The frames are distinguished on the basis of the position of the secondary load: (A) $\theta_2 = 11^\circ$ or (B) $\theta_2 = 71^\circ$.

circle. The pole returns to this longitude since it is where the great circles that are perpendicular to the load axes intersect. For values of $Q_1 \sim 1.5$, the equilibrium pole position has reached close to the point of intersection between the two great circles that are perpendicular to the load axes. In any event, the Case 2 scenario does not produce an IITPW instability; that is, the positioning of the loads along perpendicular trajectories from the initial rotation pole (Figure 5.8) will not lead to a situation where the maximum and intermediate non-hydrostatic moments of inertia become equal.

These scenarios are highly simplified, but they provide insight into the connection between load asymmetry and rotational stability. The main result is that even very small levels of asymmetry can profoundly influence the rotational stability. For components of asymmetry aligned with the great circle joining the initial pole and the primary load, this impact includes the potential initiation of IITPW events.

5.4 The Impact of Internally-Supported Inertia Perturbations

In this section I augment the theory outlined above to include perturbations in the inertia tensor dynamically supported by internal, convective motions (Figure 5.1G-I). In the case of the Earth, the present-day value of these perturbations has been estimated by subtracting a prediction of the hydrostatic form of the geopotential (Nakiboglu, 1982) from satellite observations, and mapping the residual using some version of equation (4.38). In addition, the evolution of the convection-driven contribution to the non-hydrostatic inertia tensor over the last ~ 100 Ma has been modeled using viscous flow theory constrained by a suite of geological and/or geophysical data sets (e.g., the history of plate subduction, tomographic images of present-day seismic velocity heterogeneity;

e.g., Richards et al., 1997; Steinberger & O'Connell, 1997; Forte & Mitrova, 1997; Bunge et al., 1998, 2003). Of course, few, if any, constraints currently exist on the amplitude and/or orientation of internal convective motions on other planets. Accordingly, the mathematics outlined below is, by necessity, general.

Let us begin by assuming the total gravitational potential perturbation associated with internal convective flow (including the mass heterogeneity and its induced surface deformation) is known. I denote these harmonics by $\mathcal{G}_{\ell m}^{INT}(t)$ and the corresponding inertia tensor perturbations by I_{ij}^{INT} . Let us denote the degree two zonal component of the potential by $\mathcal{G}_{20}^{INT}(t)$. Then, equation (4.38) yields

$$I_{ij}^{INT} = \frac{\sqrt{5}a^3}{G} \mathcal{G}_{20}^{\prime,INT}(t) \left(\frac{1}{3} \delta_{ij} - e_{I,i} e_{I,j} \right), \quad (5.39)$$

where δ_{ij} is the Kronecker delta and $\mathbf{e}_I = (\sin \theta_I \cos \phi_I, \sin \theta_I \sin \phi_I, \cos \theta_I)$ is a unit vector indicating the orientation of the degree two convective flow symmetry axis. It is assumed in this expression that the degree zero perturbation potential is zero; nevertheless this component does not affect the principal axes orientation.

If the degree two gravitational potential signal is normalized relative to the potential perturbation associated with the hydrostatic rotational bulge

$$Q''(t) = - \frac{\mathcal{G}_{20}^{\prime,INT}(t)}{\frac{-1}{3\sqrt{5}} a^2 \Omega^2 k_f^{T*}}, \quad (5.40)$$

then equation (5.39) becomes

$$I_{ij}^{INT} = m' \beta Q''(t) \left(\frac{1}{3} \delta_{ij} - e_{I,i} e_{I,j} \right), \quad (5.41)$$

where

$$\beta \equiv \frac{1}{1 - k_f^T/k_f^{T*}}. \quad (5.42)$$

The total inertia tensor perturbation is

$$I_{ij}^{L,LD,FB,INT}(t) = I_{ij}^L + I_{ij}^{LD} + I_{ij}^{FB} + I_{ij}^{INT}(t), \quad (5.43)$$

where a general expression for the first three terms on the right hand side is given by equation (5.11). Note that the time dependence in the evolving contribution from convective flow is retained but it is assumed that the time scale associated with this flow is much longer than the decay times that govern the viscous adjustment of the rotational bulge.

In applying equation (5.43), the appropriate expression for I_{ij}^{INT} above may be combined with previous expressions derived for the inertia tensor contribution from surface mass loading. As a simple example, let us revisit the case of the massive Tharsis feature on Mars. Assuming not

only that the surface mass load is axisymmetric, but also that the internal convection produces an axisymmetric potential field aligned with the same axis, then equations (5.11) and (5.41) (the latter with $\mathbf{e}_I = \mathbf{e}_L$) combine to give

$$I_{ij}^{L,LD,FB,INT}(t) = m' [\alpha Q' + \beta Q''(t)] \left(\frac{1}{3} \delta_{ij} - e_{L,i} e_{L,j} \right) + m' \left(e_{\Omega,i}^* e_{\Omega,j}^* - \frac{1}{3} \delta_{ij} \right). \quad (5.44)$$

Comparing equations (5.11) and (5.44) allows one to define the total effective load size as

$$Q_{eff} = \alpha Q' + \beta Q''(t). \quad (5.45)$$

We have shown that the TPW angle is governed by the effective load size. The effect of excess ellipticity may be dominant, even for $Q''(t) < Q'$, since $\beta > \alpha$. This dominance increases as the LT decreases (see Table 5.2).

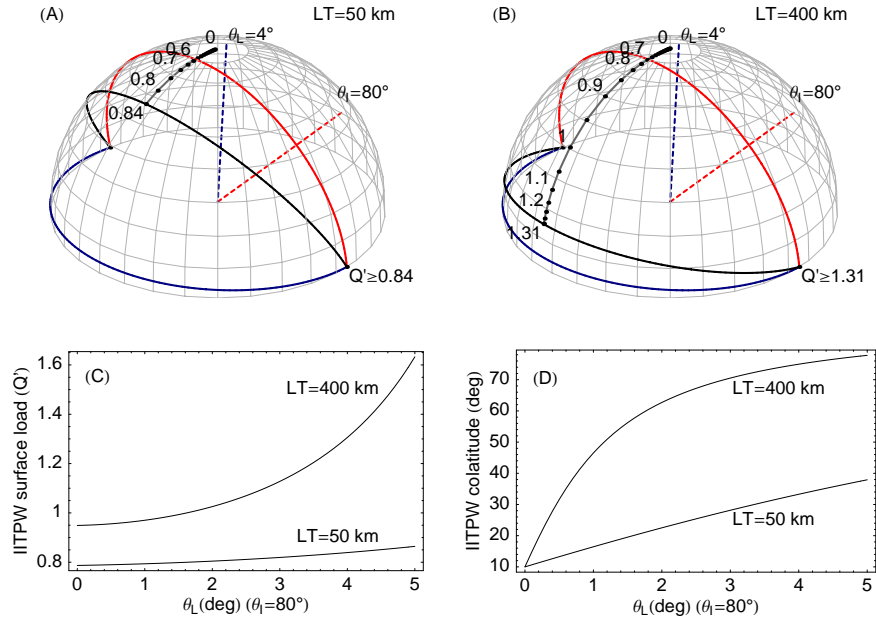


Figure 5.12 TPW driven by a combination of surface mass and internal loading. The internal load is fixed, and is characterized by an excess ellipticity which is 1% of the hydrostatic bulge of the planet ($Q'' = 0.01$). The principal axis for this component is given by the dashed red line ($\theta_I = 80^\circ$); the great circle perpendicular to this axis is given by the solid red line. Top row - predicted pole positions for the case where the surface mass load has an initial colatitude $\theta_L = 4^\circ$ and Q' is varied (as labeled). The frames are distinguished by the choice of lithospheric thickness: (A) 50 km or (B) 400 km. Bottom row - the effective surface load size (Q') required to produce an IITPW event (C), as well as the colatitude of the pole when this event is initiated (D), as a function of the initial load colatitude θ_L . Each frame shows results for LT = 50 km and 400 km.

Figure 5.12 provides a sample of the application of these governing equations. In particular, the

equilibrium rotational state for the case of a planet subject to both internal and external loading is predicted. In the top frames, the amplitude of the surface mass load (Q' , rather than Q_{eff}) is varied and its initial load colatitude is fixed to $\theta_L = 4^\circ$. The internal load is oriented so that the principal axis of this perturbation lies at $\theta_I = 80^\circ$ along the same great circle joining the rotation pole and surface mass load; the amplitude is fixed to an excess ellipticity 1% of the hydrostatic bulge of the planet. That is, $Q'' = 0.01$. Frames (A) and (B) are distinguished on the basis of the lithospheric thickness adopted in the calculations. The strong dependence on LT apparent on the figure arises because the total convection signal is imposed, a priori, while the remnant rotational bulge is a function of the lithospheric thickness. (We note that in Figures 5.10 and 5.11 the LT dependence is embedded in the value for the effective load, $Q_{eff} = Q'\alpha$, used on the figure; as previously discussed, since both the surface load and bulge adjustment are subject to compensation that is a function of LT, the balance associated with these two processes has a weaker sensitivity to LT.) As in the case of the two surface mass loads of Figure 5.10, the pole experiences an IITPW event when the combination of the surface and internal loads overcome the stabilizing effect of the remnant rotational bulge.

The bottom frames in Figure 5.12 show (C) the surface load size (Q') required for an IITPW event (we remind the reader that the internal load magnitude is fixed at $Q'' = 0.01$ for these tests), and (D) the pole colatitude at which this instability occurs, as a function of the initial surface load colatitude. As the lithosphere thins, the remnant rotational fossil bulge and uncompensated component of the surface mass load diminish. The impact of the fixed convection signal on the rotational state thus increases. The net effect is that an IITPW event is initiated for smaller values of the the surface load; the colatitude at which the IITPW event occurs also decreases. In any event, the main conclusion for this test is that relatively small (1%) convection signals can, like the secondary surface mass loads applied in Figures 5.10 and 5.11, exert a significant control on TPW, including the initiation of IITPW events.

5.5 Final Remarks

We have adopted the fluid limit of viscoelastic Love number theory to investigate the rotational stability of dynamic planets characterized by long-term (elastic) lithospheric strength. My theoretical development treats the compensation of surface mass loads independently of the adjustment of the rotational bulge (through k_f^L and k_f^T Love numbers, respectively), and I conclude, in contrast to Willemann (1984), that the equilibrium position of the rotation vector is a function of the lithospheric thickness (LT). Using fluid Love numbers computed for a model of Martian structure, I find that the TPW driven by axisymmetric surface mass loading is progressively larger than Willemann (1984)'s predictions as the lithosphere is thinned (Figure 5.6); indeed, the new theories only converge for LT values greater than ~ 400 km.

My analysis of TPW driven by axisymmetric loads, summarized in Figures and 5.4 and 5.5, bridges results from earlier, classic studies of Gold (1955) and Willemann (1984). As an example, Gold (1955) argued that TPW on a hydrostatic planet (i.e., a planet in which the rotational bulge will eventually reorient perfectly to a change in pole position) will ultimately move any uncompensated surface mass load to the equator. In the case of a planet with an elastic lithosphere, both the surface mass load and the rotational bulge will experience incomplete compensation. For such a planet, a reorientation of the load to the equator will occur in two situations (see Figure 5.4): (1) when the surface mass load is extremely large (i.e., $Q_{eff} \gg 1$), or; (2) when a load which exceeds the size of the remnant rotational bulge ($Q_{eff} > 1$) is placed at the initial pole position. In the latter case, the remnant rotational bulge is ‘canceled’ by the component of the surface mass load up to $Q_{eff} = 1$ and the residual (i.e., a load component of any size in excess of $Q_{eff} = 1$) will drive an IITPW instability.

I have also extended Willemann (1984)’s analysis to consider the impact of non-axisymmetric surface mass loads and arbitrary, convectively supported contributions to the non-hydrostatic inertia tensor, on predicted TPW paths. I find that these contributions can exert a profound influence on the rotational stability (Figures 5.10-5.12). For example, surface mass load asymmetry modeled by including a secondary load along the same great circle joining the primary (axisymmetric) load and the initial rotation pole (Case 1 in Figure 5.8) is capable of inducing an IITPW event. I have derived the stability conditions governing this event (see equations 5.33-5.35); for a given upper bound on the size of the effective surface load, a larger displacement between the primary and secondary loads increases the range of load locations that can give rise to IITPW (Figure 5.10). In contrast, load asymmetries modeled by incorporating a secondary load in a location perpendicular to the great circle joining the primary load and the initial rotation pole (Case 2 in Figure 5.8) act to deflect the pole from this great circle. The level of deflection depends on the size and location of the primary and secondary loads; note from Figure 5.11 that moving the secondary load closer to the initial rotation pole acts to increase the excursion of the rotation vector from the great circle.

The impact on the rotational dynamics of convectively-induced perturbations in the planetary shape (Figure 5.12) can be understood in these same terms, since such contributions can be expressed as equivalent uncompensated components of the surface mass load. That is, the divergence of the pole position from simple TPW paths predicted on the basis of an axisymmetric surface mass load will depend on the magnitude and orientation (relative to the initial pole and axisymmetric surface load) of the convection signal.

I conclude that the rotational stability of planets will be overestimated by analyses which are limited to simple axisymmetric loads of the type introduced by Willemann (1984) (and treated in Figures 5.4-5.6). The TPW on Mars driven by Tharsis, an example discussed at various stages through this chapter, warrants several comments in this regard. First, my correction of Willemann (1984)’s theory for axisymmetric loads yields a broader range of TPW scenarios for a Tharsis-sized

load (Figure 5.6) in the case of a relatively thin elastic lithosphere at the time of Tharsis formation. Second, in contrast to previous assertions, the equations governing the rotational stability permit a large ($> 65^\circ$) excursion of the Martian rotation pole in consequence of an axisymmetric Tharsis-sized loading (Figure 5.6). Third, asymmetries in the surface mass loading, either due to Tharsis structure or the presence of secondary loads (e.g., Elysium) on Mars, or contributions to the non-hydrostatic inertia tensor from convective processes, will introduce potentially large pole excursions off the great circle joining the initial rotation pole and the main Tharsis load. Indeed, these excursions may include an IITPW event.

Chapter 6

True polar wander of an ice-age Earth

6.1 Introduction

Predictions of perturbations in the Earth’s rotational state driven by the glacial isostatic adjustment (GIA) process have a history which dates back a quarter of a century. Indeed, modern numerical analyses of secular changes in the orientation of the rotation vector relative to the surface geography, or true polar wander (TPW), are most commonly based on theoretical treatments described in papers by [Sabadini & Peltier \(1981\)](#), [Yuen et al. \(1982\)](#), and [Wu & Peltier \(1984\)](#). Interest in glaciation-induced rotation variations remains active, and traditional applications associated with the inference of mantle structure (e.g., [Nakiboglu & Lambeck, 1980](#); [Sabadini & Peltier, 1981](#); [Yuen et al., 1982](#); [Peltier & Wu, 1983](#); [Wu & Peltier, 1984](#); [Yuen et al., 1985](#); [Spada et al., 1992a](#); [Peltier & Jiang, 1996](#); [Vermeersen & Sabadini, 1996](#); [Vermeersen et al., 1997](#)) have broadened to include studies of the feedback of rotation perturbations on a suite of other GIA observables (e.g., [Han & Wahr, 1989](#); [Bills & James, 1996](#); [Milne & Mitrovica, 1996, 1998](#); [Sabadini & Vermeersen, 1997](#); [Peltier, 1998](#); [Johnston & Lambeck, 1999](#); [Mitrovica et al., 2001](#)) as well as the signal from recent cryospheric forcings (e.g., [Gasperini et al., 1986](#); [Peltier, 1988](#); [Munk, 2002](#)).

Numerical and theoretical analyses of GIA-induced TPW have identified a suite of unique sensitivities. For example, predictions of present-day TPW speed indicate a strong sensitivity to the adopted lower mantle viscosity of the Earth model (e.g., [Sabadini & Peltier, 1981](#); [Yuen et al., 1982](#); [Wu & Peltier, 1984](#); [Yuen et al., 1985](#); [Vermeersen & Sabadini, 1996](#); [Mitrovica & Milne, 1998](#); [Johnston & Lambeck, 1999](#)), the thickness of the elastic lithosphere (e.g., [Peltier & Wu, 1983](#); [Wu & Peltier, 1984](#); [Mitrovica & Milne, 1998](#)), the treatment of the density jump at 670 km depth as some combination of phase and chemical discontinuity (e.g., [Mitrovica & Milne, 1998](#); [Johnston & Lambeck, 1999](#)), and to the choice of compressible or incompressible Earth models.

The highly non-monotonic sensitivity of the TPW predictions to variations in the adopted lower mantle viscosity provides an interesting contrast with other long-wavelength geophysical observables related to GIA. As the lower mantle viscosity (which is denoted by ν_{LM}) is increased from 10^{21} Pa s

to $\sim 3 \times 10^{21}$ Pa s, numerous studies have shown that the predicted present-day TPW speed drops by \sim a factor of two; as ν_{LM} is increased further to 10^{22} Pa s the predicted speed oscillates about a plateau, and then once again drops monotonically as the lower mantle is progressively stiffened beyond this value. The origin of this behavior is unclear.

In contrast, the predicted present-day secular variation in the degree two zonal harmonic of the Earth's geopotential, \dot{J}_2 , which is proportional to the rate of change of the Earth's axial rotation rate (e.g., Wu & Peltier, 1984; Mitrovica & Milne, 1998), shows a far simpler behavior with a straightforward physical interpretation. In particular, small amplitudes are predicted for relatively weak ($\sim 10^{21}$ Pa s) and stiff ($\sim 10^{23}$ Pa s) lower mantle regions; the former because such models would have reached close to equilibrium in ~ 6 kyr since the end of the main glaciation phase, and the latter because such models are characterized by slow rates of adjustment throughout their evolution. The highest rates are thus predicted for intermediate values of ν_{LM} , leading to a double root or 'inverted parabola' structure (e.g., Ivins et al., 1993; Mitrovica & Peltier, 1993).

The sensitivity of the TPW results becomes even more perplexing when one notes that the variation with increasing ν_{LM} takes on the inverted parabola form when one considers Earth models with very thin elastic lithospheric thicknesses (e.g., Mitrovica & Milne, 1998) or when one treats the density discontinuity at 670 km depth as a pure (adiabatic) phase boundary (e.g., Mitrovica & Milne, 1998; Johnston & Lambeck, 1999).

In a series of recent papers, Nakada (2000, 2002) argued that predictions of TPW are also sensitive to the choice of rheology for the lithosphere; finite-viscosity viscoelastic or purely elastic. In this regard, Nakada (2002) pointed out an apparent paradox in his results; namely, predictions of present-day TPW speed for the case of a viscoelastic lithosphere did not converge to the predictions based on an elastic lithosphere, even when he adopted viscosities in the former as high as 10^{40} Pa s. As we have seen, load-induced TPW will be sensitive to the response of the planetary model to the loading as well as to the background flattening of the model upon which the load is applied. Mitrovica (as cited by Nakada, 2002) suggested that the paradox highlighted by Nakada (2002)'s results may stem from an inaccuracy in the treatment of the equilibrium rotating form, and he proposed that this form should be connected to the observed flattening of the Earth. The differences in predictions based on Earth models with elastic and viscoelastic lithospheres is large (Nakada, 2002); indeed, the latter show a variation with ν_{LM} that is akin to the inverted parabola sensitivity mapped out for predictions with no lithosphere whatsoever. Thus the discrepancy warrants further investigation.

In this Chapter I present a new treatment of the linearized Euler equations (i.e., the so-called Liouville equations) that govern rotation perturbations on a viscoelastic planet driven by surface loading. My goals are to: (1) isolate the origin of the paradox noted by Nakada (2002); (2) outline a revised theory that provides an accurate treatment of GIA-induced rotation perturbations on spherically symmetric Earth models; and (3) explore the rotational stability inherent to the

traditional and new rotation theories. My results indicate a significant inaccuracy in the linearized rotation theory adopted over the last two decades. Furthermore, this inaccuracy is the source of much of the anomalous sensitivities evident in previous predictions of GIA-induced TPW.

6.2 The Linearized Euler Equations: The Liouville Equations

Perturbations in the orientation of the rotation vector associated with the GIA process are small (less than $\sim 1^\circ$) and thus linearized forms of the governing Euler equations are generally adopted as a basis for the analysis. In this section I present, without detailed derivation, time and frequency domain forms of the so-called Liouville equations derived under the assumption that the time scale of loading is much longer than the Chandler wobble period.

Let us denote the angular momentum vector of the Earth as \mathbf{L} . If no external torques act on the system, then the conservation of angular momentum requires

$$\frac{D\mathbf{L}}{Dt} = \frac{d\mathbf{L}}{dt} + \boldsymbol{\omega} \times \mathbf{L}, \quad (6.1)$$

where the left-hand-side represents a time derivative taken in an inertial (i.e., non-rotating) reference frame and the first term on the right-hand-side is a time derivative in a frame fixed to the body which rotates with an angular velocity $\boldsymbol{\omega}$. In component notation one can write $L_i = J_{ij}w_j$, where J_{ij} is the moment of inertia tensor, and the conservation law (Euler's equation) becomes

$$\frac{d}{dt}(J_{ij}w_j) + \epsilon_{ijk}w_j J_{kl}w_l = J_{ij}\dot{w}_j + \dot{J}_{ij}w_j + \epsilon_{ijk}w_j J_{kl}w_l = 0. \quad (6.2)$$

We will consider perturbations in the rotating Earth system relative to an initial state taken just prior to the onset of loading. Under the assumption that the loading involves small perturbations to both the rotation vector and moment of inertia tensor relative to this initial state, one can derive a linearized form of the Euler equations. The body reference frame is chosen with origin at the centre of mass; in the unperturbed, initial state the inertia tensor is diagonal with principal moments $I_1 = I_2 = A$, $I_3 = C$ and the angular velocity is $\boldsymbol{\Omega} = (0, 0, \Omega)$. In this case, one can write

$$\begin{aligned} w_i(t) &= \Omega[\delta_{i3} + m_i(t)] \\ J_{11}(t) &= A + I_{11}(t) \\ J_{22}(t) &= A + I_{22}(t) \\ J_{33}(t) &= C + I_{33}(t) \\ J_{ij}(t) &= I_{ij}(t) \text{ for } i \neq j, \end{aligned} \quad (6.3)$$

where it is assumed that $m_i \ll 1$ and, in addition, that perturbations in the elements of the inertia

tensor are $\ll A, C$. That is, $m_i \sim O(\epsilon)$, $I_{ij} \sim O(A\epsilon) \sim O(C\epsilon)$, with $\epsilon \ll 1$.

The three components of equation (6.2) are

$$\begin{aligned} 0 &= J_{1j}(t)\dot{w}_j(t) + \dot{J}_{1j}(t)w_j(t) + w_2(t)J_{3l}(t)w_l(t) - w_3(t)J_{2l}(t)w_l(t) \\ 0 &= J_{2j}(t)\dot{w}_j(t) + \dot{J}_{2j}(t)w_j(t) + w_3(t)J_{1l}(t)w_l(t) - w_1(t)J_{3l}(t)w_l(t) \\ 0 &= J_{3j}(t)\dot{w}_j(t) + \dot{J}_{3j}(t)w_j(t) + w_1(t)J_{2l}(t)w_l(t) - w_2(t)J_{1l}(t)w_l(t), \end{aligned} \quad (6.4)$$

and using the system of equations (6.3) in equations (6.4) yields

$$\begin{aligned} 0 &= (A + I_{11})\Omega\dot{m}_1 + I_{12}\Omega\dot{m}_2 + I_{13}\Omega\dot{m}_3 + \dot{I}_{11}\Omega m_1 + \dot{I}_{12}\Omega m_2 + \dot{I}_{13}\Omega(1 + m_3) \\ &\quad + \Omega m_2 I_{31}\Omega m_1 + \Omega m_2 I_{32}\Omega m_2 + \Omega m_2(C + I_{33})\Omega(1 + m_3) \\ &\quad - \Omega(1 + m_3)I_{21}\Omega m_1 - \Omega(1 + m_3)(A + I_{22})\Omega m_2 - \Omega(1 + m_3)I_{23}\Omega(1 + m_3) \\ 0 &= I_{21}\Omega\dot{m}_1 + (A + I_{22})\Omega\dot{m}_2 + I_{23}\Omega\dot{m}_3 + \dot{I}_{21}\Omega m_1 + \dot{I}_{22}\Omega m_2 + \dot{I}_{23}\Omega(1 + m_3) \\ &\quad + \Omega(1 + m_3)(A + I_{11})\Omega m_1 + \Omega(1 + m_3)I_{12}\Omega m_2 + \Omega(1 + m_3)I_{13}\Omega(1 + m_3) \\ &\quad - \Omega m_1 I_{31}\Omega m_1 - \Omega m_1 I_{32}\Omega m_2 - \Omega m_1(C + I_{33})\Omega(1 + m_3) \\ 0 &= I_{31}\Omega\dot{m}_1 + I_{32}\Omega\dot{m}_2 + (C + I_{33})\Omega\dot{m}_3 + \dot{I}_{31}\Omega m_1 + \dot{I}_{32}\Omega m_2 + \dot{I}_{33}\Omega(1 + m_3) \\ &\quad + \Omega m_1 I_{21}\Omega m_1 + \Omega m_1(A + I_{22})\Omega m_2 + \Omega m_1 I_{23}\Omega(1 + m_3) \\ &\quad - \Omega m_2(A + I_{11})\Omega m_1 - \Omega m_2 I_{12}\Omega m_2 - \Omega m_2 I_{13}\Omega(1 + m_3). \end{aligned} \quad (6.5)$$

Retaining terms of order $O(\epsilon)$ in these equations gives

$$\dot{m}_1(t)A + m_2(t)\Omega(C - A) = I_{23}(t)\Omega - \dot{I}_{13}(t), \quad (6.6)$$

$$-\dot{m}(t)_2A + m_1(t)\Omega(C - A) = I_{13}(t)\Omega + \dot{I}_{23}(t), \quad (6.7)$$

and

$$\dot{m}_3(t) = -\frac{\dot{I}_{33}(t)}{C}. \quad (6.8)$$

One can further simplify these equations by introducing the Euler wobble frequency

$$\sigma_r \equiv \Omega \frac{(C - A)}{A} \quad (6.9)$$

(see §B.2), and the parameters

$$\Psi_1(t) \equiv \frac{I_{13}(t)}{(C-A)} + \frac{\dot{I}_{23}(t)}{\Omega(C-A)}, \quad (6.10)$$

$$\Psi_2(t) \equiv \frac{I_{23}(t)}{(C-A)} - \frac{\dot{I}_{13}(t)}{\Omega(C-A)}, \quad (6.11)$$

and

$$\Psi_3(t) \equiv -\frac{I_{33}(t)}{C}. \quad (6.12)$$

Equations (6.6) and (6.7) become

$$\begin{aligned} \frac{\dot{m}_1(t)}{\sigma_r} + m_2(t) &= \Psi_2(t) \\ -\frac{\dot{m}_2(t)}{\sigma_r} + m_1(t) &= \Psi_1(t). \end{aligned} \quad (6.13)$$

These expressions can be written in compact form as

$$\frac{i}{\sigma_r} \dot{\mathbf{m}}(t) + \mathbf{m}(t) = \boldsymbol{\Psi}(t) \quad (6.14)$$

by introducing the complex notation $\mathbf{m}(t) = m_1(t) + im_2(t)$ and $\boldsymbol{\Psi}(t) = \Psi_1(t) + i\Psi_2(t)$. Furthermore, equation (6.8) becomes

$$\dot{m}_3(t) = \dot{\Psi}_3(t). \quad (6.15)$$

Equations (6.14) and (6.15) are the so-called Liouville equations (Munk & MacDonald, 1960) derived by various authors (e.g., Wu & Peltier, 1984). I have outlined this derivation in some detail in order to emphasize a central point: Namely, that the parameters A and C are strictly to be interpreted as the principle moments of inertia at the initial state of the system, just prior to the onset of loading.

6.3 Inertia Perturbations

The solution to the Liouville equations (6.14,6.15) proceeds by specifying the three classes of perturbation of the inertia tensor that arise in the loading problem (see Chapter 4). These contributions are associated with: (i) the direct effect of the surface mass load; (ii) the deformation of the planet driven by this surface loading; and (iii) the deformation of the planet arising from the perturbation in the rotation vector.

6.3.1 Inertia perturbations: the ice load

In this section I consider inertia perturbations associated with surface loading. As in previous treatments of GIA-induced variations in the Earth's rotational state, it is assumed that the Earth may be modeled as a spherically symmetric, linear (Maxwell) viscoelastic body. I begin by defining an arbitrary surface mass load, L , which is comprised of contributions from ice and ocean height variations as

$$L(\theta, \phi, t) = \rho_{ice}IH(\theta, \phi, t) + \rho_wOH(\theta, \phi, t), \quad (6.16)$$

where ρ_{ice} and ρ_w are the density of ice and water, respectively, and IH and OH are the variations in ice and ocean height since the initial state of the model (i.e., since the onset of loading). For an input ice history, and a similarly defined Earth model, methods exist (also based on viscoelastic Love number theory) for computing gravitationally self-consistent changes in the ocean height. These are not described here, but modern sea-level algorithms take into account loading effects as well as variations in both Earth rotation and shoreline geometry (e.g., [Milne et al., 1999](#)). One can expand the surface load using spherical harmonics $Y_{\ell m}(\theta, \phi)$ as

$$L(\theta, \phi, t) = \sum_{\ell=0}^{\infty} \sum_{m=-\ell}^{\ell} L_{\ell m}(t)Y_{\ell m}(\theta, \phi)$$

(see Appendix D). For each spherical harmonic coefficient

$$L_{\ell m}(t) = \rho_{ice}IH_{\ell m}(t) + \rho_wOH_{\ell m}(t), \quad (6.17)$$

where $IH_{\ell m}$ and $OH_{\ell m}$ are the spherical harmonic expansion coefficients for IH and OH respectively. Let us assume that the surface load has a degree two symmetry axis at the geographic point (θ_L, ϕ_L) , and that the components for a coordinate system where the symmetry axis is placed at the north pole (i.e., $\theta_L = 0$) is given by $L'_{20}(t)$. The inertia perturbations associated with the direct effect of the surface mass load are (see §4.1, equation 4.4)

$$\begin{aligned}
I_{11}^L(t) &= 4\pi a^4 \left[\frac{1}{3\sqrt{5}} L_{20}(t) - \sqrt{\frac{2}{15}} \operatorname{Re}(L_{22}(t)) \right] \\
I_{22}^L(t) &= 4\pi a^4 \left[\frac{1}{3\sqrt{5}} L_{20}(t) + \sqrt{\frac{2}{15}} \operatorname{Re}(L_{22}(t)) \right] \\
I_{33}^L(t) &= -\frac{8\pi a^4}{3\sqrt{5}} L_{20}(t) \\
I_{12}^L(t) &= \frac{8\pi a^2}{\sqrt{30}} \operatorname{Im}(L_{22}(t)) \\
I_{13}^L(t) &= \frac{8\pi a^2}{\sqrt{30}} \operatorname{Re}(L_{21}(t)) \\
I_{23}^L(t) &= -\frac{8\pi a^2}{\sqrt{30}} \operatorname{Im}(L_{21}(t)), \tag{6.18}
\end{aligned}$$

where δ_{ij} is the Kronecker delta and $e_L = (\sin \theta_L \cos \phi_L, \sin \theta_L \sin \phi_L, \cos \theta_L)$ is a unit vector indicating the orientation of the symmetry axis. Note that conservation of the surface mass load (i.e., $L_{00} = 0$) is invoked in writing equation (6.18).

The analogous equations for the inertia perturbations due to the load-induced deformation are (see §4.4, equation 4.42)

$$\begin{aligned}
I_{11}^{LD}(t) &= 4\pi a^4 \left[\frac{1}{3\sqrt{5}} L_{20}(t) * k_2^L(t) - \sqrt{\frac{2}{15}} \operatorname{Re}(L_{22}(t)) * k_2^L(t) \right] \\
I_{22}^{LD}(t) &= 4\pi a^4 \left[\frac{1}{3\sqrt{5}} L_{20}(t) * k_2^L(t) + \sqrt{\frac{2}{15}} \operatorname{Re}(L_{22}(t)) * k_2^L(t) \right] \\
I_{33}^{LD}(t) &= -\frac{8\pi a^4}{3\sqrt{5}} L_{20}(t) * k_2^L(t) \\
I_{12}^{LD}(t) &= \frac{8\pi a^4}{\sqrt{30}} \operatorname{Im}(L_{22}(t)) * k_2^L(t) \\
I_{13}^{LD}(t) &= \frac{8\pi a^4}{\sqrt{30}} \operatorname{Re}(L_{21}(t)) * k_2^L(t) \\
I_{23}^{LD}(t) &= -\frac{8\pi a^4}{\sqrt{30}} \operatorname{Im}(L_{21}(t)) * k_2^L(t), \tag{6.19}
\end{aligned}$$

where $k_\ell^L(t)$ are the viscoelastic Love numbers (4.39). One can use equation (6.18) to write the last equation as

$$I_{ij}^{LD}(t) = I_{ij}^L(t) * k_2^L(t). \tag{6.20}$$

This result was stated, without proof, in Wu & Peltier (1984, see equation 31); my derivation provides a simple proof of this result.

6.3.2 Inertia perturbations: rotational effects

Next, I consider inertia perturbations driven by rotationally induced planetary deformations. A change in the amplitude or orientation of the rotation vector leads to a perturbation in the centrifugal potential, and this perturbation is commonly termed the rotational driving potential. The driving potential can be written as $\Lambda(\theta, \phi, t) \equiv \mathcal{G}^R(\theta, \phi, t) - \mathcal{G}^{R,0}(\theta, \phi, t_0)$, where $\mathcal{G}^R(\theta, \phi, t)$ and $\mathcal{G}^{R,0}(\theta, \phi, t_0)$ are the centrifugal potentials associated with the perturbed rotation vector $\mathbf{w}(t)$ and the initial rotation vector $\mathbf{\Omega}$.

The response to the rotational driving potential is governed by tidal (or tidal effective) Love numbers $k_\ell^T(t)$ (equation 4.61). The inertia perturbations due to the planet deformation in response to the driving potential can be written as

$$I_{ij}^\Lambda \equiv I_{ij}^{RD} - I_{ij}^{RD,0}, \quad (6.21)$$

where I_{ij}^{RD} and $I_{ij}^{RD,0}$ refer to the rotationally induced inertia perturbations associated with the perturbed and initial centrifugal potentials respectively. Replacing equation (4.66) in equation (6.21) yields

$$I_{ij}^\Lambda = \frac{a^5 \Omega^2}{3G} k_2^T(t) * (e_{w,i}(t)e_{w,j}(t) - e_{\Omega,i}e_{\Omega,j}), \quad (6.22)$$

where

$$\begin{aligned} \mathbf{e}_w(t) &= (m_1(t), m_2(t), 1 + m_3(t)) \\ \mathbf{e}_\Omega &= (0, 0, 1). \end{aligned} \quad (6.23)$$

The inertia tensor perturbations that are relevant for Euler's equation are

$$\begin{aligned} I_{33}^\Lambda(t) &= \frac{\Omega^2 a^5}{3G} k_2^T(t) * [2m_3(t) + m_3^2(t)] \\ I_{13}^\Lambda(t) &= \frac{\Omega^2 a^5}{3G} k_2^T(t) * m_1(t) [1 + m_3(t)] \\ I_{23}^\Lambda(t) &= \frac{\Omega^2 a^5}{3G} k_2^T(t) * m_2(t) [1 + m_3(t)] \end{aligned} \quad (6.24)$$

These expressions are exact and they hold for any level of variation to the rotation vector. To be consistent with my derivation of the Liouville's equations, these expressions are simplified to retain terms of $O(\epsilon)$ and obtain

$$\begin{aligned}
I_{33}^\Lambda(t) &= \frac{2\Omega^2 a^5}{3G} k_2^T(t) * m_3(t) \\
I_{13}^\Lambda(t) &= \frac{\Omega^2 a^5}{3G} k_2^T(t) * m_1(t) \\
I_{23}^\Lambda(t) &= \frac{\Omega^2 a^5}{3G} k_2^T(t) * m_2(t)
\end{aligned} \tag{6.25}$$

6.4 The Liouville Equations Revisited

Let us return now to the Liouville equation (6.14). This equation can be written as

$$\frac{i}{\sigma_r} \dot{\mathbf{m}}(t) + \mathbf{m}(t) = \frac{1}{C-A} \left[\mathbf{I}(t) - \frac{i}{\Omega} \dot{\mathbf{I}}(t) \right] \tag{6.26}$$

by introducing the complex parameter $\mathbf{I}(t) = I_{13}(t) + iI_{23}(t)$. Using the results of the last section, one can rewrite this equation to include the three contribution to the inertia tensor perturbation as

$$\begin{aligned}
\frac{i}{\sigma_r} \dot{\mathbf{m}}(t) + \mathbf{m}(t) &= \frac{1}{C-A} [\mathbf{I}^L(t) + k_2^L(t) * \mathbf{I}^L(t)] + \frac{k_2^T(t)}{k_f} * \mathbf{m}(t) \\
&- \frac{i}{\Omega(C-A)} \frac{d}{dt} [\mathbf{I}^L(t) + k_2^L(t) * \mathbf{I}^L(t)] - \frac{i}{\Omega} \frac{d}{dt} \left[\frac{k_2^T(t)}{k_f} * \mathbf{m}(t) \right].
\end{aligned} \tag{6.27}$$

where k_f is a parameter given by

$$k_f = \frac{3G}{a^5 \Omega^2} (C-A), \tag{6.28}$$

and the components of the complex parameter $\mathbf{I}^L(t) = I_{13}^L(t) + iI_{23}^L(t)$ are given by equation (6.18).

Traditional GIA calculations based on spherically symmetric models commonly develop the linearized Liouville theory within the Laplace-transform domain. Taking the transform of equation (6.27) yields, after some straightforward algebra

$$\mathbf{m}(s) \left[\frac{is}{\sigma_r} + 1 - \frac{k_2^T(s)}{k_f} \left(1 - \frac{is}{\Omega} \right) \right] = \frac{1}{C-A} \mathbf{I}^L(s) \left(1 - \frac{is}{\Omega} \right) [1 + k_2^L(s)], \tag{6.29}$$

where the s-domain form of the viscoelastic Love numbers is given by

$$k_2^L(s) = k_2^{L,E} + \sum_{k=1}^K \frac{r_k^{2,L}}{s + s_k^2}, \tag{6.30}$$

and

$$k_2^T(s) = k_2^{T,E} + \sum_{k=1}^K \frac{r_k^{2,T}}{s + s_k^2}. \tag{6.31}$$

In our problem it is clear that one can assume that $s \ll \Omega$ (that is, periods are much longer than 1 day), and in this case the terms in s/Ω on both sides of equation (6.29) may be neglected. This is equivalent to ignoring the time derivative terms on the left-hand-side of equation (6.27). Accordingly, both the time and Laplace-transform domain forms of the Liouville equation can be simplified to

$$\frac{i}{\sigma_r} \dot{\mathbf{m}}(t) + \mathbf{m}(t) = \frac{1}{C-A} [\mathbf{I}^L(t) + k_2^L(t) * \mathbf{I}^L(t)] + \frac{k_2^T(t)}{k_f} * \mathbf{m}(t). \quad (6.32)$$

and

$$\mathbf{m}(s) = -i \frac{\Omega}{A} \frac{\mathbf{I}^L(s)(1 + k_2^L(s))}{[s - i\sigma_r(1 - k_2^T(s)/k_f)]}, \quad (6.33)$$

where equation(6.9) is used.

In deriving the Liouville equations, whether in the Laplace transform domain (Wu & Peltier, 1984) or the time domain (Nakada, 2002), it is also assumed that $s \ll \sigma_r$ (i.e., the period is much longer than the Chandler wobble on a rigid Earth). Note that this is the same assumption used in Chapter 2 for the TPW adiabatic invariant of a quasi-rigid body. In this case, the term in $\dot{\mathbf{m}}(t)$ on the right-hand-side of equation (6.32) and the first term in the denominator of equation (6.33) can be neglected and the equations become

$$\mathbf{m}(t) = \frac{1}{C-A} [\mathbf{I}^L(t) + k_2^L(t) * \mathbf{I}^L(t)] + \frac{k_2^T(t)}{k_f} * \mathbf{m}(t). \quad (6.34)$$

and

$$\mathbf{m}(s) = \frac{1}{C-A} \frac{\mathbf{I}^L(s)(1 + k_2^L(s))}{(1 - k_2^T(s)/k_f)}. \quad (6.35)$$

The parameter k_f in equation (6.28) is commonly termed the ‘fluid k Love number’ and is central to discussions appearing in the remainder of this Chapter. From the derivation above, and in particular my linearization of the Euler equations via the perturbation (6.3), this parameter is formally dependent on the difference $C - A$ at the initial state of the model, just prior to the onset of loading. That is, the parameter k_f is a measure of the background oblateness of the planet, and will in practice have contributions from the equilibrium form associated with the unperturbed rotation rate Ω (i.e., the hydrostatic form), as well as from long-term geophysical processes other than GIA (i.e., non-hydrostatic signals associated with fossil rotational effects, mantle convection, etc.) The linearized theory assumes that these contributions do not change over the course of the surface mass loading history, and that perturbations in the oblateness due to GIA are much smaller than the net background oblateness. As I will demonstrate below, approximations to k_f traditionally applied within the GIA literature introduce a significant error in predictions of glaciation-induced rotation perturbations. Furthermore, a recognition of this sensitivity resolves the paradox described by Nakada (2002).

6.5 k_f - The Traditional Approximation

Within the GIA literature, it has been assumed that the fluid Love number, k_f , can be approximated by the fluid, $s = 0$, limit of the s -domain k_2^T Love number (e.g., [Wu & Peltier, 1984](#); equations 63,68):

$$k_f \sim k_2^T(s = 0), \quad (6.36)$$

where, following equation (6.31), one can write

$$k_2^T(s = 0) = k_2^{T,E} + \sum_{k=1}^K \frac{r_k^{2,T}}{s_k}. \quad (6.37)$$

Within the GIA literature, spherically symmetric Earth models have generally been defined by the thickness of a purely elastic lithosphere and a radial profile of mantle viscosity. The parameter $k_2^T(s = 0)$ is independent of the latter; however, it is a function of the background density profile and the elastic lithospheric thickness (denoted as ‘ LT ’). Henceforth, I will commonly adopt a notation, $k_2^T(s = 0; LT)$, which makes this latter dependence explicit.

Using the approximation (6.36), the governing Liouville equations (6.34) and (6.35) become

$$\mathbf{m}(t) = \frac{1}{C - A} [\mathbf{I}^L(t) + k_2^L(t) * \mathbf{I}^L(t)] + \frac{k_2^T(t)}{k_2^T(s = 0; LT)} * \mathbf{m}(t). \quad (6.38)$$

and

$$\mathbf{m}(s) = \frac{1}{C - A} \frac{\mathbf{I}^L(s)(1 + k_2^L(s))}{\left(1 - \frac{k_2^T(s)}{k_2^T(s=0;LT)}\right)}. \quad (6.39)$$

where LT in $k_2^T(s = 0; LT)$ refers to the elastic lithospheric thickness adopted to compute the time and s -domain Love numbers $k_2^T(s)$, $k_2^T(t)$, $k_2^L(s)$, and $k_2^L(t)$. [Wu & Peltier \(1984\)](#) have provided analytic expressions for the inverse Laplace transform applied to equation (6.39). Their result, which involves a set of so-called ‘rotational normal modes’, is summarized in Appendix E.

Why have previous analyses adopted the approximation (6.36) for the fluid Love number k_f ? The k_2^T Love number can be used to approximate (to the accuracy of the perturbation theory upon which this number is based) the equilibrium form of a rotating planet ([Munk & MacDonald, 1960](#)). Consider a model Earth with an elastic shell of thickness LT that is set spinning at the current rotation rate of Ω . The equilibrium rotating form of this planet may be related to the fluid limit of the k_2^T Love number computed for this model. Using equation (4.82) with $\mathbf{e}_\Omega = (0, 0, 1)$ yields

$$k_2^T(s = 0; LT) = \frac{3G}{a^5 \Omega^2} (I_{33}^{RD} - I_{11}^{RD}) = \frac{3G}{a^5 \Omega^2} (C - A)_{LT}, \quad (6.40)$$

where $(C - A)_{LT}$ is the predicted difference in the polar and equatorial moment of inertia for this model rotating Earth with elastic shell thickness LT . Note that for the rotation axis at the north

pole, as has been assumed by setting $\mathbf{e}_\Omega = (0, 0, 1)$, $C = I_{33}^{RD}$ and $A = I_{11}^{RD} = I_{22}^{RD}$. Figure 6.1 shows a prediction of $k_2^T(s = 0; LT)$ as a function of LT computed using the seismic density model PREM (Dziewonski & Anderson, 1981). As one would expect, increasing the thickness of the elastic shell acts to reduce the rotationally-induced oblateness of the Earth model (see also Mound et al., 2003). The arrows on Figure 6.1 specify the observed value of k_f (i.e., equation 6.28 with observed quantities applied) and a prediction by Nakiboglu (1982) based on second order accurate hydrostatic ($LT = 0$) theory.

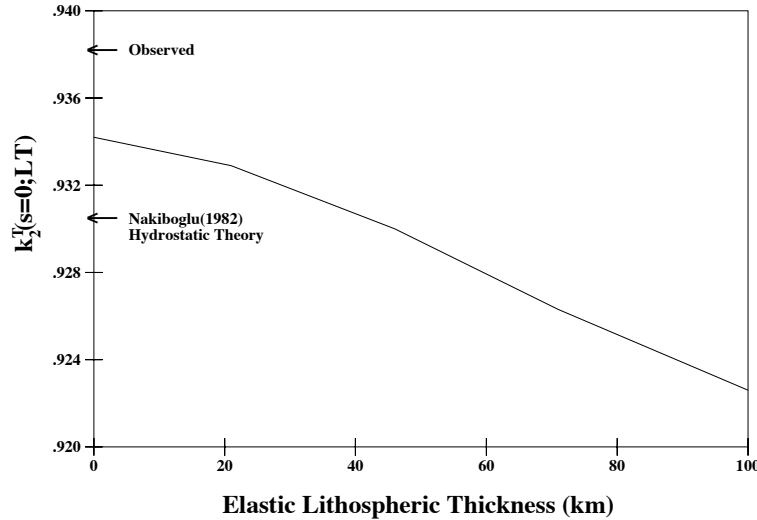


Figure 6.1 The solid line shows numerical predictions of the degree two tidal Love number in the $s = 0$ fluid limit, $k_2^T(s = 0; LT)$, as a function of the thickness of a purely elastic lithosphere (LT) adopted in the Earth model. The radial profile of density is given by PREM (Dziewonski & Anderson, 1981). The arrow at top left provides the ‘observed’ fluid Love number, as defined by equation (6.28), where present day values of Ω , C and A are adopted (as in equation 6.41). The second arrow shows the fluid Love number computed for PREM by Nakiboglu (1982) using a second-order accurate hydrostatic ($LT = 0$) theory.

A comparison of equation (6.40) with the correct expression (6.28), where the latter involves the initial (or unperturbed) difference $C - A$, makes clear the set of approximations inherent to the traditional assumption (6.36). It has previously been assumed that: (1) The difference in the polar and mean equatorial moments of inertia of the planet is governed entirely by the equilibrium rotating form of the planet associated with the present rotation rate. Thus, other geophysical processes contributing to this form, for example convection-induced dynamic ellipticity or a fossil rotational bulge are neglected; and (2) this equilibrium form can be computed with sufficient accuracy using viscoelastic Love number theory applied to the same Earth model used to compute the response of the Earth to the surface loading and rotation perturbations. That is, as discussed above, the Earth model used to compute the time and s-domain Love numbers $k_2^T(s)$, $k_2^T(t)$, $k_2^L(s)$, and $k_2^L(t)$ in the Liouville equations is the same model used to compute the background equilibrium

form.

The dependence of the prediction of $k_2^T(s=0; LT)$ on the underlying Earth model (and specifically on the adopted elastic lithospheric thickness) appears to be relatively modest, but nevertheless this dependence lies at the heart of the paradox discovered by Nakada (2002). A prediction of glaciation-induced polar wander is dependent on both the manner in which the model planet responds to the applied surface mass and rotational loading, and on the background (or unperturbed) oblateness of the planet. In the generalized theory (equations 6.34-6.35) the latter is given by k_f ; the approximation (6.36) introduces an erroneous model (i.e., LT) dependence in this background form.

The paradox Nakada (2002) discovered was as follows. His predictions of present-day TPW speed computed using a purely elastic lithosphere were different from predictions based on a viscoelastic lithosphere of the same thickness even when the viscosity of the latter lithosphere was set to an extremely high value (10^{40} Pa s). How could this be? Given the short time scale of GIA relative to the extremely long Maxwell time of a lithosphere of viscosity 10^{40} Pa s, these two models (high viscosity viscoelastic, and elastic) would certainly respond with the same deformation if subject to an identical applied surface mass load or rotational driving potential. However, by making the assumption (6.36), as all previous studies had done, Nakada (2002) was introducing a difference in the background oblateness of the two models. Specifically, $k_2^T(s=0)$ for a model with an extremely high (but still finite) viscosity, 100 km thick lithosphere is identical to $k_2^T(s=0)$ for a model with no elastic lithosphere (the left hand intercept of the curve in Figure 6.1; i.e., $LT=0$ in both cases); in contrast, $k_2^T(s=0)$ for a model with an elastic lithosphere of 100 km thickness ($LT=100$ km) is given by the right intercept on Figure 6.1. By adopting $k_2^T(s=0)$ as an approximation for k_f , the two models were implicitly given distinct initial background forms, and thus the computed TPW for the two cases should not necessarily converge.

Despite the apparently modest dependence of $k_2^T(s=0; LT)$ on elastic lithospheric thickness (Figure 6.1), Nakada (2002)'s results indicate that the impact of the approximation to k_f on predictions of TPW can be significant. Figure 6.2 presents a suite of predictions of present-day TPW speed which reproduce these general results. In these, and all subsequent predictions, a simplified model of the late Pleistocene ice load history introduced by Mitrovica & Milne (1998) (and adopted by Nakada, 2002) is adopted. Specifically, a series of eight 100 kyr glacial cycles, with each cycle defined by a 90 kyr glaciation phase and a 10 kyr deglaciation period is included. This sawtooth time history is characterized by inertia perturbations of $I_{13}^L = -6.67 \times 10^{31} \text{kgm}^2$, $I_{23}^L = 2.31 \times 10^{32} \text{kgm}^2$, and $I_{33}^L = -7.89 \times 10^{31} \text{kgm}^2$, at each glacial maximum. These values are estimated from a global reconstruction of ice volume at last glacial maximum (Tushingham & Peltier, 1991) and a complementary eustatic ocean load (Mitrovica & Milne, 1998). The last glacial cycle is assumed to end 6 kyr before present. The predictions shown on the figure are based on the time-domain Liouville equation (6.38) although it has been confirmed that predictions based on equation (6.39) yield the

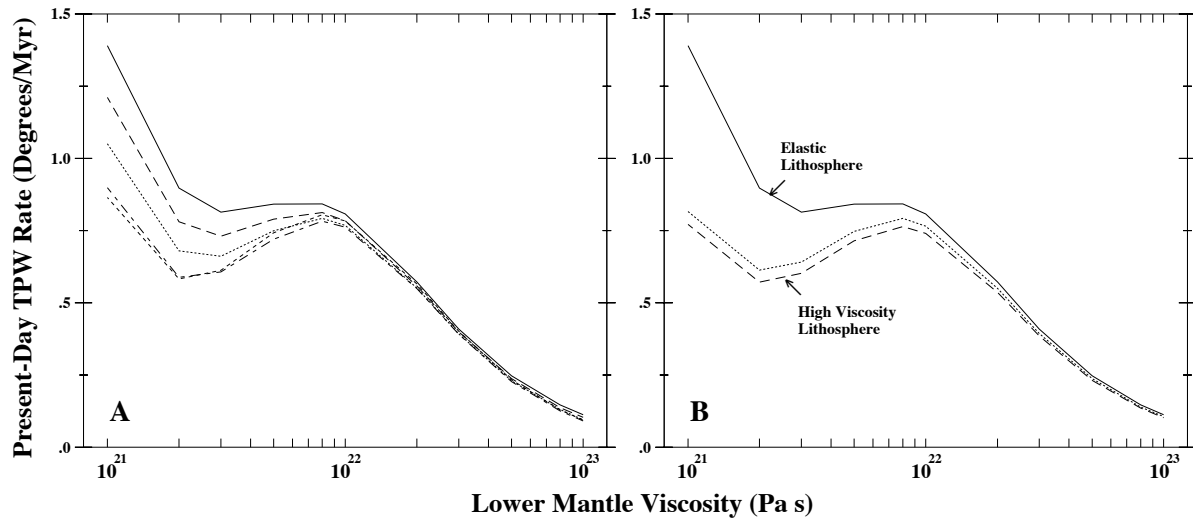


Figure 6.2 Predictions of present day true polar wander speed, as a function of the lower mantle viscosity (abscissa scale) of the Earth model, generated using the traditional treatment of k_f as $k_2^T(s=0; LT)$ (equation 6.36). The predictions are performed using the time-domain form of the governing equations (see equation 6.38). (A) A sequence of predictions distinguished on the basis of the adopted thickness of a purely elastic lithosphere: $LT = 100$ km (solid line), 71 km (dashed line), 46 km (dotted line), 21 km (dashed-dotted line) and 0 km (short dashed line). (B) Solid line is identical to the results in Frame A (i.e., $LT = 100$ km); in contrast, the remaining two lines are generated using no purely elastic lithosphere ($LT = 0$ km), but viscosities in the top 100 km of the model are set to either 10^{24} Pa s (dashed line) or 10^{28} Pa s (dotted line). In all predictions on the figure the upper mantle viscosity (below the elastic lithosphere on the left frame and below 100 km depth on the right frame) is set to 10^{21} Pa s. The surface mass load history is described in the text.

same results.

Figure 6.2A shows results for a sequence of different values of elastic lithospheric thickness, LT , ranging from 100 km (solid line) to 0 km (short-dashed line) as a function of the adopted lower mantle viscosity (ν_{LM}). This sequence of results shows the dependence on elastic lithospheric thickness observed in numerous previous studies. In Figure 6.2B the results for $LT = 100$ km are reproduced, together with predictions based on a 100 km viscoelastic lithosphere with a viscosity of either 10^{24} Pa s (dashed line) to 10^{28} Pa s (dotted line). The discrepancy between the solid and dotted lines in Figure 6.2B is an illustration of the Nakada (2002) ‘paradox’.

As previously discussed, each choice of elastic lithospheric thickness, LT , in Figure 6.2 yields a different value for $k_2^T(s = 0; LT)$ (Figure 6.1) and thus a different approximation (via equation 6.36) to the fluid Love number k_f (and background planetary oblateness). As an example, in Figure 6.2B, the solid line joins results for models with $k_2^T(s = 0; LT = 100) \sim 0.922$, while the remaining lines are constructed from models with $k_2^T(s = 0; LT = 0) \sim 0.934$ (Figure 6.1); a difference of 1.5%. The discrepancy between the solid and dotted lines in Figure 6.2B indicates that predictions of GIA-induced present-day TPW speed are progressively more sensitive to variations in the adopted (LT -dependent) background planetary oblateness as the lower mantle viscosity is reduced. Indeed, the sensitivity of the predictions to the 1.5% variation cited above is, for $\nu_{LM} \sim 10^{21}$ Pa s, remarkably large (see also Nakada, 2002).

The form of the governing equations suggests that some form of instability may be at play. In particular, note that the s -domain Liouville equation (6.39), when k_f is approximated by $k_2^T(s = 0; LT)$, becomes unstable in the fluid ($s = 0$) limit since the denominator will approach zero in this limit. This is a restatement of the well known result that the orientation of a rotating body in hydrostatic equilibrium is unstable in the presence of uncompensated surface mass changes (Goldreich & Toomre, 1969). The issue of stability is explored in detail in Figures 6.3-6.4.

Figure 6.3 shows a decomposition of the model-dependent components of the governing equation (6.39) as a function of the Laplace transform variable s . Each frame shows results for four Earth models distinguished on the basis of the lower mantle viscosity; 10^{21} Pa s (solid line), 3×10^{21} Pa s (dashed line), 10^{22} Pa s (dotted line) and 3×10^{22} Pa s (dashed-dotted line). In all cases $LT = 100$ km. Frame A gives $1 - k_2^T(s)/k_2^T(s = 0; LT = 100)$, i.e., the denominator in equation (6.39), which is a measure of the s (or frequency) dependence in the adjustment of the rotational bulge (a value of 0 reflects complete adjustment of the bulge to a perturbation in rotation). Frame B shows $1 + k_2^L(s)$, i.e., the numerator of the model-dependent term of equation (6.39), which is an s -dependent measure of the compensation of the surface mass load. Frame C provides the ratio of these two dependencies over a slightly smaller range of s values. The right (high s , short time scale) intercept represents the elastic limit, while the left (small s , long time scale) intercept is the fluid limit. The four models have the same elastic asymptotes, since PREM is adopted in all cases, and $s = 0$ fluid asymptotes, since $LT = 100$ in all cases; thus, the asymptotic trends in Figures

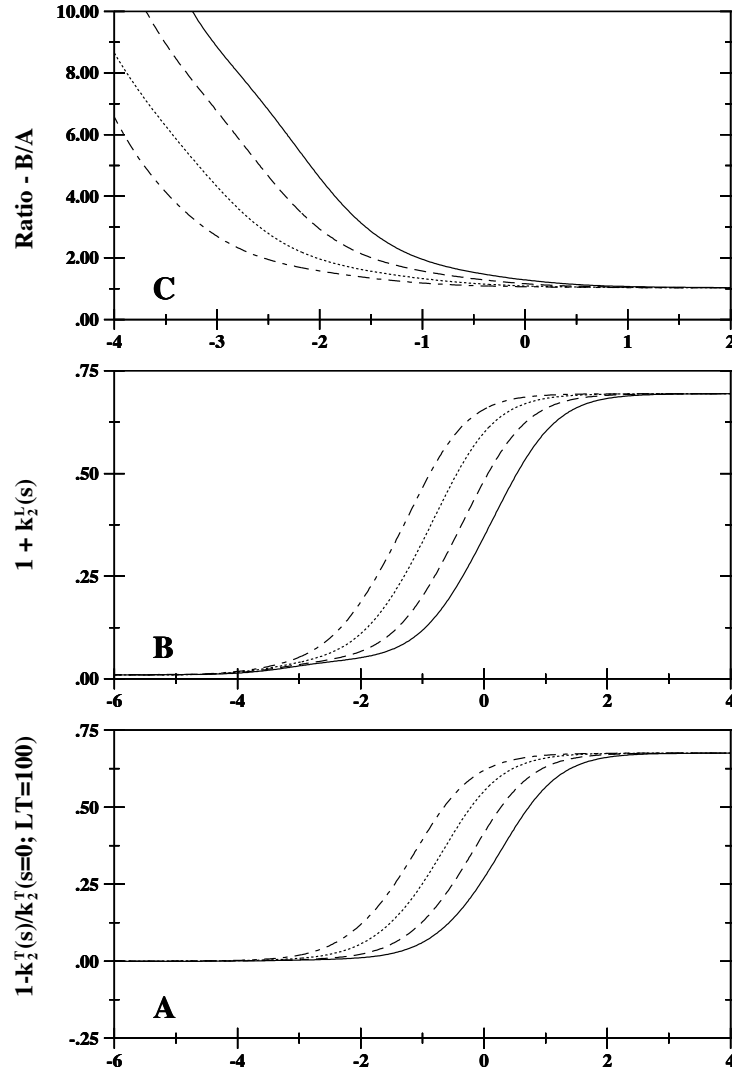


Figure 6.3 Decomposition of the model dependent components of the traditional Liouville equation (6.39) as a function of the Laplace transform variable s : (A) $1 - k_2^T(s)/k_2^T(s=0; LT)$; (B) $1 + k_2^L(s)$; and (C) the ratio (B/A) of these terms. In each frame, results are shown for four Earth models with distinct ν_{LM} : 10^{21} Pa s (solid line); 3×10^{21} Pa s (dashed line); 10^{22} Pa s (dotted line); and 3×10^{22} Pa s (dashed-dotted line). In each case, $LT = 100$ km and the upper mantle viscosity is 10^{21} Pa s.

6.3A and B converge. Not surprisingly, for a given s value, models with progressively weaker lower mantle viscosity are closer to the fluid limit associated with the response to both the surface mass and rotational forcing.

The results in Figure 6.3C, as s approaches the fluid limit, reflect the instability described above. In particular, for small s , the isostatic compensation of the surface load is less complete than the adjustment of the rotational bulge (i.e., the denominator, as shown in Figure 6.3A, converges to 0 at small s , whereas the numerator, as shown in Figure 6.3B, does not) and the result is a ratio which exhibits a rapid increase in amplitude. As the lower mantle viscosity is weakened, the instability initiates at larger values of s (smaller time scales) and the amplitude of the predicted present day TPW speed (solid line, Figure 6.2A) reflects this trend.

In Figure 6.4 I repeat the analysis of Figure 6.3 for three models with the same lower mantle viscosity (10^{21} Pa s) but distinct treatments of the lithosphere. The solid line is based on a model with an elastic lithospheric thickness of 100 km (these are identical to the solid lines in Figure 6.3). In contrast, the remaining two lines adopt $LT = 0$ and are distinguished on the basis of the viscosity within the top 100 km; either 10^{21} Pa s (i.e., the same as the remaining upper mantle; dashed-dotted lines) or 10^{28} Pa s (i.e., a high viscosity - but not elastic - lid; dotted lines). The results in Figure 6.4C indicate that the latter two models both exhibit a more stable rotational state for small s values (less than ~ 0 on the abscissa, or time scales greater than 1000 years) than the $LT = 100$ km prediction. As discussed below, the origin of this increased stability is different for the two cases.

We begin by comparing the solid and dashed-dotted lines. In this case, the models are identical in all respects with the exception that the lithospheric thickness is reduced from 100 km to 0. The models have the same elastic Love numbers, but for any s other than the elastic limit (including the fluid, $s = 0$ limit) the Love numbers will differ because of the distinct values of the adopted LT . The solid and dashed-dotted lines are nearly indistinguishable in Figure 6.4A, indicating that a simple reduction in the lithospheric thickness (from 100 km to 0) makes negligible difference to the adjustment of the rotational bulge over time scales relevant to GIA. In contrast, this reduction clearly impacts the level of isostatic compensation of the surface mass load (Figure 6.4B). As LT is reduced, while maintaining a constant sub-lithospheric upper mantle viscosity, the term $1 + k_2^L(s)$ in equation (6.39) more closely approaches zero (i.e., perfect compensation) and the rotation pole is stabilized. This explains the reduction in amplitude of the predicted TPW speed in Figure 6.2A as LT is reduced.

Finally, consider the solid and dotted lines in Figure 6.4. These lines are indistinguishable in Figure 6.4B. As previously described, this simply indicates that the isostatic compensation of the surface mass load over these time scales will be the same for both a model with an elastic lithosphere and a model with a very high viscosity lithosphere of the same thickness (i.e., over the s range in Figure 6.4B, $k_2^L(s)$ is the same for both models). However, a difference between the two

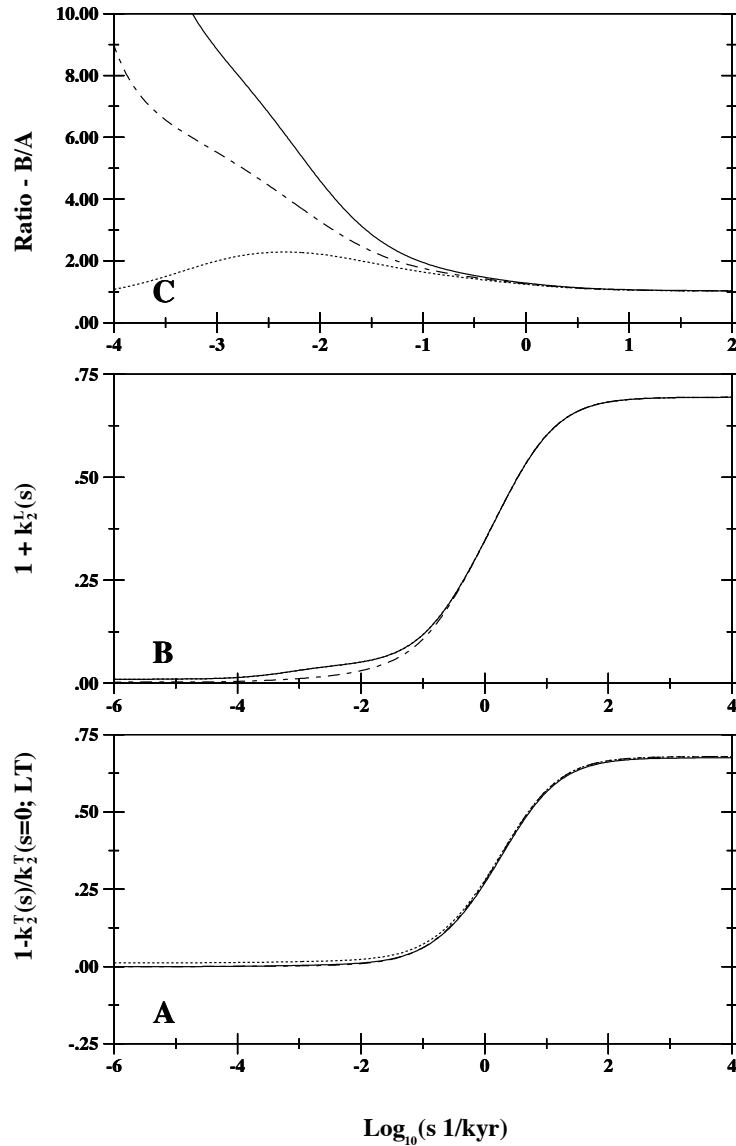


Figure 6.4 As in Figure 6.3, except for a set of three Earth models distinguished on the basis of my treatment of the lithosphere. In all cases both ν_{LM} and the upper mantle viscosity (below the lithosphere) are 10^{21} Pa s. Solid line - an elastic lithospheric thickness, $LT = 100$ km (same as solid line in Figure 6.3); Dashed-dotted line - $LT = 0$ and the viscosity of the top 100 km of the model is set to the upper mantle viscosity; Dotted line - $LT = 0$ and the top 100 km of the model is given a high viscosity (10^{28} Pa s) lithospheric lid.

model predictions is evident in Figure 6.4A. In this case, the Love number $k_2^T(s)$ is also essentially identical for the two models over the range of s values on the Figure; however, the adopted value of $k_2^T(s = 0; LT)$ (i.e., the background oblateness) will be different in the two cases. For such a high viscosity lid, s values will have to be significantly smaller (time scales significantly larger) than those shown on the Figure before the lid viscously relaxes and $k_2^T(s)$ obtains its fluid limit; thus, the term $1 - k_2^T(s)/k_2^T(s = 0; LT = 0)$ for the high viscosity lid case (dotted line) is shifted away from 0.0 relative to the $1 - k_2^T(s)/k_2^T(s = 0; LT = 100)$ case and the rotation is stabilized (Figure 6.4C). The small deviation in Figure 6.4A is thus responsible for the large difference in the predicted TPW speeds (solid, dotted line) in Figure 6.2B and the paradox described by Nakada (2002).

The relative accuracy of the TPW rate predictions in Figure 6.2 is not clear since the relation between the value of $k_2^T(s = 0; LT)$ adopted in equation (6.38) and the appropriate value for k_f is unclear. This issue is addressed in the next section, where I present predictions based on an improved expression for k_f .

6.6 k_f - A New Approach

The parameter k_f in the generalized Liouville equations (6.39) and (6.39) represents, via equation (6.28), a measure of the background oblateness of the planet upon which the Late Pleistocene glaciation cycles have been superimposed. The linearization procedure used to derive these equations assumes that perturbations in k_f (i.e., oblateness) due to GIA, or any other time-dependent geophysical process for that matter, have been small since the onset of ice age loading (several million years ago). In this case, following the suggestion by Mitrovica (see Nakada, 2002), a logical approach to the rotation problem would be to solve the generalized Liouville equations with k_f replaced by the observed (present-day) value of this parameter (which I will denote by k_f^{obs}). That is, one may use

$$k_f \sim k_f^{obs} = \frac{3G}{a^5 \Omega^2} (C - A)_{obs} \sim 0.9382 \quad (6.41)$$

in equations (6.34) and (6.39), where $(C - A)_{obs}$ is the *observed* difference in the polar and equatorial moment of inertia. The observed fluid Love number is shown superimposed on Figure 6.1. I have found, using results from a suite of numerical predictions of the GIA process, that the perturbation in k_f associated with GIA (which is proportional to the perturbation in the J_2 harmonic of the geopotential) is less than ~ 0.001 . This supports the validity of the linearization procedure, as well as Mitrovica's suggestion that equation (6.41) be adopted in the Liouville equations. The expression (6.41), in contrast to the traditional approximation (6.36), clearly introduces no model dependence in the background oblateness.

As is clear from the discussion of the last section, the stability of the rotation axis in the presence of an applied surface mass load is intimately connected to the expression $1 - k_2^T(s)/k_f$ appearing in

the denominator of the Liouville equation (6.39). From Figure 6.1, the observed fluid Love number, k_f^{obs} , is greater than $k_2^T(s=0; LT)$ for any value of LT (we comment on the origin of this difference below); thus, adopting the expression (6.41) will, in addition to improving the accuracy of the predictions, stabilize the rotation axis relative to predictions based on the approximation (6.36).

If one adopts the observed fluid Love number in place of k_f , then the accuracy of the predictions may still be impacted by errors in the viscoelastic Love number theory used to generate $k_2^T(s)$. (That is, errors incurred by ignoring second-order and higher terms in the first-order Love number theory.) To highlight this point, I also superimpose on Figure 6.1 the value of $k_2^T(s=0; LT=0)$ computed by Nakiboglu (1982) using his second-order accurate hydrostatic theory applied to PREM. The difference between this value (0.9305) and the left intercept of the solid line, which represents the hydrostatic form predicted using Love number theory, provides a measure of the accuracy of the latter. This error, interestingly a 1 part in 300 overestimate, would have implications for the predicted stability of the rotation axis. In particular, the expression $1 - k_2^T(s)/k_f^{obs}$, where $k_2^T(s)$ is based on viscoelastic Love number theory, will approach zero more closely than would a second-order accurate theory; thus, predictions based on this theory will still underestimate the true stability of the rotation pole, even when k_f has been appropriately replaced by the observed value, as in equation (6.41).

In the remainder of this section I propose two conceptually independent, but ultimately equivalent, approaches to further improving the accuracy of TPW predictions beyond the level obtainable with the combined equations (6.39) and (6.41).

Nakada (2002) suggested that one possible route to avoiding the paradox in his results (for a very high viscosity lithosphere and an elastic lithosphere of equal thickness; Figure 6.2B) was to use the approximation

$$k_f \sim k_2^T(s=0; LT=0) \quad (6.42)$$

in the Liouville equations. That is, he suggested that, regardless of the model used to predict the deformational response to the surface mass load and rotation perturbation, one adopt the fluid limit of the $k_2^T(s)$ Love number computed for a model with no elastic lithosphere ($LT=0$) as a proxy for the fluid Love number in the Liouville equations (6.34) or (6.39). (In Figure 6.1, $k_2^T(s=0; LT=0) = 0.934$.)

While this suggestion might seem ad-hoc, there is some reasonable justification for considering it. In particular, in the absence of other geophysical contributors (e.g., plate tectonics) or a fossil rotational bulge, the equilibrium rotating form of the Earth would be most accurately computed for models with no purely elastic strength in the lithosphere (i.e., pure hydrostatic theory); note, in this regard, that $k_2^T(s=0; LT)$ tends toward k_f^{obs} in Figure 6.1 as LT approaches zero. This hydrostatic rotational form would be set early in Earth history, when $LT \sim 0$, and any subsequent increase in elastic strength would develop on this pre-existing form. That is, a slowly developing elastic

strength of the lithosphere as the planet cools would exert no elastic stresses on this pre-existing form; however, the elastic strength would be important, and should be included (as it generally is), when considering any recent response of the planet to a surface mass or rotational load. (As a digression, [Mound et al. \(2003\)](#) have recently considered the equilibrium form of a rotating planet with a thin elastic shell; although the theory they describe is correct, it has limited relevance to understanding the present-day oblateness of the Earth; the usual hydrostatic theory with $LT = 0$ is more appropriate.) Thus, LT might be set to zero when considering the background oblateness, but LT should not be zero when treating the Pleistocene deformational response of the planet to a surface mass or rotational loading.

Of course, the primary problem with the approximation (6.42) is that it ignores other geophysical contributions to the background oblateness of the planet. In reference to Figure 6.1, the difference between the observed fluid Love number and that obtained by second order hydrostatic theory ($0.938 - 0.9305 \sim 0.008$) represents an excess ellipticity (henceforth β) of the planet that is widely interpreted as being dynamically supported by mantle convective flow. A more accurate prediction of the rotational response of the planet would be obtained by revising the approximation (6.42) to include this excess ellipticity:

$$k_f \sim k_2^T(s = 0; LT = 0) + \beta = 0.942 \quad (6.43)$$

(where $\beta = 0.008$). When this equation is applied to the s -domain Liouville equation (6.39), the denominator of the model-dependent term becomes $1 - k_2^T(s)/[k_2^T(s = 0; LT = 0) + 0.008]$; this expression clearly includes the stabilizing influence of the Earth's inferred excess ellipticity, while having the advantage of involving terms ($k_2^T(s)$, $k_2^T(s = 0; LT = 0)$) that are computed using a consistent (Love number, first order) level of accuracy.

As a second approach, I begin with the expression (6.41). In contrast to the approximation (6.36) or (6.42), adopting the observed fluid Love number in place of k_f in the Liouville theory implicitly incorporates all processes contributing to the background form (e.g., mantle convection, etc.) However, when equation (6.41) is combined with the s -domain Liouville equation (6.39), the denominator of the governing equation becomes $1 - k_2^T(s)/k_2^{obs}$, and, as discussed above, the accuracy of this expression is impacted by errors in the first-order accurate viscoelastic Love number theory used to compute $k_2^T(s)$. The difference between the hydrostatic ($LT = 0$) predictions based on viscoelastic Love number theory and [Nakiboglu \(1982\)](#)'s second-order approach (see Figure 6.1), suggests a fractional error in the former of $\epsilon = (0.934 - 0.9305)/0.9305 \sim 0.0037$. Assuming that this error holds for all s values, and not simply the hydrostatic ($s = 0$) case, one can scale $k_2^T(s)$ computed using viscoelastic Love number theory by a factor $(1 - \epsilon)$ to correct for the error in the first-order theory. In this case, the denominator in the governing s -domain equation would become

$1 - k_2^T(s)(1 - \epsilon)/k_2^{obs}$. Since $\epsilon \ll 1$, this is equivalent to revising equation (6.41) for k_f to:

$$k_f \sim k_f^{obs}(1 + \epsilon) = 0.942. \quad (6.44)$$

While conceptually different approaches to derive equations (6.43) and (6.44) have been used, the final expressions for k_f are identical.

The traditional approach to computing GIA-induced perturbations in the Earth's rotation vector (equations 6.38, 6.39) should be replaced by a combination of the general Liouville equations (6.34, 6.39) and the expression (6.43) or (6.44) for the fluid Love number k_f . The new theory avoids the erroneous, model-dependent treatment of the background form that is inherent to the traditional theory, while incorporating the stabilizing influence on the rotation axis of the excess (i.e., non-hydrostatic) bulge of the planet.

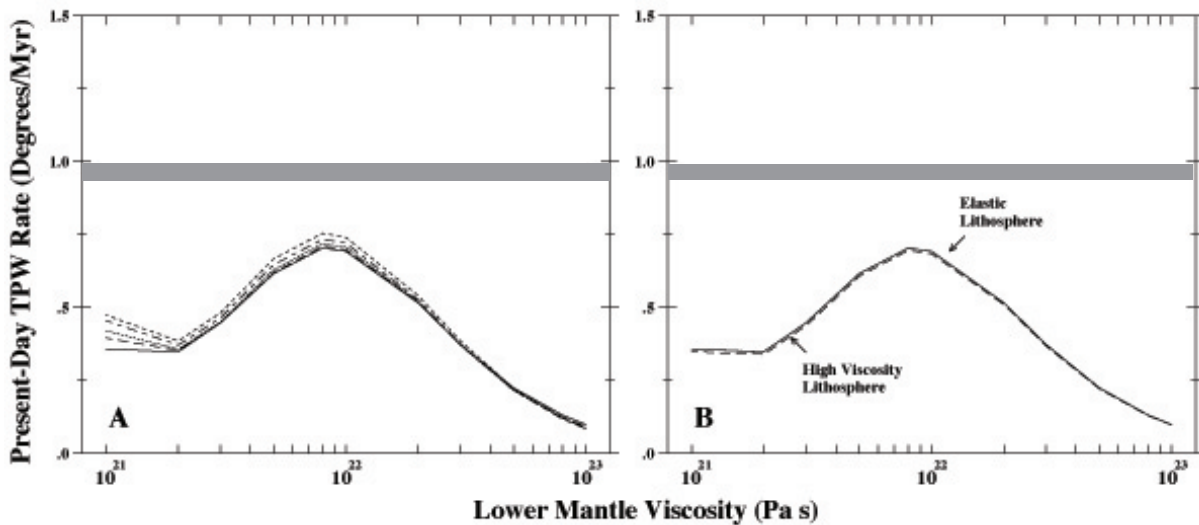


Figure 6.5 As in Figure 6.2, except the predictions are generated using the generalized time-domain Liouville equations (6.34; with k_f given by equation 6.43) (or equation 6.44). Note that the dotted line on the right frame is indistinguishable from the solid line. The shaded region encompasses observational constraints (McCarthy & Luzum, 1996; Gross & Vondrak, 1999) in two studies of astronomical records.

Figure 6.5 shows predictions of present-day TPW speed generated using the new theory for the same set of Earth models adopted in Figure 6.2. A comparison of Figures 6.2 and 6.5 indicates profound differences. The results in Figure 6.5A show that predictions of present-day TPW speed due to GIA are, in contrast to conclusions based on the traditional rotation theory, insensitive to variations in the adopted elastic lithospheric thickness. In reference to remarks in Section 6.1, I also conclude that the unique sensitivities evident in previous predictions of present-day TPW speed (e.g., Figure 6.2A), relative to other long wavelength observables associated with GIA (e.g., \dot{J}_2), are a result of the error introduced by the approximation (6.36) for the background form of the

planet.

Figure 6.5B shows results for predictions with $LT = 100$ km (solid line) and a pair of Earth models with a viscoelastic lithosphere of increasing viscosity. The very high viscosity (10^{28} Pa s) lithosphere results (dotted line; not evident below the solid) have converged to the $LT = 100$ km suite of predictions. My revised theory ensures that *both* the deformational response to surface mass and rotational loading associated with GIA and the background form (oblateness) of the planet are identical for models with a high viscosity lithosphere and an elastic lithosphere of equal thickness. The ‘paradox’ introduced by the previous approximation (6.36) thus disappears.

The stabilizing influence of using equations (6.43) or (6.44) in place of the traditional approximation (6.36) is explored in detail in Figures 6.6 and 6.7, where a decomposition of the model-dependent terms in the s -domain Liouville equation (6.39): (A) $1 - k_2^T(s)/k_f$, (B) $1 + k_2^L(s)$, and (C) their ratio is considered. These figures may be directly compared to analogous plots for the traditional TPW theory, Figures 6.3 and 6.4, respectively. Since the only difference between the old and new approaches is in the treatment of k_f , Figures 6.3B and 6.6B, as well as Figures 6.4B and 6.7B, are identical.

Figure 6.6 shows results for a suite of models with different lower mantle viscosities and $LT = 100$. Following equation (6.43), $k_f = 0.942$ as opposed to $k_f = k_2^T(s=0; LT=100) \sim 0.923$ (Figure 6.1) adopted using the traditional theory. As a consequence, the denominator $1 - k_2^T(s)/k_f$ is shifted away from zero in Figure 6.6A relative to Figure 6.3A, and the result is a dramatic stabilization of the rotational state (compare Figures 6.3C, 6.6C). Figure 6.7 involves three models, all with $\nu_{LM} = 10^{21}$ Pa s. The solid line is the case for $LT = 100$, while the dotted line (which is indistinguishable from the solid) was computed using a high viscosity (10^{28} Pa s) lid of the same thickness but with $LT = 0$. Since the s -domain Love numbers $k_2^T(s)$ and $k_2^L(s)$ for these two models are the same over the s range considered in the plot, and since the new theory removes any model (LT) dependence in k_f , no difference is seen between the two predictions of the rotational state and its contributions; thus, the paradox observed by Nakada (2002) is reconciled (as in Figure 6.5B). The dashed-dotted line in Figure 6.7B is a prediction for $LT = 0$ and no lithospheric lid; in this case, the Earth model shows higher levels of compensation in response to the rotational forcing on the bulge (frame A) and the surface mass load (frame B), relative to the $LT = 100$ case, and the net effect is a ratio (frame C) reflecting comparable rotational stability for the two cases ($LT = 0, 100$ km). Hence, predictions of present-day TPW speed based on the new theory are relatively insensitive to variations in LT (Figure 6.5A).

To this point I have focused entirely on predictions of present-day TPW speed. Figure 6.8 compares predictions of the pole displacement, relative to the present value (hence all curves pass through zero at present), over roughly the last ~ 90 kyr. These predictions were computed using models with an elastic lithospheric thickness of 100 km, and two values of lower mantle viscosity (as labeled by ‘LM’ on each frame). Furthermore, in each case the time-domain Liouville equation

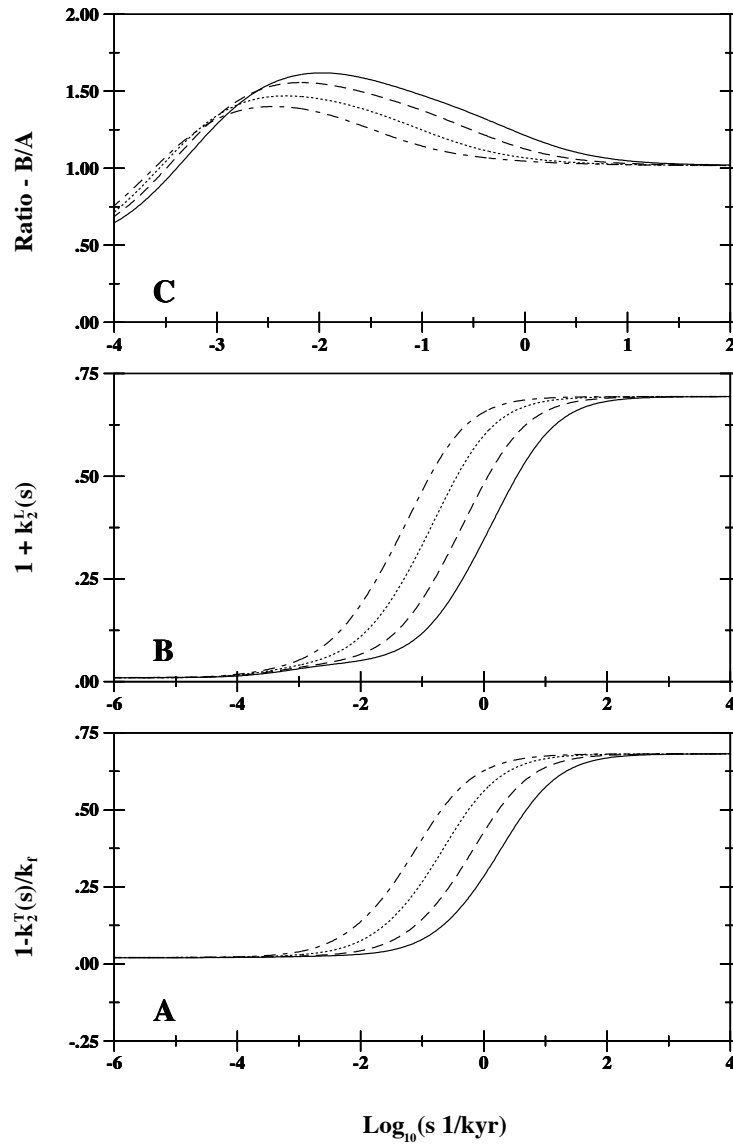


Figure 6.6 Decomposition of the model dependent components of the generalized Liouville equation (6.39) as a function of the Laplace transform variable s : (A) $1 - k_2^T(s)/k_f$, where k_f is given by equation (6.43) or (6.44); (B) $1 + k_2^J(s)$; and (C) the ratio (B/A) of these terms. In each frame, results are shown for four Earth models with distinct ν_{LM} : 10^{21} Pa s (solid line); 3×10^{21} Pa s (dashed line); 10^{22} Pa s (dotted line) and 3×10^{22} Pa s (dashed-dotted line). In each case, $LT = 100$ km and the upper mantle viscosity is 10^{21} Pa s. Note that Frame B is identical to Figure 6.3B.

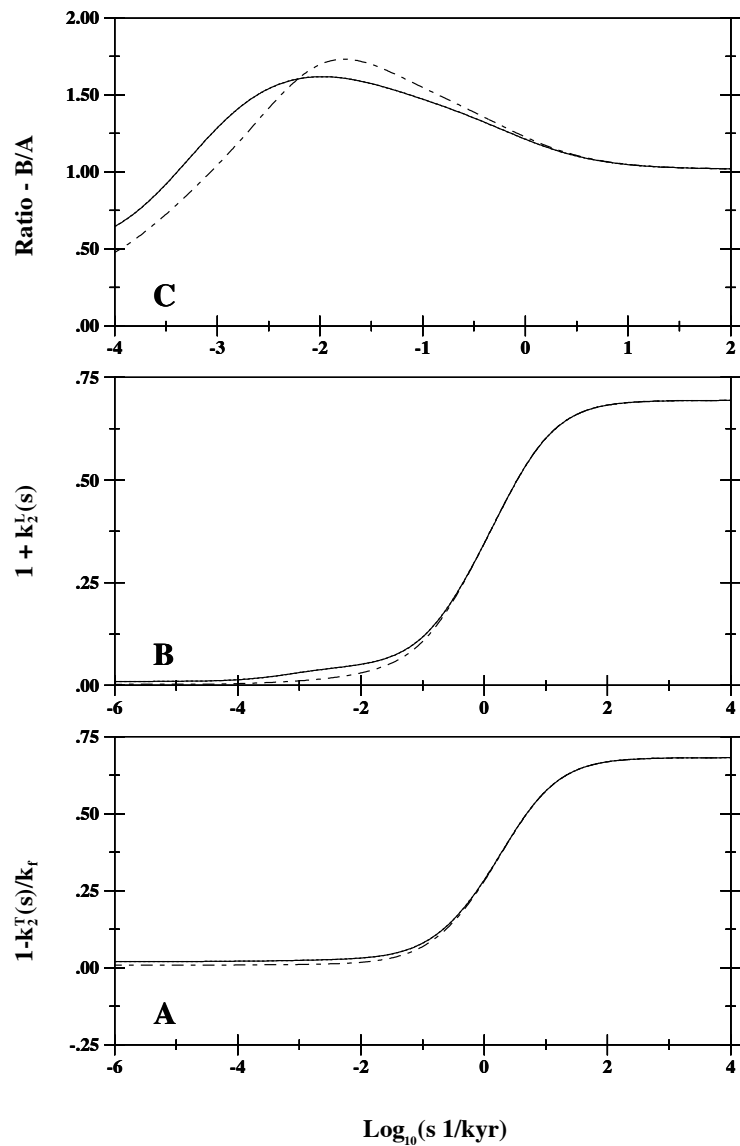


Figure 6.7 As in Figure 6.6, except for a set of three Earth models distinguished on the basis of my treatment of the lithosphere. In all cases both ν_{LM} and the upper mantle viscosity (below the lithosphere) are 10^{21} Pa s. Solid line - an elastic lithospheric thickness, $LT = 100$ km (same as solid line in Figure 6.6); Dashed-dotted line - $LT = 0$ and the top 100 km of the model is set to the bulk upper mantle viscosity; Dotted line - $LT = 0$ and the top 100 km of the model is given a high viscosity (10^{28} Pa s) lithospheric lid. The dotted line is indistinguishable from the solid in all frames. Note that Frame B is identical to Figure 6.4B.

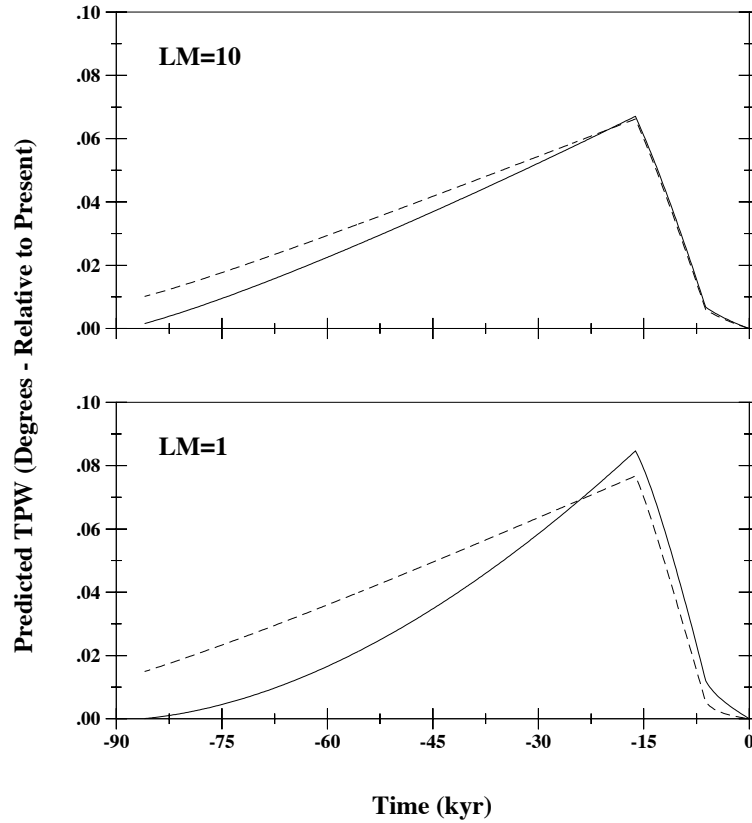


Figure 6.8 Predictions of the displacement of the rotation pole over the last ~ 90 kyr of the loading history, relative to the present position, computed using an Earth model with a purely elastic lithosphere of thickness 100 km, an upper mantle viscosity of 10^{21} Pa s, and a lower mantle viscosity of either 10^{21} Pa s (bottom frame) or 10^{22} Pa s (top frame). In each frame the solid line was generated using a time-domain form of the governing Liouville equation with k_f given by the traditional approximation (6.36) (i.e., $k_f = k_2^T(s = 0; LT)$). The dashed line uses my new formulation (equation 6.43 or 6.44) for the fluid Love number. The surface mass loading is described, in detail, in the text.

(6.34) is solved, with the fluid Love number k_f given either by the traditional approximation (6.36; solid line), or the new approach (6.43, 6.44; dashed line). Figure 6.9 shows analogous results, except for the variation in TPW speed over the same period.

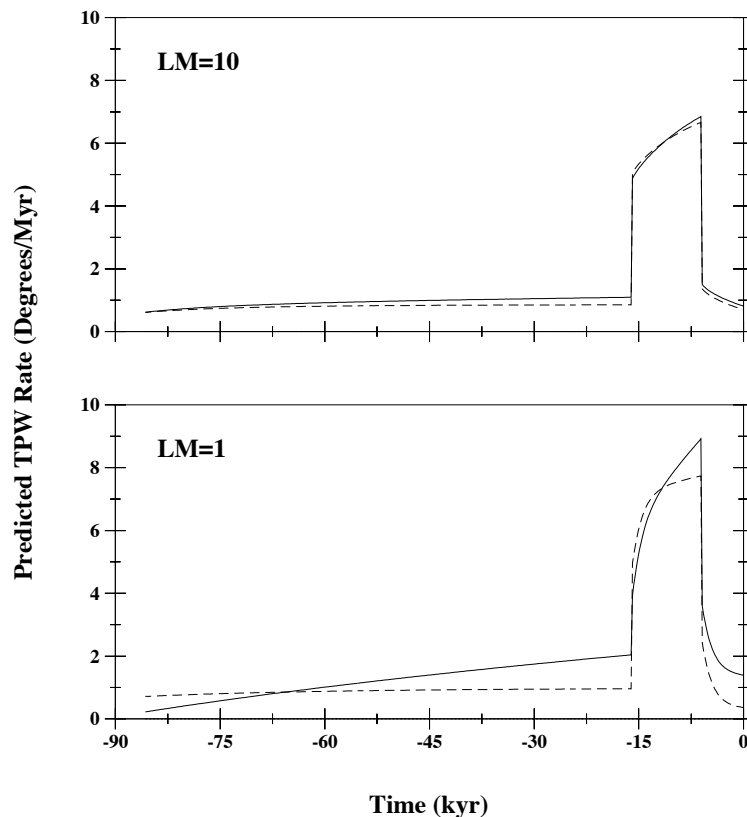


Figure 6.9 As in Figure 6.8, except for the speed of the rotation pole.

In both figures it is clear that the traditional approximation adopted in the GIA literature, that the background oblateness in the Liouville equations can be specified using $k_2^T(s=0; LT)$ yields predictions of the pole path which are significantly different from predictions where the oblateness is a model-independent reflection of the hydrostatic form plus excess ellipticity. As one would expect from Figures 6.2 and 6.5, the predicted discrepancy is smaller for the model with the higher lower mantle viscosity of 10^{22} Pa s. Also note, in reference to Figure 6.9, that the discrepancy in the predicted present-day TPW speed between Figures 6.2 and 6.5 is established by the end of the deglaciation event, at 6 kyr before present; that is, the absolute change in the predicted TPW speed over the last 6 kyr is largely the same in the two formulations.

The derivation of my new expressions for the fluid Love number k_f assumes a value of $\beta = 0.008$ for the contribution associated with the excess (i.e., non-hydrostatic) ellipticity of the planet; this assumption is explicit in equation (6.43) and implicit in equation (6.44). This value of β is inferred from the difference between the observed k_f and the fluid Love number predicted by Nakiboglu (1982) using a second-order accurate hydrostatic theory (Figure 6.1). Since the latter depends on

the density model (Nakiboglu used the PREM density profile), the inference of β is subject to some uncertainty. To explore this issue the $LT = 100$ calculations shown in Figure 6.5A (solid line, $\beta = 0.008$) have been repeated for a suite of different choices for the β parameter in equation (6.43). The results are shown in Figure 6.10.

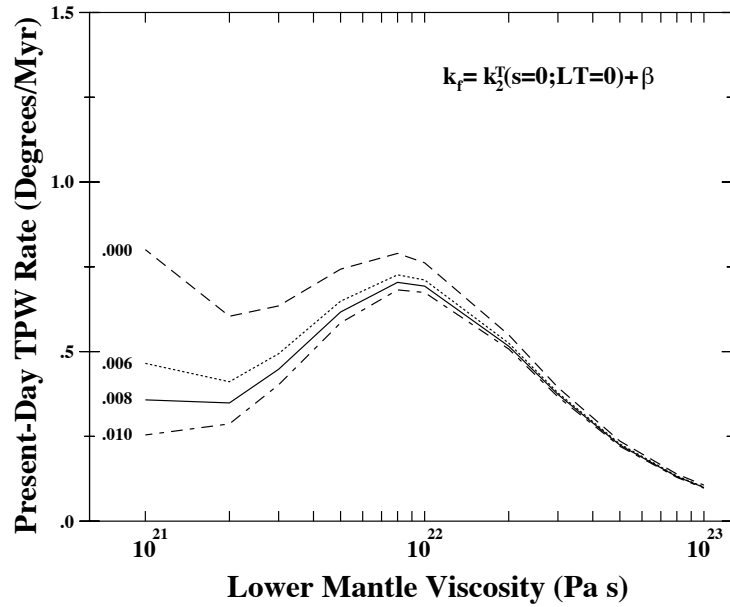


Figure 6.10 Summary of predictions of present TPW speed, as a function of the lower mantle viscosity (abscissa scale) of the Earth model, generated using the time-domain Liouville equation (6.34). The predictions are generated using the new formulation (6.43) for the fluid Love number, and each line is distinguished on the basis of the choice for the parameter β (i.e, the contribution to k_f associated with the excess ellipticity of the Earth; as labeled at left). In particular, $\beta = 0.0$ (dashed line; i.e., the Nakada (2002) approach in equation 6.42), 0.006 (dotted line), 0.008 (solid line; as assumed in equation 6.43 following the difference between the ‘observed’ and ‘Nakiboglu’ results in Figure 6.1), and 0.010 (dashed-dotted line). All calculations adopt an upper mantle viscosity of 10^{21} Pa s, and $LT = 100$ km. The surface mass load history is described in the text.

Not surprisingly, as the β value is increased from 0.0 to 0.010, the stability of the rotation pole increases and the amplitude of the predicted TPW speed monotonically falls. In the $\beta = 0$ case, the general expression (6.43) reduces to the approach (6.42) considered by Nakada (2002). The difference between this case and the results for $\beta \sim 0.008$ highlights the significance of incorporating the excess ellipticity of the planet into predictions of GIA-induced TPW. The range $0.06 < \beta < 0.010$ provides a reasonable estimate of the uncertainty associated with the excess ellipticity, and, accordingly, the zone between the dotted and dashed-dotted lines in Figure 6.10 represents a measure of the uncertainty in the predicted TPW speed associated with GIA.

6.7 The Physics of GIA-Induced TPW: A Summary

The numerical predictions summarized above have highlighted subtle, and previously unappreciated, issues related to the rotational stability of an ice age Earth. The viscoelastic GIA problem has important similarities to, and significant differences with, classic treatments of the rotational stability of rotating inviscid planets (Gold, 1955; Goldreich & Toomre, 1969; Willemann, 1984). In this section I provide a general physical framework for understanding the traditional and new (see Chapter 5) GIA predictions within the context of these earlier seminal studies. My discussion will be supported by the schematic illustrations in Figure 6.11.

Traditional predictions of GIA-induced TPW assume no underlying geodynamic contributions to the inertia tensor. That is, no account is taken, for example, of any excess ellipticity driven by mantle convective flow. Furthermore, these predictions assume that the equilibrium rotating form of the planet is a function of the elastic lithospheric thickness. Conceptually, the latter assumes that the equilibrium form was established by first starting with a non-rotating model having an elastic lid of thickness LT and then considering the infinite time, equilibrium form generated by imposing the present rotation rate onto this idealized model. With this in mind, one can consider two sub-cases; $LT = 0$ and $LT \neq 0$. These are illustrated in Figures 6.11A and B, respectively, with the left-most panel in each case showing the initial, equilibrium form.

For the first of these cases, $LT = 0$, one may still suppose that the lithosphere acts as a zone of high viscosity in its response both to the ice load and to the change in centrifugal forcing. Now suppose a surface mass loading is instantaneously applied, for example an ice load upon Hudson Bay (Figure 6.11A2). The rotation axis responds by moving away from Hudson Bay. (In Figure 6.11 the green arrows acting on the rotation pole refer to the TPW driven by the ‘green’ surface mass load dimple.) That is, the adjustment will tend to move the ice load toward the point furthest from the rotation axis, the equator. Initially, though, the rotation axis will not move very far, because as it gets displaced the large equatorial (i.e., C-A) bulge moves off the equator, and this will induce a restoring force on the rotation axis. (In Figure 6.11 the blue arrow acting on the rotation pole refers to the TPW driven by any unrelaxed rotational bulge.) In time, the equatorial bulge viscously adjusts to the perturbation in the centrifugal force caused by the displaced rotation axis, rearranging mass towards the new equator; the axis is then free to shift further away from the ice load (Gold, 1955; Goldreich & Toomre, 1969). At the same time, of course, the Earth beneath the ice load relaxes viscously, so that the axis is not pushed away from the load quite so strongly. This trend is reflected by the gradual subsidence toward isostatic equilibrium of the surface mass load in Figure 6.11A and the gradual diminution of the load-induced TPW signal (green arrow).

In the limit of infinite time, the load-induced forcing will vanish since the surface mass load will be perfectly compensated when $LT = 0$. In addition, at infinite time the rotationally induced bulge will have relaxed completely to the orientation of the new rotation axis, and thus the ellipsoidal form

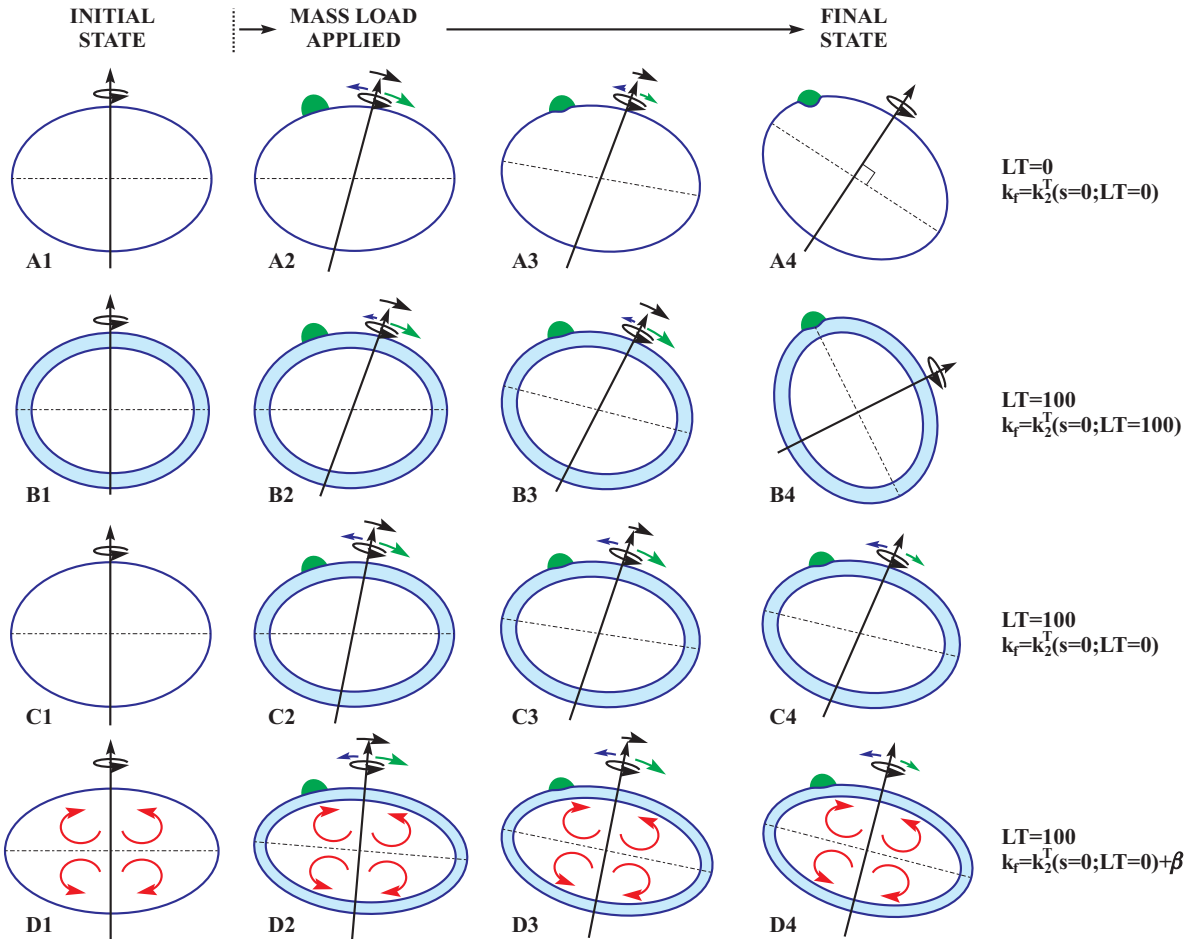


Figure 6.11 Schematic illustrating the physics of GIA-induced TPW for various modeling scenarios. Details of the figure are provided in the text. On the right margin, the LT value refers to the thickness of the elastic lithosphere associated with the response to both a surface mass load and rotational driving potential (shaded blue region superimposed on the Earth models); furthermore, k_f is the fluid Love number that governs the equilibrium background form of the planet (β is the contribution from excess ellipticity; see equation 6.43). The long and straight black arrow passing through the models is the rotation axis. The green dimple on the various frames represents a surface mass load, which is subject to some degree of isostatic compensation, while the red arrows within the planetary interior denote any underlying geodynamic processes (e.g., mantle convection). The green arrow represents the TPW signal driven by the surface mass loading, while the blue arrow is the TPW signal connected to any remnant bulge effects (e.g., due to an unrelaxed rotational form subsequent to a TPW event, or long-term excess ellipticity).

in Figure 6.11A4 is simply a re-oriented version of the form in Figure 6.11A1. Thus, both the green and blue arrows have disappeared in the final, equilibrium state (Figure 6.11A4). At this stage, the rotation pole will have shifted a finite, but non-zero amount, governed by the balance between the two processes of viscous relaxation. Furthermore, the rate of polar motion will have fallen off to zero. This result can also be inferred, mathematically, from the Laplace transform inversion of equation (6.39), given in Appendix E. In the case of a viscous lithosphere, $k_2^L(s=0) = -1$ and thus the load compensation term $D_2 = 0$. Thus, the response is well behaved in the long time limit since the linear term in time, t , in equation (E.7) vanishes. In any event, at infinite time, the pole has not returned to where it started, even though the ice load is completely compensated. Without any underlying geodynamic contributions to the inertia tensor, the Earth has no preferred location for its rotation axis.

Next, consider an Earth model in which $LT \neq 0$ (Figure 6.11B), and where the fluid Love number is computed using equation (6.36) with this same non-zero lithospheric thickness. In this case, there is still a non-zero load imposed on the planet at infinite time since the surface mass load is never fully compensated (Figure 6.11B2-4). In contrast, the equatorial bulge can, at least in principle, relax completely to a change in the orientation of the rotation axis. That is, there will be no remnant bulge since the model used to compute the background oblateness (i.e., $k_2^T(s=0; LT)$) is the same as the model used to compute the response to the driving potential. Thus, at infinite time, the rotation axis will continue to be pushed away from the load, but there will be no residual bulge to supply an opposing force. This can again be confirmed mathematically with reference to equation (E.7); when $LT \neq 0$, $D_2 = 1 + k_2^L(s=0) \neq 0$, and thus the displacement of the pole increases linearly in time while the rate of motion does not converge to 0. In a non-linear theory, the displacement would, of course, cease when the load reaches the equator, as in Figure 6.11B4.

This example ($LT \neq 0$) is consistent with the basic physics addressed by Gold (1955) and Goldreich & Toomre (1969), and one arrives at the same conclusion: The rotation of an Earth model in the presence of an uncompensated mass load, and in the case where the equatorial bulge can relax completely, is unstable. Note that Gold (1955) and Goldreich & Toomre (1969) arrived at this conclusion using a hybrid model that was hydrostatic in its response to a perturbation in rotation and rigid in its response to a surface mass load.

In contrast to Figure 6.11B, the first scenario (Figure 6.11A) provides an extension of the Goldreich & Toomre (1969) physics to the case where there is also perfect, at infinite time, compensation of the surface mass load (since $LT = 0$). In this case, the compensation acts to stabilize the rotation pole. The increased stability of the pole as $LT \rightarrow 0$ is the key to understanding the trends for different values of LT in the ‘traditional’ calculations of Figure 6.2A (see also the discussion related to Figure 6.3B).

Next, let us turn to the case in which the background oblateness is consistent with an entirely fluid planet, while the Earth’s response to the surface mass load and centrifugal driving potential

over GIA time scales involves an elastic lithosphere of thickness $LT \neq 0$ (Figure 6.11C). It is continued to assume that there are no underlying geodynamic contributions to the background oblateness. In contrast to the above, $LT \neq 0$ scenario (row B), it is presumed that either: (1) the equilibrium form is hydrostatic and that it was set early in Earth history when there was no lithosphere; or (2) that while the lithosphere might maintain elastic strength over GIA time scales and stress levels, it might not do so in the presence of much larger, and long-term, rotation. Regardless, this scenario is consistent with the case where the expression (6.42) is used within the Liouville equations.

The final GIA-induced polar wander in this case (Figure 6.11C4) is characterized by a finite, but non-zero shift, and the rate of polar motion converges to zero. The reason is that while the rotation axis continues to be pushed away from the incompletely compensated load (the load-induced, green arrow, TPW signal in Figure 6.11C does not vanish), the equatorial bulge cannot relax completely to the change in pole position. That is, there will be a remnant rotational bulge, and eventually a final, equilibrium balance at non-zero distance from the original pole position is achieved. The incomplete relaxation of the bulge is a consequence of the fact that the background oblateness is hydrostatic, while the response to the TPW is, in contrast, subject to a perfectly elastic lithosphere.

This third scenario can be considered an extension of the Goldreich & Toomre (1969) results to the case where the rotational bulge is not permitted to relax completely; see Chapter 5 for a discussion of the final, equilibrium state in this scenario (Figure 6.11C4). The stabilization of the rotation pole associated with this extension (Figure 6.11C4 compared to Figure 6.11B4) is the underlying reason why the prediction of GIA-induced TPW rate based on the expression 6.42 (dashed line, Figure 6.10) has less amplitude than the traditional prediction (solid line; Figure 6.2) based on equation (6.36), where both adopt $LT = 100$ km in predicting the response to the surface mass load and TPW.

The third scenario highlights a general principle. In the case where the lithosphere has elastic strength in response to a changing surface mass load and rotational driving potential, the stability of the rotation pole at infinite time (i.e., the displacement of the pole to a position less than 90° from the imposed load) requires that the background oblateness be larger than the equilibrium form obtained after a change in the pole position. That is, the fluid Love number has to be greater than $k_2^T(s = 0; LT)$ in the symbolism adopted in the text. The scenario in Figure 6.11C achieves this by having the background form coincide with the hydrostatic state of the planet; from Figure 6.1, note again that $k_2^T(s = 0; LT = 0) > k_2^T(s = 0; LT \neq 0)$.

An additional way of ensuring that the background oblateness be larger than the post-TPW equilibrium form is to incorporate an excess ellipticity of the planet originating from a static, relative to the time scale of GIA, geodynamic process such as mantle convection. This case is described by equations (6.43) and (6.44) and it is the subject of Figure 6.11D. At infinite time, when $LT \neq 0$, the uncompensated surface mass load will continue to push the pole away, while the

incomplete relaxation of the rotational bulge will resist this trend (as in Figure 6.11C4). In addition, the underlying geodynamic contribution, that is the convection-induced excess ellipticity, will not relax, and will thus contribute a further, stabilizing influence on the pole position (compare Figure 6.11D4 and C4). As before, a balance will be achieved; the net pole displacement will diminish as the adopted level of excess ellipticity increases. Indeed, the monotonically stabilizing effect of increasing the excess ellipticity is clearly evident in Figure 6.10. This is a further extension to the basic physics of a rotating Earth elucidated by Gold (1955) and Goldreich & Toomre (1969).

A final scenario is worthy of a brief comment. Let us return to the case where the Earth model has no elastic strength in the presence of a surface mass or rotation-induced potential loading (i.e., $LT = 0$). In the case of a hydrostatic background form, i.e. when there is no underlying geodynamic contribution of an excess ellipticity, the scenario of Figure 6.11A indicates the pole will ultimately be stabilized by the complete (at infinite time) compensation of the surface mass load. What if an excess ellipticity into the $LT = 0$ scenario of Figure 6.11A is introduced, or, equivalently, what if $LT = 0$ in the scenario treated in Figure 6.11D? In this case, the pole would return, at infinite time, to its initial location prior to loading since the geodynamically-supported excess flattening will not relax, except perhaps over time scales that are long relative to the geodynamic process. The geodynamic contributions provide a preferred location for the rotation axis in this scenario, and the surface mass loading introduces only a transient perturbation in the pole location.

6.8 Final Remarks

The prediction of GIA-induced variations in the Earth's rotation axis has a modern history which dates back to theoretical work, based on viscoelastic normal mode theory, from the early 1980's. The stability of the rotation pole on a viscoelastic planet loaded by a surface mass depends on both the deformational response of the planet to the mass and (associated) rotational load as well as on the background oblateness upon which this deformation is applied. The main conclusion of this Chapter is that traditional GIA calculations have erred in using a strongly model-dependent prediction of this background form, rather than a (model-independent) oblateness that reflects the excess ellipticity of the planet from its hydrostatic form. The traditional approximation is, in practice, embedded in an assumption that the so called fluid Love number, k_f , appearing in the linearized Euler, or Liouville equations may be replaced by the fluid ($s = 0$) limit of the s -domain k_2^T tidal Love number computed for the same Earth model used to predict the load-induced deformation. As discussed above, this assumption introduces an error that is a strong function of the elastic lithospheric thickness in the adopted Earth model.

We propose an alternate theoretical treatment, where the fluid Love number is based on either: (1) the hydrostatic ($LT = 0$, $s = 0$) form computed using viscoelastic Love number suitably augmented to include the independently inferred excess ellipticity of the Earth (equation 6.43);

or (2) the observed (i.e., present-day) oblateness and rotation rate of the planet with a scaling applied to account for errors in the Love number theory adopted to compute the response of the Earth model to a mass load or centrifugal forcing (equation 6.44). These treatments ultimately lead to identical expressions for k_f ; predictions based upon them show a more stable rotation pole, relative to traditional predictions, with lower predicted amplitudes for present-day TPW speed. Significantly, the new results do not show sensitivities, for example to the adopted lithospheric thickness or rheology, that have characterized previous studies and that have heretofore defied explanation.

It is not uncommon within the GIA literature to compute Love numbers using highly simplified Earth models which, in some bulk sense, approximate the Earth's elastic and density structure. Predictions of TPW which mix calculations of $k_2^T(s)$ with the observed value of the fluid Love number, k_f , would, in this case, be subject to potentially large errors. My new formulations (6.43) and (6.44) ensure, either explicitly or implicitly, that the denominator and numerator of the ratio $k_2^T(s)/k_f$ appearing in the Liouville equation differ by the excess ellipticity of the planet as the fluid limit is approached. Thus, they also have the advantage of limiting the error incurred in TPW predictions that adopt such simplified Earth models.

Predictions of present-day polar wander speed based on the new theory of rotational stability raise an important issue. The observed rate of TPW (Figure 6.5) can be fit by a model of GIA when the old theory is used as a basis for the calculation. However, no model of GIA appears capable of reconciling the data when the new theory is applied. Thus, some other geophysical process, for example mantle convection (Steinberger & O'Connell, 1997) or present-day melting of ice sheets would have to be invoked to explain the residual. If the latter is significant, then the melting would have to be sourced to Greenland, since mass flux from the Antarctic will not drive significant excursions of the rotation pole.

Chapter 7

Summary

The major aim of this thesis has been to study the rotational stability of planets in the context of true polar wander (TPW).

A quasi-rigid body can be defined as a body for which changes in the inertia tensor occur on time scales that are longer than the slowest of the nutations experienced at any stage. The rotational adiabatic invariance discussed in Chapter 2 is valid for a quasi-rigid body and it allows one to assume that TPW is solely governed by the non-hydrostatic inertia tensor variations.

In Chapter 3, following the analysis of Goldreich & Toomre (1969), I considered the rotational stability of simple quasi-rigid bodies consisting of randomly distributed mass anomalies (beetles) on the surface of a sphere. In these simple models, the only non-hydrostatic inertia tensor perturbations are associated with the random mass distributions. In application to planets, external or internal processes such as surface loading or mantle convection respectively may be regarded as the random mass anomalies. Planets differ from these models in that they can deform in response to these processes. Nevertheless, the rotational stability of these simplified quasi-rigid bodies serves to illustrate the basic physics involved. In this case, the TPW speed is determined by the mass redistribution speed (if the rotational bulge relaxation is ignored since no deformation is assumed). For a large number of mass anomalies N the TPW speed exceeds the mass redistribution speed by a factor $\sim N^{1/2}$. Hence, even very modest relative displacements of small mass anomalies can result in large scale polar wandering of the pole for large N .

Rapid and large TPW events occur whenever the memory of the quasi-rigid body for an earlier mass distribution is lost. The shorter the memory, the faster and larger the TPW. For a quasi-rigid body consisting of a colony of randomly crawling beetles, the number of random crawl steps associated with the memory is $n_{mem} \sim N^{-1}\delta\theta^{-2}$, where $\delta\theta$ is the opening angle of each random crawl. Hence, the memory becomes short for a large number of mass anomalies (beetles) or a large mass redistribution speed (which is proportional to $\delta\theta$). The fastest and largest TPW events, referred to as inertia interchange TPW (IITPW) events, occur when the two largest principal axes exchange their moments, and thus, the pole wanders by $\sim 90^\circ$. Translated to planetary terms, in

the case of mass anomalies driven by convection, the rotation pole may wander by $\sim 90^\circ$ in a time slightly longer than the duration of a typical convection element (i.e., the memory) if one assumes that the rotational bulge can relax faster than this.

Planets may be regarded as quasi-rigid bodies if the time scales associated with the processes responsible for mass redistribution, including deformation, are longer than the nutation periods at any stage, and thus, one can invoke the adiabatic invariant discussed in Chapter 2. In this case, as mentioned above, TPW is solely governed by the non-hydrostatic inertia tensor variations.

In Chapter 4, I considered non-hydrostatic inertia tensor perturbations arising from the direct contribution from surface loads, the planet deformation in response to these loads, or the rotationally induced planet deformation. I assumed spherically symmetric, linear (Maxwell) viscoelastic planets to derive general expressions for the time dependent and fluid limit (i.e., time scales much longer than the viscoelastic decay times) inertia tensor variations associated with these causes. I derived a general mapping between the gravitational potential harmonics associated with these causes and the corresponding inertia tensor perturbations. The inertia tensor perturbations are functions of only the degree zero ($\ell = 0$) and two ($\ell = 2$) harmonics of the above causes responsible for these perturbations.

In Chapter 5, I revisited the classic problem of the long-term (secular) rotational stability of planets in response to loading using a generalized theoretical development based on the fluid limit of viscoelastic Love number theory. Gold (1955) and Goldreich & Toomre (1969) considered the stability of a hydrostatic planet subject to an uncompensated surface mass load and concluded that a surface mass of any size (e.g., a ‘beetle’) would drive a true polar wander (TPW) that ultimately reorients the load to the equator. Their work was extended by Willemann (1984) who treated the more self-consistent problem where the presence of a lithosphere leads to both imperfect load compensation and a remnant rotational bulge. Willemann (1984) treated axisymmetric loads and concluded that the equilibrium pole location was governed by a balance, independent of elastic (long-term) lithospheric thickness, between the load-induced TPW and stabilization by the remnant bulge.

My analysis extended Willemann (1984)’s study in several important ways. First, the generalized theory demonstrates that the equilibrium pole position is a function of the lithospheric strength, with a convergence to Willemann (1984)’s results evident only at very high values of elastic thickness (> 400 km for an application to Mars), and significantly larger predicted TPW for planets with thin lithospheres. Second, I derived equations governing the stability of the rotation pole in the case of non-axisymmetric surface mass loads and internal (convective) contributions to the non-hydrostatic inertia tensor. I found that such contributions, even when they are small relative to axisymmetric contributions, can profoundly influence the rotational stability. Indeed, the relatively permissive conditions under which non-axisymmetric forcing initiate an IITPW event were demonstrated. These results suggest that Willemann (1984)’s axisymmetric load analysis signifi-

cantly underestimates the potential excursions of the planetary rotation vector. Finally, [Willemann \(1984\)](#)'s analysis is often cited to argue for a small ($< 18^\circ$) TPW of Mars driven by the development of a Tharsis-sized load. I showed that, even in the absence of the above-noted destabilizing effects of load asymmetry, the equations governing the rotational stability permit higher excursions of the Martian rotation vector than has previously been appreciated.

It has recently been suggested that an IITPW event is a natural consequence of forming the ‘‘Tharsis plume’’ early in Martian history and the subsequent construction of the Tharsis plateau above this plume ([Wieczorek et al., 2005](#)). According to [Wieczorek et al. \(2005\)](#), the Tharsis plume may have been initially aligned with the rotation axis since a buoyant plume corresponds to a negative load (i.e., a negative Q'' following the terminology used in Chapter 5) which pulls the rotation axis toward the plume’s degree two symmetry axis. After this occurs, volcanic construction by cooling of the plume material would produce a positive surface load (i.e., a positive Q'), which pushes the rotation vector toward the equator.

The above scenario supports the case for an IITPW event on Mars. However, it assumes that there is no remnant rotational flattening. I have shown that the second stage in the above scenario, driven by the Tharsis load, is permitted by the equations governing TPW. The prior alignment of the Tharsis plume with the rotation axis must include the opposing and stabilizing effect of the remnant rotational bulge. My analysis in Chapter 5 suggests that large TPW ($> 45^\circ$) to align the Tharsis plume with the rotation axis is only possible if the effective plume size $Q''_{eff} = \alpha_p Q'' < -1$, where α_p is given by equation (5.13) with the appropriate Love numbers. The plume size $|Q''| \ll Q'$, where Q' denotes the size of the Tharsis load, since the plume size is proportional to the density difference between the plume and the mantle while the load size is proportional to the density of the volcanic construction. The upper bound value for the Tharsis region load size is estimated to be $Q' \lesssim 1.74$ by [Willemann \(1984\)](#). Therefore, the alignment of the Tharsis plume with the rotation axis requires $\alpha_p \gg 1$.

My correction to [Willemann \(1984\)](#)'s theory (5.11) introduces a dependence on lithospheric thickness (LT), and, more generally, on the detailed internal structure of the planet (since the fluid Love numbers depend on both) that has previously not been appreciated. Physically, [Willemann \(1984\)](#) assumed that the planet deformation in response to surface loads or perturbations in the centrifugal potential is the same (i.e., $k_f^I = -k_f^T$). This is incorrect. I verified this numerically by adopting the 5-layer model of Martian structure described by [Bills & James \(1999\)](#) (see Table 5.2).

An interesting special case of the generalized set of equations (5.43) and (5.44) is the inertia tensor perturbation associated with internal convective flow (including the mass heterogeneity and its induced surface deformation) and the remnant rotational bulge,

$$I_{ij}^{INT,FB} = I_{ij}^{INT} + I_{ij}^{FB}. \quad (7.1)$$

Using equation (5.11), where the the terms associated with loading (i.e., the terms associated with Q') are ignored, and equation (5.41) yields

$$I_{ij}^{INT,FB}(t) = m' \beta Q''(t) \left(\frac{1}{3} \delta_{ij} - e_{I,i} e_{I,j} \right) + m' \left(e_{\Omega,i}^* e_{\Omega,j}^* - \frac{1}{3} \delta_{ij} \right), \quad (7.2)$$

where δ_{ij} is the Kronecker delta, and \mathbf{e}_I and \mathbf{e}_{Ω}^* are unit vectors indicating the orientation of the degree two convective flow symmetry axis and the initial rotation axis respectively.

These equations raise an important issue. In geophysical studies of the Earth's history of TPW (e.g., Spada et al., 1992b, 1996; Ricard et al., 1993; Richards et al., 1997, 1999; Steinberger & O'Connell, 1997; Greff-Lefftz, 2004) it has been assumed, following the arguments by Gold (1955) and Goldreich & Toomre (1969), that the rotational bulge of the Earth will ultimately respond hydrostatically to a change in the orientation of the rotation vector. (This hydrostatic adjustment is either imposed, a priori, or it is embedded in the long-time scale, secular, limit of the governing stability equations.) That is, the assumption is made that there is no remnant rotational flattening (i.e., $I_{ij}^{FB} = 0$). However, the development of the Earth's lithosphere implies that a non-zero non-hydrostatic rotational bulge may contribute to the rotational stability.

As discussed in §5.4, the exact nature of this non-hydrostatic bulge may be more complicated than equation (7.2) implies. Since most studies of the Earth's long-term TPW have been concerned with the recent (last ~ 100 Ma) geological record, the remnant bulge would reflect an integration of the incremental changes in some globally averaged 'effective' lithospheric strength oriented with reference to the contemporaneous location of the rotation pole. Nevertheless, these expressions can be used to assess whether the assumption made in previous simulations of long-term TPW on Earth might be sensitive to the presence of a lithosphere (i.e., remnant rotational flattening) (Daradich et al., 2005).

In Chapter 6, I explored the time dependent rotational stability by considering an ice age Earth. Predictions of glaciation-induced changes in the Earth's rotation vector exhibit sensitivities to Earth structure that are unique within the suite of long-wavelength observables associated with glacial isostatic adjustment (GIA) and, despite nearly a quarter of a century of research, these sensitivities remain enigmatic. Previous predictions of present-day true polar wander (TPW) speed driven by GIA have indicated, for example, a strong sensitivity to variations in the thickness of the elastic lithosphere and the treatment (phase or chemical?) of the density discontinuity at 670 km depth. Nakada (2002) presented results which suggest that the predictions are also sensitive to the adopted rheology of the lithosphere; however, his results have introduced an intriguing paradox. In particular, predictions generated using a model with an extremely high viscosity lithospheric lid do not converge to results for a purely elastic lithosphere of the same thickness. Mitrovica (see Nakada, 2002) has suggested that the paradox originates from an inaccuracy in the traditional rotation theory (e.g., Wu & Peltier, 1984) associated with the treatment of the background equilibrium

rotating form upon which any load and rotation-induced perturbations are superimposed.

We revisited these issues using a new treatment of the linearized Euler equations governing load-induced rotation perturbations on viscoelastic Earth models. I demonstrated that the revised theory, in which the background form of the planet combines a hydrostatic component and an observationally-inferred excess ellipticity, resolves the apparent paradox. Calculations using the revised theory indicate that earlier predictions based on Earth models with purely elastic lithospheric lids are subject to large errors; indeed, previously noted sensitivities of TPW speed predictions to the thickness and rheology (elastic versus viscous) of the lithosphere largely disappear in the application of the new theory. Significant errors are also incurred by neglecting the stabilizing influence of the Earth's excess ellipticity.

As discussed in §3.4, if the processes responsible for changes in the inertia tensor occur with a random distribution, the principal moments of inertia associated with the non-hydrostatic inertia tensor are expected to differ by almost equal increments. That is, the non-hydrostatic figure of the planet is expected to be triaxial. In application to Earth, [Goldreich & Toomre \(1969\)](#) showed that the non-hydrostatic inertia tensor is indeed triaxial. The linearized Euler's equations used here assume an unperturbed initial state in which the two smallest principal moments are equal (see equation 6.3) and the initial rotation axis is aligned with the principal axis associated with the largest moment of inertia. Thus, the initial unperturbed figure is prolate. In future work, I will extend the revised theory to include a triaxial initial unperturbed state. Alternatively, one can assume an initial unperturbed spherical state and include the inertia tensor perturbations associated with convection as an additional time dependent perturbation by using equation (7.2).

Part III

Appendices

Appendix A

Numerical solution for the viscous diffusion equation

Equation (2.7) can be solved numerically using a backward time finite differencing scheme [Press et al. \(1992\)](#). The advantage of this scheme is that it is stable for any combination of time step δt and radial distance step δR , provided the boundary conditions are well determined. I rewrite equation (2.7) as

$$\frac{\partial \Sigma}{\partial t} = \frac{3}{R} [\Sigma''(\nu R) + \Sigma' (3\nu/2 + 2\nu' R) + \Sigma (3\nu'/2 + \nu'' R)], \quad (\text{A.1})$$

where the primes denote derivatives with respect to the radius R . I introduce the logarithmic variable $y \equiv \ln(R/R_0)$ since the disk covers various order of magnitudes in the radial scale. With this new variable, I can write $dy = dR/R$, and the derivatives take the form

$$\begin{aligned} \frac{\partial X}{\partial R} &= \frac{1}{R} \frac{\partial X}{\partial y} = e^{-y} \frac{\partial X}{\partial y} \\ \frac{\partial^2 X}{\partial R^2} &= -\frac{1}{R^2} \frac{\partial X}{\partial y} + \frac{1}{R^2} \frac{\partial^2 X}{\partial y^2} = e^{-2y} \left(\frac{\partial^2 X}{\partial y^2} - \frac{\partial X}{\partial y} \right). \end{aligned}$$

I rewrite equation (A.1) as

$$\begin{aligned} \frac{\partial \Sigma}{\partial t} &= 3e^{-y} \left\{ e^{-2y} (\Sigma'' - \Sigma') \nu e^y + e^{-y} \Sigma' \left(\frac{3\nu}{2} + 2\nu' \right) + \Sigma \left(\frac{3}{2} e^{-y} \nu' + e^{-y} (\nu'' - \nu') \right) \right\} \\ &= 3e^{-2y} \left\{ (\Sigma'' - \Sigma') \nu + \Sigma' (3\nu/2 + 2\nu') + \Sigma (\nu'/2 + \nu'') \right\} \\ &= 3e^{-2y} \left\{ \Sigma''(\nu) + \Sigma'(\nu/2 + 2\nu') + \Sigma(\nu'/2 + \nu'') \right\} \\ &= 3e^{-2y} [A\Sigma'' + B\Sigma' + C\Sigma], \end{aligned}$$

where

$$A \equiv \nu, \quad B = \nu/2 + 2\nu', \quad C = \nu'/2 + \nu''.$$

Finally, replacing the derivatives by the finite differences

$$\begin{aligned}\frac{\partial \Sigma}{\partial t} &= \frac{\Sigma_j^{n+1} - \Sigma_j^n}{\delta t} \\ \Sigma' &= \frac{\Sigma_{j+1}^{n+1} - \Sigma_{j-1}^{n+1}}{2\delta y} \\ \Sigma'' &= \frac{\Sigma_{j+1}^{n+1} + \Sigma_{j-1}^{n+1} - 2\Sigma_j^{n+1}}{\delta y^2}\end{aligned}$$

gives

$$\frac{\Sigma_j^{n+1} - \Sigma_j^n}{\delta t} = 3 \exp^{-2y} \left[A \left(\frac{\Sigma_{j+1}^{n+1} + \Sigma_{j-1}^{n+1} - 2\Sigma_j^{n+1}}{\delta y^2} \right) + B \left(\frac{\Sigma_{j+1}^{n+1} - \Sigma_{j-1}^{n+1}}{2\delta y} \right) + C \Sigma_j^{n+1} \right], \quad (\text{A.2})$$

where n is the n^{th} time-step, and j is the j^{th} radial location. The variable x is where δt is the time step and δR is the radial distance step. The time and disk radius are given by $t = n\delta t$ and $R = R_{min} + j\delta R$. Equation (A.2) can be written in the tridiagonal form

$$\begin{aligned}\Sigma_j^n &= \Sigma_{j+1}^{n+1} \left[\frac{3\delta t e^{-2y}}{\delta y} \left(-\frac{B}{2} - \frac{A}{\delta y} \right) \right] + \Sigma_j^{n+1} \left[1 + 3\delta t e^{-y} \left(\frac{2A}{\delta y^2} - C \right) \right] \\ &\quad + \Sigma_{j-1}^{n+1} \left[\frac{3\delta t e^{-y}}{\delta y} \left(\frac{B}{2} - \frac{A}{\delta y} \right) \right].\end{aligned} \quad (\text{A.3})$$

To solve equation (A.3), it is necessary to solve a set of simultaneous linear equations at each time step for the Σ_j^{n+1} given an initial solution and the boundary conditions at the inner edge R_{min} and the outer edge R_{max} . I use the boundary conditions $\Sigma(R_{min}) = \Sigma(R_{max}) = 0$.

Appendix B

Rotational stability of free rigid bodies

B.1 Geometric description using the energy ellipsoid and the angular momentum sphere

We follow the analysis of [Landau & Lifshitz \(1959\)](#) to describe the rotational stability of rigid bodies undergoing force-free rotation with a geometrical solution. The inertia tensor \mathbf{I} of an arbitrary body can be reduced to diagonal form by the appropriate choice of reference frame. Two constants of motion are given by conservation of energy and angular momentum:

$$\begin{aligned} E &= \frac{L_1^2}{2I_1} + \frac{L_2^2}{2I_2} + \frac{L_3^2}{2I_3} \\ L^2 &= L_1^2 + L_2^2 + L_3^2, \end{aligned} \tag{B.1}$$

where the energy E and the magnitude of the angular momentum L are given constants. From these equations one can draw some conclusions concerning the rotational stability of rigid bodies. These expressions, regarded as functions of the angular momentum components, L_i , are the equation of an ellipsoid with semi-axes $\sqrt{2EI_1}$, $\sqrt{2EI_2}$, and $\sqrt{2EI_3}$; and that of a sphere of radius L . In the reference frame of the principle axes, the angular momentum vector \mathbf{L} must move along the curves arising from the intersection of these two surfaces. [Figure B.1](#) shows a number of such lines of intersection as the energy E and the ratio between the principal moments of inertia are varied. As one further simplification to the equations for conservation of energy and angular momentum, one can assume, with no loss of generality, that $I_1 \leq I_2 \leq I_3$. The existence of a solution requires that the radius of the sphere lies between the least and greatest semi-axes of the ellipsoid. This

condition corresponds to the energy constraint

$$\frac{L^2}{2I_3} \leq E \leq \frac{L^2}{2I_1}. \quad (\text{B.2})$$

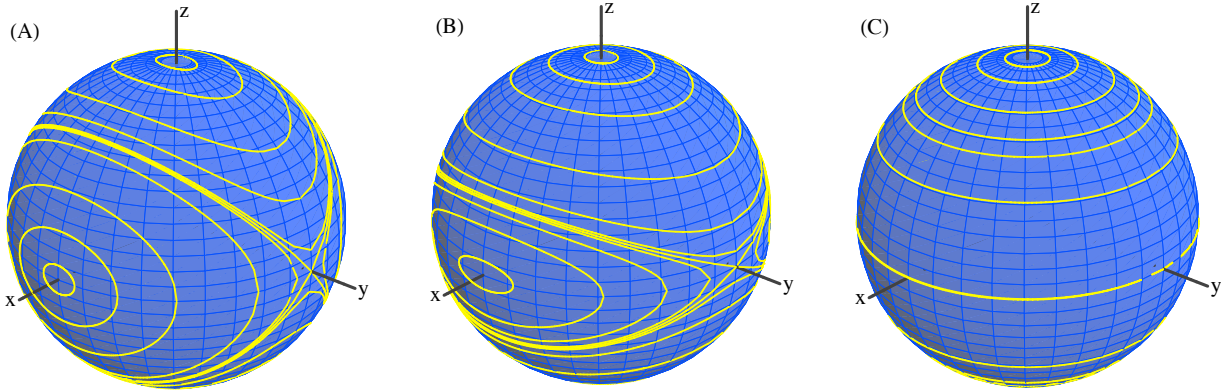


Figure B.1 Curves arising from the intersection of a sphere with an ellipsoid corresponding to conservation of angular momentum and energy (equation B.1). The frames show intersections for different energies in the permitted range (equation B.2) and are distinguished on the basis of the ratio between the the principal moments of inertia: (A) $I_1 : I_2 : I_3 = 8 : 9 : 10$, (B) $I_1 : I_2 : I_3 = 83 : 90 : 100$, and (C) $I_1 : I_2 : I_3 = 8 : 8 : 10$.

We can describe the rotational stability of rigid bodies by examining the paths of intersection. When the energy is slightly greater than the minimum value $L^2/2I_3$ the ellipsoid intersects the sphere in small closed curves around the z -axis, which is the principal axis with the greatest moment of inertia. As the energy approaches its minimum value, these curves shrink to a point at the poles of the z -axis. As the energy increases, the curves become larger, and for $E = L^2/2I_2$ they become two plane curves (circles) which intersect at the poles of the y -axis. When the energy increases further, two separate closed paths appear again, but now around the poles of the x -axis. As the energy approaches its maximum value $E = L^2/2I_1$ the curves shrink to a point at the poles of the x -axis.

Since all the paths are closed, the motion of the angular momentum vector \mathbf{L} must be periodic. Rotation around the principal axis corresponding to either the greatest or smallest moment of inertia (the x and z axes in this case) is stable, while rotation around the principal axis corresponding to the intermediate moment (the y axis in this case) is unstable. Stable here means that if the body is made to deviate slightly from such a state, the resulting motion is close to the original one. Near the x and z axes, the paths lie in the vicinity of the corresponding poles, but the paths which pass near the poles on the y axis go elsewhere, to larger distances from those poles, no matter how close to the poles they start. The minimum energy state corresponds to the stable rotation around the principal axis associated with the largest moment of inertia.

As $I_1 \rightarrow I_2$ (see Figure B.1, A→C), the two plane curves corresponding to $E = L^2/2I_2$ approach

each other and the small closed curves around the x -axis become more elongated. When the rigid body is an oblate ellipsoid with $I_1 = I_2$ (see Figure B.1, C) the two plane curves which intersect the y -axis become co-planar and the small closed curves around the x -axis, which are bounded by these plane curves, disappear. All the paths of intersection become plane curves and the only stable solutions correspond to small circles around the z -axis. Therefore, rotation around the principal axis associated with the greatest moment of inertia is stable, while rotation around the remaining two axes (with the same moments of inertia) is unstable. Note that the only stable solution in this case corresponds to the state of minimum energy.

B.2 Equation of motion for a rigid oblate ellipsoid

For illustration, and completeness, I consider the rotational stability of an oblate rigid ellipsoid by explicitly solving the equation for angular momentum conservation (commonly referred to as Euler's equation, see §2.1)

$$\frac{d\mathbf{L}}{dt} + \boldsymbol{\Omega} \times \mathbf{L} = 0, \quad (\text{B.3})$$

where \mathbf{L} is the angular momentum vector and the first term represents a time derivative in a reference frame fixed to the rotating body with angular velocity $\boldsymbol{\Omega}$. In component notation, one can write $L_i = I_{ij}\Omega_j$, where I_{ij} is the moment of inertia tensor, and the angular momentum conservation law becomes

$$\frac{d}{dt}(I_{ij}\Omega_j) + \epsilon_{ijk}\Omega_j I_{k\ell}\Omega_\ell = I_{ij}\dot{\Omega}_j + \dot{I}_{ij}\Omega_j + \epsilon_{ijk}\Omega_j I_{k\ell}\Omega_\ell = 0. \quad (\text{B.4})$$

We can ignore the term associated with changes in the inertia tensor ($\dot{I}_{ij}\Omega_j$) since the derivative is taken in the body frame and a rigid body is assumed. The body principal axes reference frame is chosen so that the inertia tensor is diagonal. For an oblate ellipsoid, one can assume, with no loss of generality, $I_{11} = I_{22} \equiv A < I_{33} \equiv C$ to write Euler's equation as

$$\begin{aligned} I_1\dot{\Omega}_1 + \Omega_2 I_3 \Omega_3 - \Omega_3 I_2 \Omega_2 &= 0 \rightarrow \dot{\Omega}_1 = -\Omega_2 \frac{\Omega_3(C-A)}{A} \\ I_2\dot{\Omega}_2 + \Omega_3 I_1 \Omega_1 - \Omega_1 I_3 \Omega_3 &= 0 \rightarrow \dot{\Omega}_2 = \Omega_1 \frac{\Omega_3(C-A)}{A} \\ I_3\dot{\Omega}_3 + \Omega_1 I_2 \Omega_2 - \Omega_2 I_1 \Omega_1 &= 0 \rightarrow \dot{\Omega}_3 = 0. \end{aligned} \quad (\text{B.5})$$

The motion of the oblate ellipsoid proceeds such that Ω_3 (and $L_3 = C\Omega_3$) is constant (see Figure B.2). Defining the constant angular velocity $\sigma_r \equiv \Omega_3(C-A)/A$, multiplying the first line in equation B.5 by $i \equiv \sqrt{-1}$, and adding the resulting equation to the second line yields

$$\dot{\Omega}_1 + i\dot{\Omega}_2 = -i\sigma_r(\Omega_1 + i\Omega_2). \quad (\text{B.6})$$

Introducing the new variable $\eta \equiv \Omega_1 + i\Omega_2$ gives

$$\dot{\eta} = i\sigma_r\eta, \quad (\text{B.7})$$

with solutions $\eta = |\eta|e^{i\sigma_r t} = |\eta|\cos(\sigma_r t) + i|\eta|\sin(\sigma_r t)$, where $|\eta| = (\Omega_1^2 + \Omega_2^2)^{1/2} \equiv \Omega_R$. The complete solutions for the rotation vector $\boldsymbol{\Omega}$ are

$$\begin{aligned} \Omega_1 &= \Omega_R \cos(\sigma_r t) \\ \Omega_2 &= \Omega_R \sin(\sigma_r t) \\ \Omega_3 &= \text{constant}. \end{aligned} \quad (\text{B.8})$$

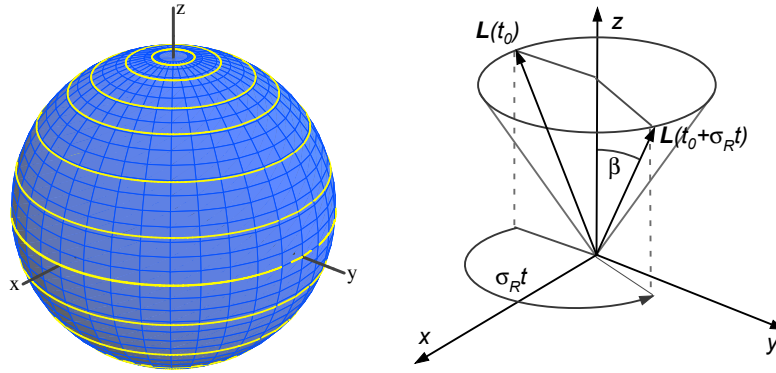


Figure B.2 Left, curves arising from the intersection of a sphere with an oblate ellipsoid corresponding to conservation of angular momentum and energy (see equations B.1). The frame shows intersections for different energies in the permitted range (see equation B.2). Right, the evolution of the angular momentum vector \mathbf{L} in the principal axes body frame.

The rotation vector $\boldsymbol{\Omega}$ revolves around the z axis with constant angular amplitude $\alpha = \tan^{-1}(\Omega_R/\Omega_3)$ and period $2\pi/\sigma_r$. In the principal axes body reference frame, the angular momentum takes the simple form

$$\begin{aligned} L_1 &= A\Omega_1 = A\Omega_R \cos(\sigma_r t) \\ L_2 &= A\Omega_2 = A\Omega_R \sin(\sigma_r t) \\ L_3 &= C\Omega_3 = \text{constant}, \end{aligned}$$

and thus, the angular momentum vector \mathbf{L} revolves around the z axis with the same period ($2\pi/\sigma_r$) and angular amplitude $\beta = \tan^{-1}(A\Omega_R/C\Omega_3)$. This solution is consistent with the family of curves arising from the intersection of the angular momentum sphere with the energy ellipsoid discussed in the previous section. It is important to note that for an external observer the angular momentum must be fixed and the rigid body librates around the constant angular momentum vector (with

period $2\pi/\sigma_r$ and constant angular amplitude β).

It is expected that the Earth rotation axis exhibits this free precession (in addition to forced precessions due to external torques). The ratio of the moments of inertia is such that $(C - A)/A \sim 1/300$; therefore, the precession frequency is $\sigma_r \sim \Omega_3/300$. Given that the angular amplitude of the precession is very small (i.e., $\alpha \ll 1$), one can assume $\Omega_3 = \Omega \cos \alpha \sim \Omega = (2\pi/1\text{day})$, which predicts a period of precession of about 300 days. Observations show that the rotation axis amplitude spectrum is characterized by two main peaks, one centred at 12 months, the other at about 434 days (Lambeck, 1980). The annual period motion is a forced wobble driven by seasonal redistribution of mass within and between the atmosphere, oceans, and ground surface waters (e.g., Lambeck, 1980; Chapter 7). The second component is known as the Chandler wobble or the free Eulerian precession and its frequency is associated with the free precession frequency σ_R derived above. The discrepancy between the predicted free precession period of ~ 300 days and the observed period of ~ 434 days arises due to the fact that the Earth is not a rigid body. The influence of oceans increases the Chandler period by ~ 28 days (Dahlen, 1976). If the Earth rheology were completely fluid then the figure axis would instantaneously adjust to the rotation axis and there could be no precession.

Appendix C

Inertia tensor for a distribution of mass anomalies on a sphere in the centre of mass reference frame

We calculate the inertia tensor for a quasi-rigid body consisting of a homogeneous sphere with mass M and radius a , and a collection of N mass anomalies on the surface of the sphere with masses m_n and position vectors \mathbf{a}_n .

For illustration, let us calculate the inertia tensor in a reference frame with origin at the centre of the sphere. The inertia tensor for the sphere can be written as

$$I_{ij}^{\circ} = \int_V dV \rho [\delta_{ij} r^2 - r_i r_j], \quad (\text{C.1})$$

where $\rho = 3M/4\pi a^3$ is the density of the sphere, and $dV = r^2 dr \sin \theta d\theta d\phi$ is an infinitesimal volume element at the position vector $\mathbf{r} = r(\sin \theta \sin \phi, \sin \theta \cos \phi, \cos \theta)$. The inertia tensor of the mass anomalies can be written as

$$I_{ij}^N = \frac{2}{5} M a^2 + \sum_{n=1}^N m_n (\delta_{ij} a_n^2 - a_{n,i} a_{n,j}), \quad (\text{C.2})$$

where \mathbf{a}_n is the position vector for the n th mass anomaly.

Let us now consider these inertia tensor perturbations in the centre of mass reference frame. First, I find the position vector for the centre of mass, which is denoted as \mathbf{R} , relative to the centre of the sphere:

$$\mathbf{R} = \frac{\sum_{n=1}^N m_n \mathbf{a}_n}{M + \sum_{n=1}^N m_n}. \quad (\text{C.3})$$

Next, I write the position vector for the sphere volume elements and mass anomalies relative to the centre of mass reference frame as $\mathbf{r}' = \mathbf{r} - \mathbf{R}$ and $\mathbf{a}' = \mathbf{a} - \mathbf{R}$. The inertia tensor for the sphere becomes

$$\begin{aligned} I_{ij}^{\circ'} &= \int dV \rho (\delta_{ij} r'^2 - r'_i r'_j) \\ &= \int dV \rho [\delta_{ij} (\mathbf{r} - \mathbf{R})^2 - (r_i - R_i)(r_j - R_j)] \\ &= \int dV \rho [\delta_{ij} r^2 - r_i r_j] + \int dV \rho [\delta_{ij} R^2 - R_i R_j] + \int dV \rho [2\delta_{ij} r_i R_j + r_i R_j + r_j R_i] \end{aligned} \quad (\text{C.4})$$

On the right-hand-side in the last equation, the last integral vanishes since $\int \rho dV r_i = \int dm r_i = 0$ (i.e., the centre of mass of the sphere is at the centre of the sphere); and the first integral is equivalent to equation (C.1). Similarly, the inertia tensor associated with the mass anomalies becomes

$$\begin{aligned} I_{ij}^{N'} &= \sum_{n=1}^N m_n (\delta_{ij} a_n'^2 - a'_{n,i} a'_{n,j}) \\ &= \sum_{n=1}^N m_n [\delta_{ij} (\mathbf{a}_n - \mathbf{R})^2 - (a_{n,i} - R_i)(a_{n,j} - R_j)]. \end{aligned} \quad (\text{C.5})$$

Finally, the total inertia tensor in the centre of mass reference frame becomes

$$I'_{ij} = \frac{2}{5} M a^2 \delta_{ij} + M R^2 \delta_{ij} - M R_i R_j + \sum_{n=1}^N m_n [\delta_{ij} (\mathbf{a}_n - \mathbf{R})^2 - (a_{n,i} - R_i)(a_{n,j} - R_j)]. \quad (\text{C.6})$$

Appendix D

Spherical harmonic convention adopted in this thesis

In our derivations, I normalize the spherical harmonic functions $Y_{\ell m}$ such that

$$\int_{\Omega} d\Omega Y_{\ell' m'}^{\dagger}(\theta, \phi) Y_{\ell m}(\theta, \phi) = 4\pi \delta_{\ell \ell'} \delta_{m m'}, \quad (\text{D.1})$$

where Ω denotes the complete solid angle and $\delta_{\ell m}$ is the Kronecker delta. Note that $Y_{\ell, -m} = (-1)^m Y_{\ell m}^{\dagger}$, where \dagger represents the complex conjugate.

These spherical harmonics can be written as

$$Y_{\ell m}(\theta, \phi) = \sqrt{4\pi} J_{\ell m}, \quad (\text{D.2})$$

where $J_{\ell m}(\theta, \phi)$ are the spherical harmonics adopted by [Jackson \(1999\)](#). The completeness relation (e.g., [Jackson, 1999](#)) for the spherical harmonics adopted here becomes

$$\sum_{\ell=0}^{\infty} \sum_{m=-\ell}^{\ell} Y_{\ell m}^{\dagger}(\theta', \phi') Y_{\ell m}(\theta, \phi) = 4\pi \delta(\phi - \phi') \delta(\cos \theta - \cos \theta'). \quad (\text{D.3})$$

The degree zero and two spherical harmonics used here are

$$\begin{aligned} Y_{00} &= 1 \\ Y_{20}(\theta) &= \sqrt{5} \left(\frac{3}{2} \cos^2 \theta - \frac{1}{2} \right) \\ Y_{21}(\theta, \phi) &= -\sqrt{\frac{15}{2}} \sin \theta \cos \theta e^{i\phi} \\ Y_{22}(\theta, \phi) &= \frac{1}{2} \sqrt{\frac{15}{2}} \sin^2 \theta e^{2i\phi}. \end{aligned} \quad (\text{D.4})$$

An arbitrary function $f(\theta, \phi)$ can be expanded in spherical harmonics as

$$f(\theta, \phi) = \sum_{\ell=0}^{\infty} \sum_{m=-\ell}^{\ell} B_{\ell m} Y_{\ell m}(\theta, \phi). \quad (\text{D.5})$$

The expansion coefficients can be found by evaluating the integral

$$B_{\ell m} = \frac{1}{4\pi} \int d\Omega Y_{\ell m}^{\dagger}(\theta, \phi) f(\theta, \phi), \quad (\text{D.6})$$

where the orthogonality condition (D.1) is used. The coefficients associated with our normalization $B_{\ell m}$ are related to the coefficients with Jackson (1999)'s normalization $A_{\ell m}$ by

$$B_{\ell m} = \frac{1}{4\pi} \int d\Omega Y_{\ell m}^{\dagger}(\theta, \phi) f(\theta, \phi) = \frac{1}{\sqrt{4\pi}} \int d\Omega J_{\ell m}^{\dagger}(\theta, \phi) f(\theta, \phi) = \frac{A_{\ell m}}{\sqrt{4\pi}} \quad (\text{D.7})$$

The addition theorem for spherical harmonics relates the angular distance γ between two vectors \mathbf{r} and \mathbf{r}' with spherical coordinates (θ, ϕ) and (θ', ϕ') respectively (see e.g., Jackson 1999). The addition theorem with the normalization adopted here reads

$$Y_{\ell 0}(\cos \gamma) = P_{\ell}(\cos \gamma) = \frac{1}{\sqrt{2\ell + 1}} \sum_{m=-\ell}^{\ell} Y_{\ell m}^{\dagger}(\theta', \phi') Y_{\ell m}(\theta, \phi), \quad (\text{D.8})$$

where $\cos \gamma = \cos \theta \cos \theta' + \sin \theta \sin \theta' \cos(\phi - \phi')$.

A useful expansion for calculating gravitational potentials is the multipole expansion

$$\frac{1}{|\mathbf{r} - \mathbf{r}'|} = \frac{1}{r_{>}} \sum_{l=0}^{\infty} \left(\frac{r_{<}}{r_{>}} \right)^l P_l(\cos \gamma) = \frac{1}{r_{>}} \sum_{l=0}^{\infty} \frac{1}{(2l + 1)} \left(\frac{r_{<}}{r_{>}} \right)^l \sum_{m=-l}^l Y_{\ell m}^{\dagger}(\theta', \phi') Y_{\ell m}(\theta, \phi), \quad (\text{D.9})$$

where $r_{<}$ and $r_{>}$ are the magnitudes of the smaller and larger vector respectively.

Appendix E

Inverse Laplace transform of the linearized Liouville equation

Wu & Peltier (1984, equations 79-80) inverted the s -domain Liouville equation (6.39) to obtain the following time domain solution:

$$\mathbf{m}(t) = \frac{\Omega}{A\sigma_o} \left\{ D_1 \mathbf{I}^L(t) + D_2 \int_{t=0}^t \mathbf{I}^L(t') dt' + \sum_{k=1}^{K-1} E_k [\mathbf{I}^L(t) * \exp(-\lambda_k t)] \right\} \quad (\text{E.1})$$

where σ_o is the wobble frequency on the deformable Earth,

$$D_1 = 1 + k_2^{L,E}, \quad (\text{E.2})$$

$$D_2 = [1 + k_2^L(s=0)] \frac{\prod_{l=1}^K s_l}{\prod_{l=1}^{K-1} \lambda_l}, \quad (\text{E.3})$$

and

$$E_k = - \frac{\frac{1+k_2^L(s=0)}{\lambda_k} \prod_{l=1}^K (s_l - \lambda_k) + \sum_{j=1}^K \frac{r'_j}{s_j} \prod_{l \neq j}^K (s_l - \lambda_k)}{\prod_{q \neq i}^{K-1} (\lambda_q - \lambda_k)}. \quad (\text{E.4})$$

The inverse decay times λ_i represent the $K - 1$ roots of the equation:

$$Q_{K-1}(s) = \sum_{j=1}^K g_j^T \prod_{i \neq j}^K (s + s_i). \quad (\text{E.5})$$

where

$$g_j^T = \frac{\frac{r''_j}{s_j}}{\sum_{q=1}^K \frac{r''_q}{s_q}} \quad (\text{E.6})$$

In the text the case of a single load component applied and retained on the Earth at some time t_0 is discussed. In this case one can write $\mathbf{I}^L(t) = \mathbf{I}^L H(t - t_0)$, where H is the Heaviside step

function. Using the above equations, the rotational response to the loading is given by:

$$\mathbf{m}(t) = \frac{\Omega}{A\sigma_o} \left\{ D_1 \mathbf{I}^L + D_2 \mathbf{I}^L t + \mathbf{I}^L \sum_{k=1}^{K-1} \frac{E_k}{\lambda_k} [1 - \exp(-\lambda_k t)] \right\} \quad (\text{E.7})$$

Bibliography

- Adams, F. C., Hollenbach, D., Laughlin, G., & Gorti, U., Photoevaporation of Circumstellar Disks Due to External Far-Ultraviolet Radiation in Stellar Aggregates. 2004, *ApJ*, 611, 360 [\[ADS\]](#)
- Adams, F. C., Lada, C. J., & Shu, F. H., Spectral evolution of young stellar objects. 1987, *ApJ*, 312, 788 [\[ADS\]](#)
- Alexander, R. D., Clarke, C. J., & Pringle, J. E., Constraints on the ionizing flux emitted by T Tauri stars. 2005, *MNRAS*, 358, 283 [\[ADS\]](#)
- Arfken, G. & Weber, H. 1995, *Mathematical methods for physicists*, 4th edn., *Mathematical methods for physicists*, 4th edn. (Academic Press) [\[ADS\]](#)
- Arkani-Hamed, J., Giant impact basins trace the ancient equator of Mars. 2005, *J. geophys. Res.*
- Arkani-Hamed, J. & Boutin, D., Paleomagnetic poles of Mars: Revisited. 2004, *Journal of Geophysical Research (Planets)*, 3011 [\[ADS\]](#)
- Bally, J., O'Dell, C. R., & McCaughrean, M. J., Disks, Microjets, Windblown Bubbles, and Outflows in the Orion Nebula. 2000, *AJ*, 119, 2919 [\[ADS\]](#)
- Banerdt, W. B., Golombek, M. P., & Tanaka, K. L. 1992, Stress and tectonics on Mars, *Stress and tectonics on Mars (Mars)*, 249–297 [\[ADS\]](#)
- Barnes, J. W. & Fortney, J. J., Measuring the Oblateness and Rotation of Transiting Extrasolar Giant Planets. 2003, *ApJ*, 588, 545 [\[ADS\]](#)
- Beauge, C. & Aarseth, S. J., N-body simulations of planetary formation. 1990, *MNRAS*, 245, 30 [\[ADS\]](#)
- Bertout, C., Basri, G., & Bouvier, J., Accretion disks around T Tauri stars. 1988, *ApJ*, 330, 350 [\[ADS\]](#)
- Besse, J. & Courtillot, V., Apparent and true polar wander and the geometry of the geomagnetic field over the last 200 Myr. 2002, *Journal of Geophysical Research (Solid Earth)*, 6 [\[ADS\]](#)

- Bills, B. G. & James, T. S., Late Quaternary variations in relative sea level due to glacial cycle polar wander. 1996, *Geophys. Res. Lett.* , 23, 3023 [ADS]
- Bills, B. G. & James, T. S., Moments of inertia and rotational stability of Mars: Lithospheric support of subhydrostatic rotational flattening. 1999, *J. geophys. Res.* , 104, 9081 [ADS]
- Bodenheimer, P., Hubickyj, O., & Lissauer, J. J., Models of the in Situ Formation of Detected Extrasolar Giant Planets. 2000, *Icarus*, 143, 2 [ADS]
- Boss, A. P., Proximity of Jupiter-Like Planets to Low-Mass Stars. 1995, *Science*, 267, 360 [ADS]
- , Possible Rapid Gas Giant Planet Formation in the Solar Nebula and Other Protoplanetary Disks. 2000, *ApJL*, 536, L101 [ADS]
- Bunge, H., Hagelberg, C. R., & Travis, B. J., Mantle circulation models with variational data assimilation: inferring past mantle flow and structure from plate motion histories and seismic tomography. 2003, *Geophysical Journal International*, 152, 280 [ADS]
- Bunge, H., Richards, M. A., Lithgow-Bertelloni, C., Baumgardner, J. R., Grand, S. P., & Romanowicz, B. A., Time Scales and Heterogeneous Structure in Geodynamic Earth Models. 1998, *Science*, 280, 91 [ADS]
- Calvet, N. & Gullbring, E., The Structure and Emission of the Accretion Shock in T Tauri Stars. 1998, *ApJ*, 509, 802 [ADS]
- Calvet, N., Magris, G. C., Patino, A., & D'Alessio, P., Irradiation of Accretion Disks around Young Objects. II. Continuum Energy Distribution. 1992, *Revista Mexicana de Astronomia y Astrofisica*, 24, 27 [ADS]
- Chambers, J. E., Making More Terrestrial Planets. 2001, *Icarus*, 152, 205 [ADS]
- Chiang, E. I. & Goldreich, P., Spectral Energy Distributions of T Tauri Stars with Passive Circumstellar Disks. 1997, *ApJ*, 490, 368 [ADS]
- Clarke, C. J., Gendrin, A., & Sotomayor, M., The dispersal of circumstellar discs: the role of the ultraviolet switch. 2001, *MNRAS*, 328, 485 [LINK]
- Cuzzi, J. N., R., D. A., & M., C. J., Particle-Gas Dynamics in the Midplane of a Protoplanetary Nebula. 1993, *Icarus*, 106, 102 [LINK]
- Dahlen, F. A., The passive influence of the oceans upon the rotation of the Earth. 1976, *Geophys. J. R. astr. Soc.* , 46, 363
- D'Alessio, P., Calvet, N., Hartmann, L., Lizano, S., & Cantó, J., Accretion Disks around Young Objects. II. Tests of Well-mixed Models with ISM Dust. 1999, *ApJ*, 527, 893 [ADS]

- D'Alessio, P., Canto, J., Calvet, N., & Lizano, S., Accretion Disks around Young Objects. I. The Detailed Vertical Structure. 1998, *ApJ*, 500, 411 [\[ADS\]](#)
- Daradich, A. L., Matsuyama, I., & Mitrovica, J. X., Mantle Dynamics and the Long-Term Rotational Stability of the Earth. 2005, in preparation
- Dziewonski, A. M. & Anderson, D. L., Preliminary reference Earth model. 1981, *Physics of the Earth and Planetary Interiors*, 25, 297 [\[ADS\]](#)
- Feigelson, E. D. & Montmerle, T., High-Energy Processes in Young Stellar Objects. 1999, *ARAA*, 37, 363 [\[ADS\]](#)
- Fisher, D., Some more remarks on polar wandering. 1974, *Journal of Geophysical Research*, 79, 4041
- Font, A. S., McCarthy, I. G., Johnstone, D., & Ballantyne, D. R., Photoevaporation of Circumstellar Disks around Young Stars. 2004, *ApJ*, 607, 890 [\[ADS\]](#)
- Forte, A. M. & Mitrovica, J. X., A resonance in the Earth's obliquity and precession over the past 20 Myr driven by mantle convection. 1997, *Nature*, 390, 676
- Frank, J., King, A., & Raine, D. 2002, *Accretion power in astrophysics*, *Accretion power in astrophysics* (Cambridge University Press. 3rd ed.) [\[ADS\]](#)
- Galli, D. & Shu, F. H., Collapse of Magnetized Molecular Cloud Cores. I. Semianalytical Solution. 1993, *ApJ*, 417, 220 [\[ADS\]](#)
- Gasperini, P., Sabadini, R., & Yuen, D. A., Excitation of the earth's rotational axis by recent glacial discharges. 1986, *Geophys. Res. Lett.* , 13, 533 [\[ADS\]](#)
- Gold, T., Instability of the Earth's axis of rotation. 1955, *Nature*, 175, 526
- Goldreich, P. & Toomre, A., Some remarks on polar wandering. 1969, *Journal of Geophysical Research*, 74, 2555
- Goldreich, P. & Tremaine, S., The excitation of density waves at the Lindblad and corotation resonances by an external potential. 1979, *ApJ*, 233, 857 [\[LINK\]](#)
- , Disk-satellite interactions. 1980, *ApJ*, 241, 425 [\[LINK\]](#)
- Goldreich, P. & Ward, W. R., The Formation of Planetesimals. 1973, *ApJ*, 183, 1051 [\[LINK\]](#)
- Goodman, J. & Pindor, B., Secular Instability and Planetesimal Formation in the Dust Layer. 2000, *Icarus*, 148, 537 [\[LINK\]](#)

- Greff-Lefftz, M., Upwelling plumes, superwells and true polar wander. 2004, *Geophys. J. Int.* , 159, 1125
- Grimm, R. E. & Solomon, S. C., Tectonic tests of proposed polar wander paths for Mars and the moon. 1986, *Icarus*, 65, 110 [[ADS](#)]
- Gross, R. & Vondrak, J., Astrometric and space-geodetic observations of polar wander. 1999, *Geophys. Res. Lett.* , 26, 2085 [[LINK](#)]
- Gullbring, E., Calvet, N., Muzerolle, J., & Hartmann, L., The Structure and Emission of the Accretion Shock in T Tauri Stars. II. The Ultraviolet-Continuum Emission. 2000, *ApJ*, 544, 927 [[ADS](#)]
- Haisch, K. E., Lada, E. A., & Lada, C. J., Disk Frequencies and Lifetimes in Young Clusters. 2001, *ApJL*, 553, L153 [[ADS](#)]
- Han, D. & Wahr, J. 1989, *AGU Mono. Series 49*, 1
- Hartmann, L. 1998, *Accretion processes in star formation*, *Accretion processes in star formation (Accretion processes in star formation / Lee Hartmann. Cambridge, UK ; New York : Cambridge University Press, 1998. (Cambridge astrophysics series ; 32) ISBN 0521435072.)* [[ADS](#)]
- Hartmann, L., Calvet, N., Gullbring, E., & D'Alessio, P., Accretion and the Evolution of T Tauri Disks. 1998, *ApJ*, 495, 385 [[ADS](#)]
- Hartmann, L., Hewett, R., & Calvet, N., Magnetospheric accretion models for T Tauri stars. 1: Balmer line profiles without rotation. 1994, *ApJ*, 426, 669 [[ADS](#)]
- Hillenbrand, L. A., *Young Circumstellar Disks and Their Evolution: A Review*. 2002 [[LINK](#)]
- Hollenbach, D., Johnstone, D., Lizano, S., & Shu, F., Photoevaporation of disks around massive stars and application to ultracompact H II regions. 1994, *ApJ*, 428, 654 [[ADS](#)]
- Hollenbach, D. J., Yorke, H. W., & Johnstone, D., Disk Dispersal around Young Stars. 2000, *Protostars and Planets IV*, 401 [[ADS](#)]
- Holman, M. J. & Murray, N. W., Chaos in High-Order Mean Resonances in the Outer Asteroid Belt. 1996, *AJ*, 112, 1278 [[ADS](#)]
- Ikoma, M., Nakazawa, K., & Emori, H., Formation of Giant Planets: Dependences on Core Accretion Rate and Grain Opacity. 2000, *ApJ*, 537, 1013 [[ADS](#)]
- Ivins, E. R., Sammis, C. G., & Yoder, C. F., Deep mantle viscous structure with prior estimate and satellite constraint. 1993, *J. geophys. Res.* , 98, 4579 [[ADS](#)]

- Jackson, J. 1999, Classical electrodynamics, Classical electrodynamics (John Wiley & Sons, 1998)
- Johns-Krull, C. M., Valenti, J. A., & Linsky, J. L., An IUE Atlas of Pre-Main-Sequence Stars. II. Far-Ultraviolet Accretion Diagnostics in T Tauri Stars. 2000, *ApJ*, 539, 815 [[ADS](#)]
- Johnston, P. & Lambeck, K., Postglacial rebound and sea level contributions to changes in the geoid and the Earth's rotation axis. 1999, *Geophysical Journal International*, 136, 537 [[ADS](#)]
- Johnstone, D., Hollenbach, D., & Bally, J., Photoevaporation of Disks and Clumps by Nearby Massive Stars: Application to Disk Destruction in the Orion Nebula. 1998, *ApJ*, 499, 758 [[LINK](#)]
- Königl, A., Disk accretion onto magnetic T Tauri stars. 1991, *ApJL*, 370, L39 [[ADS](#)]
- Kasting, J. F., Whitmire, D. P., & Reynolds, R. T., Habitable Zones around Main Sequence Stars. 1993, *Icarus*, 101, 108 [[ADS](#)]
- Kenyon, S. J. & Hartmann, L., Spectral energy distributions of T Tauri stars - Disk flaring and limits on accretion. 1987, *ApJ*, 323, 714 [[ADS](#)]
- Kenyon, S. J., Hartmann, L., Imhoff, C. L., & Cassatella, A., Ultraviolet spectroscopy of pre-main-sequence accretion disks. 1989, *ApJ*, 344, 925 [[ADS](#)]
- Kirschvink, J. L., Ripperdan, R. L., & Evans, D. A., Evidence for a Large-Scale Reorganization of Early Cambrian Continental Masses by Inertial Interchange True Polar Wander. 1997, *Science*, 277, 541 [[LINK](#)]
- Konacki, M. & Wolszczan, A., Masses and Orbital Inclinations of Planets in the PSR B1257+12 System. 2003, *ApJL*, 591, L147 [[ADS](#)]
- Lambeck, K. 1980, The earth's variable rotation: Geophysical causes and consequences, The earth's variable rotation: Geophysical causes and consequences (Cambridge University Press) [[LINK](#)]
- Landau, L. & Lifshitz, E. 1959, Fluid mechanics, Fluid mechanics (Course of theoretical physics, Oxford: Pergamon Press, 1959) [[ADS](#)]
- Larson, R. B., Gravitational torques and star formation. 1984, *MNRAS*, 206, 197 [[ADS](#)]
- Laskar, J., Joutel, F., & Robutel, P., Stabilization of the earth's obliquity by the moon. 1993, *Nature*, 361, 615 [[ADS](#)]
- Laskar, J. & Robutel, P., The chaotic obliquity of the planets. 1993, *Nature*, 361, 608 [[ADS](#)]
- Lenard, A., Adiabatic invariance to all orders. 1959, *Annals of Physics*, 6, 261
- Liffman, K., The Gravitational Radius of an Irradiated Disk. 2003, *Publications of the Astronomical Society of Australia*, 20, 337 [[ADS](#)]

- Lin, D. N. C. & Papaloizou, J., On the tidal interaction between protoplanets and the protoplanetary disk. III - Orbital migration of protoplanets. 1986, *ApJ*, 309, 846 [\[LINK\]](#)
- Lin, D. N. C. & Papaloizou, J. C. B. 1993, in *Protostars and Planets III*, in *Protostars and Planets III*, 749–835 [\[LINK\]](#)
- Liou, J. C. & Malhotra, R., Depletion of the outer asteroid belt. 1997, *Science*, 275, 375 [\[ADS\]](#)
- Lynden-Bell, D. & Pringle, J., The evolution of viscous discs and the origin of the nebular variables. 1974, *MNRAS*, 168, 603 [\[ADS\]](#)
- Matsuyama, I., Johnstone, D., & Hartmann, L., Viscous Diffusion and Photoevaporation of Stellar Disks. 2003, *ApJ*, 582, 893 [\[ADS\]](#)
- Mayer, L., Quinn, T., Wadsley, J., & Stadel, J., Formation of Giant Planets by Fragmentation of Protoplanetary Disks. 2002, *Science*, 298, 1756 [\[ADS\]](#)
- Mayor, M. & Queloz, D., A Jupiter-Mass Companion to a Solar-Type Star. 1995, *Nature*, 378, 355 [\[ADS\]](#)
- McCarthy, D. D. & Luzum, B. M., Path of the mean rotation pole from 1899 to 1994. 1996, *Geophys. J. Int.* , 125, 2085
- Melosh, H. J., Tectonic patterns on a reoriented planet - Mars. 1980, *Icarus*, 44, 745 [\[ADS\]](#)
- Meyer, M. R., Calvet, N., & Hillenbrand, L. A., Intrinsic Near-Infrared Excesses of T Tauri Stars: Understanding the Classical T Tauri Star Locus. 1997, *AJ*, 114, 288 [\[ADS\]](#)
- Milne, G. A. & Mitrovica, J. X., Postglacial sea level change on a rotating Earth: first results from a gravitationally self-consistent sea level equation. 1996, *Geophys. J. Int.* , 126, F13
- , Postglacial sea level change on a rotating Earth. 1998, *Geophys. J. Int.* , 133, 1
- Milne, G. A., Mitrovica, J. X., & Davis, J. L., Near-field hydro-isostasy: the implementation of a revised sea-level equation. 1999, *Geophysical Journal International*, 139, 464 [\[ADS\]](#)
- Mitrovica, J. X. & Milne, G. A., Glaciation-induced perturbations in the Earth's rotation: A new appraisal. 1998, *J. geophys. Res.* , 103, 985 [\[LINK\]](#)
- Mitrovica, J. X., Milne, G. A., & Davis, J. L., Glacial isostatic adjustment on a rotating earth. 2001, *Geophys. J. Int.* , 147, 562 [\[LINK\]](#)
- Mitrovica, J. X. & Peltier, W. R., Present-day secular variations in the zonal harmonics of earth's geopotential. 1993, *J. geophys. Res.* , 98, 4509 [\[ADS\]](#)

- Mound, J. E., Mitrovica, J. X., & Forte, A. M., The equilibrium form of a rotating earth with an elastic shell. 2003, *Geophysical Journal International*, 152, 237 [\[ADS\]](#)
- Munk, W. H., Twentieth century sea level: An enigma. 2002, *Proc. Nat. Acad. Sci.*, 99, 6550
- Munk, W. H. & MacDonald, G. J. F. 1960, *The rotation of the earth; a geophysical discussion*, The rotation of the earth; a geophysical discussion (Cambridge [Eng.] University Press, 1960.) [\[LINK\]](#)
- Murray, N., Hansen, B., Holman, M., & Tremaine, S., Migrating Planets. 1998, *Science*, 279, 69 [\[LINK\]](#)
- Nakada, M., Effect of the viscoelastic lithosphere on polar wander speed caused by the Late Pleistocene glacial cycles. 2000, *Geophysical Journal International*, 143, 230 [\[ADS\]](#)
- Nakada, M., Polar wander caused by the Quaternary glacial cycles and fluid Love number. 2002, *Earth and Planetary Science Letters*, 200, 159 [\[LINK\]](#)
- Nakiboglu, S. M., Hydrostatic theory of the earth and its mechanical implications. 1982, *Physics of the Earth and Planetary Interiors*, 28, 302 [\[ADS\]](#)
- Nakiboglu, S. M. & Lambeck, K., Deglaciation effects upon the rotation of the Earth. 1980, *Geophys. J. R. astr. Soc.* , 62, 49
- Navarro, L. & Garrido, L. M., Generalized adiabatic invariants in classical mechanics . 1968, *Journal of Physics A Mathematical General*, 1, 326 [\[ADS\]](#)
- Peltier, W. R., The impulse response of a Maxwell Earth. 1974, *Rev. Geophys.*, 12, 649
- , Glacial isostatic adjustment, II, the inverse problem. 1976, *Geophys. J. R. Astro. Soc.*, 46, 669
- , Global Sea Level and Earth Rotation. 1988, *Science*, 240, 895 [\[ADS\]](#)
- , Postglacial variations in the level of the sea: Implications for climate dynamics and solid-earth geophysics. 1998, *Reviews of Geophysics*, 36, 603 [\[ADS\]](#)
- Peltier, W. R. & Jiang, X., Glacial isostatic adjustment and Earth rotation: Refined constraints on the viscosity of the deepest mantle. 1996, *Geophys. J. Int.* , 101, 3269
- Peltier, W. R. & Wu, P., Continental lithospheric thickness and deglaciation induced true polar wander. 1983, *Geophys. Res. Lett.* , 10, 181 [\[ADS\]](#)
- Pollack, J. B., Hubickyj, O., Bodenheimer, P., Lissauer, J. J., Podolak, M., & Greenzweig, Y., Formation of the Giant Planets by Concurrent Accretion of Solids and Gas. 1996, *Icarus*, 124, 62 [\[ADS\]](#)

- Poppe, T., Blum, J., & Henning, T., Experiments on Collisional Grain Charging of Micron-sized Preplanetary Dust. 2000, *ApJ*, 533, 472 [\[LINK\]](#)
- Prévoit, M., Mattern, E., Camps, P., & Daignières, M., Evidence for a 20 deg tilting of the Earth's rotation axis 110 million years ago. 2000, *Earth and Planetary Science Letters*, 179, 517 [\[ADS\]](#)
- Press, W., Teukolsky, S., Vetterling, W., & Flannery, B. 1992, *Numerical recipes in C. The art of scientific computing*, Numerical recipes in C. The art of scientific computing (Cambridge: University Press, 2nd ed.) [\[ADS\]](#)
- Pringle, J., Accretion discs in astrophysics. 1981, *ARAA*, 19, 137 [\[ADS\]](#)
- Rasio, F. A. & Ford, E. B., Dynamical instabilities and the formation of extrasolar planetary systems. 1996, *Science*, 274, 954 [\[ADS\]](#)
- Ricard, Y., Spada, G., & Sabadini, R., Polar wandering of a dynamic earth. 1993, *Geophys. J. Int.*, 113, 284
- Richards, M. A., Bunge, H. P., Ricard, Y., & Baumgardner, J. R., Polar wandering in mantle convection models. 1999, *Geophys. Res. Lett.*, 26, 1777 [\[LINK\]](#)
- Richards, M. A., Ricard, Y., Lithgow-Bertelloni, C., Spada, G., & R., S., An explanation for the long-term stability of Earth's rotation axis. 1997, *Science*, 275, 372
- Richling, S. & Yorke, H. W., Photoevaporation of Protostellar Disks. V. Circumstellar Disks under the Influence of Both Extreme-Ultraviolet and Far-Ultraviolet Radiation. 2000, *ApJ*, 539, 258 [\[ADS\]](#)
- Sabadini, R. & Peltier, W. R., Pleistocene deglaciation and the Earth's rotation: implications for mantle viscosity. 1981, *Geophys. J. R. astr. Soc.*, 66, 553
- Sabadini, R. & Vermeersen, L. L. A., Ice-age cycles: Earth's rotation instabilities and sea-level changes. 1997, *Geophys. Res. Lett.*, 24, 3041 [\[ADS\]](#)
- Sager, W. W. & Koppers, A. A. P., Late Cretaceous Polar Wander of the Pacific Plate: Evidence of a Rapid True Polar Wander Event. 2000, *Science*, 287, 455 [\[ADS\]](#)
- Sasselov, D. D. & Lecar, M., On the Snow Line in Dusty Protoplanetary Disks. 2000, *ApJ*, 528, 995 [\[LINK\]](#)
- Schultz, P. & Lutz, A. B., Polar wandering of Mars. 1988, *Icarus*, 73, 91 [\[LINK\]](#)
- Schultz, P. H. & Lutz-Garihan, A. B., Grazing impacts on Mars: A record of lost satellites. 1982, *J. geophys. Res.*, 87, 84 [\[ADS\]](#)

- Sekiya, M., Gravitational instabilities in a dust-gas layer and formation of planetesimals in the solar nebula. 1983, *Progress of Theoretical Physics*, 69, 1116 [\[LINK\]](#)
- Sekiya, M., Quasi-Equilibrium Density Distributions of Small Dust Aggregations in the Solar Nebula. 1998, *Icarus*, 133, 298 [\[LINK\]](#)
- Shakura, N. I. & Sunyaev, R. A., Black holes in binary systems. Observational appearance. 1973, *A&A*, 24, 337 [\[ADS\]](#)
- Shu, F. H., Johnstone, D., & Hollenbach, D., Photoevaporation of the solar nebula and the formation of the giant planets. 1993, *Icarus*, 106, 92 [\[ADS\]](#)
- Spada, G., Sabadini, R., Yuen, D. A., & Ricard, Y., Effects on postglacial rebound from the hard rheology in the transition zone. 1992a, *Geophys. J. Int.*, 109, 683
- Spada, G., Ricard, Y., & Sabadini, R., Excitation of true polar wander by subduction. 1992b, *Nature*, 360, 452 [\[ADS\]](#)
- Spada, G., Sabadini, R., & Boschi, E., Long-term rotation and mantle dynamics of the Earth, Mars, and Venus. 1996, *J. geophys. Res.*, 101, 2253 [\[ADS\]](#)
- Störzer, H. & Hollenbach, D., Nonequilibrium Photodissociation Regions with Advancing Ionization Fronts. 1998, *ApJ*, 495, 853 [\[ADS\]](#)
- Störzer, H. & Hollenbach, D., Photodissociation Region Models of Photoevaporating Circumstellar Disks and Application to the Proplyds in Orion. 1999, *ApJ*, 515, 669 [\[ADS\]](#)
- Steinberger, B. & O'Connell, R. J., Changes of the Earth's rotation axis owing to advection of mantle density heterogeneities. 1997, *Nature*, 387, 169
- Tanaka, H., Takeuchi, T., & Ward, W. R., Three-Dimensional Interaction between a Planet and an Isothermal Gaseous Disk. I. Corotation and Lindblad Torques and Planet Migration. 2002, *ApJ*, 565, 1257 [\[ADS\]](#)
- Terebey, S., Shu, F. H., & Cassen, P., The collapse of the cores of slowly rotating isothermal clouds. 1984, *ApJ*, 286, 529 [\[ADS\]](#)
- Tinney, C. G., Butler, R. P., Marcy, G. W., Jones, H. R. A., Penny, A. J., McCarthy, C., & Carter, B. D., Two Extrasolar Planets from the Anglo-Australian Planet Search. 2002, *ApJ*, 571, 528 [\[ADS\]](#)
- Tushingham, A. M. & Peltier, W. R., Ice-3g - A new global model of late Pleistocene deglaciation based upon geophysical predictions of post-glacial relative sea level change. 1991, *J. geophys. Res.*, 96, 4497 [\[ADS\]](#)

- Valenti, J. A., Johns-Krull, C. M., & Linsky, J. L., An IUE Atlas of Pre-Main-Sequence Stars. I. Co-added Final Archive Spectra from the SWP Camera. 2000, *ApJS*, 129, 399 [ADS]
- Vermeersen, L. L. A., Fournier, A., & Sabadini, R., Changes in rotation induced by Pleistocene ice masses with stratified analytical Earth models. 1997, *J. geophys. Res.*, 102, 27689 [ADS]
- Vermeersen, L. L. A. & Sabadini, R., Significance of the fundamental mantle relaxation mode in polar wander simulations. 1996, *Geophys. J. Int.*, 127, F5
- Ward, W. R. 1992, Long-term orbital and spin dynamics of Mars, Long-term orbital and spin dynamics of Mars (Mars), 298–320 [ADS]
- , Protoplanet Migration by Nebula Tides. 1997, *Icarus*, 126, 261 [LINK]
- Weidenschilling, S. J., Aerodynamics of solid bodies in the solar nebula. 1977, *MNRAS*, 180, 57 [LINK]
- Wieczorek, M. A., Greff-Lefftz, M., Labrosse, S., van Thienen, P., Rouby, H., Besse, J., & Feldman, W. C. 2005, in 36th Annual Lunar and Planetary Science Conference, in 36th Annual Lunar and Planetary Science Conference, 1679–+ [ADS]
- Wilhelm, K., Lemaire, P., Dammasch, I. E., Hollandt, J., Schuehle, U., Curdt, W., Kucera, T., Hassler, D. M., & Huber, M. C. E., Solar irradiances and radiances of UV and EUV lines during the minimum of sunspot activity in 1996. 1998, *A&A*, 334, 685 [LINK]
- Willemann, R. J., Reorientation of planets with elastic lithospheres. 1984, *Icarus*, 60, 701 [LINK]
- Wolszczan, A., Confirmation of Earth Mass Planets Orbiting the Millisecond Pulsar PSR:B1257+12. 1994, *Science*, 264, 538 [ADS]
- Wu, P. & Peltier, W. R., Pleistocene deglaciation and the earth's rotation - A new analysis. 1984, *Geophysical Journal*, 76, 753 [ADS]
- Youdin, A. N. & Shu, F. H., Planetesimal Formation by Gravitational Instability. 2002, *ApJ*, 580, 494 [LINK]
- Yuen, D. A., Sabadini, R., & Boschi, E. V., Viscosity of the lower mantle as inferred from rotational data. 1982, *J. geophys. Res.*, 87, 10745 [ADS]
- , Viscosity stratification of the lower mantle as inferred from the J_2 observation. 1985, *Ann. Geophys.*, 3, 647
- Zuber, M. T. & Smith, D. E., Mars without Tharsis. 1997, *J. geophys. Res.*, 102, 28673 [ADS]